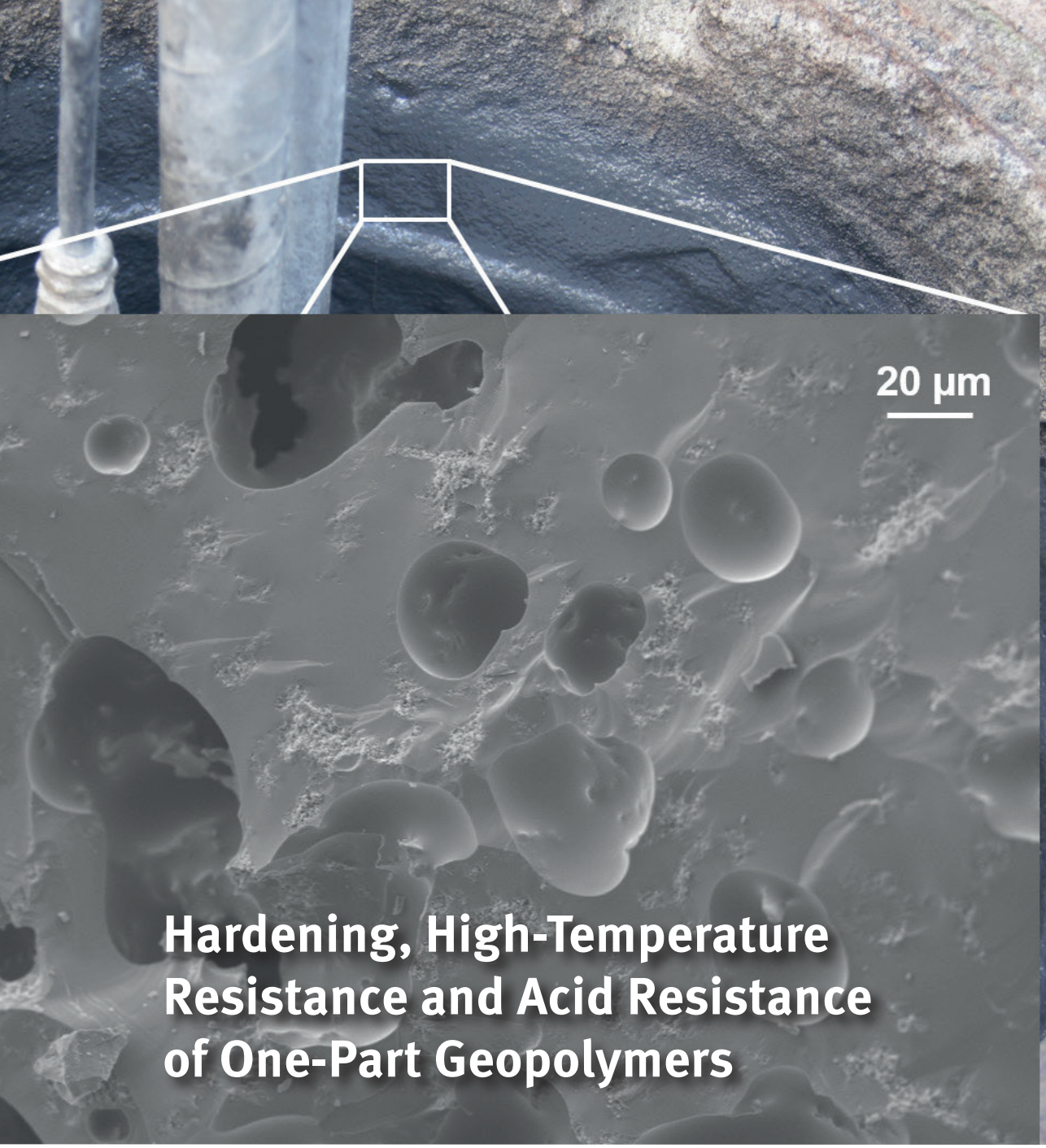

Hardening, High-Temperature Resistance and Acid Resistance of One-Part Geopolymers

Patrick Sturm

/ Department of the Built Environment

bouwstenen 249

Hardening, High-Temperature Resistance and Acid Resistance of One-Part Geopolymers

Patrick Sturm, 2018

Eindhoven University of Technology/ Department of the Built Environment

Title
Hardening, High-Temperature Resistance and Acid Resistance of One-Part Geopolymers

PhD Thesis, Eindhoven University of Technology, the Netherlands, 2018

ISBN 978-90-386-4524-7
Bouwstenen 249
NUR 955

Ph.D. Thesis, Eindhoven University of Technology, the Netherlands
Cover design: Patrick Sturm
Printed by: ProefschriftMaken, Vianen

Hardening, High-Temperature Resistance and Acid Resistance of One-Part Geopolymers

PROEFSCHRIFT (thesis)

ter verkrijging van de graad van doctor aan de Technische Universiteit Eindhoven, op gezag van de rector magnificus prof.dr.ir. F.P.T. Baaijens, voor een commissie aangewezen door het College voor Promoties, in het openbaar te verdedigen op maandag 2 juli 2018 om 16:00 uur

door

Patrick Sturm

geboren te Lutherstadt Eisleben, Duitsland

Dit proefschrift is goedgekeurd door de promotoren en de samenstelling van de promotiecommissie is als volgt:

Voorzitter:	prof.ir. E.S.M. Nelissen
1st promotor:	prof.dr.ir. H.J.H. Brouwers
Co-promotor:	Dr.-Ing. G.J.G. Gluth (Bundesanstalt für Materialforschung und -prüfung
leden:	Prof.Dr. M.C. Bignozzi (Università di Bologna) Prof.Dr.-Ing. L. Lohaus (Leibnitz Universität Hannover) Prof.Dr.Dr. H. Pöllmann (Martin-Luther-Universität Halle-Wittenberg) prof.dr.ir. E.J.M. Hensen prof.ir. S.N.M. Wijte

Het onderzoek of ontwerp dat in dit proefschrift wordt beschreven is uitgevoerd in overeenstemming met de TU/e Gedragscode Wetenschapsbeoefening.

In honor of my mother, Marion Sturm

PREFACE

This Ph.D. thesis is the result of the work of the last 5 years and I have to thank many people for their help during that time. While colleagues and project partners especially helped me to improve my scientific personality and to expand my life experience, my family and friends gave me the private backing especially during the hard times, I think every Ph.D. student goes through. Without the lucky combination of people in my life, it would have been impossible to reach this point. Thank you for the support, I sincerly appreciate all of it, but I would like to adress some persons in particular. First of all I want to gratitude prof.dr.ir. H.J.H. (Jos) Brouwers, for giving me the chance to do my Ph.D. research. Thank you for the guidance and the critical evaluations but also for the trust and the related freedom to deploy my work.

A special thanks goes to my daily supervisor in Berlin Dr.-Ing. G.J.G. Gluth from Bundesanstalt für Materialforschung- und prüfung (BAM), for giving the oppertunity to start and continue working at BAM. I learned so much from you about continous reliable work, writing and also how to be a better person and how hard it is to be a role model for others every day.

The first part of the thesis was conducted with the financial support from BAM within the MIS program (proposal Ideen_2012_36). In a second project, the devolopment of a repair mortar for sewer maintanance was focused. This project was funded by the BMWI and the Fa. *Hermes Technologie*. I want to acknowledge the financial support and especially I want to thank Rainer Hermes. With his great experience he guided us, making the step out of the lab into real life applications and facing the issues on cite.

I also want to thank prof.dr.ir E.J.M. Hensen and prof.ir. S.N.M. Wijte (Technische Universiteit Eindhoven) for the participation to my Ph.D. committee. Furthermore, I would like to thank the external committee members Prof.Dr.Dr. H. Pöllmann (Martin-Luther-Universität Halle-Wittenberg), Prof.Dr.-Ing. L. Lohaus (Leibnitz Universität Hannover) and Prof.Dr. M.C. Bignozzi (Univeristá di Bologna). The Ph.D. thesis was part of bigger proposal and I want to thank Dr. Sebastian Greiser and his supervisor Prof. Dr. C. Jäger from BAM (division 1.3). Sebastian, you finished first and I can only say thank you very much, working with you was always a pleasure.

I would like to thank the whole Division 7.4 of BAM, epecially the staff of the concrete laboratory, F. Haamkens, S. Schacht and I. Schulz, as well as the members of the chemistry laboratory, C. Hagemeister and M. Lindemann. A special thanks

goes to Dr. H.-C. Kühne, the head of division 7.4, for the critical talks and many inspirations. Furthermore, I want to thank all the students, that supported my work, especially J. Winkler and C. Paltzer who did their B.Eng. theses under my daily supervision. Special thanks go to my mom and my grandma. Everything I achieved in life, I owe you.

I wish everyone health and all the best for the future.

Patrick Sturm

Eindhoven, May 2018

CONTENTS

1. INTRODUCTION

1.1. General introduction

The alkali-activation of mineral binders is a subject of research and industries since more than 100 years. The first patent on alkali-activation of calcium containing slags with solid sodium containing activators, such as sodium carbonate or sodium sulfate was introduced by H. Kühl in 1908 [1]. The first investigations on the hardening mechanisms followed in 1930 [2] and in the 1970s the alkali-activation of slags was already commercially established, especially in the Ukraine [3]. A more detailed historical overview can be found in the latest state of the art report of RILEM TC 224-AAM [4].

Geopolymers (GP) are a sort of alkali-activated materials (AAM), that form aluminosilicate networks, without the necessity of calcium availability for the hardening. The term Geopolymers was originally introduced in the late 1970s and early 1980s, especially for high-temperature applications [5-8]. Since that time, GP have been subject of many research studies.

Geopolymers are inorganic materials with a wide range of possible applications including heat-resistant coatings and adhesives [9-15] as well as repair mortars with high acid-resistance [16] and excellent bond strengths [17, 18] or concretes with lower associated CO_2 emissions than Ordinary Portland Cement (OPC)-based concretes [19]. Because of this great potential, geopolymers have been extensively studied, in particular in terms of mechanical properties, microstructure and their properties at high-temperatures. These studies focused on conventional "two-part" geopolymer systems – *i.e.* geopolymers made from solid aluminosilicates (e.g. metakaolin (MK) or fly ash (FA)) and highly alkaline liquids, usually sodium silicate (SS = waterglass) or sodium hydroxide solutions at ambient or slightly elevated temperatures (cf., e.g., [4, 20]).

The production of GP can be realized with the use of industrial waste materials, what can make them a cheap alternative for conventional cementitious systems, e.g. OPC or Calcium Aluminate Cements (CAC) [20, 21] and help to reduce the amounts of landfilled industrial wastes. Simultaneously GP can contribute to a further decrease of the OPC production related CO_2 emissions, that are recently about 5-8% of the yearly worldwide anthropogenic CO_2 emissions [21-23], in context of a steadily increasing demand. Compared to OPC, the production of geopolymers releases up to 90% less CO_2 [20].

In the reaction systems, before the formation of geopolymers starts, dissolution processes occur in the raw materials. In the highly alkaline milieu, the building blocks of the aluminosilicates transform into hydrated monomers. In the course of the reaction, the monomers condense into dimers, oligomers and finally into a network,

forming the solid geopolymer gel [24, 25]. GP are aluminosilicate compounds whose network structure closely resembles those of zeolites [6, 26-28]. The geopolymeric gel is amorphous to X-rays [29], but in many cases the material contains crystalline zeolites (e.g. [20, 29, 30]). The geopolymeric gel can thus be regarded as metastable amorphous zeolites without long-range order that were unable to crystallize due to deficiency in water in the reaction system or the lack of time [31-33]. Essential progress for the understanding of the structure of the X-ray amorphous geopolymers have been realized by Nuclear Magnetic Resonance (NMR) spectroscopy [26-28, 34, 35]. The investigations revealed generally a tridimensional structural network of crosslinked SiO_4 and AlO_4 tetrahedra, including charge balancing alkali ions. Fundamental factors for the properties of geopolymers are the initial SiO_2/Al_2O_3 ratio and its changes over the time, as well as the type and amount of alkali ions. Pure Al-O-Al bonds are unstable in this aluminosilicate compounds and thus virtually absent, due to Loewenstein's rule [36]. Furthermore, a strong influence is related to the curing conditions of the fresh pastes, in terms of temperature, water availability (relative humidity; r.H.) and curing time [26, 35, 37, 38].

A new approach, that was established in the last years is the synthesis of so called "one-part" geopolymers (OPG) [39-42], which are produced by a different synthesis route. One-part geopolymers contain the activator in solid form and therefore only water must be added to initiate the hardening, *i.e.* mixing is performed in the same way as for conventional Portland cements. By applying this approach, it is not necessary to store and handle highly alkaline SS or sodium hydroxide solutions, which avoids problems with carbonation and aging of these solutions as well as problems with health and safety issues. This can provide a higher social and economic acceptance of these new binder materials [41, 43] and contribute to a further establishment of AAM.

Different ways to synthesize one-part geopolymers have been described [41, 44-47] and few structural, mechanical and rheological properties have been reported in the meantime [39-42, 44-46, 48-51]. However, compared to conventional geopolymers, much less is known about their microstructure, the processes during geopolymerization and the factors influencing the latter. In a previous study [40] a one-part geopolymer based on a silica rich by-product of the chlorosilane production (CR) and sodium aluminate (SA) has been investigated. The degree of reaction of the silica was measured to be about 50 %, proving that the composition of the reaction products differed considerably from the composition of the starting mix. In earlier studies on similar systems [39, 41] the SiO_2/Al_2O_3 and H_2O/Na_2O ratios of the starting composition were varied and microstructural differences of the hardened geopolymers observed, while the fraction of reacted silica was not determined.

In general, OPG systems often contain significant amounts of crystalline tectosilicates (zeolites) and the reported compressive strength is usually lower than for conventional two-part geopolymers [40, 41, 44, 46, 48, 50-53]. The reactions were mainly based on silica rich industrial by-products [40, 41, 48, 50, 51], as well as on alkali-thermal activation of minerals and industrial waste materials [44, 46, 52]. Besides industrial silicas, microsilica (MS) and CR, also biogenic Rice Husk Ash (RHA) was used as silica feedstock [49, 54]. RHA has been investigated for its use in various industrial applications including the use as supplementary cementitious material for conventional cement-based binder systems (cf. e.g., [55-57]) too. Recent studies also investigated the production of sodium silicate solutions from RHA for use as activating solution in conventional "two-part" geopolymers systems [58-61].

Specific geopolymers develop high compressive strength during geopolymerization reaction, but provide a decrease of the initial strength after certain times. The reason is related to the included water, but so far not sufficiently clarified. Especially shrinkage is a problem that often occurs. When compared to OPC pastes, mortars or concretes, AAM often show significantly more intense shrinkage under various conditions [62-65]. The factors influencing the properties of hardened geopolymers are not satisfyingly clarified, as well [26, 27, 37, 38, 66]. Furthermore, the influence of impurities (e.g. chloride, sulfate, magnesium), that occur in various residues, on the process of geopolymerization is still not systematically studied, as well as the availability of reactive silica and alumina species. Previous knowledge cannot easily be transferred to the new class of one-part geopolymers. To make use of the whole potential of these materials, it is thus important to gain further information on their formation and the factors influencing the properties of the reaction products.

1.2. Outline of the thesis

After the general introduction, the starting materials for the OPG synthesis and the related mortars, as well as the additional feedstocks and reference materials will be characterized. In the following the syntheses route for the OPG will be presented, including the design of the OPG pastes and mortars. Fig. 1.1 presents a framework of the outline of this work.

General fresh paste properties of pure OPG pastes will be studied in Chapter 3. Additionally the influence of several superplastisizers on the fresh pastes will be considered. The hardening and microstructure of the OPG pastes in terms of chemical composition and curing conditions will be focused in Chapter 4. This includes the determination of the degree of reaction in dependence of the initial SiO_2/Al_2O_3

ratio and the type of silica feedstock as well as the determination of the mineralogical phase assemblage and compressive strength after curing at various temperatures.

The properties of the synthesized OPG at high temperatures, including thermal dehydration and the related deformation behavior, as well as the development of the phase assemblage and the residual strength up to 1000 °C are studied in Chapter 5.

On this basis, the second part of the thesis focuses on OPG mortars. Therefore, Chapter 6 discusses general aspects of the workability of the fresh mortars and Chapter 7 studies their hardening. Chapter 8 presents the results of shrinkage and bond behavior of the mortars at ambient conditions, that are central factors for certain applications like concrete maintanance. Another important factor is the chemical durabilty and in the context of sewer systems especially the resistance against sulfuric acid attack. Therefore, the resistance of the OPG against H_2SO_4 in terms of the residual strength of the mortars and the microstructural alteration of the pastes are studied in Chapter 9.

General aspects of the OPG regarding additive manufacturing by Laser-induced slip casting (LIS) will be summerized in Chapter 10, regarding the fresh paste behavior, the phase formation and the influence of an additional alkaline activator (lithium aluminate). The last Chapter 11 will finally summarize the conclusions of this thesis.

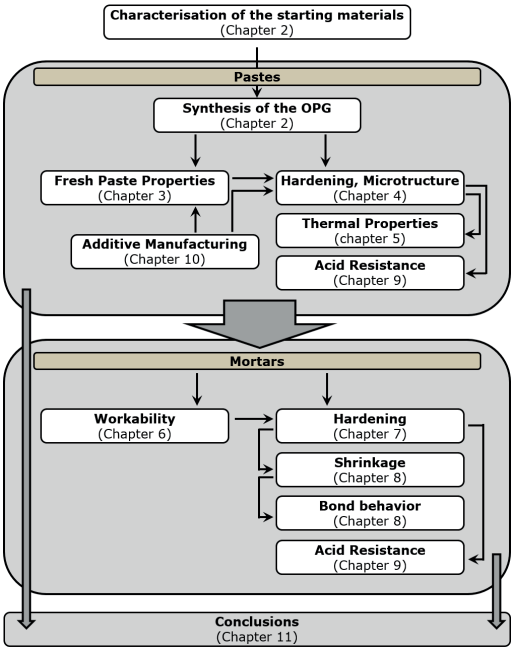

Figure 1.1: Framework of the thesis.

2. MATERIALS AND METHODS

2.1 Methods

2.1.1 Fresh paste properties

Viscometer tests

The focus of this work is on the properties of the OPG in the hardened state. Nevertheless, a test program was conducted for the characterization of the general rheological properties of the OPG fresh pastes. Therefore, the fresh pastes were measured in a viscometer (*Viskomat NT, Schleibinger Geräte, Germany*). Two specific cells with different geometries (mortar measuring cell with a wing stirrer for relative values; double gap measuring cell for absolute values) were applied.

Since huge parts of the SA dissolved immediately after the addition of water the behavior of the starting pore solution is strongly influenced by sodium and aluminate species. The nature of the pore solution has a great influence on the rheology of geopolymer binders [67]. Therefore, the viscosity of a saturated sodium aluminate solution was determined with a rheometer (*Anton Paar MCR 501*).

Spread flow testing of the fresh pastes

In addition to the viscometer tests also spread flow tests, using a small cylinder (d ≈ 5.10 cm, h ≈ 8.04 cm, V ≈ 164.02 cm^3), as proposed in [68] ("mini-cone" test) were performed (Section 3.2.). The inner wall of the cylinder was coated with formwork oil as release agent to ensure a complete release of the sticky fresh pastes.

The fundamental influence of several conventional superplasticizers on the workability of OPG fresh pastes has been studied, using the mini-cone test as well. Another small cylinder (d ≈ 38.4 cm, h ≈ 6.1 cm, V ≈ 70.9 cm^3) was used to investigate the slump flows and spread flows of the pastes (Section 3.3.). The spread flows were measured by putting 15 strikes on the slump flowed pastes on the Hägermann table as proposed in DIN EN 1015-3: 2007 [69]).

Spread flow testing of the fresh mortars

The workability of the fresh mortars was investigated using the spread flow method (Hägermann table), in accordance with DIN EN 1015-3: 2007 [69] but slightly adjusted. The difference was the use of conventional formwork oil as release agent instead of a thin water film that is proposed in the standard. The reason for that was the, compared to the pure pastes decreased but still sticky character, especially for mortars with a high paste content. After the measurement, the material was always removed due its contamination.

PH measurements

The pH value of specific pastes within the first 30 minutes after the addition of water was measured. In addition, pH measurements were performed on various sodium aluminate solutions. All Measurements were conducted using a METTLER DELTA 350 device with Metrom pH-electrode. Calibration of the electrode was done with standard buffer solutions of pH 7 and pH 10.

2.1.2. Characterization of solids

2.1.2.1. Starting materials and hardened pastes

ICP-OES

Chemical analysis of the solids was done by inductively coupled plasma optical emission spectrometry (ICP-OES) after total microwave digestion, using an "*iCAP 6000 Duo*" emission spectrometer from *Thermo Scientific*.

XRD analysis

All X-ray diffraction (XRD) measurements were recorded on a *Rigaku Ultima IV* diffractometer under the following conditions: Bragg-Brentano geometry; Cu Kα radiation (λ = 1.5419 Å); divergence slit: 10 mm and scanning range: 3–63° 2θ *or 5–65° 2*θ. The powdered samples rotated at a speed of 15 min^{-1}.

The solid feedstocks (except SA), as well as most of the hardened OPG have been conducted on powdered samples using a sampling interval of 0.02° 2θ and a scan rate of 0.5° 2θ min^{-1}. Due to the hygroscopic character of SA, those samples have been measured at a scan rate of 1.0° 2θ min^{-1}. The insoluble residues from the chemical determination of the degree of reaction, as well as the as-cured OPG samples of the same Section (Section 4.2.2.) and the MS- and CR-based OPG of the high-temperature investigations (Section 5.3.) have been measured at a sampling interval of 0.01° 2θ and a scan rate of 0.2° 2θ min^{-1}.

In the discussion it is assumed that a higher relative intensity of a phase in a diffractogram corresponds with a higher fraction of that phase in the investigated material, compared to a material with lower intensities of that phase. Though no quantitative analysis (e.g. Rietveld analysis) of the diffractograms has been undertaken, it is assumed that this approach allows at least a semi-quantitative estimation and interpretation of the results, particularly since the observed major crystalline phases (zeolites) that occurred in the OPG formulations have a cubic crystal structure, and thus preferred orientation effects are absent.

IR analysis

Attenuated total reflection Fourier transform infrared spectroscopy (ATR FT-IR) measurements were conducted on a *Bruker Tensor 27* device with a diamond ATR module and a RT-DLaTGS detector. The measuring range was 4000–400 cm^{-1}, with a resolution of 4 cm^{-1} and 16 scans per sample for an average spectrum.

Additional experiments on RHA(2)-based OPG were performed on a *Perkin Elmer Spectrum One* FT-IR spectrometer with an universal ATR sampling accessory. The measuring range was 4000–650 cm^{-1}, with a resolution of 4 cm^{-1} and 8 scans per sample.

SEM investigations

The scanning electron microscopy (SEM) investigations were performed on a *Carl Zeiss EVO MA10* device with a secondary electron (SE) detector and an accelerating voltage of 7–10 kV. The investigation of specific solid feedstocks was performed on powdered samples, whereas the investigations of the OPG specimens was performed on fracture surfaces. The aim was to avoid the destruction of metastable materials, such as hydrated phases, due to grinding and polishing. Samples were sputtered with gold before measurements.

NMR analysis

The cited solid state nuclear magnetic resonance (NMR) spectra, except the experiments regarding the acid resistance (cf. Chapter 9) are from the PhD thesis of Sebastian Greiser [70] or joint publications [48, 51]. The NMR spectra of Chapter 9 were recorded by Prof. Ch. Jäger in division 1.3 of BAM.

The ^{29}Si MAS NMR experiments of this work were performed on a *Bruker Avance 600 spectrometer* (119.2 MHZ) using a 4 mm triple-resonance probe with a sample spinning frequency of 12.5 kHz. The single pulse spectra were recorded at room temperature with a 90° pulse of 7.7 µs and at least 24 scans were accumulated. The recycle delay was 900 s because of long relaxation times of Q^4 species. The ^{29}Si MAS NMR shift was referenced using kaolinite as secondary chemical shift standard with –91.5 ppm for the upfield peak.

Laser granulometry

The particle size distributions (PSD) of the powder feedstocks were determined by laser granulometry, using a *HELOS/BR* laser granulometer with an open measuring cell. The preparation of the powders was done by dry dispersion.

Heat treatment

The heat treatment of paste cube specimens (20 mm × 20 mm × 20 mm) was done in muffle furnaces (*Carbolite CWF 12/5*; T_{max} = 1200 °C or *Nabertherm LT 5/11*; T_{max} = 1100 °C).

The processing of biogenic RHA (RHA(2)), for the removing of remaining carbon and organics was done at 600 °C, in the same muffle furnaces or in a rotary kiln (RT 1700) from *Thermal Technology*. The rotary kiln consisted of corundum, with a full length of 2000 mm, a heating zone of 1000 mm and a diameter of 100 mm. After several adjustments, the rotation speed of the tube was set to 2 min^{-1}. A slope of 1.0° was chosen for the kiln and the heating rate was set to 2.5 °C/min. The maximum temperature alternated between 600 ± 25 °C. The re-calcined ashes have been mixed after the burning.

TG analysis

Thermogravimetric (TG) investigations were conducted either on a Netzsch device (STA 449 C Jupiter) in N_2 atmosphere (MS- and CR-based OPG) or on a Perkin Elmer device (TGA 4000) in Ar atmosphere (RHA-based OPG), at a heating rate of 5 K min^{-1}, treating ≈ 20 mg sample mass. Experiments have been carried out between 20 °C and 1000 °C.

High-temperature dilatometry

The high-temperature dilatometry measurements of the OPG pastes were conducted on a vertical dilatometry device (*Bähr TMA 801*) from ambient temperature up to 900 °C. Samples were prepared with a high precision diamond saw blade to form square tablets of 5 mm height and 5 mm side lengths. Samples were heated at a rate of 5 K min^{-1} in air atmosphere. The loading force was 0.05 N. Changes of samples height were recorded during heating.

Degree of reaction of the silica

The procedure for the chemical determination of the degree of reaction of the silica sources was presented in Sturm et al. [51] and adapted from Fernández-Jiménez et al. [71], who introduced it for the determination of the degree of reaction of fly ash in conventional FA-based geopolymers. During the procedure all geopolymerization products, including zeolites, are virtually completely dissolved by theory, while the silica(te) starting material (FA or silica) remain largely unaffected. The dissolution method will be compared to results of another, NMR-based method, and critically discussed.

For the procedure, the hardened OPG specimens were crushed and ground in a disc mill for 18 s. The resulting powders were dried in a vacuum chamber at p = 40 mbar until a constant mass (defined as Δm < 0.2 wt.% within 24 h) was reached. The powders thus prepared completely passed a 63 µm width sieve.

Powder masses of (1.0000 ± 0.0005) g were stirred with 250 ml HCl (1:20) at ambient temperatures for three hours using a magnetic stirrer at a rotation speed of 750 rpm. After three hours the suspensions were filtered through ash free "red ribbon" filter paper. The insoluble residue and the filter paper was burned with a Bunsen burner using platinum crucibles as sampling holders. The samples were then transferred into a pre-heated oven (*Carbolite CWF 12/5*) at 1000 °C for at least five hours. After cooling down to ambient temperature in a desiccator the sample masses of the residues were determined. The percentage of insoluble residue was calculated from the latter mass, the initial sample weight and corrected for the dissolution of the pure silica in HCl. For each geopolymer the procedure was repeated on three samples and the results were averaged. The standard deviation of the percentage insoluble residue, *IR*, thus determined was lower than 0.2 wt.% in most cases and never greater than 0.55 wt.%.

From the measurements the degree of reaction of the silica (MS, CR or RHA(1)) in the OPG was calculated as follows: The insoluble residue of the dried geopolymer sample is defined as has been published in Sturm et al. [51]:

$$IR = \frac{m_{IR}}{m}, \tag{2.1}$$

where IR is the insoluble residue of the dried powder, m is the initial weight of the sample and m_{IR} is the sample weight after acid-treatment and ignition at 1000 °C. An analogous definition applies to the silica starting materials. The remaining silica after drying (but before acid-treatment) in the sample is then:

$$R_s = \frac{1}{IR_{silica}} \cdot IR_{geopolymer}\ , \tag{2.2}$$

where R_S is the remaining silica, IR_{silica} is the insoluble residue of the pure silica used (97.4 wt.% for MS; 86.4 wt.% for CR and 80.1 wt.% for RHA(1)) and $IR_{\mathrm{geopolymer}}$ is the insoluble residue of the dried geopolymer sample under investigation.

From the mix-design of the pastes and the water content of the vacuum dried powders (measured as loss on ignition (LOI) or calculated from the mass loss during hardening and drying) the total amount of silica (reacted and unreacted) in the dried powders can be calculated as:

$$c_{silica,dried} = c_{silica,paste} \cdot \frac{1-w_{dried}}{1-w_{paste}}, \tag{2.3}$$

where $c_{silica,dried}$ is the total amount of silica in the dried powder, $c_{silica,paste}$ is the amount of silica in the paste, w_{dried} is the water content of the dried powder and w_{paste} is the water content of the paste. Using *RS* and $c_{silica,dried}$, the degree of reaction of the silica in the geopolymer under investigation can then be calculated as follows:

$$\alpha[HCl] = 1 - \frac{R_s}{c_{silica,dried}}, \quad (2.4)$$

where α[HCl] is the degree of reaction of the silica, based on the dissolution method.

Compressive strength of the pastes

The compressive strength tests of pastes were performed on cube specimens (20 mm × 20 mm × 20 mm) on a *ToniPRAX* device, at a loading rate of 240 N/s, which is one tenth of the loading rate for the compressive strength testing of mortar prisms (2400 N/S) of DIN EN 196-1: 2005 [72]. This was equivalent to 0.6 MPa/s for the investigated specimen geometry.

2.1.2.2. Mortars

Compressive and flexural strength

The testing of the compressive and flexural strength of mortar prisms (40 mm × 40 mm × 160 mm) was carried out in accordance with DIN EN 196-1: 2005 [72], using a *ToniPRAX* device for combined measurements of compressive strength and flexural strength.

Shrinkage

The measurement of the shrinkage of the OPG mortars at ambient conditions was performed on standard mortar prisms (40 mm × 40 mm × 160 mm) in accordance with DIN EN 12617-4: 2002 [73], using a *Heidenhain MT12* (D-K-17552-01-00) measuring device. Two different curing conditions were applied (23 °C/ 50% r.H. and 23 °C/ ≈ 100% r.H.).

Pull-off tests

The determination of the bond strength was carried out by pull-off tests in accordance with DIN EN 1542:1999 [74], including adjustments. The mortars have been applied to standard MC 0.40 (w/b =0.40 by mass) concrete specimens or MC 0.90 (w/b =0.90 by mass) concrete specimens. Those concrete specimens have been produced in accordance with DIN EN 1766: 2017 [75]. The suggested dimensions of the specimens (300 mm × 300 mm × 300 mm) were adjusted to 250 mm × 250 mm × 50 mm. Thus, only four pull-off tests were conducted per concrete specimen.

One day before the testing, the surface of specimens was adjusted by grinding and the testing spots were prepared by core drilling (d = 50 ± 1 mm). Afterwards the specimens were transferred back to the specific curing conditions until testing. For the actual pull-off tests dollies have been glued to the high-pressure air cleaned surface of the core drills with a two-component adhesive (HF/MC-Quicksolid). After a hardening time of ≥ one hour at room temperature (RT) the adhesive was ready for use. The pull-off tests were carried out with a *F15D EASY M2000* device (1.5–15 kN) at a loading rate 100 N/s (≈ 0.05 MPa/s) until the failure occurred.

Sulfuric acid resistance

The investigation of the resistance against sulfuric acid was conducted on the basis of DIN 19573: 2016 (Appendix A) [76]. Moderate adjustments of the pre-treatment were applied. For every sample series 5 mortar prisms were prepared. The mortars were produced as described in DIN EN 196-1: 2005 [72]. After preparation of the mortar specimens (40 mm x 40 mm x 160 mm), the OPG mortars were subsequently transferred to an oven with climate conditioning and cured for 24 hours at a certain temperature and relative humidity.

After one day, the specimens were removed from the containers and each side of the prisms was ground manually for 15 seconds with abrasive paper (graining 320). To provide a gentle regime for the further hardening, in the following all prisms were stored at 23 °C and 50% r.H. for 25 days and to avoid early dilution of the activator solution (pore solution) samples were not stored under water between 2 days and 7 days after the production as proposed in the standard but at 23 °C/50% r.H., respectively. The prisms were cut into half (40 mm × 40 mm × 80 mm) at an age of 7 days and the dimension have been measured. At an age of 26 days the samples were transferred to a water bath (23 °C) to saturate the pores.

At an age of 28 days half of the cut prisms were transferred to sulfuric acid (pH = 1) and the other half remained under water. The sulfuric acid test specimens were covered with at least 5 mm in a volume of 8 l sulfuric acid (2 prisms) or 9.6 l (3 prisms). An automatic titration system (*Multi_T 2.2 digital titrator*) from *JENSEN SYSTEMS* was used to control pH value. Additionally, once a week the whole acid volume was exchanged with fresh H_2SO_4 solution. The specimens were placed on grates and a magnetic stirrer was used to provide a continuous homogenization of the acid solution. After 70 days under acid storage (age 98 days) the samples were removed from the acid bath.

In the following the samples have been brushed and the dimensions have been measured again. The ends of the prisms have been cut off, to provide a sample

height of 40 mm. After a further storage at 23 °C and 50% r.H. for 2 days the samples were tested for their residual compressive strength. The residual strength was calculated from the crushing load and referred to an uncorroded 1600 mm² base area. The values were compared to the compressive strength of the reference samples, which were stored under water. The reference specimens were prepared equally after removing from the water. The strength testing was done in accordance with DIN EN 196-1: 2005 [72]. From the residual strength and the initial dimensions, the effective strength related corrosion depth ($X_{f,D}$) was calculated as follows:

$$X_{f,D} = 0.5 \cdot d_0 \cdot \left[1 - \sqrt{\frac{F_{D,acid}}{F_{D,water}}}\right] [76] \quad (2.5)$$

$$d_0 = \sqrt{(a \cdot b)}\ [76] \quad (2.6)$$

where d_0 is the initial average edge length of the cross section (a×b) before the acid-treatment and F_D are the failure loads for the acid stored sample ($F_{D,acid}$) and the reference sample ($F_{D,water}$).

Optical microscopy

Optical microscopy was conducted on the pull-off test specimens, using an *Olympus SZX 16* stereo microscope with an integrated ultraviolet (UV) mode. Samples were embedded in epoxy resin(Conpox Resin BY 158; Conpox Hardener HY 2996) under vacuum. Additionally, an UV-active pigment (EPODYE) was added, for an investigation of micro cracks in the UV-mode.

2.2. Starting materials

2.2.1. Introduction

In this study OPG formulations were synthesized and investigated for their properties and possible applications. Therefore, separated solid silica and alumina sources have been mixed to yield specific molar SiO_2/Al_2O_3- ratios and just water had to be added to initiate the reaction. To exclude external contaminations, deionized water was used for the laboratory investigations.

Three different silica sources and two alumina sources were the primary feedstocks for the synthesis of the one-part formulations. Two industrial and one biogenic residue have been used as silica feedstocks. Microsilica (MS), *i.e.* silica fume, was used with only few chemical impurities. Virtually the whole amount of the yearly produced MS (1-2.3 Mt/a) is in use [77]. A silica rich residue from the chlorosilane production (CR), with a yearly volume of ca. 5000–10000 t/a per production site [40] was used, as second industrial silica. Silica CR is produced in several steps

during the wastewater treatment of the chlorosilane production [40]. Currently the material is deposited. Mainly due its critical chloride content, it is inappropriate for the cement industry as filler material.

Rice husk ash (RHA) is a silica-rich agriculture waste material, typically consisting of 90–95 wt.% SiO_2 [78]. In 2010 over 700 million tons of rice were produced worldwide [79] in a context of a steadily increasing demand. This led to an occurrence of about 140 million tons of husks. Calcination of the husks leaves about 25 wt.% of the initial mass is ash, the so-called RHA [80]. This ash is mainly dumped and causes huge deposits and significant land damages. The world leading rice producer India has a yearly occurrence of ≈ 20 Mt/a [80]. Highly reactive, amorphous RHA can be produced at calcination temperatures ≤ 800 °C [49, 54, 81-84], which is significantly below the temperatures for the production of conventional OPC clinkers. Heating at higher temperatures is not beneficial for alkali-activation, because it leads to the formation of crystalline high-temperature silicas like cristobalite and tridymite in the ash [84], which decreases its reactivity.

Sodium aluminate (SA) was used as alumina source for the main part of this work. The alumina feedstock contained the alkaline activator, *i.e.* sodium, in the solid state. Huge parts of the feedstock immediately dissolve after the addition of water and thus, the activator solution forms *in situ*. Additionally, lithium aluminate (LA) was applied for special investigations, especially regarding additive manufacturing of OPG.

A CEM I 42.5 R (CEM I) was used as reference for the evaluation of the general rheological properties of the fresh pastes. Additionally, ground granulated blast furnace slag (SL) was used as supplementary material, to study the influence of a calcium rich feedstock on the hardening and the durability of the reaction systems. CEM III/B was used as reference material for the investigations on the effects of heat treatment on the mechanical and structural properties of the OPG. A commercial calcium aluminate cement-based repair mortar (CAC_REF), containing a considerable amount of OPC phases, was the reference for the evaluation of the chemical durability, in terms of resistance against the attack of sulfuric acid, the shrinkage, and the bond behavior of the investigated OPG mortars. The OPG mortars have been produced either with CEN standard sand aggregates (RS) in accordance with DIN EN 196-1 [72] or with a commercial, finer grained sand (S1), with typical grain size distribution for repair mortars.

2.2.2. Characterization of the starting materials

The chemical composition of the starting materials (Tab. 2.1) was characterized by ICP-OES after microwave digestion. Two MS batches (MS(1); MS(2)) were used and both batches consisted of ≈ 95 wt.% SiO_2. XRD indicated virtually the whole feedstock consists of amorphous silica, *i.e.* the diffractogram showed an amorphous hump with a maximum at ≈ 21.5 ° 2θ (Fig. 2.1), without hints for incorporated crystalline SiO_2 phases. Furthermore, both batches showed traces of silicon (PDF # 00-027-1402) and silicon carbide (PDF # 00-049-1429), The Si impurity was a bit more pronounced in MS(2), whereas the content of MS(1) was close to the detection limit of the XRD device. Due to the similarity of both batches, in the following MS(1) and MS(2) are referred to MS.

Silica CR contained ≈ 84 wt.% SiO_2 virtually fully amorphous silica and the maximum of the hump was centred at ≈ 21.5 ° 2θ. Additionally, minor amounts of quartz (PDF # 00-046-1045) were observed. In contrast to MS, silica CR contained ≈ 4 wt.% Al_2O_3 and 3 wt.% CaO (Tab. 2.1). The CaO content was expressed as calcite (PDF # 01-086-0174) in the diffractogram of CR (Fig. 2.1), as well as through an increased loss on ignition (LOI) of ≈ 5 wt.%, with related > 4 wt.% CO_2. Some samples additionally showed traces of silicon.

Table 2.1: Chemical composition of the feedstocks.

Oxide	wt.%								
	MS (1)	**MS (2)**	**CR**	**RHA (1)**	**RHA (2)**	**SA (1)**	**SA (2)**	**SA (3)**	**SL**
SiO_2	95.16	94.57	84.23	88.49	93.72	0.61	-	1.07	35.10
Al_2O_3	0.17	0.17	4.18	0.58	0.05	60.85	59.74	60.89	11.03
Fe_2O_3	0.04	0.04	0.43	0.31	0.10	0.06	0.02	0.02	0.42
TiO_2	<0.01	0.01	0.06	0.03	0.01	0.00	<0.01	<0.01	<0.01
CaO	1.71	1.15	2.97	1.00	0.97	0.26	0.39	0.52	40.64
MgO	0.28	0.23	0.17	0.88	0.38	0.02	0.01	0.01	8.26
Na_2O	0.19	0.14	0.22	0.24	0.26	36.07	36.35	36.78	0.55
K_2O	0.65	0.71	0.03	2.91	1.33	0.03	0.01	0.56	0.49
SO_3	0.25	0.21	0.16	0.54	0.35	0.16	0.04	0.08	2.20
P_2O_5	-	0.14	-	1.83	0.63	-	-	-	-
LOI*	1.12	1.84	5.08	2.48	1.74	1.73	2.63	1.00	1.05
CO_2	-	-	4.20	-	-	0.18	0.03	0.03	0.36
Res.	0.45	0.82	2.51	0.74	0.49	0.23	0.82	0.16	0.29
ρ	2.26	2.21	2.26	2.26	2.27	2.59	2.59	2.59	2.93

LOI...loss on ignition at 1000 °C Res…Residual

-…not determined ϱ…apparent density determined with He-pycnometer (g/cm^3)

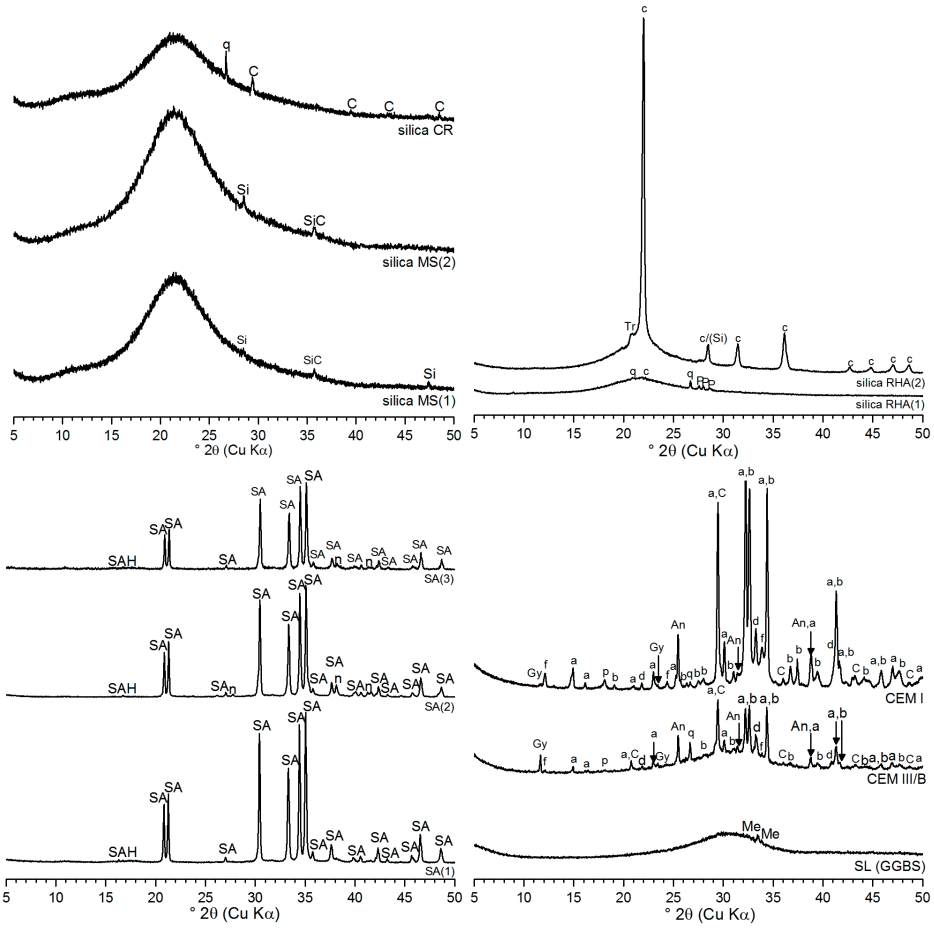

Figure 2.1: XRD diffractograms of the feedstocks CR, MS(1), MS(2), RHA(1), RHA(2), SA(1), SA(2), SA(3), CEM I, CEM III/B and SL (q = quartz; C = calcite; Si = silicon; SiC = silicon carbide; Tr = tridymite; c = cristobalite; P = potassium magnesium phosphate; SA = anhydrous sodium aluminate; SAH = sodium aluminate hydrate; n = natrite; Gy = gypsum; An = anhydrite; a = alite/C_3S; b = belite/C_2S; d = C_3A; f = brownmillerite/C_4AF; p = portlandite; Me = merwinite).

One of the employed RHA batches (RHA(1)) was prepared at the Rheinisch-Westfälische Technische Hochschule (RWTH) Aachen in Germany. Rice husks from Tanzania were calcined at 650 °C for 90 minutes and then allowed to cool down to room temperature within the oven. After cooling down, the material was transferred to BAM. The RHA was ground for 18 seconds in a disc mill (*Fa Siebtechnik TS.250*; 1000 rpm, stainless steel containers). Few particles did not pass a sieve with 63 µm mesh size and were ground for further 18 seconds. After the second milling all particles passed the applied sieve. The RHA contained ≈ 88.5 wt.% SiO_2. XRD showed a major amorphous hump, centered at ≈ 22.0° 2θ, and

low amounts of crystalline quartz (PDF # 00-046-1045). RHA(1) included almost 3 wt.% potassium oxide (K_2O), as well as ≈ 1 wt.% magnesium oxide (MgO) and ≈ 2 wt.% phosphor oxide (P_2O_5), expressed as potassium magnesium phosphate $KMgPO_4$ (PDF # 00-050-0146). Additionally, cristobalite (PDF # 00-039-1425), and calcite (PDF # 01-086-0174) were identified (Fig. 2.1). The potassium and phosphate contents of RHA strongly depend on the fertilization of the rice plants and varies with the geographical origin of the material.

RHA(2) is a commercially available feedstock from a German supplier, whereas the material was produced in Asia. Preliminary investigations of the total carbon content (TC) > 12 wt.% showed, that the material contained significant amounts of remaining, organic material. Therefore, the ash was re-calcined, using two muffle furnaces (Carbolite CWF 12/5 and Nabertherm LT 5/11) and a rotary kiln (Thermal Technology RT 1700). The carbon content could thus be reduced to ≤ 0.2 wt.%. Due to the necessary adjustments of the rotary kiln at the beginning of the treatment. Remaining carbon contents varied between 0.35 wt.% and 4 wt.%. Only material with less than 1.5 wt.% remaining carbon was further used. The batches were mixed and homogenized using the Zyklos concrete mixer (5 min; 70 rpm). No grinding was applied and the material was stored in plastic barrels until further use.

After the re-calcining RHA(2) contained ≈ 93.7 wt.% SiO_2. Besides amorphous phase, XRD (Fig. 2.1) indicated crystalline cristobalite (PDF # 00-039-1425) and minor amounts of tridymite (PDF # 00-042-1401). Since the crystallinity did not change after the re-calcination, the as-received RHA(2) had already seen higher temperatures, than the applied 600 ± 25 °C. Especially at ≥ 800 °C the formation of cristobalite and tridymite is enhanced in RHA [84]. The main goal of commercial burning of rice husk is the production of energy. In this context the exothermic reaction of the burning organics has to be taken into account. This was also one reason for the adjustments during the rotary kiln experiments. Even with the already lowered organic content of the as-received RHA(2), the maximum temperature reached values above 600 °C, depending on the transport speed and the adjusted temperature. Those effects can be even more pronounced in technical scale processes. Furthermore, partially reducing conditions in the muffle furnace at BAM and during the technical process of the pretreated as-received RHA(2) cannot be excluded. Silicon, as a hint, could not be qualitatively identified by XRD, because the main peak (28.5° 2θ) is covered from a cristobalite peak. The properties of the pastes during hardening at elevated temperatures suggests at least the presence of silicon traces, as will be discussed below. The re-calcined and mixed RHA(2) provided a LOI of ≈ 1.7 wt.% (Tab. 2.1).

The observed K_2O content of RHA(2) (≈ 1.3 wt.%) was less than half of the K_2O content of RHA(1). This indicates a different fertilization in Asia (RHA(2)) and Africa (RHA(1)). The Na_2O and Al_2O_3 contents (Tab. 2.1) of the employed sodium aluminates SA(1), SA(2) and SA(3) provided virtually stoichiometric molar Na/Al ratios of 0.98, 1.00 and 0.99, respectively. No further significant differences in the chemical composition could be observed, except moderate variations of the LOI (1.0-2.7 wt.%). This was mainly attributed to the hygroscopic character of $NaAlO_2$. XRD indicated traces of hydrated sodium aluminate (SAH), either $NaAlO_2{\cdot}3H_2O$ (PDF # 00-002-1025) or $NaAlO_2{\cdot}1.25\ H_2O$ (PDF # 01-083-0315), besides anhydrous SA (PDF # 00-033-1200).

Additionally, traces of sodium carbonate (PDF # 01-077-2082) have been observed, which is attributed to the carbonation tendency of alkaline compounds in contact with air. SA(1) and SA(2) were standard laboratory quality sodium aluminates. SA(3) was a technical grade SA.

The ground granulated blast furnace slag (SL) had a typical chemical composition, providing 41 wt.% CaO, ≈ 35 wt.% SiO_2, ≈ 11 wt.% Al_2O_3 and ≈ 8 wt.% MgO (Tab. 2.1). Besides a hump, representing the amorphous phases of the slag, only traces of merwinite $Ca_3Mg(SiO_4)_2$ (PDF # 00-035-0591) could be observed by XRD. According to DIN EN 197-1: 2011 [85] a SL containing blast furnace cement (CEM III/B) typically consist of 20-34 wt.% OPC clinker and 66-80 wt.% GGBS [85]. XRD (Fig. 2.1) indicated the typical OPC clinker phases C_3S (alite; PDF # 01-073-0599), C_2S (belite; PDF # 00-033-0302), C_4AF (brownmillerite; PDF # 00-030-0226), C_3A (PDF # 01-070-0839) as well as gypsum (PDF # 00-033-0311) and anhydrite (PDF # 00-037-1496). Calcite was observed, as well as traces of portlandite (PDF # 00-044-1481) and quartz. A hump indicated the presence of the slag. No slag related hump occurred for the pure CEM I, but all crystalline phases observed for CEM III/B have been identified in CEM I as well (Fig. 2.1). The XRD analysis of the used lithium aluminate (LA) indicated not a pure phase, but a mixture of various compounds (Fig. 2.2). Two different anhydrous lithium aluminate phases were found. Besides $LiAlO_2$ (PDF # 00-038-1464) also $LiAl_5O_8$ (PDF # 00-038-1425) was observed and additionally a hydroxy hydrate $LiAl_2(OH)_{7}{\cdot}_2H_2O$ (PDF # 00-040-0710). Minor amounts of corundum (PDF # 00-046-1212) have been detected, as well as traces of Li_2CO_3 (PDF # 00-022-1141).

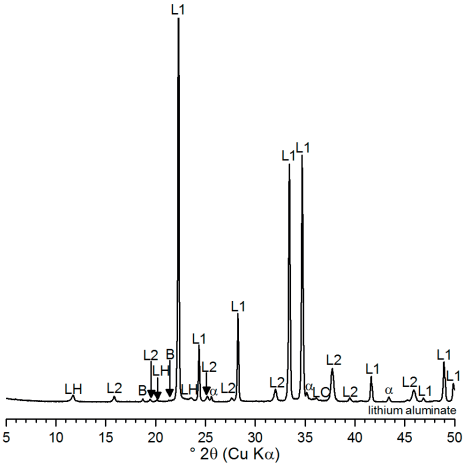

Figure 2.2: XRD diffractogram of lithium aluminate (L1 = $LiAlO_2$; L2 = $LiAl_5O_8$; LH = $LiAl_2(OH)_7 \cdot 2H_2O$; α = α-Al_2O_3/corundum; LC = Li_2CO_3; B = bayerite).

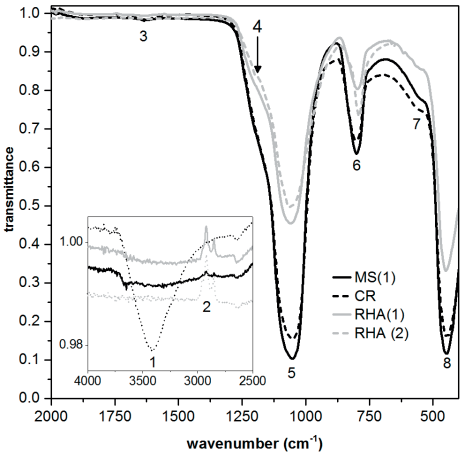

Figure 2.3: ATR FT-IR spectra of the silica feedstocks MS; CR, RHA(1) and RHA(2) (1 = $\nu_{as,s}$ H_2O; 2 = ν C-H ; 3 = δ H_2O; 4 = ν_{as-1} Si-O-Si; 5 = ν_{as-2} Si-O-Si; 6 = ν_s Si-O-Si; 7 = (complex band); 8 = δ O-Si-O).

Fig. 2.3 shows the ATR FT-IR spectra of the silica feedstocks MS(1), CR, RHA(1) and RHA(2). Bands around 3400 cm^{-1} (1) represent overlapping asymmetric and symmetric stretching vibration and the bending vibration (at 1635 cm^{-1}) (3) of water. Those absorption centres only occurred in the spectrum of silica CR, the original filter cake that was dried to a certain extent. No distinct carbonate bands have been identified for the low amounts of incorporated calcite in silica CR. C-H stretching vibrations (2) [86] indicate residues of organic material in the rice husk ashes or from an impurity (e.g. organic solvent). The asymmetric Si-O-Si (5) (ν_{as-2}) stretching vibrations (1051-1060 cm^{-1}) were one of the two strongest absorption bands in the spectra of all silica feedstocks, typical for crystalline and amorphous SiO_2 compounds [87]. A shoulder (4) represent the additional asymmetric stretching vibration (ν_{as-1}) of the crystalline cristobalite impurity [87, 88] in RHA(2). It did not occur in the spectra of the virtually fully amorphous silica feedstocks (MS, CR) and it was hardly to identify for the cristobalite residues of silica RHA(1)).

The according symmetric stretching vibrations (ν_s Si-O-Si) of the silica feedstocks (6) occurred in between 791 cm^{-1} and 798 cm^{-1}. The weak signals (7) around 560 cm^{-1} occur from complex vibrations of higher order [87, 89, 90]. The O-Si-O (8) deformation vibration (δ O-Si-O) were one of the two strongest absorption bands besides ν_{as-2}, which is typical for amorphous and crystalline silicas [87]. In case of the RHA batches the intensity of the band was increased compared to ν_{as-2}.

Fig. 2.4 presents the results of the particle size distribution (PSD) measurements of specific feedstocks. The median of the PSD of RHA(1) was determined to d_{50} = 11.1 µm (and d_{90} = 39.8 µm), which is in line with SEM micrographs (Fig. 2.5) of RHA(1). SEM investigations further indicated a more angular shape of the particles compared to the spherical particles of the industrial silicas (MS, CR). This provides a higher geometrical surface to volume ratio. The BET specific surface area (Tab. 2.2) of the ground RHA(1) and for the unground RHA(2) was determined to be 49.6 m^2/g and 13,9 m^2/g, using N_2 sorption at 77 K.

Table 2.2: Specific surface area (N_2-sorption) of the silica feedstocks.

Parameter	MS(1)	CR	RHA(1)	RHA(2)
BET (m^2/g)	20.1	32.3	49.6	13.9

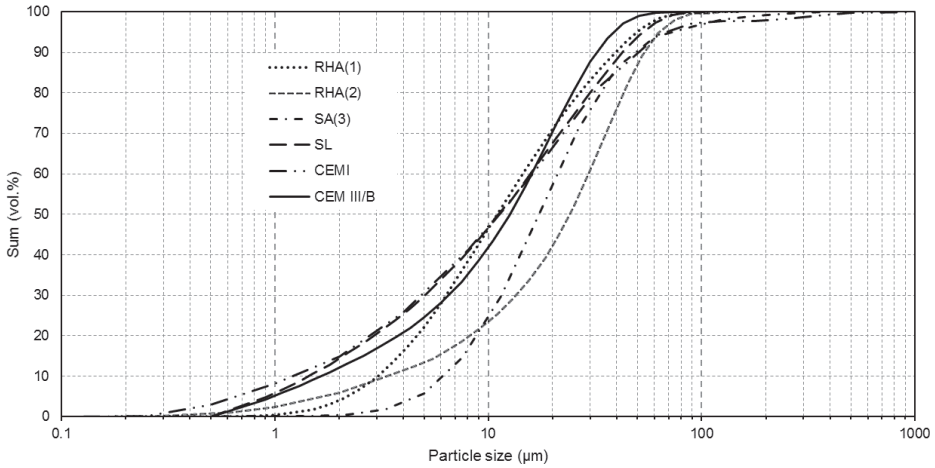

Figure 2.4: Particle size distributions of the feedstocks RHA(1), RHA(2), SA(3), SL, CEM I and CEM III/B.

RHA(2) was significantly coarser than RHA(1). D_{50} of RHA(2) is 24.1 µm (d_{90} = 54.0 µm). The batch provided angular particles aswell. Furthermore, RHA(2) showed signs of intra particulate porosity (Fig. 2.5). Previous investigations found major importance of the burning temperature on the particle/ crystallite sizes but only marginal effects of the coarseness and milling times of RHA on its reactivity [91-94].

The representative SA(3) provided a significant coarser PSD compared to the silica feedstocks, except RHA(2), with d_{50} = 17.3 µm and d_{90} = 49.9 µm. However, the main part of the SA feedstocks readily dissolved after adding water (see below). SL

had d_{50} = 11.3 µm and d_{90} = 42.4 µm; CEM I had d_{50} = 11.9 µm and d_{90} = 53.0 µm and CEM III/B had d_{50} = 12.6 µm and d_{90} = 32.3 (Fig. 2.4). No PSDs are presented for the two finest silica feedstocks MS and CR. Since the dispersion of the very fine particles could not be realized satisfyingly (*i.e.* dispersion of agglomerates), the PSD curves showed the distribution of silica particles and agglomerates. The primary particles are strongly glued together from the formation process. SEM (Fig. 2.5) investigations revealed primary particle sizes of about 50-200 nm with spherical shape for both industrial silica feedstocks, which causes interparticle porosity. On the other hand, the apparent densities (Tab. 2.1) of CR (2.26 g/cm³) and MS(1) (2.26 g/cm³) where similar to RHA(1). Despite its coarser PSD, RHA(1) had a higher specific surface area (49.6 m^2/g) than MS and the residue from chlorosilane production (20.1 m^2/g and 32.3 m^2/g, respectively), due to its more angular shaped particles and apparently rougher surface (cf. Fig 2.5) when compared to the particles of MS and CR. The typical intraparticle porosity could not be observed for RHA(1) by SEM, but for RHA(2). This RHA provided open pores with openings of ≤ 1 µm (Fig. 2.5). Tab. 2.3 presents the used feedstocks for the OPG synthesis in the according Chapters.

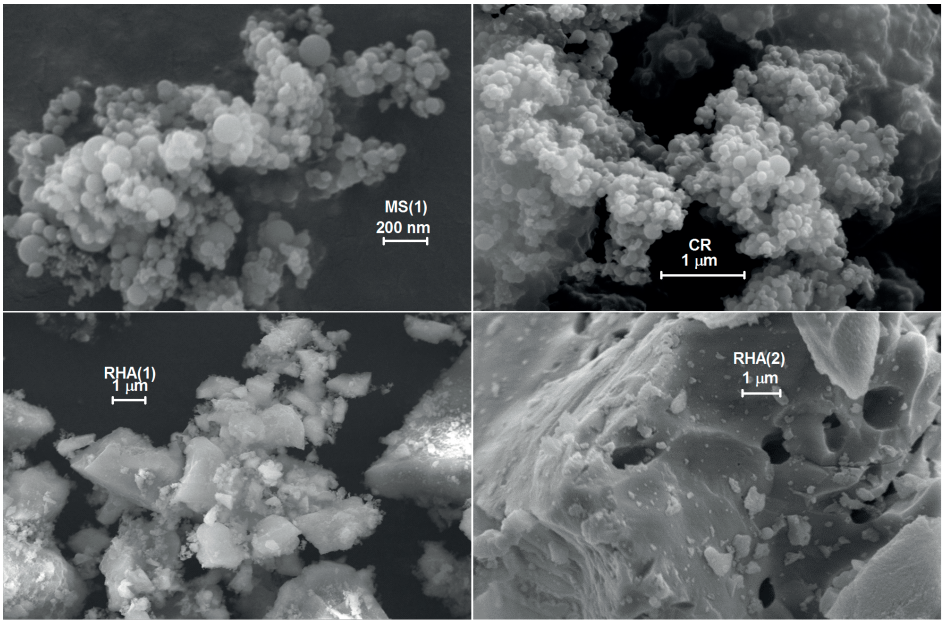

Figure 2.5: SEM SE micrographs of powdered samples of the silica feedstocks MS(1), CR, RHA(1) and RHA(2).

Table 2.3: Used solid feedstocks in the according Chapters.

	Chapter	MS (1)	MS (2)	CR	RHA (1)	RHA (2)	SA (1)	SA (2)	SA (3)	SL	LA
1	*Introduction*										
2	*Materials and methods*	×	×	×	×	×	×	×	×	×	×
3	*Fresh paste properties*	×		×			×				
4	*Hardening; microstructure*	×		×	×	×	×	×	×		
5	*Heat treatment*	×		×		×		×	×		
9	*Acid resistance*		×			×			×	×	
6	*Workability of the mortars*		×	×				×	×		
7	*Hardening of the mortars*		×	×		×		×	×	×	
8	*Shrinkage of the mortars*		×			×			×	×	
8	*Bond strength of the mortars*		×			×			×	×	
9	*Acid resistance*		×	×		×			×	×	
10	*Li + additive manufacturing*		×						×		×
11	*Conclusions and recommendations*	×	×	×	×	×	×	×	×	×	×

For comparison and evaluation of the mortar properties in terms of hardening, shrinkage, bond behavior and acid resistance, a commercial sewer repair mortar was used as reference. By information of the supplier the product was based on calcium aluminate cement (CAC). The chemical composition of this reference mortar (CAC_REF) was unknown, but the dry mortar contained > 50 wt.% binder. Fig. 2.6 presents the XRD analysis of CAC_REF. Besides quartz, the typical CAC phases monocalcium aluminate (CA) (PDF # 01-070-0134) and gehlenite (C_2AS) (PDF # 01-073-2041) were identified. The mortar further contained OPC clinker phases C_3S, C_2S, C_3A and traces of C_4AF, besides anhydrite and some portlandite. Thus, it can be concluded the CAC_REF mortar does not contain only CAC but a mixture of CAC- and OPC-type cements.

Two different sands have been used for the preparation of the OPG mortars. Besides CEN standard sand (RS) in accordance with DIN EN 196-1:2005 [72], a significantly finer sand (S1) was applied. Fig. 2.7 presents the grain size distributions of the reference sand (RS) with a maximum grain size of 2 mm and the finer S1 sand with a maximum grain size of 1 mm. S1 is a common sand for repair mortars. The grain size distributions have been determined by sieving, in accordance with DIN EN 933-1 [95]. 80% of the grains were smaller than 0.5 mm for S1, whereas 70% of RS were smaller than 1 mm. In the following, the specific water demand of the aggregates was not considered.

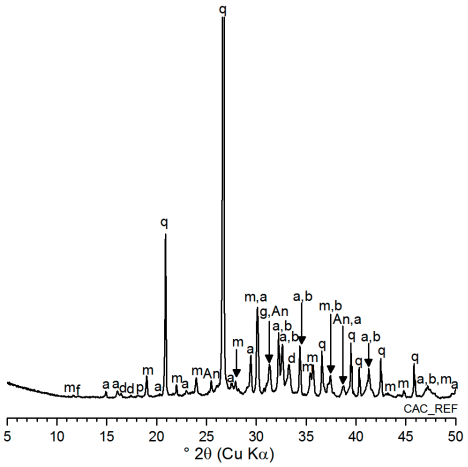

Figure 2.6: XRD of CAC_REF (q = quartz; An = anhydrite; m = CA; a = alite/C_3S; b = belite/C_2S; d = C_3A; f= C_4AF; g = gehlenite; p = portlandite).

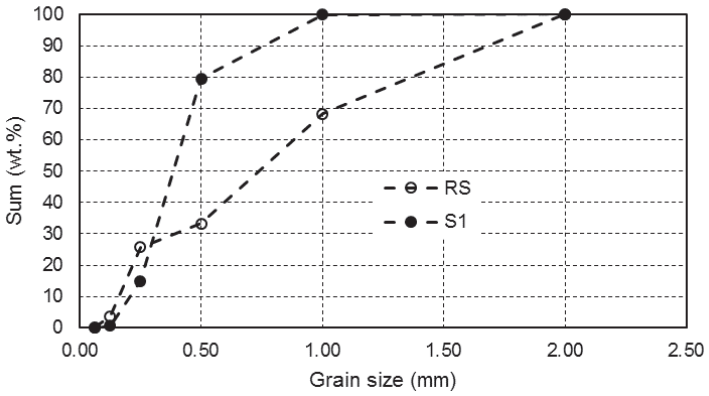

Figure 2.7: Grain size distributions of the sands RS and S1.

2.3. Sample preparation

One-part geopolymers were synthesized by mixing solid silicas (MS, CR, RHA) and the solid alkaline activator SA (or LA), and subsequently adding water at different water/binder ratios (w/b) by mass to yield specific molar Al_2O_3/SiO_2 ratios and according Na_2O:Al_2O_3:SiO_2:H_2O ratios. The main part of SA dissolves immediately in water (see below), and thus water only had to be added to initiate the reactions. For certain formulations parts of the original binder haven been exchanged with SL, in order to provide a specific CaO content.

2.3.1. Geopolymer design

The calculation of the binders and the pastes was based on the chemical composition of the solid silica and alumina feedstocks. The silica feedstocks had specific SiO_2 contents (mol/g) and Al_2O_3 contents (mol/g) (cf. Section 2.2.2.; Tab. 2.1). The low Si content of alumina feedstocks was not taken into account. Samples were prepared at specified molar silica/alumina- ratios ($2 \leq SiO_2/Al_2O_3$: ≤ 8 mol/mol). $SiO_2/Al_2O_3 < 2$ mol/mol are not considered since Al-O-Al bonds are not stable in aluminosilicates according to Loewenstein's rule [36]. Specific mixes of the investigations on the fresh paste properties (cf. Chapter 3.) provided alumina contents slightly below Loewenstein's rule, due to an error of the LOI of a certain SA batch (see below).

The specific molar ratios were defined and the ratio of the two feedstock masses ($R_m = m_{silica}/m_{alumina}$ in g/g) to reach the specified molar SiO_2/Al_2O_3 ratios (R_M) in the binder have been calculated as follows:

$$R_M = \frac{SiO_2}{Al_2O_3} = \frac{m_{silica} \cdot c_{silica}(SiO_2)}{m_{silica} \cdot c_{silica}(Al_2O_3) + m_{alumina} \cdot c_{alumina}(Al_2O_3)} \quad (2.7)$$

$$R_m = \frac{m_{silica}}{m_{alumina}} = \frac{R_M \cdot c_{alumina}(Al_2O_3)}{c_{silica}(SiO_2) - R_M \cdot c_{silica}(Al_2O_3)} \quad (2.8)$$

where $c_{silica}(SiO_2$ or $Al_2O_3)$ is the amount of SiO_2 and Al_2O_3, respectively, in the silica material; $c_{alumina}(Al_2O_3)$ is the amount of Al_2O_3 in the alumina material; R_M is the specified molar SiO_2/Al_2O_3 ratio of the binder formulation; and R_m is the mass ratio of the silica and the alumina feedstocks to reach R_M.

For the subsequent calculation of the pastes, the total mass was set to 100 g. Based on the specified water to binder ratio by mass ($w/b = m_{water}/(m_{silica} + m_{alumina})$), the total amounts of the solids (b), *i.e.* the mass of silica and alumina feedstock, and the mixing water (w) per 100 g of paste have been calculated as follows:

$$b \equiv m_{silica} + m_{alumina} \quad (2.9)$$

$$b + w = 100\ g \quad (2.10a)$$

$$b = \frac{100\ g}{(1 + w/b)} \quad (2.10b)$$

$$w = 100\ g - b \quad (2.10c)$$

Based on the specified molar SiO_2/Al_2O_3 ratio of the binders and the specified w/b of the one-part geopolymer pastes, the composition of the pastes was calculated as follows:

$$m_{alumina} = \frac{b}{1 + R_m} \quad (2.11)$$

$$m_{silica} = b - m_{alumina} \quad (2.12)$$

The total mass composition of the paste (m_{OPG}) is then:

$$m_{OPG} = w + b = m_{water} + m_{silica} + m_{alumina} = 100g \tag{2.13}$$

Additional experiments have been conducted on OPG binders where parts of the original OPG paste have been exchanged with slag to provide specific CaO contents. The mass factors (q_1; q_2) for the slag containing pastes (OPG_SL) with specified CaO content have been calculated as follows, based on the original OPG paste:

$$\frac{q_1}{q_2} = \frac{a_{OPG\_SL}\,(CaO) - a_{OPG}(CaO)}{a_{slag}(CaO) - a_{OPG\_SL}(CaO)} \tag{2.14}$$

$$q_1 = a_{OPG\_SL}(CaO) - \frac{m_{silica} \cdot a_{silica}(CaO) + m_{alumina} \cdot a_{alumina}(CaO)}{b} \tag{2.15}$$

$$q_2 = a_{OPG\_SL}(CaO) - a_{slag}(CaO) \tag{2.16}$$

Where b, m_{silica} and $m_{alumina}$ are the binder mass, and the masses of the solid silica and alumina feedstocks, respectively, of the *OPG* without slag (from equations 2.10–2.12); a_{OPG_SL}(CaO) (in wt.%) is the intended CaO content of the OPG_SL; a_{OPG}(CaO) (in wt.%) is the CaO content of the OPG (from impurities in the silica); a_{slag}(CaO) (in wt.%) is the measured CaO content of the slag; a_{silica}(CaO) (in wt.%) is the measured CaO content of the silica; and $a_{alumina}$(CaO) (in wt.%) is the measured CaO content of the alumina. From q_1, q_2 and b, the quotient (q_n) for the determination of the slag mass was calculated as:

$$q_n = \frac{b}{q_1 + q_2} \tag{2.17}$$

The mass of slag (m_{slag}) for a specified CaO content in OPG_SL is then:

$$m_{slag} = q_1 \cdot q_n \tag{2.18}$$

From the calculated mass of slag and the original masses of the silica and alumina feedstocks, the adjusted masses (*ma*) of the silica and alumina feedstocks per 100 g of SL-containing paste can be calculated:

$$ma_{silica} = \frac{b - m_{slag}}{b} \cdot m_{silica} \tag{2.19}$$

$$ma_{alumina} = \frac{b - m_{slag}}{b} \cdot m_{alumina} \tag{2.20}$$

Thus, the total mass of paste, including slag (m_{OPG_SL}), is then:

$$m_{OPG\_SL} = ma_{silica} + ma_{alumina} + m_{slag} + m_{water} = 100\ g \tag{2.21}$$

For larger (or smaller) batches, the masses calculated with the above stated formulas where simply scaled according to the batch size (*i.e.* multiplied with f = (batch mass/100 g)).

2.3.2. Design of the mortars

The calculation of the mortars was based on the CEM I- and CEN standard sand (RS)-based reference mortar composition of DIN EN 196-1:2005 [72]. The composition of the standard reference mortar is given in Tab. 2.4. The first OPG mortars were calculated to have the same paste volume as the standard reference mortar (*i.e.* 368.3 cm^3); deviating from this value, also other mix-designs were developed (see below).

Table 2.4: Composition of the reference mortar based on CEM I from DIN EN 196-1: 2005 [72].

Component	m (g)	ϱ (g/cm^3)	V (cm^3)	V (cm^3)
Cement	450	3.14	143.3	368.3
Water	225	1.00	225.0	
CEN standard sand	1350	2.64	511.4	511.4
total:	*2025*		*879.7*	*879.7*

First, the volume of 100 g of paste for a given composition ($V_{paste(100g)}$) was calculated from the composition of the according paste and the densities of the starting materials (Tab. 2.1), assuming a physical mixture (*i.e.* neglecting dissolution). Then, the masses of the silica, the alumina and water in the mortar where calculated according to:

$$m_{silica,mortar} = m_{silica} \cdot \frac{368.3\ cm^3}{V_{paste\ (100g)}} \quad (2.22)$$

$$m_{alumina,mortar} = m_{alumina} \cdot \frac{368.3\ cm^3}{V_{paste\ (100g)}} \quad (2.23)$$

$$m_{water,mortar} = m_{water} \cdot \frac{368.3\ cm^3}{V_{paste\ (100g)}} \quad (2.24)$$

where m_{silica}, $m_{alumina}$, and m_{water} are the masses of the respective feedstocks in 100 g of paste; and $m_{silica,mortar}$, $m_{alumina,mortar}$, and $m_{water,mortar}$ are the masses of the respective feedstocks in the mortar (with a total volume of 879.7 cm^3).

For slag containing OPG_SL mortars, an analogous calculation was done, *i.e.*:

$$m_{silica,mortar} = ma_{silica} \cdot \frac{368.3\ cm^3}{V_{paste\ (100g)}} \quad (2.25a)$$

$$m_{\text{alumina,mortar}} = ma_{\text{alumina}} \cdot \frac{368.3\ \text{cm}^3}{V_{\text{paste (100}g\text{)}}} \tag{2.25b}$$

$$m_{\text{water,mortar}} = m_{\text{water}} \cdot \frac{368.3\ \text{cm}^3}{V_{\text{paste (100}g\text{)}}} \tag{2.25c}$$

$$m_{\text{slag,mortar}} = m_{\text{slag}} \cdot \frac{368.3\ \text{cm}^3}{V_{\text{paste (100}g\text{)}}} \tag{2.25d}$$

The mass of the sand was always set to 1350 g, as for the reference mortars of DIN 196-1 (Tab. 2.4).

$$m_{\text{sand,mortar}} = 1350\ g$$

Thus, the total mass of OPG mortars, is then:

$$m_{\text{mortar}} = m_{\text{silica,mortar}} + m_{\text{alumina,mortar}} + m_{\text{water,mortar}} + m_{\text{sand,mortar}} \tag{2.26}$$

or, for slag-containing OPG_SL mortars,

$$m_{\text{mortar}} = m_{\text{slag,}mortar} + m_{\text{silica,mortar}} + m_{\text{alumina,mortar}} + m_{\text{water,mortar}} + m_{\text{sand,mortar}} \tag{2.27}$$

For some mortars, the volume of paste was modified from the base value of 368.3 cm^3; *i.e.* these mortars contained multiples of this volume. To simplify calculations, the factor was always referred to a constant sand mass, 1350 g; the masses of the other feedstocks were calculated with the factor x (see sample nomenclature below) as follows:

$$m_{\text{silica,mortar\_x}} = m_{\text{silica,mortar}} \cdot x \tag{2.28}$$

$$m_{\text{alumina,mortar\_x}} = m_{\text{alumina,mortar}} \cdot x \tag{2.29}$$

$$m_{\text{water,mortar\_x}} = m_{\text{water,mortar}} \cdot x \tag{2.30}$$

$$m_{\text{slag,mortar\_x}} = m_{\text{slag,mortar}} \cdot x \tag{2.31}$$

Own experiences have revealed, values of x below 0.6 and above 3.0 were not feasible for the investigated one-part geopolymers and used sand aggregates. Therefore, x was limited to: $0.60 \leq x \leq 3.00$.

2.3.3. Sample nomenclature

Tab. 2.5. presents the primary feedstocks and the used abbreviations for the sample nomenclature of the OPG formulations.

Based on the nomenclature of the silica feedstocks, Tab. 2.6 presents the silicas, ranges and arrangements for the specification of the OPG or OPG_SL paste and mortar samples, respectively.

Table 2.5: Primary Feedstocks and their abbreviations.

Feedstock class	Feedstock	Abbreviation
Silica	microsilica/ silica fume	MS
	chlorosilane residue	CR
	rice husk ash	RHA
Alumina	sodium aluminate	SA
	lithium aluminate	LA
Slag	ground granulated blast furnace slag	SL
Aggregates	CEN standard sand (≤ 2 mm)	RS
	fine sand (≤ 1 mm)	S1

Table 2.6: General values for the nomenclature of OPG and OPG_SL pastes and mortars.

	Silica	SiO_2/Al_2O_3 (mol/mol)	Slag	w/b	Paste value (x)	Sand
Paste	MS/CR/RHA	2-8	SL	0.36-0.8	-	-
Mortar	MS/CR/RHA	3.5-6	SL	0.36-0.8	0.60-3.00	RS/S1

A formulation is named after its silica source and its molar SiO_2/Al_2O_3 ratio. Therefore, a microsilica (MS)-based OPG formulation with a molar SiO_2/Al_2O_3 ratio of 3.5 is presented as:

- MS_3.5

An OPG formulation based on this reference, but with a certain amount of exchanged slag will be written as:

- MS_3.5_SL

The according OPG mortar of MS_3.5 with the standard paste volume and RS aggregates is then:

- MS_3.5_RS

If the paste value (paste mass) of the reference mortar MS_3.5_RS was decreased to 0.9, the adjusted OPG mortar is:

- MS_3.5_0.9_RS

An OPG mortar based on MS_3.5_0.9_RS, where parts of the binder are exchanged with slag will be written as:

- MS_3.5_SL_0.9_RS

2.3.4. Mixing procedures

Pastes

The mixing of the pastes was conducted either in a planetary centrifugal mixer (*Thinky ARV-320CE*) with a maximum rotation speed of 2000 min^{-1} and an additional vacuum function ($\geq$ 2 mbar) for outgassing or in a standard mortar mixer in accordance with DIN 196-1:2005 [72] for bigger batches.

Mortars

The preparation of small batches of mortars was carried out in the standard mortar mixer as well. Bigger batches with a volume of 3–10 l fresh mortar have been produced in an *Eirich Intensive Mixer* (*Type RV02*), at rotation speed 1. Binder and sand have been homogenized by dry mixing for two minutes. Then the water was added and the fresh mortars have been mixed for further five minutes. Additional rotating paddles (400 min^{-1}) further enhanced the mixing in the rotating body.

Fresh mortar batches of more than 10 l have been produced using a rotating pan *Zyklos mixer* with a maximum volume of 30 l. Binder and sand have been homogenized in dry environment for two minutes. Then the water was added and the fresh mortars have been mixed for further five minutes. The rotation speed of the mixer was adjusted to 70 min^{-1}. Fixed paddles enhanced the mixing additionally to the rotating body.

2.3.5. Curing

Curing at elevated temperatures was carried out in a *Memmert CTC 256* environmental test chamber. The device works in a temperature range from -43 °C to +190 °C with a spatial temperature distribution of $\pm$ 0.5-2.0 K. In the temperature range from 10 °C to 95 °C specific relative humidity of 10-98% ($\pm$ 1%) can be adjusted. Curing of the OPG pastes and mortars was carried out in a temperature range between 50 °C and 90 °C with an applied r.H. of 80-98%.

Curing of pastes and mortars at ambient conditions was done in climate chambers with standard reference conditions of 23 °C/ 50 r.H. or 20 °C/ 65 °C r.H., respectively. Specific specimens have been stored in boxes at 23 °C above water, with an equilibrium r.H. of virtually 100 %, or under water at the same temperature.

3. FRESH PASTE PROPERTIES*

The workability of the fresh pastes of mineral binders plays an important role for possible applications and their properties after hardening. Furthermore, AAM are known to provide usually worse workability compared to conventional OPC based systems for equal mass related water contents and properties cannot be easily transferred from one system to another. Therefore, the following Chapter considers the general fresh paste properties of the OPG fresh pastes compared to OPC. Besides the generally decreased workability of AAM, common superplasticizers of the cement industry usually don't work in the highly-alkaline reaction systems. Section 3.3 considers therefore additionally the influence of several potential superplasticizers on the workability of the OPG fresh pastes of this work.

The investigated OPG pastes of this Chapter were synthesized from MS(1) and SA(1). CEM I was used as reference material for the evaluation of the fresh paste properties. Investigations on the influence of superplasticizers (Section 3.3) have been conducted on OPG formulations based on MS(2), SA(2) and SL.

3.1. Introduction

A limited number of works dealing with the rheology of conventional geopolymers (e.g. [67, 96-103]) is presented in the published literature. The reported results regarding the rheological behavior of AAM are quite manifold in general. For example, Favier et al. [98] described MK-based geopozlymer fresh pastes as highly viscous Newtonian fluids with almost no yield stress, while others reported Herschel-Bulkley or Bingham behavior for slag-based AAM, depending on the nature of the activator solution [104]. Criado et al. [97] investigated FA-based geopolymers and suggested Bingham behavior. Thus, it is obvious that there are several influences on geopolymer paste's rheology and results for one system cannot easily be transferred to other systems.

In general, the rheology of the GP fresh pastes is dominated by highly viscous activating solutions and by particle shapes and size distributions and porosities, as well as the reactivity of the solids. For example, MK tends to form platy particles, whereas fly FA or MS provides spherical particles. Accordingly, MK-based pastes generally appear to be stiffer than FA-based pastes at identical w/b [105].

* The main content of Section 3.2. was published in Sturm et al: Rheological properties of microsilica and sodium aluminate based one-part geopolymers compared to ordinary Portland cement. Proceedings of the 5th International Conference on Non-Traditional Cement & Concrete. Brno, Czech Republic, ISBN 978-80-214-4867-4, p. 241-244 (2014).

In the presented study, the general rheological properties of MS- and SA-based OPG mixes are considered and compared to an OPC (CEM I) paste.

3.2. General fresh paste properties

3.2.1. Experimental program

A test program was conducted with the variation of molar SiO_2/Al_2O_3 ratios, that have been adjusted compared to Sturm et al. [106], because an error with the determined water content of SA(1) (> 12 wt.%) [106] due to its water absorption during storage of the according sample for the analysis and was later found to be only (≈ 1.7 wt.%). Therefore, the ratios have been re-calculated and are lower, due to the relative increased alumina content (lower water content of the alumina source), as well as for the OPG in Section 4.2. (Tab. 4.1) and Sturm et al. [51]. However, the sample nomenclature was not changed.

To investigate influences of both parameters on the early rheological properties, pastes were prepared with the standard mortar mixer. After the addition of water to the solids, the material was mixed for one minute at low rotation speed. The following minute was used to scratch unmixed material from the walls and the stirrer into the pre-mixed pastes. Afterwards the material was mixed at the high rotation speed for another minute.

Subsequently the pastes were filled into the viscometer. Two specific cells with different geometries (mortar measuring cell with a wing stirrer for relative values and double gap measuring cell for absolute values) were used. To generate comparable states of the fresh pastes, all measurements started ten minutes after the addition of water. Within these ten minutes also a small cylinder was filled with paste for a determination of the spread flows, as proposed by Roussel et al [68] (“mini-cone” test). The inner wall of the cylinder was coated with formwork oil to ensure a complete release of the sticky pastes.

A ramp measurement program was chosen for the viscometer experiments. The rotation speed was raised linearly to 50 min^{-1}, held for 2 minutes and afterwards decreased to zero. The procedure was repeated after specific time steps (20 min, 40 min and 60 min) to detect changes over the course of time. Additional tests with conventional cement (CEM I) were conducted to compare these values.

Table 3.1: Molar SiO_2/Al_2O_3 and w/b ratios (by mass) of the pastes for the rheological investigations.

Sample	SiO_2/Al_2O_3 (mol/mol)	w/b by mass		w/b by volume	
MS_2	1.86	0.6	0.7	1.47	1.72
MS_3	2.82			1.45	1.69
MS_3.5	3.38			1.44	1.69
MS_4	3.75			1.44	1.68
MS_5	4.66			1.43	1.67
MS_6	5.35			1.42	1.66
CEM I	-	0.45		1.40	

From the literature it can be found, that the dissolution of sodium aluminate in water takes place very quickly, but gives only metastable solutions of sodium and aluminum, which will precipitate aluminum hydroxide (gibbsite) over time [107]. In addition, atmospheric CO_2 leads to carbonation of the solution over time. The initial (metastable) solubility of technical sodium aluminate has been reported as 400 g per 1 kg at ambient temperature [108] and 600 g per 1 kg water at 75 °C [109]. The dissolution reaction is strongly exothermic. However, own investigations showed, that the dissolution of the sodium aluminate takes place incongruently. After the addition of water immediately a strongly NaOH dominated solution forms and a white gel was precipitated and identified as aluminum hydroxide by XRD [50]. That is readily explained by the fact that in the Na_2O-Al_2O_3-H_2O system the equilibrium concentration of sodium is always higher than of the aluminum component [110]. However, the nature of the pore solution has a great influence on the rheology of geopolymer pastes [67]. Therefore, the viscosity of a pure SA solution (c = 600 g/l) was additionally determined with a rheometer. The SA solution can be considered as Newtonian fluid. In comparison to water (1.0 mPa·s) it has a significantly higher dynamic viscosity of ≈ 67 mPa·s.

3.2.2. Results and discussion

The flow curves of the pastes showed shear thinning behavior at low shear rates (Fig. 3.1). Since the state of shear with the used measurement cell is not known, the torque to velocity relation is affected by local effects and does not inevitably render the behavior of the entire fluid. Therefore, only moderate and high shear rates were considered for the evaluation. At moderate to high shear rates the curves possessed a linear slope. This means that the curves can be best fitted using the Bingham model and the relative plastic viscosities and the extrapolated yield stresses were calculated with this model. Due to the setup of the cell, all results generated with the mortar

measuring cell only provide qualitative information about the rheology, *i.e.* a torque gradient (relative viscosity) and an intercept with the ordinate (relative yield stress). However, their changes can be observed.

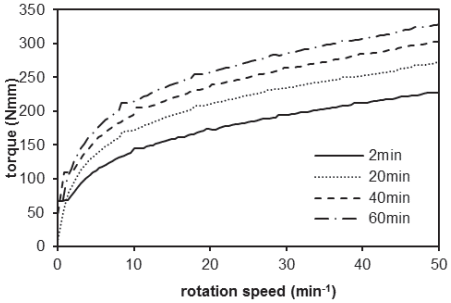

Figure 3.1: Flow curves of geopolymer paste MS_6 (SiO_2/Al_2O_3 = 5.35 mol/mol; w/b = 0.6) over the time of one hour.

For w/b = 0.6 all pastes showed significant changes of the rheological properties over the time of one hour after the addition of water (mortar measuring cell). Within the measurement time the relative yield stresses and relative plastic viscosities increased for all considered SiO_2/Al_2O_3. The increase of viscosity over time is likely to be caused by partial dissolution of MS and the formation of (alumino)silicate dimers and oligomers in the pore solution and may also be affected by the evaporation of water over the time.

In contrast to the yield stress a maximum viscosity was observed at a certain silica content (SiO_2/Al_2O_3 = 4.66). Between 2 min and 22 min the material with w/b = 0.6 showed the highest detected increase of viscosity between two consecutive measuring point. For the next higher molar SiO_2/Al_2O_3 = 5.35 the relative viscosities were lower and only increased slightly over time, indicating a decreasing reaction speed for the highest silica content. The maximum viscosity was even lower than for MS_4 with SiO_2/Al_2O_3 = 3.75 (Fig. 3.2).

Independent from the observed incongruent dissolution behavior, and the previously assumed solubility of 600 g $NaAlO_2$ per 1 kg water (*i.e.* the value given in Ref. [109]), likely the saturation index of SA decreased below 0 at about $SiO_2/Al_2O_3 \approx 5$, previously suggested 5.5 for w/b = 0.6 [106], due to the error of the water content of SA. Thus, at $SiO_2/Al_2O_3 > 5$, the solution is not fully saturated with respect to the readily dissolved part of SA and with increasing SiO_2/Al_2O_3 its viscosity will decrease below the viscosity of the saturated solution. As can be seen in Fig. 3.2, MS_ 5 (SiO_2/Al_2O_3 = 4.66) is the ratio at which the viscosity of the pastes has a maximum (SiO_2/Al_2O_3 = 5 was not tested). This indicates that at $SiO_2/Al_2O_3 > 5$ the paste viscosity is dominated by the viscosity of the sodium aluminate solution, while

at $SiO_2/Al_2O_3 < 5$ (when the initial solution viscosity is constant) the paste viscosity is determined by another parameter. It is obvious that this latter parameter is the w/b-ratio (by volume) of the paste, which increases with decreasing SiO_2/Al_2O_3 (Tab. 3.1) and accordingly paste viscosity decreases with decreasing SiO_2/Al_2O_3 for $1.9 < SiO_2/Al_2O_3 \leq 4.7$; in this range it is the interactions of the solid particles, that dominate the paste viscosity (cf. Ref. [98]). Furthermore. the decreasing observed viscosity increase over the time for the formulation with the highest silica content (MS_6) indicates a lower reaction speed (decreased activator concentration).

The fresh paste properties with an applied w/b of 0.7 slightly differed from w/b = 0.6. As for w/b = 0.6, the yield stress increased with increasing silica content, but the changes over time were much lower for w/b = 0.7. Particularly, for the highest and the lowest silica contents (SiO_2/Al_2O_3 = 2 and 6) there were almost no changes over the time. As expected, relative yield stresses and viscosities of the pastes with higher water content were lower than for w/b = 0.6 (Fig. 3.2).

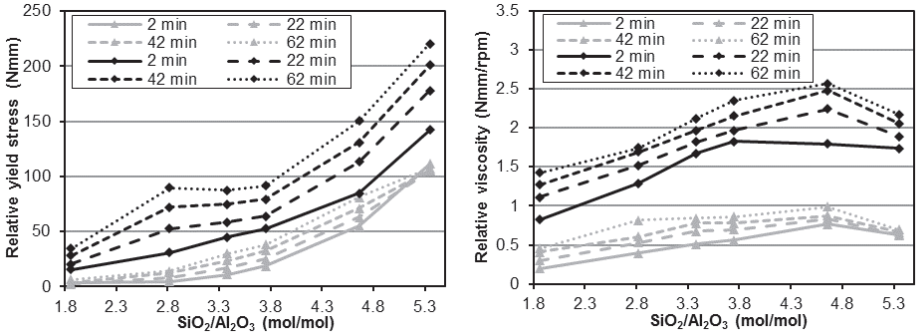

Figure 3.2: Relative yield stresses (left) and viscosities (right), of the MS-based OPG for w/b = 0.6 (black lines) and w/b = 0.7 (grey lines), as measured in the mortar measuring cell.

In contrast to the plastic viscosity, yield stresses showed no specific maximum at a certain SiO_2/Al_2O_3 ratio (Fig. 3.2); instead, the yield stresses rose consistently with decreasing w/b (by volume) of the pastes (Tab. 3.1), *i.e.* with increasing starting silica MS content. Thus, the yield stress of the pastes is stronger influenced by the content of solid particles in the system. For w/b = 0.7 the same trends as for w/b = 0.6 were observed, but less pronounced as well. The yield stresses increased less strongly with increasing silica content, than for w/b = 0.6. This is caused by the lower solid volume fraction, which causes less particle interactions at w/b = 0.7 than at w/b = 0.6.

The results of the mini-cone tests and the yield stress measurements were in good agreement. With increasing silica content, the spread flow decreased while the calculated yield stresses increased. Furthermore, the observed spread flows for w/b = 0.6 exhibited a linear correlation with the SiO_2/Al_2O_3-ratio (Fig. 3.3).

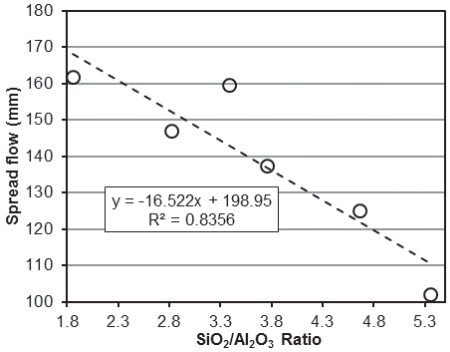

Figure 3.3: Results of the mini-cone tests for the MS-based OPG with w/b = 0.6.

To facilitate comparison, also tests with a double gap measuring cell, which yield absolute values of plastic viscosity and yield stress, were done with selected OPG pastes and CEM I. The results are presented in Fig. 3.3.

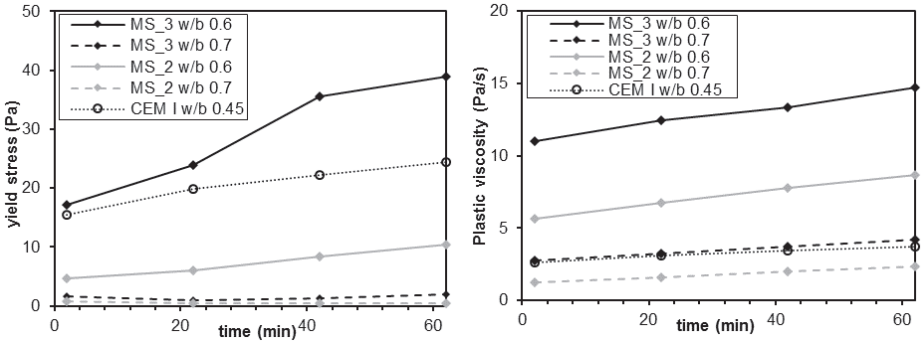

Figure 3.4: Yield stresses (left) and plastic viscosities (right) for selected OPG pastes at different w/b and for CEM I (w/b = 0.45), determined with the double gap cell.

The solid MS particles provide primary particles of 50-200 nm (Section 2.2.2; Fig. 2.5) with a considerable higher surface area than the significantly coarser CEM I particles (Section 2.2.2.; Fig. 2.4), providing increased water demand. Furthermore, the volume related w/b of the OPG is lower at equal mas related w/b, due to the higher apparent density of CEM I (3.12 g/cm^3) compared to SA (2.59 g/cm^3) and MS (2.26 g/cm^3) and is further decreased with increasing silica MS content. Even at lower mass related w/b of (0.45), CEM I provides comparable volume related w/b as MS_6 at w/b = 0.6 by mass of 1.4 by volume (Tab. 3.1).

To summarize, lower amounts of mixing water and higher SiO_2/Al_2O_3-ratios lead to an increase of yield stress and viscosity (with the exception of viscosity at SiO_2/Al_2O_3 > 4.7). This behavior is readily explained by the decrease of the w/b (by volume) and increasing SiO_2/Al_2O_3. The decreasing viscosity with an increase of SiO_2/Al_2O_3 from 4.7 to 5.4 and lower increase over the time, can be explained by the fact that at $SiO_2/Al_2O_3 \approx 4.7$ the pore solution becomes undersaturated with respect to the SA feedstock (w/b = 0.6) [106], thus, its viscosity is lower than for lower SiO_2/Al_2O_3-ratios.

3.3. Influence of superplasticizers

3.3.1. Experimental program

The general influence of conventional superplasticizers on the rheological behavior of the one-part geopolymer fresh pastes was studied by determining the spread flows of specific OPG pastes. Referring on the mini-cone test [68] a small cylinder (d ≈ 38.37 cm, h ≈ 6.13 cm, V ≈ 70.89 cm^3) was used. The spread flows were determined by applying 15 strikes to the pastes after the determination of the slump flow on the Hägermann table.

The superplasticizers were tested on the formulation MS_6 (w/b = 0.7) and a modified mix MS_6_SL (w/b = 0.7) with a total amount of 10 wt.% CaO (≈ 22.2 wt.% SL). The aim was to investigate the effect of the superplasticizers with and without a significant amount of calcium in the fresh pastes. Four different superplasticizers have been studied: two lignin sulfonates (LiS a) and LiS b)), one naphthalenesulfonate (NFS) and one polycarboxylate ether (PCE).

3.3.2. Results and discussion

The results of the experiments on the spread flows of MS_6 and MS_6_SL are presented in Fig. 3.5 and Fig. 3.6. The spread flow of MS_6 without any superplasticizer was determined to be 8.7 cm. In the following this value is regarded as 100% spread flow, *i.e.* relative changes of the spread flow are based on this value. For the calcium free MS_6 mix, the PCE was found to have no positive effect at all (Fig. 3.5). By adding 0.25 wt.% of PCE, the spread flow decreased to 90% of the starting value, *i.e.* the MS_6 mix without PCE. With further increasing PCE content (up to 1.00 wt.%) the spread flow slightly re-increased (95% at c = 1.00 wt.%), but remained less than 100 %. For the NFS a slightly but almost negligible (positive) effect was observed for medium concentration (0.50–0.75 wt.%). Further

increasing of the NFS concentration (1.00 wt.%), led to a significant decrease of the spread flow below the reference value.

In contrast to the above-mentioned additives, the ligninsulfonates clearly showed a more pronounced effect on the spread flow of MS_6. LiS a) steadily increased the spread flow from 105% at the lowest concentration (c = 0.25 wt.%) to 114% at the highest concentration (c = 1.00 wt.%). The effect of LiS b) was even more pronounced. At a concentration of 0.85 wt.% the spread flow increased to 125 %. Further increasing concentration of LiS b) led to a slight decrease.

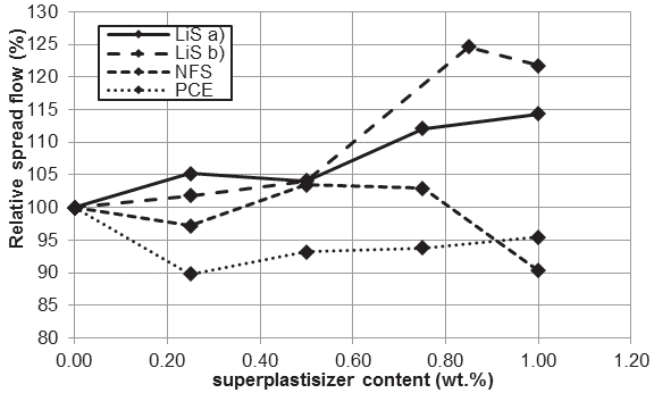

Figure 3.5: Relative spread flow changes of MS_6 (w/b = 0.7) at different contents of superplasticizers LiS a), LiS b), NFS and PCE.

The spread flow of the calcium containing MS_6_SL mix without any superplasticizer was determined to 8.4 cm (= 100 %). Thus, the addition of ≈ 22 wt.% SL did not lead to significant changes of the flowability of the according paste. In contrast to the calcium free system the PCE had no negative effect at very low concentrations for MS_6_SL but decreased below the reference value at the highest concentration (Fig. 3.6). NFS again had a very slight positive effect up to a concentration of 0.50 wt.%. Thus can be concluded, PCE and NFS provided only slight or negligible effects in the regarded OPG systems.

As for the slag free mix, the ligninsulfonates provided an increase of the spread flow. Both additives reached the maximum positive effect at a concentration of 0.75 wt.%. Also, the maximum values for LiS a) (132. %) and LiS b) (131 %) were virtually equal. The relative increase of the spread flow was even more pronounced than in the calcium free system. With further increasing concentration a significant decrease of the spread flow of more than 10% was observed.

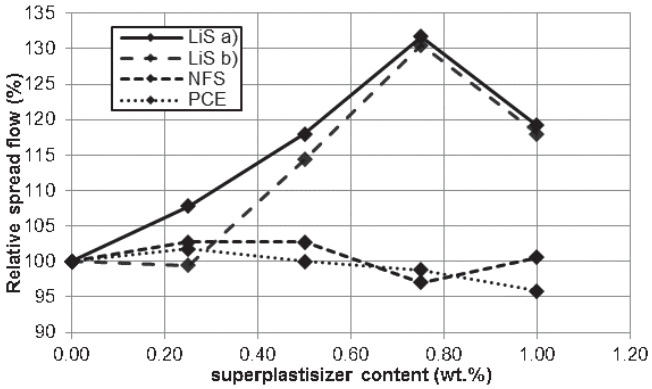

Figure 3.6: Relative spread flow changes of MS_6_SL (w/b = 0.7) with 10 wt.% CaO in the binder, at different contents of superplasticizers LiS a), LiS b), NFS and PCE.

There is still a lot of research necessary on potential additives, for alkali activated materials, such as geopolymers. In this context, the aim was to find a class of superplasticizers that could be focused in further, more detailed investigations. Naphthalene-based additives were found to have a positive influence on the workability of OPG fresh pastes [47]. However, the used NFS additive of this work had only slight effects in both mixes. For both mixes the ligninsulfonates showed the most promising results. In this context LiS b) had a more pronounced effect in the Ca-free MS_6 mix. In the CaO containing MS_6_SL mix both additives provided further improved behavior. The spread flow could be increased by ≈ 25% for the mix MS_6 and by > 30% for the mix MS_6_SL. Fig. 3.7 shows photographs of the slump flow and the spread flow experiments of MS_6_SL with a concentration of 0.25 wt.% of LiS b) and 0.75 wt.% of LiS b). Those additives should be considered in further studies, e.g. regarding the development of the mechanical strength of the OPG under the influence of the additives.

Figure 3.7: Slump flow and spread flow of MS_6_SL (10 wt.% CaO, w/b = 0.7), left: with an addition of 0.25 wt.% of LiS b); right: with an addition of 0.75 wt.% LiS b).

4. STRUCTURAL PROPERTIES AND HARDENING OF THE OPG PASTES*

The presented results of Chapter 3 showed that for comparable mass based w/b, the silica based OPG fresh pastes provide higher viscosities than OPC pastes, which may cause higher water contents for the OPG in different applications. Furthermore, the rheological properties vary significantly with the chemical composition of the binder formulation. This chapter Chapter therefore considers the reactivity, the microstructure and the resulting hardening of the OPG for different paste compositions, at different curing conditions and for different silica feedstocks.

The investigated OPG pastes were synthesized from MS(1), CR, RHA(1), RHA(2), SA(1), SA(2) and SA(3), respectively.

4.1. Introduction

OPG systems are often dominated by crystalline tectosilicates (zeolites) and the reported compressive strengths are often lower than for conventional two-part geopolymers or not even stated [40, 41, 44, 46, 48, 50-53]. The mixes in the literature are mainly based on silica-rich industrial by-products [40, 41, 48, 50, 51], as well as on alkali-thermal activated minerals and industrial waste materials [44, 46, 52]. Except specific mixes of Feng et al. [44], all syntheses in the aforementioned studies did not form only geopolymers, but geopolymer-zeolite composites. However, new formulations, based on biogenic rice husk ash (RHA) show that the RHA is highly reactive and can form a typical geopolymer gel with higher compressive strength than generally observed for OPG [49, 54].

Therefore, the following Chapter studies the influence of the chemical composition of the OPG on the strength development, based on the different industrial and biogenic silica feedstocks, and the resulting microstructure at various curing conditions.

* The results of the MS- and CR-based OPG of Section 4.2.2 and RHA(1)-based OPG of Section 4.3.2 have been published in Sturm et al: Degree of reaction and phase content of silica-based one-part-geopolymers investigated using chemical and NMR spectroscopic methods. Journal of Materials Science, Vol. 50, p. 6768-6778 (2015); Sturm et al: The effect of heat treatment on the mechanical and structural properties of one-part geopolymers-zeolite composites. Thermochimica Acta, Vol. 635, p. 41-58 (2016); Sturm et al: Synthesizing one-part geopolymers from rice husk ash. Construction and Building Materials, Vol. 124, p. 961-966 (2016) and Greiser et al: Differentiation of gel, zeolite phases and water species in geopolymer-zeolite composites, Ceramics International, Vol. 43, p. 2202-2208 (2017).

4.2. Chemical Composition and degree of reaction of MS- and CR-based OPG

4.2.1. Experimental program

To obtain general information about the influence of the composition of the considered OPG on their hardening behavior, OPG were synthesized from the two different industrial silicas MS and CR and SA at three different SiO_2/Al_2O_3 ratios (Tab. 4.1) and a nominal w/b ratio of 0.50 by mass. The differences between the molar SiO_2/Al_2O_3 ratios and the according sample name is due to the measurement error of the LOI of the used SA. The sample for chemical analysis was insufficient sealed during storage, hydrated and pretended a water content that was higher than it actually was for the SA batch (cf. also Section 3.2.). The formulations for the samples of the later described high-temperature investigations have been adjusted (cf. Section 5.2; Tab. 5.1).

The samples were mixed in the contact free planetary centrifugal mixer for three minutes at a rotation speed of 1750 rpm to form homogenous pastes. Subsequently, the pastes were cast into 20 mm × 20 mm × 20 mm cube molds and cured in the open molds at 80 °C and ≥ 80% r.H. for 1, 3 or 7 days in an oven with climate conditioning.

Table 4.1: Oxide composition and molar ratios of the OPG.

Sample	Na_2O	Al_2O_3	SiO_2	H_2O	Na_2O/Al_2O_3	SiO_2/Al_2O_3	H_2O/Al_2O_3
	(wt.%)	(wt.%)	(wt.%)	(wt.%)	(mol/mol)	(mol/mol)	(mol/mol)
CR_2	13.40	23.74	25.01	34.17	0.93	1.79	8.15
CR_3.5	9.85	18.12	33.37	34.10	0.89	3.13	10.65
CR_6	6.61	13.00	40.97	34.04	0.84	5.35	14.82
MS_2	14.17	23.86	26.20	34.25	0.98	1.86	8.12
MS_3.5	10.63	17.88	35.58	34.21	0.98	3.38	10.83
MS_6	8.03	13.47	42.49	34.17	0.98	5.35	14.36

The phase assemblage of the cured OPG was investigated by XRD, and the degree of reaction of the silicas in the OPG after curing at elevated temperature was calculated from the chemical dissolution method: chemical attack with HCl to dissolve the reaction products (cf. detailed description Section 2.1.2.1.). The resulting degrees of reaction were compared and related to the phase assemblage of the geopolymers, thus giving insights into the behavior of the silica and the composition of the hardened geopolymers.

The results of the chemical dissolution method were compared to a second quantification method, the evaluation of peak areas of ^{29}Si MAS NMR spectra, using the fact that the intensity of each peak corresponds to the abundance of the Si-sites in the different compounds. The NMR results are part of the Ph.D. thesis of Sebastian Greiser [70] and will be discussed in comparison to the results of the chemical dissolution method.

The procedure was also applied to the both silica starting materials (MS and CR) and a sample of zeolite A. The silica materials differed in their dissolution behavior during the acid attack: while (2.6 ± 0.2) wt.% of MS were dissolved; (13.6 ± 0.3) wt.% of CR were dissolved. This is readily explained by the lower amount of SiO_2 and the higher amount of impurities in CR. Zeolite A was virtually completely (99.7 ± 0.1 wt.%) dissolved during the acid-treatment.

4.2.2. Results and discussion

Fig. 4.1 shows the diffractograms of the OPG after curing for one day at 80 °C. The reaction did not lead to only amorphous reaction products, but also crystalline aluminosilicate tectosilicates. In the MS-based geopolymers, the major crystalline phases after curing were hydrated zeolite A (PDF # 00-039-0222) and a hydrosodalite (HS) of intermediate water content, $Na_6(AlSiO_4)_6{\cdot}4H_2O$ (PDF # 00-042-0216). This HS was e.g. also identified by Hajimohammadi et al. [45] and Zhang et al. [111] in geopolymers (one-part and metakaolin-based, respectively). The latter authors determined the average size of the HS crystallites in their samples to be ca. 21 nm; also in the present study the broad reflections indicate either a small crystallite size or a considerable degree of disorder. The relative amount of HS *versus* the amount of zeolite A increased with decreasing silica content in the starting mix (Fig. 4.1). A small hump around 18 ° 2θ gives hints for the presence of poorly crystalline gibbsite (PDF # 00-033-0018) in MS_2.

In the CR-based OPG (Fig. 4.1), zeolite A was the dominant crystalline phase for all starting SiO_2/Al_2O_3 ratios. All CR-based specimens incorporated also small amounts of calcite (PDF # 01-083-1762) and quartz (PDF # 00-046-1045) as remainders from the silica feedstock (cf. Section 2.2.2; Fig. 2.1). At low silica content (CR_2), low amounts of sodalite-type phase occurred, giving the best match with a sodalite *sensu stricto* reference, *i.e.* containing Cl^- in the cavities of the aluminosilicate framework (PDF # 01-072-0029). Chloride is supplied by the CR silica (*cf.* Section 2.2.2.; Tab. 2.1). At high silica CR content, the chloride was precipitated as halite (PDF # 00-005-0628). In addition, these specimens contained low amounts

of faujasite (PDF # 00-038-0239) and zeolite EMT (PDF # 00-046-0566). The structure of zeolite EMT is related to that of faujasite and these zeolites tend to form (disordered) intergrowths [112-115], which makes the presence of both zeolites reasonable. Additionally, zeolite P (PDF # 00-040-1464) was identified in low amounts in the low silica mixes MS_2 and CR_2

Compared to the diffractograms of the silica starting materials (Section 2.2.2.; Fig. 2.1), the hump in the diffractograms of the cured geopolymers is broadened to higher diffraction angles, which indicates the formation of amorphous geopolymeric gel [29]. High silica MS_6 or CR_6 formulations showed less pronounced decrease of the initial silica hump. In general, the considered OPG formulations did not form a fully condensed network of amorphous geopolymers, but geopolymer-zeolite composites, as typical for the OPG synthesis route [40, 41, 44, 46, 47, 50, 51].

The differences in the phase assemblage of the cured composites can be partly explained by the differences in pH of the fresh pastes. Besides the kind of silica feedstock, SA plays an important role for the evolution of the phases of the OPG mixes. It is known that in the Na_2O-Al_2O_3-H_2O system at temperatures up to 150 °C the equilibrium concentration of Na is always higher than that of Al (also when Cl^- or CO_3^{2-} impurities are present) [110], *i.e.* in $NaAlO_2$ solutions the precipitation of $Al(OH)_3$ is expected, as previously discussed regarding the fresh paste properties of the OPG (cf. Section 3.2.2.). This is confirmed by own auxiliary experiments, in which it was found that a sodium aluminate suspension (25 g sodium aluminate in 50 g water) rapidly precipitates a white gel. XRD revealed that after several days aging at 80 °C the gel had crystallized to gibbsite (PDF # 00-033-0018); no sodium-containing phase was found in the precipitation product. The pH of the SA suspension was determined 10 minutes after the addition of water to be 14.4. A sodium aluminate suspension with 28.48 g sodium aluminate suspended in 25.00 g water, *i.e.* simulating the conditions in MS_2 and CR_2 (*cf.* Tab. 5.1), had pH = 14.7 after 8 minutes.

MS_2 had pH = 14.5 10 minutes after adding water, and pH = 14.7 after 30 minutes. CR_2 pastes had pH = 14.7 after 10 minutes as well. On the contrary, the fresh high-silica (SiO_2/Al_2O_3 = 6) pastes had pH values of only 14.2 (MS_6) and pH = 13.4 (CR_6) after 10 minutes, in line with the decreasing SA content and the decreasing viscosity of the fresh pastes for SiO_2/Al_2O_3 > 5, due to the decreasing of the saturation index of SA below 0 (Section 3.2.2.). The higher pH in the MS_2 mix is assumed to be the reason for the enhanced direct formation of HS or early transformation of zeolite A into HS structures (*cf.* Ref. [116]). The higher pH in the low-silica samples (MS_2 and CR_2) will also cause faster dissolution of the silica

in the hardening pastes. This is possibly the reason for the formation of faujasite and zeolite EMT in CR_2 samples. These zeolites have an anionic framework with silicon excess over aluminum (Si:Al > 1), which implies a higher initial availability of dissolved silica [117], and are only present in the low-silica mixes. Depending on template (like metal ions or organic ions) various zeolites can be synthesized from almost equal chemical compositions [118]. In this context it is noted that the silica feedstock CR incorporated more impurities, such as Ca, Fe or Cl (cf. Section 2.2.2; Tab. 2.1) and more diverse crystalline tectosilicates.

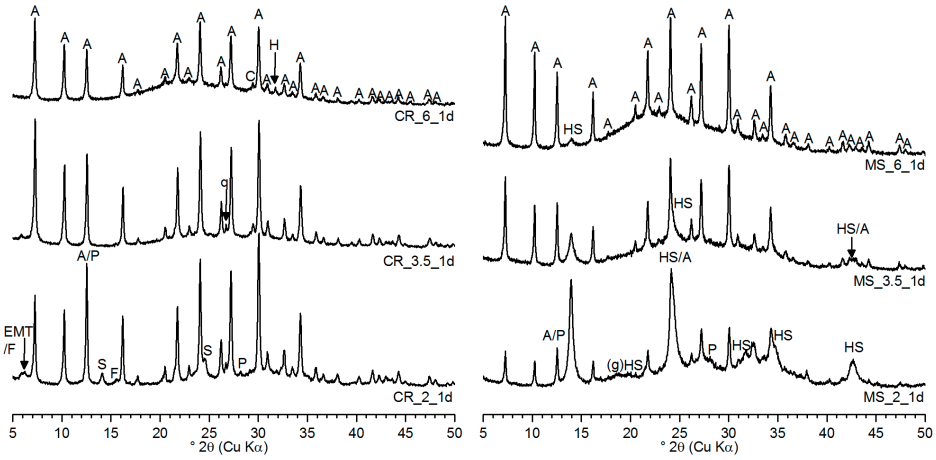

Figure 4.1: X-ray diffractograms of the MS (left side) and CR-based (right side) OPG, cured for one day at 80 °C and 80% r.H. (A = zeolite A; HS = hydrosodalite; EMT = zeolite EMT; F = faujasite; S = sodalite; P = zeolite P; C = calcite; q = quartz, g = gibbsite; H = halite).

The relative intensities of the three peaks of zeolite A at the lowest diffraction angles (7.17°, 10.16° and 12.47° 2θ) varied between the samples. For reference zeolite A (Section 5.3.; Fig. 5.3.1) their intensities are decreasing from the first (7.17° 2θ) over the second (10.16° 2θ) to the third (12.47° 2θ), as for the Na A-type structure [112]. However, depending on the mix-design of the composites the intensity of the third of these peaks was increased, in particular for the low-silica mixes. This is most likely related to small variations of stoichiometry (Si/Al ratio) and/or water content of the A-type zeolites framework: In the diffractograms of conventionally synthesized zeolite A samples, presented by Radulović et al. [119], comparable changes in peak intensities were observed on going from $1.05Na_2O{\cdot}1.06Al_2O_3{\cdot}2.00SiO_2$ to $1.05Na_2O{\cdot}1.00Al_2O_3{\cdot}2.05\ SiO_2$, though the cell parameters of the zeolites did not differ significantly. In addition, calculated XRD patterns of hydrated and dehydrated zeolite A [112] reveal a more pronounced decrease of the peak height of the third peak on dehydration, compared to the height of the other two peaks at

lower 2θ. Comparable tendencies were observed during heating (dehydration) of the considered composite samples (cf. Section 5.3.).

With increasing content of dissolved silica content in the reaction system, zeolite P forms instead of zeolite A [120], identified as traces for virtually fully reacted CR_2 and MS_2 mixes, (Fig. 4.1). As is shown in Fig. 4.2 for the representative example of CR_3.5, the qualitative phase assemblage did not change over the curing time, independent from the composition and silica feedstock.

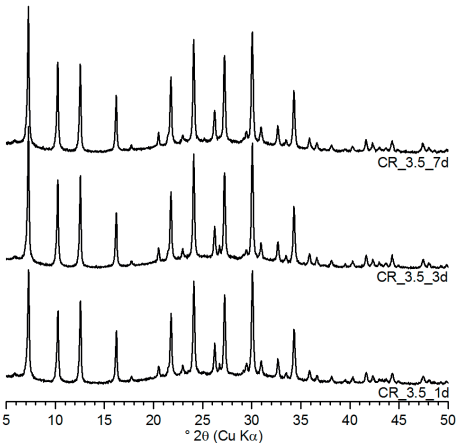

Figure 4.2: X-ray diffractograms of CR_3.5 cured for different times (1 day, 3 days and 7 days) at 80 °C and 80% r.H., respectively.

For the MS-based and the CR-based OPG, the degree of reaction of the silica (α[HCl]; cf. Section 2.1.2.1.), increased with decreasing silica content in the starting mix but generally did not change significantly with increasing curing time (Fig. 4.3).

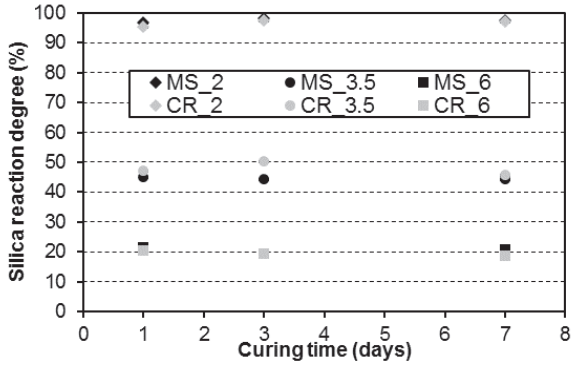

Figure 4.3: Degree of reaction of the silica (MS; CR) in the cured OPG, determined by the dissolution method (HCl).

This is in good agreement with the XRD analyses, where virtually no changes were observed for curing times, longer than one day at 80 °C. The low-silica samples (MS_2 and CR_2) exhibited nearly 100% reacted silica. Medium-silica (MS_3.5 and CR_3.5) and high-silica (MS_6 and CR_6) samples exhibited considerably lower degrees of reaction of ≈ 45% and ≈ 20 %, respectively (Fig. 4.3). The differences in the degree of reaction are also reflected in the XRD results: the more unreacted silica remained in the OPG, the less pronounced is the shift to higher 2θ values in the diffractograms.

Specific insoluble residues after the dissolution procedure (HCl + 1000 °C) were investigated by XRD. For the low-silica samples not enough sample mass could be obtained (α[HCl] ≈ 100 %). All investigated samples provided a shifted back maximum of the hump to lower diffraction angles, matching the maximum of the hump in the diffractograms of the silica sources. The only detectable crystalline phases were cristobalite (PDF # 01-076-0941) for MS-based geopolymer residues, and cristobalite as well as quartz (PDF # 00-046-1045) and traces of mullite (PDF # 01-073-1389) in the CR-based samples. Apparently, the quartz is a residue from the silica CR. The presence of mullite can be explained by low amounts of Al_2O_3 remaining in the system after dissolution in HCl and the subsequent high-temperature treatment at 1000 °C, indicating only a virtually full dissolution of aluminosilicate reaction products in HCl. Fig. 4.4 shows the example of CR_6_1d before and after HCl-treatment compared with pure silica CR. The back shifted hump mainly represents the silica rich residue, *i.e.* the unreacted silica after acid-treatment. The diffraction maximum of silica CR and insoluble residue are equal.

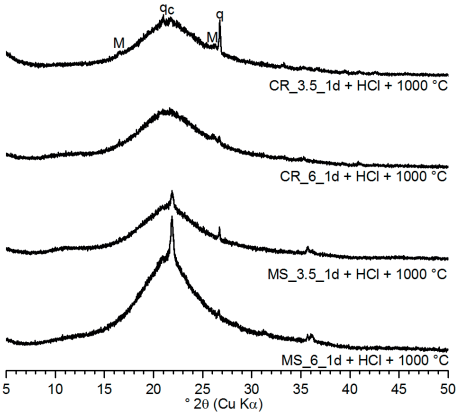

Figure 4.4: XRD diffractograms of the insoluble residues (HCl + 1000 °C) of the OPG with SiO_2/Al_2O_3 ≈ 3.5 and SiO_2/Al_2O_3 ≈ 6, cured for one day at 80 °C and 80% r.H. (*M*: mullite; *q*: quartz; *c*: cristobalite).

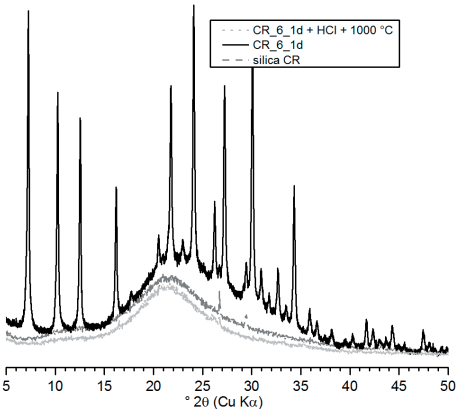

Figure 4.5: XRD diffractograms of silica CR, the OPG CR_6 with $SiO_2/Al_2O_3 \approx 6$ cured for one day at 80 °C and 80% r.H., and the insoluble residue (HCl + 1000 °C) of the same OPG.

NMR investigations on the same OPG [48] showed in the cured samples with remaining silica (MS_3.5 and MS_6) an increased amount of Q^3 (0Al) sites and a decreased amount of Q^4 (0Al) sites. These changes are related to the alteration/hydration of the silica surface during dissolution. This interpretation is in line with previous studies [121, 122], in which it was observed that dissolution of MS in alkaline (Ca-dominated) media led to the formation of Q^3 species. These were assigned fully [121] or in large part [122] to the silica. In the latter study it was shown by ^1H-^{29}Si CP MAS NMR, that these species can be assigned to a hydrated layer on the surface of MS. Another study [123] found that formation of a significant amount of Q^3 species took place also during dissolution of MS in 1 mol/l NaOH solution.

Deviations exist between the results of dissolution in HCl and ^{29}Si MAS NMR for the measurement of the degree of reaction of the silica in the OPG. In all cases the reaction degree as determined by NMR spectra curve fitting was larger than the results based on the dissolution method and the deviations increased with decreasing degree of reaction from MS_2 (3.3 %) to MS_6 (13.5 %) [51, 70].

A possible reason for the observed deviations between the results of the two methods is incomplete dissolution of the reaction products during the HCl-treatment (*cf.* Refs. [124, 125]). While ^{29}Si MAS NMR measures only silicon atoms in the samples, the results of the dissolution method are based on the accuracy of the measurements of the insoluble residue, and the assumption that the insoluble residue contains only remaining (silica) feedstock but no reaction products [71]. However, ^{27}Al MAS NMR spectra of samples MS_3.5 and MS_6 after dissolution in HCl and heating to

1000 °C reveal that a significant amount of aluminum (1–2 at. %), *i.e.* considerably more than in the starting MS silica, remained in the samples [51, 70]. These observations together with observed mullite indicate that the chemical attack with HCl on the reaction products was not complete and hence the calculated silica reaction degrees α[HCl] are too low. This explanation, however, cannot fully account for the observed differences between the methods: allowing for 1–2 wt.% of aluminum in the samples after the dissolution procedure results in reaction degrees, α[HCl], that are only 1–3% (abs.) higher than the values of Fig. 4.3. An additional error probably occurs from the formation of a secondary silica gel that contributes to the residual mass as will be discussed in Chapter 9 for the sulfuric acid attack.

Despite the bias of the dissolution method, its results can serve to identify changes of the degree of reaction of the silica, e.g. with curing time and/or temperature. In the present context, it is important to note that under the employed curing conditions the dissolution of the silica did not proceed significantly after a curing time of one day (Fig. 4.3). In line with this, only very minor changes of the diffractograms of the geopolymers could be observed after this curing time (Fig. 4.2). The degree of reaction of the silica was nearly 100% in the geopolymers with starting $SiO_2/Al_2O_3 \approx 2$ (low-silica), but considerably lower in the medium and high-silica geopolymers (Fig. 4.3). Unlike the paste SiO_2/Al_2O_3 ratio, the source of the silica starting material, *i.e.* MS or CR was of minor importance for its degree of reaction in the considered reaction systems. It can be assumed that the error made in the determination of the degree of reaction of the silica CR by the chemical method is similar to the error for the MS-based samples.

From the degrees of reaction of the silica MS-based OPG, as determined by NMR [51, 70], the composition of the silica feedstock (cf. Section 2.2.2.; Tab. 2.1) and the starting composition of the geopolymers (Tab. 4.1) the SiO_2/Al_2O_3 ratio of the reaction products were estimated. The SiO_2/Al_2O_3 ratios of the obtained reaction products, when a full reaction of SA is assumed, are slightly below 2 mol/mol (*i.e.* ≈ 1.9 mol/mol) for all starting MS contents [51], what is forbidden according to Loewenstein's rule [36]. Excess alumina is included. This may be the reason for the occurring low intensity signals of octahedral aluminum in the ^{27}Al MAS NMR spectra of the according specimens MS_2, MS_3.5 and MS_6 [51]. No peaks of octahedral coordinated Al-containing phases could be identified by XRD for these samples, except an assumed poorly crystalline gibbsite impurity in MS_2 (Fig. 4.1). Especially for RHA(2) based OPG crystalline aluminum hydroxide (gibbsite, bayerite) precipitated during the synthesis, due to an excess of SA in the system (see below).

However, from this assumption and the almost identical degrees of reaction (Fig. 4.3) it follows that also for all CR-based geopolymers the SiO_2/Al_2O_3 ratio of the reaction products is close to 2 too. Thus, it appears that under the employed synthesis conditions silica MS and CR are dissolved only to an extent that the reaction products achieve a SiO_2/Al_2O_3 ratio of ≈ 2 mol/mol; afterwards dissolution of the silica ceases. Nevertheless, CR_2 contained small amounts of faujasite and zeolite EMT, whose SiO_2/Al_2O_3 ratios are 4.8 and 6.6, respectively, and low amounts zeolite P (SiO_2/Al_2O_3 = 6.9) in CR_2 and MS_2 indicating SiO_2/Al_2O_3 ratios > 2 of the fresh paste at least at a certain time.

Besides an increased pH value of the fresh pastes no major hint for the increased HS formation in MS_2 mixes was found. The increased pH, correlating with an increased reactivity of the paste and an increased availability of network forming species, perhaps also leads to an increased reaction speed and therefore to an increased seeding tendency, that enhances the formation of HS over zeolite A or its transformation from it. The transformation of zeolite A to HS over the time at ambient and elevated temperatures [116, 120, 126-128] is generally enhanced with increasing sodium content [120, 126], what contributes to the increasing HS formation with increasing SA content. The HS formation is further enhanced with decreasing water availability [120], what suggests an enhanced HS formation at later reaction times, due to the consumption of reaction water and a further decrease due to the applied relative humidity (80 %) at the relatively high temperature (80 °C). The increasing HS content with increasing curing time at higher curing temperatures (90 °C; cf. Section 4.4.2) further supports the enhanced HS formation at later curing times.

The observed differences in the amount of unreacted silica and in the phase assemblage of the cured OPG determine their mechanical properties, if additional overlapping factors are excluded. A previous investigation [106] showed that the compressive strength of MS-based one-part geopolymers (water/solids ratio 0.60) increased consistently with increasing starting SiO_2/Al_2O_3 ratio; the highest strength was obtained at SiO_2/Al_2O_3 = 6 [106]. The strength presented in this Section are the 3d strength, *i.e* the as-cured strength, of the OPG composites of the high-temperature investigations (cf. Section 5.3), since the formulations of Section 5.3 are more properly composed (no SA LOI error was included; Section 5.2; Tab. 5.1).

The strength increase of the MS-based OPG pastes (Fig. 4.2.2.7) with increasing SiO_2/Al_2O_3 ratio can be attributed, at least partly, to the unreacted silica of the mixes [129]. In this context the remaining silica particles, which may act as micro-aggregates, and/or differences in porosity and pore sizes of the cured geopolymers contribute to the mechanical strength as well. As pointed out by Oh et al. [130], also

the relative amounts of different kinds of zeolites (and/or the similarity geopolymeric gel to these zeolites) can significantly impact on the mechanical properties of the cured geopolymers. However, the latter authors reported only on benefits of the bulk modulus of basic hydrosodalite, while the major crystalline phases in the present MS-based geopolymers were zeolite A at high starting SiO_2/Al_2O_3 ratio and (non-basic) HS at low starting SiO_2/Al_2O_3 ratios. The composites of the present study exhibited significantly lower strength than pure geopolymer gels which can possess compressive strengths in excess of 80 MPa [13, 117]. This is very probably related to the significant content of crystalline zeolites in the composite materials (*cf.* Refs. [29, 52]), their porous microstructure (cf. Section 4.3.2.) and the correlating more particulate overall microstructure of the hardened pastes as will be discussed more detailed below. The formation of composites, causing comparably low strength, due to the decreased amount and increased interruptions of the main strength forming phase, the aluminosilicate N-A-S(-H) gel network, is very typical for OPG [40, 41, 44, 46, 50-53]. However, the compressive strengths (up to ≈ 19 MPa) appear to be sufficient for various applications such as heat-resistant coatings or repair mortars etc. However, significantly higher compressive strength of the OPG can be achieved by adjusting the w/b, especially for mortars, as will be discussed in Section 7.2.

In addition to the microstructure, the macroporosity of a solid is important in controlling its strength. The fresh mixes exhibited swelling and macro pore formation during curing. Own experiments showed this is mainly related to the formation and release of hydrogen due to the reaction of a silicon impurity of the silica feedstock and the effect of foaming silica fume was also observed by Prud`homme et al. [131]. A minor effect is probably related to gas formation of the silicon carbide impurity, as proven by own experiments on adding fine SiC powder to the OPG pastes. These processes were much more significant in the MS-based mixes, and increased with increasing degree of reaction of MS. More reacted silica led to more release of the gas forming agents. This means that the macroporosity increased with decreasing SiO_2/Al_2O_3 ratio in the pastes. The expansion caused microcracks and macrocracks (cf. Section 4.3.2.; Fig. 4.9 and Section 8.3.3.; Fig. 8.7), that weakness the structure and led to foam like specimens for MS_2 formulations. This behavior is considered to be a major reason for the decrease in strength of the MS-based mixes with decreasing SiO_2/Al_2O_3 ratio, overlapping the microstructure.

On the other hand, a reversed trend for the CR-based mixes was observed (Fig. 4.6). CR_2 provided the highest compressive strength (13 MPa) of the CR-based OPG. Swelling occurred as well for the CR-based formulations but it was much less pronounced, thus another mechanism is responsible for the dependency. This shows a high degree of reaction can enhance the mechanical strength, when overlapping

factors are decreased. On the other hand, at high SiO_2/Al_2O_3 ratios the workability of the CR-based pastes was considerably inferior to the workability of the MS-based pastes.

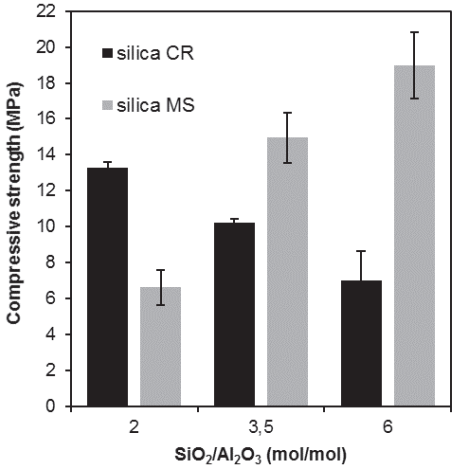

Figure 4.6: Compressive strength of the MS- and CR-based geopolymer-zeolite composites after 3 days of curing at 80 °C. Error bars represent one standard deviation in each direction.

The workability decreased with increasing SiO_2/Al_2O_3 ratio, but much more pronounced than for the MS-based mixes. Silica CR provided an increased BET surface (32.3 m^2/g) compared to MS (20.1 m^2/g) and significantly increased average pore diameters (29.3 nm for CR and 17.0 nm for MS) causing increased water demand for silica CR. This may partly explain the lower strengths of the CR-based composites at medium and high SiO_2/Al_2O_3 ratios, as insufficient workability of the fresh pastes impacts on the compressive strength of the cured composites by introducing inhomogeneities and flaws into the material. The influence of the impurities of silica CR has to be further regarded in this context. The affection of the impurities on the properties of the hardened OPG can be controlled in general by adjusting the chemical composition of the pastes and the related, expectable degree of reaction of the silica MS.

4.3. Influence of the silica feedstock

4.3.1. Experimental program

OPG were synthesized by mixing RHA(1) and solid SA(2), and subsequently adding water at a nominal water/binder ratio (w/b) of 0.5 by mass to yield molar silica to alumina ratio of 3.5 (Tab. 4.2). The mix-design was chosen to facilitate comparison with the complementary MS_3.5 and CR_3.5 (Section 4.2) formulations with the same molar ratios, that lead to the formation of geopolymer-zeolite composites.

The mix design and mixing procedure in the planetary centrifugal mixer of the MS and CR mixes are equal to the mixes, presented in 5.2 where the formulations were slightly adjusted, due to the delayed recognition of a wrong determined water content of the SA for mixes in the previously discussed Section 4.2. The mixing of the RHA(1)-based mix was conducted in a planetary centrifugal mixer as well, for 4 minutes at a rotation speed of 1200 min^{-1}.

Additional experiments on a technical grade RHA (RHA(2)) and a technical grade SA(3) have been conducted to investigate the transferability of the results of the well prepared RHA(1)-based OPG. Therefore, the pastes were prepared at specific molar SiO_2/Al_2O_3 (Tab. 4.3) and a nominal w/b of 0.4. The preparation of SiO_2/Al_2O_3 = 2 was not reasonable, because of intensive swelling (comparable to MS_2).

Table 4.2: Mix-designs and molar ratios of the OPG MS/CR/RHA(1)_3.5 and w/b 0.5.

Sample	m(Na_2O)	m(Al_2O_3)	m(SiO_2)	m(H_2O)	Na_2O/Al_2O_3	SiO_2/Al_2O_3	H_2O/Al_2O_3
	(wt.%)	(wt.%)	(wt.%)	(wt.%)	(mol/mol)	(mol/mol)	(mol/mol)
RHA_3.5	10.17	16.76	34.46	35.03	1.00	3.48	11.81
MS_3.5	10.42	17.52	36.31	34.20	0.98	3.52	11.05
CR_3.5	9.13	16.99	35.19	34.09	0.88	3.51	11.35

Table 4.3: Mix-design and molar ratios of the OPG based on RHA(2) with w/b = 0.4.

Sample	SiO_2/Al_2O_3	Na_2O/Al_2O_3	H_2O/Al_2O_3
	(mol/mol)	(mol/mol)	(mol/mol)
RHA_3.5	3.58	1.00	8.85
RHA_6	6.12	1.01	12.48
RHA_8	8.17	1.01	15.38

Two series with different mixing regimes have been investigated for the RHA(2)-based OPG. One series was prepared using the planetary centrifugal mixer at a rotation speed of 1100^{-min} in three steps (3 × 3 min) to allow the mixer to cool down. Before the mixing, the pastes have been stored in sealed containers for 30 minutes after the addition of water. Due to the high demanded number of samples, also for thermal investigations as presented below (Section 5.3.), a second series was prepared, mixing the pastes in the standard mortar mixer for 20 minutes at the lower speed and further 40 minutes at the higher speed (sum = 60 min). For this series, the pastes have been stored 60 minutes after adding the water and before starting the mixing. The unconventional procedures were necessary to obtain workable pastes and this shows the general deficit of the feedstock RHA(2) compared to RHA(1). Regarding the economic aspect, both mixing procedures were not applicable.

Independent from the presented properties of the hardened OPG, derived from RHA(2), the technical process, leading to RHA(2) must be improved for practical applications of the OPG, in terms of workability of the fresh pastes. Nevertheless, in contrast to silica MS, high silica RHA_6 and even RHA_8 were prepared at w/b 0.4. CEM III/B was used as a reference for the evaluation of the hardening. The CEM III/B pastes were prepared at the same w/b (0.4) by mass. CEM III/B was chosen as reference because of its high slag content and commercial use for applications at elevated temperature range (Chapter 5).

All pastes have been poured into cube molds with the dimensions 20 mm × 20 mm × 20 mm. Subsequently, OPG have been cured for one day at 80 °C and 80% r.H. in an oven with climate conditioning. The pastes have been removed from their molds and either tested or additionally stored at 80 °C until 3d or 7d of age (RHA(1)-based OPG), or at 23 °C and 50% r.H. until further use (RHA(2)-based OPG) for a maximum of 56 days. CEM III/B was stored at 23 °C under water. After removing from their molds after 24 hours, the cubes were tested or further stored at the same curing conditions as within the first 24 hours. Besides the observation of the compressive strength development, structural investigations, including XRD, ATR FT-IR and SEM were performed on the hardened specimens.

4.3.2. Results and discussion

4.3.2.1. Structural analysis of RHA(1)-based OPG

The XRD results of the OPG RHA_3.5, derived from RHA(1) are presented in Fig. 4.7. The hump of the RHA, with a maximum located at 21.82° 2θ, disappeared after curing and a new hump with its maximum at 27.68° 2θ, representing the geopolymeric gel [29], occurred after curing. The disappearance of the hump from the RHA indicates its virtually complete reaction, *i.e.* a degree of reaction of the RHA close to 100 %. This contrasts the previously investigated OPG systems based on the industrial MS and CR silicas, in which the silica feedstocks reacted only partly, depending on the initial SiO_2/Al_2O_3 ratio. At SiO_2/Al_2O_3 = 3.5 mol/mol the degree of the silica feedstocks (MS, CR) in these investigations was only ≈ 56% (cf. Section 4.2.2 and [51, 70]).

The diffractograms of the 1d, 3d and 7d cured specimens indicated almost completely amorphous reaction products. No crystalline aluminosilicates, such as zeolites, were observed; different to the character of the zeolite-containing composites MS_3.5 and CR_3.5. Low amounts of thermonatrite ($Na_2CO_3 \cdot H_2O$; PDF # 00-008-0448) were identified in the geopolymers, due to minor carbonation of the

highly alkaline system. The phosphate and the calcite, present in the starting RHA, disappeared after curing, indicating their dissolution. On the contrary, cristobalite and quartz remained in the system (Fig. 4.7). Curing for longer than 1d did not lead to significant changes in the phase assemblage, as observed by XRD. This leads to the conclusion that after one day of curing the reactions were almost finished. This behavior fits quite well into the observations of the MS- and CR-based OPG, when cured at 80 °C (cf. Section 4.2.2).

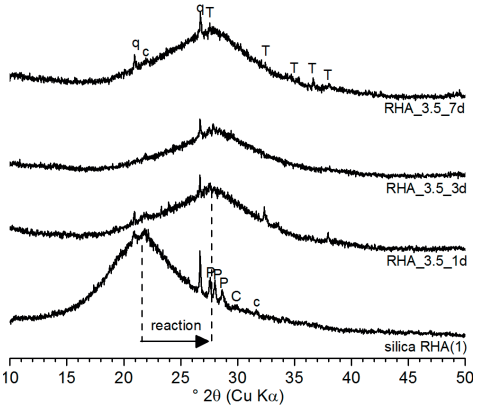

Figure 4.7: XRD patterns of pure silica RHA(1) and the according OPG RHA_3.5 after 1d, 3d and 7d of curing at 80 °C and 80% r.H., respectively. (q = quartz, c = cristobalite, P = potassium magnesium phosphate; C = calcite, T = thermonatrite)

The infrared spectra of the unreacted RHA(1) and the cured geopolymers are shown in Fig. 4.8. All spectra, particularly the spectra of the cured geopolymers, exhibited broad and overlapping absorption bands, which demonstrates the amorphous character of the compounds. Bands around 3350 cm^{-1} (vibration 1; numbers refer to designations in Fig. 4.8) correspond to overlapping asymmetric and symmetric stretching vibrations and the bending vibration (vibration 2) of the incorporated water and are only present in the geopolymer samples. No water bands occurred in the RHA spectra, consistent with the fact that the material was produced by calcination at 650 °C. Bands around 1440–1400 cm^{-1} (vibration 3) in the OPG are attributed to carbonate [132], *i.e.* the signals are caused by the incorporated thermonatrite, which has been observed by XRD (Fig. 4.7). These carbonate absorption bands were only found in the geopolymer samples, *i.e.* the marginal amount of calcite in the anhydrous RHA was not expressed in its infrared spectrum. Signals at 1059 cm^{-1} (vibration 4) and between 985–975 cm^{-1} (vibration 5) correspond to asymmetric stretching vibrations of Si-O-Si in the RHA and Si-O-T (T = Si or Al) in the geopolymers, respectively. The absorption bands of asymmetric Si-O-T

stretching vibrations in tectosilicates shift to lower wavenumbers with increasing aluminum content, due to the change of the bond lengths [87, 89, 90]. Therefore, this shift reveals the incorporation of aluminum into the gel network. The Si-O-Si symmetric stretching vibration of the RHA(1) at 797 cm^{-1} (vibration 6) did not remain in the geopolymer samples. Instead, Si-O-T (T = Si or Al) absorptions were observed at 684–680 cm^{-1} (vibration 7). There was a shift to lower wavenumbers and the disappearance of the characteristic vibration 6 (ν_s Si-O-Si) was a further indication of a high degree of reaction of the silica feedstock. Absorption bands in the range of 575–573 cm^{-1} (vibration 8) in the geopolymers are attributed to complex vibrations (CB = complex band) of stretching and bending vibrations (ν_s Si-O-Si; δ O-Si-O) of higher order [133]. Bands at 451 cm^{-1} (vibration 9) and at 421–419 cm^{-1} (vibration 10) represent O-Si-O bending vibrations in the RHA feedstock (cf. Section 2.2.2.; Fig. 2.3) and the geopolymers, respectively [87, 134].

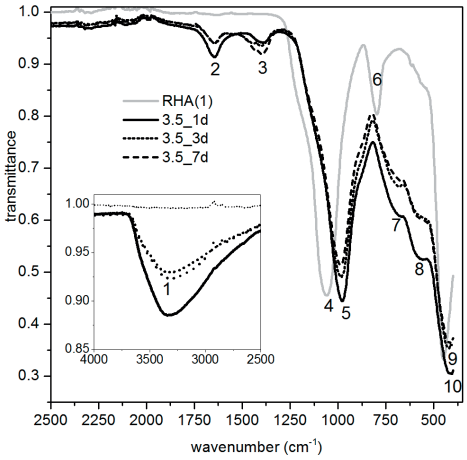

Figure 4.8: ATR FT-IR spectra of RHA(1) and the OPG RHA_3.5 after 1d, 3d and 7d of curing at 80 °C and 80% r.H., respectively. (1 = $\nu_{as,s}$ H_2O; 2 = δ H_2O; 3 = carbonate; 4 = ν_{as} Si-O-Si; 5 = ν_{as} Si-O-T (T = Si or Al); 6 = ν_s Si-O-Si; 7 = ν_s Si-O-T (T = Si or Al); 8 = CB (complex band); 9 = δ O-Si-O in RHA; 10 = δ O-Si-O in geopolymers)

The BET specific surface area of RHA(1) was determined to 49.6 m^2/g, and thus, significantly higher than for MS and CR. Fig. 2.5 (Section 2.2.2.) presents the micrographs of the used silica feedstock MS, CR and RHA(1). CR and especially MS form spherical particles of about 100 nm to 200 nm diameter. Furthermore, the particles tend to form agglomerates. Comparable particle shapes were observed for CR. The very small, spherical particles of less than 500 nm diameter tend to form agglomerates as well. In contrast to this, the particles of the ground RHA(1) have a more angular shape and thus a rougher surface. The higher surface area is regarded

to be a main reason for the higher reactivity of RHA(2) compared to MS and CR. The increased reactivity of RHA(2) was also expressed through the higher solubility, determined by the chemical dissolution method (HCl method). 20 wt.% of the pure RHA(1) feedstock dissolved in HCl (1:20), whereas only 13.6 wt.% of CR dissolved and 2.6 wt.% of MS, respectively.

SEM micrographs of the 3d cured MS-based geopolymer-zeolite composites and geopolymer (RHA_3.5) are shown in Fig. 4.9. The low-silica mixes, in particular MS_2, provided more pronounced expansion during curing, associated with a further increased volume of air voids and large pores (Fig. 4.9). Also, Krivenko and Kovalchuk [135] reported that certain geopolymer mixes comprising MS expanded during curing, without attempting to explain this behavior. Prud'homme et al. [131] observed foam formation at 70 °C in highly alkaline aluminosilicate systems controllable by silica fume. A hydrogen release due to the dissolution and oxidation of silicon impurity was proposed to be the cause of this behavior. With progressing polycondensation reaction the mix became stiffer and finally initially consolidated; simultaneous ongoing hydrogen gas development resulted in foaming and expansion. This process was the main reason for the expansion also for the considered OPG. Gas release was observable as bubble formation at the surface of samples MS_2, MS_3.5, MS_6, CR_2 and CR_3.5 at the very early stage of curing at 80 °C. A possible explanation for the more pronounced expansion tendency at low SiO_2/Al_2O_3 ratios is the higher pH of the pore solution and the lower viscosity of the pastes (cf. Section 3.2.2.). The higher pH may have caused the "foaming" reactions to proceed faster and to a higher extent than in the high-silica mixes, which had lower sodium aluminate fractions and consequently higher H_2O/Na_2O ratios (equal to $(H_2O/Al_2O_3)/0.98$, cf. Section 5.2.; Tab. 5.1). Compared to MS_2, the CR_2 samples expanded much less, which is probably a reason for their considerably higher compressive strength. Si was only observed in some preliminary investigations and not in the batch, used for this work. However, the varying chemical composition of the industrial residue CR [40, 51, 136, 137] may have provided traces of silicon below the detection limit of the used XRD device.

At higher magnifications, the SEM micrographs of the composites revealed a porous microstructure, consisting of particles with an approximate diameter of ca. 100 nm. This parallels previous findings on OPG composites produced from silica CR [26]. The microstructure of the one-part geopolymer-zeolite composites is less compact than that of typical conventional geopolymers (e.g. based on FA and MK [12, 13, 31, 53, 138, 139]). As mentioned in Section 4.2.2., this more porous microstructure, including zeolites, causes a particulate structured network with many interfaces and contributes to the comparatively low strength of the composites besides the

swelling, when compared to conventional geopolymers. In Fig. 4.9 it appears that the microstructure of MS_6 is more compact than the microstructure of MS_2 and MS_3.5, which provides an additional explanation (in addition to the lower expansion) for the higher strength of MS_6.

That microstructure was found typically also for partially reacted MK [140] and FA- based [141] geopolymers. Especially with increasing sodium and aluminum content an increasing crystalline character of the polymers and an increased volume of bigger pores was observed by SEM [117, 126, 140, 141]. For molar SiO_2/Al_2O_3 < 2.8 an increase of network interruptions due to a more crystalline character and an increase of large pores was observed [117]. The spherical shape of the particles further indicates the agglomeration of crystallites. In addition, the shape is typical for transformation of zeolite A crystals into HS under alkaline conditions [126].

No silicon or silicon carbide was found in RHA(1) (cf. Section 2.2.2.; Fig. 2.1) and no significant expansion occurred for the mix. At lower magnification (Fig. 4.9), a microstructure with homogeneously distributed and small sized pores compared to the composites, was observed for RHA_3.5. At higher magnification, the geopolymer exhibits mainly the dense and homogeneous microstructure that is observed for well-cured conventional geopolymers (e.g., based on FA and MK [13, 117, 141]) too. The SEM investigations of RHA_3.5 fit quite well into the other structural investigations and the literature, where an increased silicon content in the reaction products was found to enhance a glassy network structure and rather low amounts of large pores [117, 140, 141]. Especially for $SiO_2/Al_2O_3 \geq 3.2$ homogenous, dense, glassy structures were found, whereas further increasing silica content did not provide significant further changes of the microstructure [117]. All structural investigations (XRD, ATR FT-IR, SEM) and the comparison with the literature indicate a high degree of reaction and correlating high content of silica in the reaction products of RHA_3.5 with a molar SiO_2/Al_2O_3 ratio of at least close to 3.5 after curing at 80 °C.

The dissolution in HCl for the estimation of the degree of the reaction was additionally applied to the mix too. The high determined solubility of the feedstock RHA(1) in HCl (≈ 20 wt.%) compared to the solubility of CR (≈ 14 wt.%) and MS (≈ 3 wt.%) was another evidence for the high reactivity of the feedstock. The determined degree of reaction based on the dissolution method of RHA_3.5 was thus expected to be at least higher, than for the according MS and CR mixes (α[HCL] ≤ 50 %). But the calculated degree of reaction of RHA_3.5 (< 22 %,) was significantly lower, than for the complementary MS- and CR-based mixes.

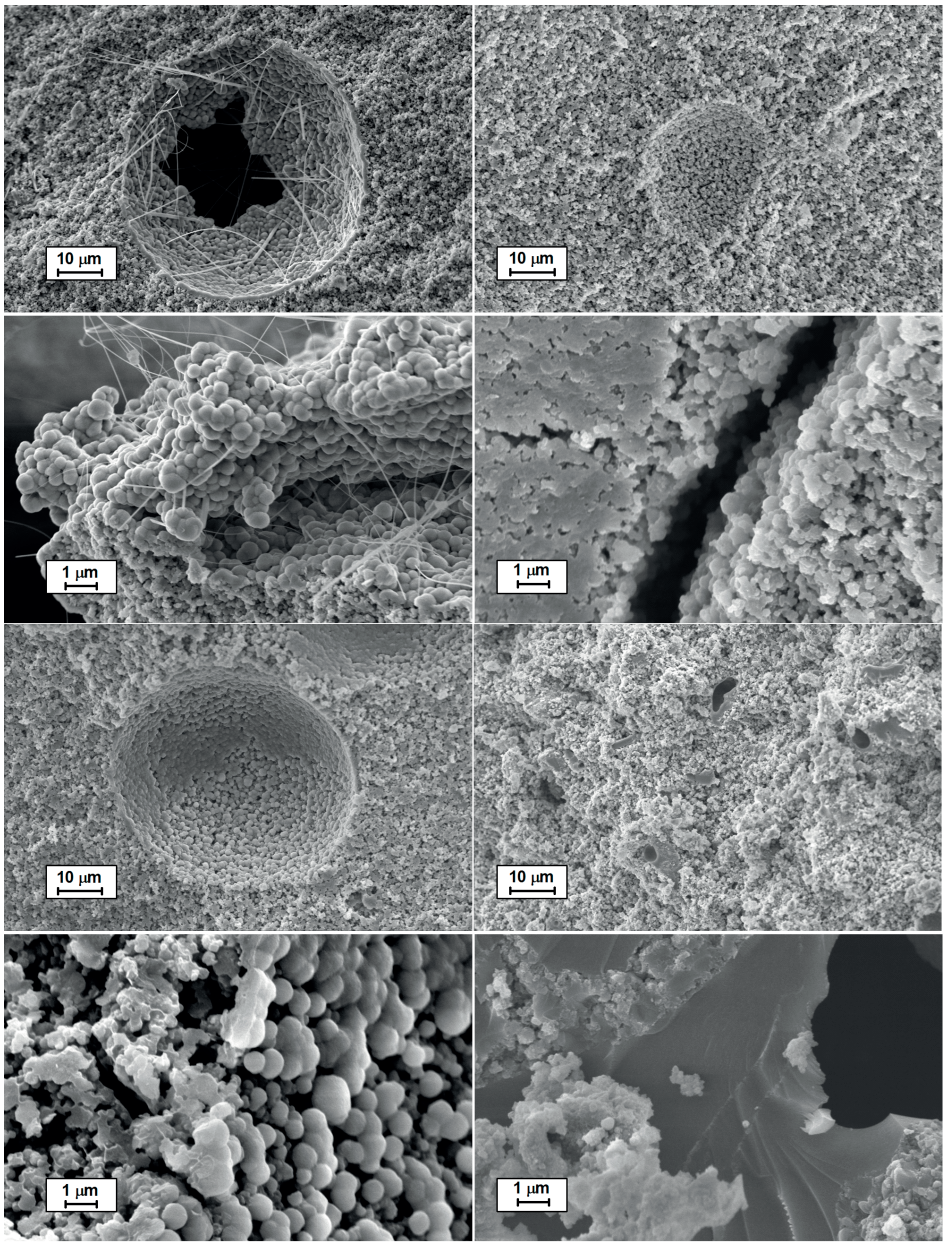

Figure 4.9: SEM SE micrographs of fracture surfaces of the OPG MS_2 (top left column) and MS_6 (top right column), and MS_3.5 (bottom left column) and RHA_3.5 (bottom right column), after curing at 80 °C and 80% r.H. respectively.

Hartman and Fogler [124] investigated the dissolution behavior of zeolites with specific $SiO_2/Al_2O_3 \geq 2$ of the anionic framework in HCl. Zeolite A rapidly led to the dissolution of the aluminosilicate framework ($SiO_2/Al_2O_3 = 2$), leading to the formation of a secondary aluminosilicate gel phase. With increasing silica content, more of the structure remained stable. Own experiments (> 99 %) indicated virtually full dissolution of zeolite A in HCl (1:20) too. Due to the initial exchange of non-framework alkalis (Na^+) with protons (H_3O^+) and subsequently replacement of aluminum by the latter ones as well [124, 125, 142], the framework of the multioxide phase is fully destroyed without necessarily destruction of the Si-O bonds [143]. Whereas a comparable behavior is assumed for HS and the N-A-S(-H) gel with $SiO_2/Al_2O_3 = 2$ (cf. Section 4.2.2.), literature also shows that zeolites with a framework of $SiO_2/Al_2O_3 > 2$ mol/mol do not fully dissolve and the higher the ratio, the more of a silica enriched (amorphous) structure remains, whereas crystalline quartz is virtually fully stable [125]. A comparable behavior is assumed after dissolution of the alumina species from the high-silica aluminosilicate network in RHA_3.5. Significant amounts of the then virtually aluminum free gel remained and contributed to the remaining mass, pretending a lower degree of reaction, as it actually was. Thus, can be concluded, the chemical dissolution method can be an easy and helpful tool for the estimation of the degree of reaction in OPG, when the qualitative phase assemblage is known and aluminosilicate reaction products are mainly characterized by $SiO_2/Al_2O_3 \approx 2$. When this ratio is increased, the dissolution method is inadequate and provides thus biased evaluations.

However, Fernández Jimenéz et al. [71] found good agreement for the dissolution method, ^{29}Si NMR quantification and XRD-based Rietveld quantification of the degree of reaction of FA-based geopolymers, but the NMR and XRD were normalized to the insoluble residues and no independent results were presented for the two evaluation methods. The reaction products contained e.g. significant amounts of chabazite ($SiO_2/Al_2O_3 = 4$), however residues were not investigated by XRD, after firing at 1000 °C. Furthermore, the concluded amounts of residual (unaffected) glassy FA in the insoluble residues and therefrom concluded amounts of amorphous aluminosilicate reaction products and degrees of reaction of the FA did not consider the high-temperature phase formation of the remaining insoluble residue, including remaining feedstock. The observed high amounts of amorphous phase in the mentioned literature (> 65 %) suggest a considerable degree of partial melting, as well as the significantly increased mullite content suggests sintering contribution [71] that possibly also affected remaining FA of the insoluble residue during high-temperature treatment.

The other main difference to the own experiments was the calculation of the degree of reaction only from the insoluble residue after HCl attack of the activated FA [71], but not taking into account the dissolution rate of the pure FA in HCl, and thus the amount of unreacted FA in the cured geopolymer systems that is dissolved from acid besides the actual reaction products. This was done for the silicas (MS, CR and RHA(1)) in the present work and included to the presented results (cf. Sections 2.1.2.1. and 4.2.2.). The mentioned FA contained major impurities (e.g. Fe_2O_3, CaO, K_2O [144]) and provided major differences of the total amount of amorphous phase and amorphous SiO_2 and Al_2O_3 contents [71]. Consequently, the calculated degrees of reactions were higher than they would be by including the dissolution rate of FA [71].

4.3.2.2. Structural analysis of RHA(2)-based OPG

Fig. 4.10 shows the diffractograms of the RHA(2) based OPG of both investigation series (series 1 was prepared with the vacuum mixer and series 2 with the standard mortar mixer, cf. Section 4.3.1.) of the equally composed OPG after curing for one day at 80 °C. The diffractograms of RHA_6 and RHA_8 are quite similar. Parts of the silica feedstock remained unreacted, indicated by the remaining cristobalite and the remaining silica related hump with a maximum at ≈ 21.9 °2θ. A new hump, representing the formation of aluminosilicate gel, occurred at higher diffraction angles for RHA_6 (≈ 27.7 °2θ) and RHA_8 (≈ 28.1 °2θ). No major differences could be observed by XRD for RHA(2)-based OPG at molar silica to alumina ratios $6 \leq SiO_2/Al_2O_3 \leq 8$. No crystalline aluminosilicates, such as zeolites, were identified. This shows the formation of zeolites can be avoided at 80 °C, as well as for RHA(1). Gibbsite (PDF # 00-033-0018) and residues of (thermo)natrite (Na_2CO_3, PDF # 00-037-0451) revealed an excess of the alumina feedstock, because of the significant content of unreactive crystalline SiO_2 (cristobalite). This led to the precipitation of crystalline aluminum hydroxide and carbonation of excess sodium to (hydrated) sodium carbonate. No significant differences between series 1 and series 2 could be observed after all. Thus, the mixing procedures had no major influence on the phase formation of the high silica RHA(2) OPG formulations.

Significant differences occurred in the diffractograms of RHA_3.5_1 and RHA_3.5_2 (Fig. 4.10). A new hump at higher diffraction angles occurred for RHA_3.5_1 (≈ 27.9 °2θ) and RHA_3.5_2 (≈ 28.1) °2θ). Parts of RHA(2) remained unreacted, expressed through the remaining cristobalite related peaks. This is a difference to the RHA_3.5 formulation, synthesized from RHA(1), where virtually the whole silica feedstock reacted. The crystalline silica phase is regarded as the main reason for the

lower reactivity. As presented before, also the very low amounts of cristobalite and quartz in RHA(1) remained in the specimens after curing at 80 °C (Fig 4.7). Compared to RHA_6 and RHA_8 the new hump was more pronounced, *i.e.* a higher degree of reaction of the silica was reached and a higher amount of amorphous aluminosilicate reaction products formed. Gibbsite and traces of (thermo)natrite indicated an incomplete implementation of the alumina feedstock. Like RHA_6 and RHA_8, RHA_3.5_2 showed no signs of zeolite formation, in line with the mix RHA_3.5, that was synthesized from RHA(1) (Fig. 4.7). In contrast to that RHA_3.5_1 was the only mix of all RHA(2) based OPG that indicated the presence of zeolite A and an additional aluminum hydroxide phase (bayerite). The further increased amount of alumina precipitation is due to the not reactive, crystalline part (cristobalite) of RHA(2), unable to react sufficiently with SA and leading to an access in aluminum.

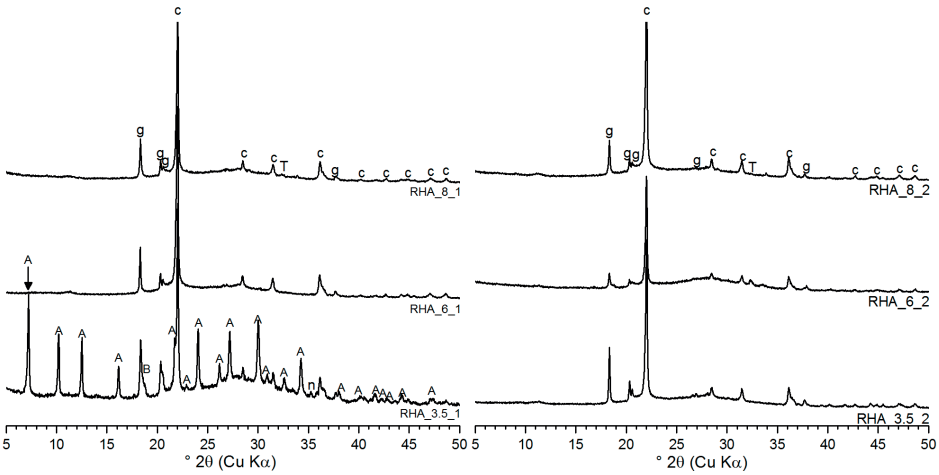

Figure 4.10: X-ray diffractograms of the OPG of RHA(2)-based OPG series 1 (RHA_(3.5,6,8)_1) and 2 (RHA_(3.5;6;8)_2) cured for one day at 80 °C and 80% r.H. (A: zeolite A; c = cristobalite; g = gibbsite; B = bayerite; T = thermonatrite; n = natrite).

Fig. 4.11 shows SEM micrographs of the OPG formulations RHA_3.5_1, RHA_3.5_2; RHA_6_1 and RHA_8_1 after curing at 80 °C. RHA_8 provided dense and homogenous microstructure, in line with the literature for high SiO_2/Al_2O_3 ratios of the aluminosilicate reaction products [117]. Besides few needles, probably (hydrated) sodium carbonate and rather isomorphic gibbsite, that occurred in all samples, no crystalline phases were found. RHA_6 provided a glassy matrix as well. The irregular pore shapes (Fig. 4.11) with smooth interfaces indicate the partial but incomplete dissolution of silica particles, *i.e.* the RHA and the incorporation of the residues into the network of the amorphous reaction products. The irregular

shape of the pores is further possibly related to artificial of partially reacted RHA particles (e.g. cristobalite, that was removed during cracking preparation at the sample surface [117]).

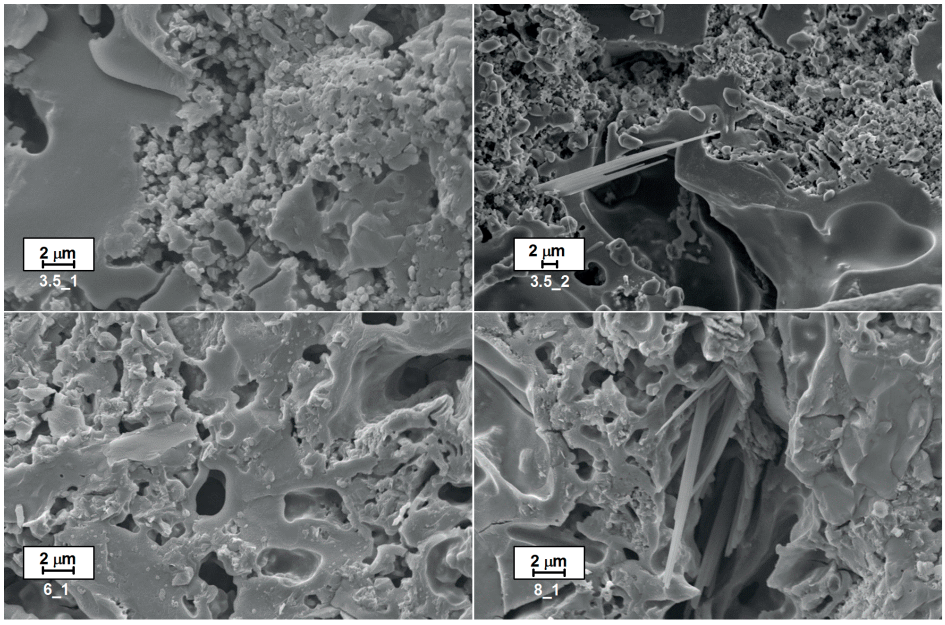

Figure 4.11: SEM SE micrographs of RHA_3.5_1, RHA_3.5_2; RHA_6_1 and RHA_8_1 cured for one day at 80 °C and 80% r.H. and stored for 56 d at 23 °C and 50% r.H., respectively.

Besides amorphous phase RHA_3.5_1 showed spherical agglomerated zeolite A crystals, as presented for the geopolymer-zeolite composites based on MS, growing from the gel phase at the interfaces of the pores, as observed for geopolymers that were produced from colloidal silica and SA or sodium silicate solution [29], but the gel formation seems to be still more pronounced as for MS_3.5 (Fig. 4.9). Less interfaces occurred, but a coherent glassy matrix, *i.e.* the geopolymers and remaining silica RHA(2). RHA_3.5_2 provided a glassy structure but showed fine particles as well, especially at pore interfaces. Compared to RHA_6 and RHA_8, the gel provided a rather fragmentary character. Besides course fragments also very fine particles that resemble the proposed zeolites of RHA_3.5_1 have been observed but less particular and more irregular shaped (Fig. 4.11). Since the only obvious difference of the formulations was the mixing, and no significant difference of the spread flows of the fresh pastes was observed (Fig. 4.14), another reason must be of major importance for the phase formation in RHA_3.5_1 and RHA_3.5_2, respectively. The samples were cured at 80 °C and 80% r.H. in an oven with climate conditioning function. The formation of zeolites at elevated temperatures generally occurs

very quickly and accelerates with increasing temperature [120]. Besides possible inhomogeneities of the small samples, the curing time and the temperature have a major influence on the structural properties. The comparable microstructure of both RHA_3.5 mixes, where the crystallites in RHA_3.5_1 grow from the gel phase, leads to the assumption, that moderate errors of the actual temperature (the oven was used under almost maximum conditions) led to the differences in the observed phase contents. Both mixes were in a limit state and elongation of the curing time probably have led to the formation of zeolite A crystals as well in RHA_3.5_2, as observed for comparable one-part geopolymer mixes at elevated temperatures over the time (e.g. [29] and Section 4.4.2.).

The previous investigations showed, silica-based OPG formulations from industrial residues (CR, MS) tend to form geopolymer-zeolite composites when cured at 80 °C and 80% r.H., respectively, independent from the composition of the pastes. On the other hand, the formation of zeolites was avoided for intermediate composed OPG mixes by using biogenic silica RHA(1). The investigations on technical grade RHA(2) proved the avoidance of zeolites is basically possible with a technical grade RHA too. The different formulations ($3.5 < SiO_2/Al_2O_3 \leq 8$) were successfully synthesized at 80 °C/80% r.H. without the formation of the typical zeolite A and HS impurities. The high silica mixes provided quite similar phase contents, whereas for RHA_3.5 either zeolite-free or zeolite-containing mixes were observed. SEM investigations suggest much less zeolite A in RHA_3.5_1, compared to the MS- and CR-based geopolymer-zeolite composites (cf. Section 4.3.2.; Fig. 4.9). The microstructure of both mixes gives evidence for the importance of the curing time at elevated temperature curing.

Compared to the MS- and CR-based composites a more distinct new maximum of the amorphous hump occurred at higher diffraction angles for $SiO_2/Al_2O_3 = 6$ and even for $SiO_2/Al_2O_3 = 8$. The intensity of the new maximum was more pronounced for the medium silica formulations, *i.e.* $SiO_2/Al_2O_3 = 3.5$, than for the high silica mixes. No NMR spectroscopic analyses were performed on the mixes, but considering the previous results, it can be concluded silica RHA(2) reached a higher degree of reaction at lower silica concentrations and therefore a higher amount of reaction products formed, fitting into the relative behavior of all other silica feedstocks. TG analyses (cf. Section 5.3.) further support the assumption, since an increased mass loss in the dehydration range correlates with a decreased amount of starting silica, *i.e.* with an increased degree of reaction and a related increased formation of water containing reaction products.

In contrast to the formulation RHA_3.5, based on RHA(1), that provided virtually full reaction of the silica, the degree of reaction of RHA(2) was probably lower at the same SiO_2/Al_2O_3 ratio. All specimens showed remaining cristobalite after curing at elevated temperatures. The unground RHA(2) provided by far the lowest BET surface (≈ 14 m^2/g) of all silica feedstocks, especially a much lower BET than RHA(1) (≈ 50 m^2/g) and contained a significant amount of crystalline SiO_2, obviously decreasing its reactivity, but the general avoidance of zeolites in the amorphous microstructure indicates in general a high initial availability of the reactive (glassy) SiO_2 of the feedstock [117]. The amorphous part of the RHA batches provides improved reactivity as the amorphous silica from MS and CR. The crystalline content (cristobalite) is virtually unreactive.

4.3.2.3. Compressive strength

Fig. 4.12 presents the compressive strength development of the OPG pastes RHA_3.5 (synthesized with RHA(1)), MS_3.5 and CR_3.5, prepared at Is it possible to put the page number back to the header (top of the page). = 0.5, after curing for 1, 3, and 7 days at 80 °C and 80% r.H, respectively. The main part of the strength development occurred within the first 24 hours. The compressive strength of the zeolite-free RHA_3.5 (RHA(1)) mix was considerably higher than of the geopolymer-zeolite composites (MS_3.5 and CR_3.5). After three days of curing the compressive strength of MS_3.5 (22.6 MPa) was 69% (two thirds) of RHA_3.5 (32.7 MPa), whereas CR_3.5 reached only 37% (one third; 12.2 MPa). The major reasons for the higher strength of the OPG produced from RHA(1) is assumed to be the higher degree of reaction of the silica, the correlated including of more silicon into the aluminosilicate network and the absence of zeolites, leading to a more condensed network. In addition, the lower content of interconnected pores and air voids with expansion related crack introduction, further improves the network structure of RHA_3.5 over the MS- and CR-based geopolymer-zeolite composites. Curing for longer than three days at 80 °C and 80% r.H. resulted in slight to moderate strength losses for all considered mixes (Fig. 4.12), *i.e.* also for the zeolite-free mix. This is likely related to a further introduction of microcracks due to drying and release of structural important water at elevated temperatures [38].

Generally, zeolite containing OPG provide comparatively low strengths. In the published literature the presented compressive strengths are usually significantly below 30 MPa or strength data is not reported [40, 41, 46, 50-53]. However, Feng et al. [44] produced OPG with a comparatively low content of incorporated crystallites, which reached compressive strengths of >30 MPa after 7 days of curing at 25

°C. Hajimohammadi et al. [54] successfully synthesized zeolite-free OPG at 40 °C from high carbon content RHA and SA. The mortars provided lower strength as the presented RHA_3.5 paste, but a clear trend was found, that with increasing SA content, the formation of zeolites was enhanced and the compressive strength decreased [54]. The observations of the present work fit well into the observations of the literature, that avoiding the formation of crystalline by-products during geopolymerization enhances the strengths of OPG, if overlapping factors (e.g. expansion) are excluded or minimized. Furthermore, the experiments on RHA(2) showed, that the formation of crystalline tectosilicates is enhanced by increasing the SA content as well, i.e. no zeolites occurred for starting compositions of $SiO_2/Al_2O_3 > 3.5$.

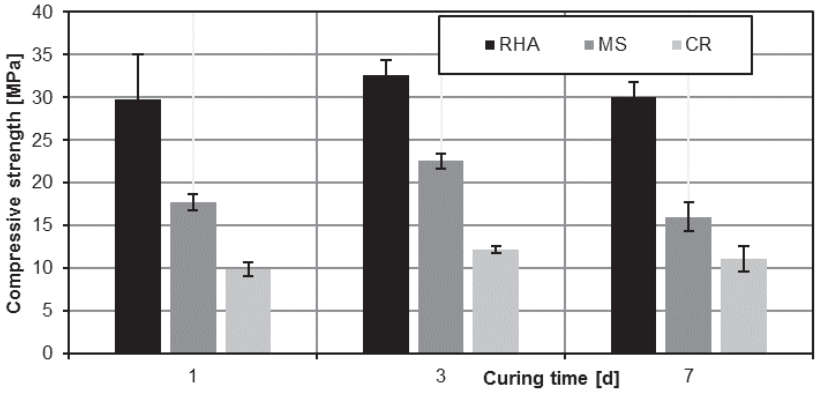

Figure 4.12: Compressive strength of the OPG RHA_3.5, derived from RHA(1); MS_3.5 and CR_3.5 at w/b = 0.5 after curing for 1d, 3d and 7d at 80 °C and 80% r.H., respectively.

The OPG produced from RHA(1) exhibited a virtually complete reaction of the silica feedstock (RHA(1)), as indicated by XRD, ATR FT-IR spectroscopy and SEM, and the pastes transformed into amorphous sodium aluminosilicate (N-A-S(-H)) gel. This N-A-S(-H) gel is considered to be mainly responsible for the strength development of low-calcium AAM [29, 145]. The strength of geopolymers is thus dependent on the amount of N-A-S(-H) gel formed, its composition and its microstructure. As shown in Fig. 4.10 the RHA(1)-based OPG exhibited a dense and homogeneous microstructure. In contrast, the microstructure of the one-part geopolymers based on the other silica materials (*i.e.* MS or CR) appeared to be more particulate, consisting of ca. 100–200 nm-sized particles and possessing a significant amount of interparticle pores [40, 50]. This difference can be attributed to the SiO_2/Al_2O_3 ratio of the geopolymeric gel. It can thus be concluded that the high degree of reaction of the RHA, led to a high SiO_2/Al_2O_3 ratio > 3.2 (*i.e.* close to 3.5) [117] and consequently to a denser microstructure, which caused a higher compressive strength the hardened material.

Summarizing, the high compressive strengths of the RHA(1)-based OPG is mainly attributed to the absence of significant amounts of crystalline by-products, and the almost complete reaction of the RHA, which resulted in a higher SiO_2/Al_2O_3 ratio and a denser microstructure of the aluminosilicate N-A-S(-H) gel than in OPG produced from other silica sources and the absence of swelling of the hardening paste.

Fig. 4.13 presents the compressive strength results of the OPG pastes, synthesized from RHA(2) at w/b = 0.4 (0.5 for the previous samples) after curing at 80 °C/ 80 % r.H. (1d) and the further development at 23 °C/ 50% r.H., as well as the strength development of the CEM III/B until an age of 56d. CEM III/B was chosen due to its high GGBS content, that was also considered for the high-temperature behavior. RHA_8_1 and RHA_8_2 provided comparable strength development. After one day of curing at 80 °C and 80% r.H., the mixes provided 20 MPa and 24 MPa, respectively. After 7 days (23 °C/ 50% r.H.) the strength of both mixes increased to 34 MPa. After 28 days (44 MPa), the strength remained virtually constant (46 MPa after 56 days) The compressive strength of RHA_8_2 was always slightly below the values of series 1.

The relative strength development of RHA_6_1 and RHA_6_2 was quite similar as well but with significantly increased differences of the absolute values (Fig. 4.13). After one day of curing at 80 °C RHA_6_1 had a compressive strength of 22 MPa. After further curing at 23 °C the strength increased to 54 MPa after 28 days. In contrast to the RHA_8 formulations, after 56 days a moderate strength decrease was observed (47 MPa). RHA_6_2 had a significantly higher initial strength of 40 MPa after one day of curing at 80 °C. After 28 days at 23 °C the strength reached 62 MPa. This was the highest strength of all considered OPG pastes independent from the composition and the curing time. Like for RHA_6_1 a considerable reduction of the compressive strength down to 56 MPa was observed after 56 days. The absolute difference decreased from 18 MPa after one day of curing (80 °C/ 80% r.H.) to 9 MPa after 56 days within the standard deviations.

After one day of curing at 80 °C RHA_3.5_1 (w/b = 0.4) reached a compressive strength of 14 MPa. This was the lowest initial compressive strength of all RHA(2) based OPG. The mix provided a linear strength improvement until an age of 14 days up to 27 MPa, when further cured at 23 °C. The main part of the strength development ceased afterwards. After 56 days 33 MPa was the final observed strength. The formulation provided no decreasing strength after a certain time of ambient temperature curing. In contrast to the former one, RHA_3.5_2 provided the highest initial compressive strength (56 MPa) after one day curing at 80 °C. This

means the formulations with the assumable highest content of reaction products, either produced the lowest or the highest initial strength. However, in contrast to the composite and all other considered OPG, the mix provided no further strength improvement when additionally stored at 23 °C and 50% r.H., but a slightly continuous and virtually linear decrease of the strength until an age of 56 days (49 MPa) within the standard deviations (Fig. 4.13).

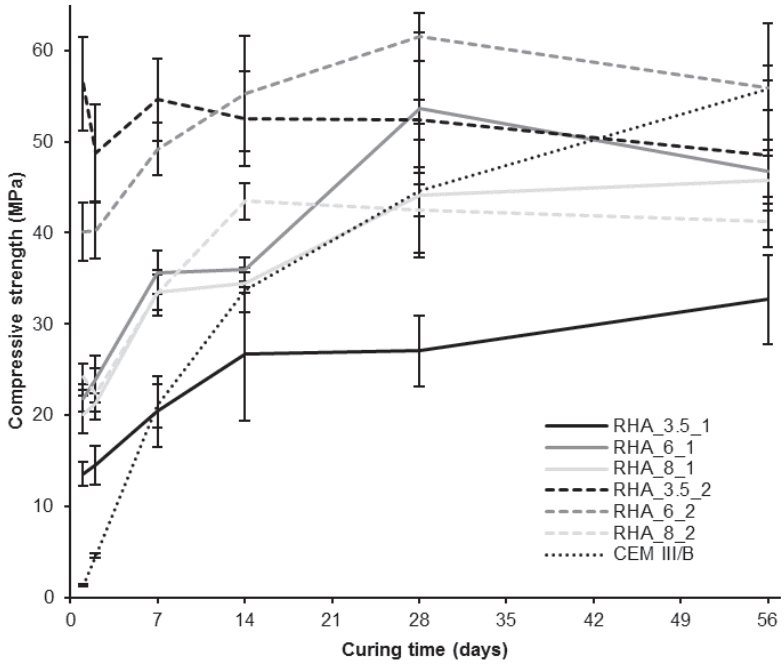

Figure 4.13: Compressive strength development of the RHA(2)-based OPG pastes (w/b = 0.4) after curing for one day at 80 °C and 80% r.H. and further curing at 23 °C and 50% r.H. for RHA_3.5-8_1 (full lines), RHA_3.5-8_2 (dashed lines) and the CEM III/B reference (dotted line).

CEM III/B achieved 1.3 MPa after one day without curing at elevated temperature. After 7 days a significant increase was detected (21 MPa), matching the compressive strength of the low strength OPG composite RHA_3.5_1 (20 MPa). After 14 days the strength increased to 34 MPa and matched the strength level of RHA_6_1 and RHA_8. After a further increase up to 28 days (45 MPa) and 56 days (56 MPa) CEM III/B provided similar strength as the OPG formulation with the highest final strength (RHA_6_2, Fig. 4.13). For the evaluation of the strength results one must take into account the high standard deviations at some points, due to rather poor workability, inhomogeneities and the small sample sizes. This, and the generally increased strength (Fig. 4.14) of the RHA(2) based mixes is caused by the lower applied w/b (0.4) by mass than for the previously discussed MS, CR and RHA(2)

based mixes (w/b = 0.5, Fig. 4.12). In this context it should be noted, that for example pure MS_6 pastes were not workable at a nominal w/b of 0.4. Series 1 and 2 provided an optimum of the 56 days compressive strength, after initial curing at 80 °C, at SiO_2/Al_2O_3 = 6, but the values of RHA_6 and RHA_8 were quite similar for series 1.

The composite RHA_3.5_1 provided the lowest initial strength (14 MPa), but the zeolite-free RHA_3.5_2 mix provided by far the maximum initial strength of all considered OPG samples after curing at 80 °C for one day (56 MPa). This clearly supports the previous observations of this work and the literature, that avoiding of zeolites in OPG leads to better mechanical strength [40, 41, 44, 49-51, 54]. However, the high initial strength RHA_3.5_2 mix showed slight decrease at ambient conditions (23 °C/ 50 %) r.H. over the time of 56 days, whereas the composite provided no decrease but an increase of the strength. All other OPG formulations provided further strength increase at ambient temperature, as well. In this context the main part of the additional hardening occurred until an age of 14 days. With further curing time at 23 °C the slope of the hardening curves flattened, *i.e.* the samples reached a plateau, and only slight further improvement or even slight deterioration occurred after 28 days.

The decrease in strength was also observed for the intermediary silica content OPG, for curing times > 3 days at 80 °C and is mainly attributed to the introduction of cracks due to the release of water [38]. Therefore, less dynamic, but in the consequence comparable processes likely also occur at ambient temperature. In the literature a high importance of a critical minimum water content for the structural stability of N-A-S(-H) and C-A-S-H gels in AAM was found [38, 146, 147]. As will be shown in Chapter 5, the thermal dehydration of the CR- and MS-based zeolite containing composites, including zeolitic water, provided very pleasant shrinkage behavior in the thermal dehydration range and all OPG mortars provided excellent ambient shrinkage behavior after initial elevated temperature curing (cf. Section 8.1.). However, a detailed study on the ambient shrinkage of the pure pastes needs to be conducted in the future for a sufficient evaluation.

RHA_3.5 formulations, derived from RHA(2) provided expansion during hardening at 80 °C, unlike RHA_3.5 derived from RHA(1). The possible main peak from silicon, that leads to the formation of hydrogen during curing, is covered from a cristobalite related peak in RHA(2) and reducing conditions during the technical preparation process of RHA(2) cannot be excluded, as stated above (cf. Section 2.2.2.). The fundamental difference of both series was the preparation procedure for the fresh pastes. Series 1 was mixed for shorter times and in a planetary centrifugal

mixer and series 2 was mixed in a standard mortar mixer for longer times (cf. Section 4.3.1.). Fig. 4.14 shows additional results of slump flow and spread flow measurements on the pastes, using the mini-cone test [68] with a cylinder mold (d = 38.48 mm; h = 61.28 mm). No major differences for RHA_3.5 from series 1 and 2 could be identified. Thus, differences of the curing in the oven are considered to be the main reason for the differences of the phase assemblage and related compressive strength development of the two RHA_3.5 formulations. The observed decreasing slump and spread flows with increasing silica content are in line with the previously reported fresh paste behavior of the MS based OPG (cf. Section 3.3.) and MS and CR based mortars (cf. Section 6.2).

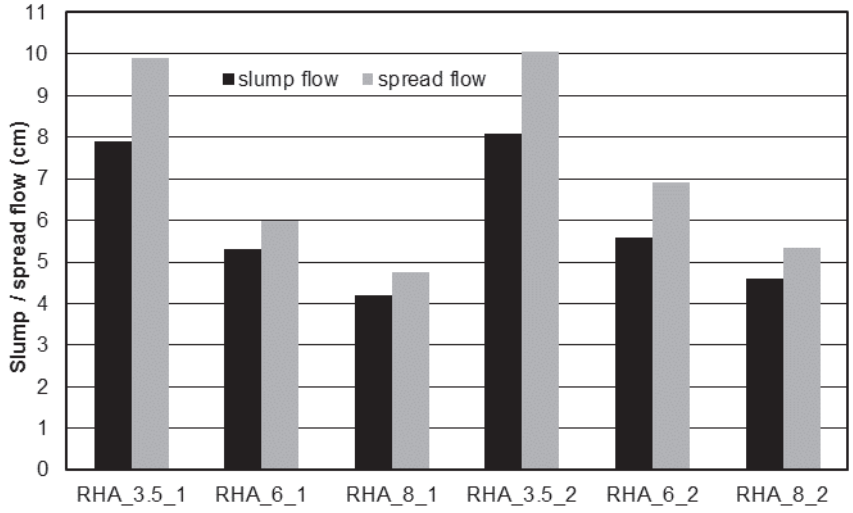

Figure 4.14: Slump flows (black columns) and spread flows (grey columns) of the RHA(2)-based OPG (w/b = 0.4) pastes. The dimensions of the cylinder were h = 61.3 mm and d = 38.5 mm.

4.4. Curing conditions

4.4.1. Experimental program

CR and MS were mixed with SA(2) to yield specific silica/alumina ratios (SiO_2/Al_2O_3 mol/mol) of 2 (low silica) and 6 (high silica). Water was added for a nominal w/b = 0.5. Tab. 4.4 presents the sample compositions. Intermediate compositions (SiO_2/Al_2O_3 = 3.5) are not considered in this Chapter, since the properties of such mixes are in between those of the high-silica mixes and the low-silica mixes (cf. Sections 4.2.2; 5.3. and [50, 51]). Fresh pastes were mixed in a contact free planetary centrifugal mixer for 2 minutes at a rotation speed of 2000 min^{-1}. After the mixing procedure samples were instantly casted into 20 mm × 20 mm × 20 mm cube

molds. Subsequently the samples were cured at specific temperatures (60 °C, 70 °C, 80 °C, 90 °C) and 80% r. H. for specific times (1d, 2d, 3d, 4d, 7d for T ≤ 70 °C and 1d, 3d, 7d for T > 70 °C).

Table 4.4: Compositions of the OPG pastes for the experiments on the curing conditions.

Sample	SiO_2/Al_2O_3	Na_2O/Al_2O_3	H_2O/Al_2O_3	H_2O/Na_2O
	(mol/mol)	(mol/mol)	(mol/mol)	(mol/mol)
CR_2	2.02	0.92	8.54	9.26
CR_6	6.01	0.82	16.04	19.58
MS_2	2.02	0.98	8.37	8.57
MS_6	6.02	0.98	15.51	15.82

Specimens were removed from the containers after one day and tested for their compressive strength or further cured under the according conditions. Fracture pieces of the strength testing were used for XRD measurements. After preparation of the powders, samples were stored in a desiccator above dry silica gel until further use. No alteration occurs under these conditions, as proven by XRD and NMR [48, 148]. Preparation of the powders was done manually with mortar and pestle (agate) to provide a gentle treatment for hydrated phases.

4.4.2. Results and discussion

After curing at the lowest temperature (60 °C) MS_6 showed a broadening of the hump and hydrated zeolite A as reaction products (Fig. 4.15). After one day of curing only low intensities of the zeolite were observed. After two days the intensities increased and remained virtually constant for further increasing curing time. At a curing temperature of 70 °C all diffractograms (*i.e.* independent from the curing time) were equal and again only zeolite A occurred. The same time resolved behavior was observed for the samples cured at 80 °C, but additionally low amounts HS were introduced and traces of gibbsite were identified. This is in good agreement with the previously presented composites, synthesized at 80 °C and generally suggests a good reproducibility for the formulation in terms of phase formation at equal curing conditions. Increasing the temperature to 90 °C led to the formation of the same crystalline phases, but more HS. In contrast to the medium temperatures (70 °C, 80 °C) an alteration of the phase content was observed, since the HS related peaks increased versus zeolite A (Fig. 4.15). This is a further evidence for the proposed partial transformation of the zeolite A phase into HS in the OPG at elevated curing temperatures. Increasing sodium content in the pore solution enhances the

transformation of zeolite A into HS by hydroxide attack leading to an increased and more heterogeneous nucleation (cf. HS peak shapes; Fig. 4.15 and Fig. 4.16) due to increasing supersaturation, which is further enhanced by increasing reaction temperature [111, 116, 119, 120, 128, 149]. After curing at various temperatures (60 °C, 70 °, 80 °C, 90 °C) huge parts of the MS feedstock remained unreacted. This shows the rather low degree of reaction, as discussed above (cf. Section 4.2.2.).

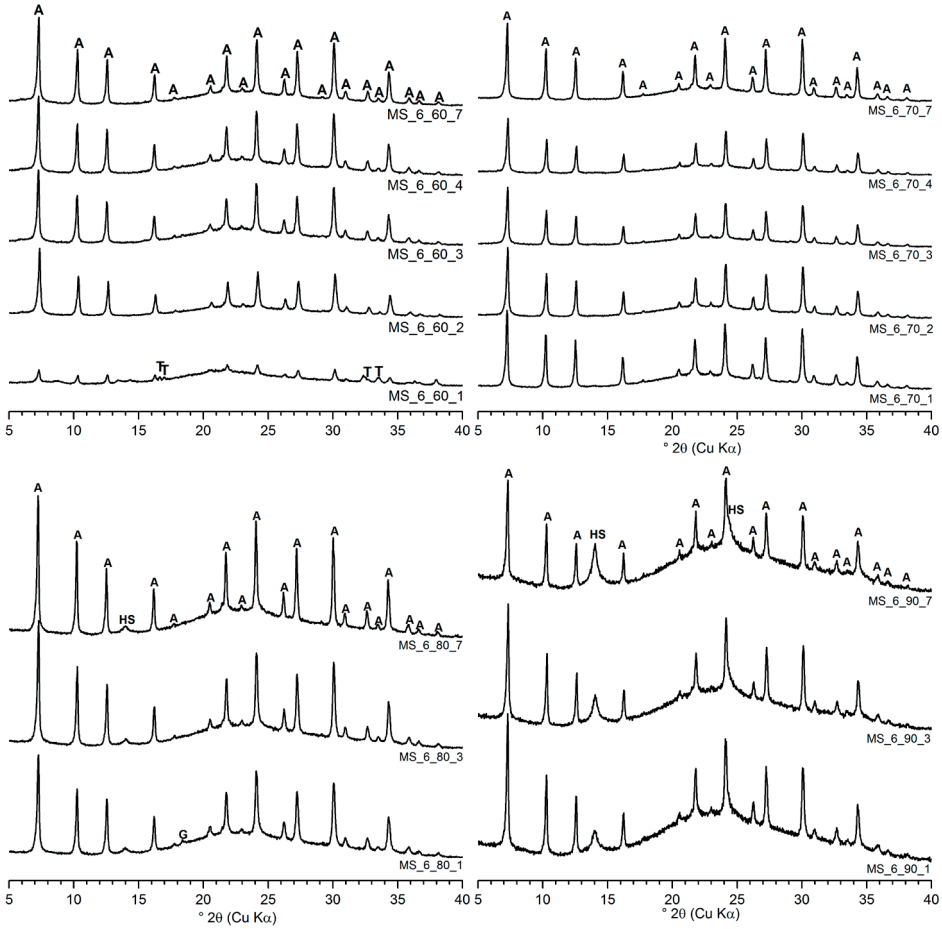

Figure 4.15: XRD diffractograms for the mix MS_6 after different curing temperatures (60 °C; 70 °C; 80 °C, 90 °C and 80% r.H.); A = zeolite A, HS = hydrosodalite, G = gibbsite.

After curing at 60 °C for 1d no crystallites occurred for MS_2 (Fig. 4.16). This was the only MS-based sample, providing no zeolites at any curing temperature and time and proves the generally possible avoidance of zeolites in the regarded MS-based OPG at elevated temperatures. Clearly a second maximum of the hump at ≈ 30.3 °2θ was identified with relative higher intensity than the remaining maximum

of MS, indicating the reaction of the silica feedstock. It was shown that at a higher temperature (80 °C) almost 100% of the silica reacted in the MS_2 mix (cf. ch 4.2.2.) within only one day. However, after two days of curing at 60 °C zeolite A occurred as well as traces of HS. Thermonatrite was observed because of carbonation of the moist powders after only two days of curing at 60 °C. After three days of curing the intensity of the zeolite A related peaks increased significantly. Furthermore, zeolite EMT and faujasite-type zeolites occurred. No major changes were found for longer curing times.

After one day of curing at 70 °C already the complete qualitive phase assemblage formed. Zeolite A was the dominant phase and additionally HS formed. After two days the intensity of the HS and zeolite A related peaks increased and more HS related intensity occurred compared to 60 °C. For longer curing times no further significant changes were observed. Additionally, all samples showed traces of thermonatrite. The exaggerated intensity of the third zeolite A peak (≈ 12.48 ° 2θ), especially for T ≥ 70 °C was observed previously for equal composed samples cured at 80 °C and was mainly attributed to small changes in the stoichiometry of zeolite A, though the cell parameters of the zeolites did not change significantly [119]. At a certain time, with increasing content of dissolved silica in the system, zeolites with increased silicon content [120], such as faujasite-type or zeolite P formed instead of zeolite A.

The results obtained for the 80 °C cured samples were in good agreement to the equal composed mixes from Section 4.2.2. and in excellent agreement with the as-cured samples for the investigation of the thermal properties (Section 5.3), indicating a good reproducibility of MS_2 as well. The slight differences in phases compared to the samples from Section 4.2.2. are probably related to the differences in the chemical composition (cf. Section 4.2.2., Tab. 4.1 and Tab. 4.4). In contrast to the lower temperatures (60 °C and 70 °C) not zeolite A, but HS was the new crystalline main phase and it may have heterogenous character and include higher hydrated forms e.g. $Na_6(AlSiO_4)_6{\cdot}8H_2O$ (PDF # 00-040-0102), and/or basic HS ($Na_8(AlSiO_4)_6OH_2{\cdot}xH_2O$) (PDF # 00-040-0101; PDF # 00-041-0009), noticeable as asymmetric peak shapes of the very broad main peaks (Fig. 4.16). Because of the fairly broad shape and low maximum intensities, it can be further assumed that rather small crystallite sizes [111, 120, 150] formed in the reaction system. Besides HS and zeolite A, traces of zeolite P and additionally low amounts of chabazite $NaAlSi_2O_6{\cdot}3H_2O$ (PDF # 00-019-1178), another zeolite with increased silica content compared to HS and zeolite A, formed. After one day of curing no further changes were found. This fits into the results of Section 4.2.2., were a ceasing of the reaction was found for curing times of > 1d at 80 °C. Curing at 90 °C led to the

formation of HS, zeolite A and chabazite as well, but the low amounts of the latter ones virtually fully disappeared after 3 days and only residues of zeolite A remained after 7 days (Fig. 4.16). Additionally, hydroxycancrinite, $Na_8Al_6Si_6O_{24}(OH)_2{\cdot}_2H_2O$ (PDF # 00-046-1457) and gibbsite, were found. The hydroxycancrinite provides a comparable structure as HS but includes an increased amount of sodium as well as hydroxide.

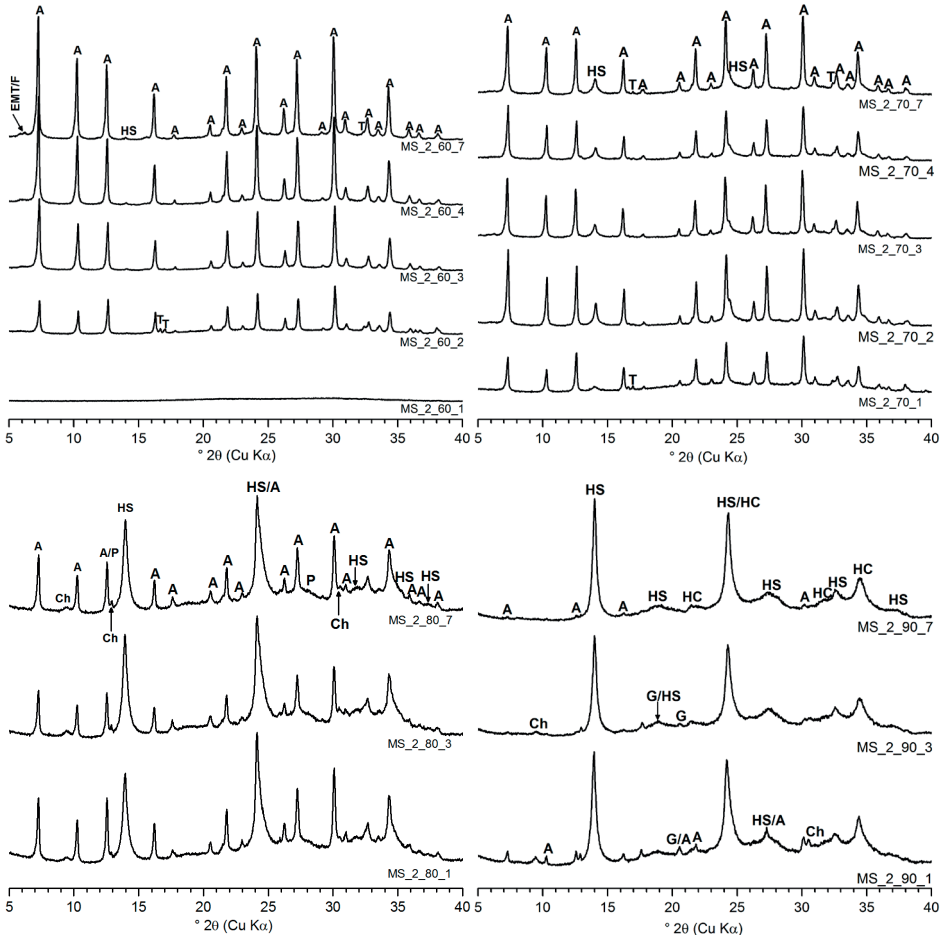

Figure 4.16: XRD diffractograms for the mix MS_2 after different curing temperatures (60 °C; 70 °C; 80 °C, 90 °C and 80% r.H.); A = zeolite A, HS = hydrosodalite, HC = hydroxycancrinite, Ch = chabazite, P = zeolite P; EMT = zeolite EMT, F = faujasite type zeolite, T = thermonatrite, G = gibbsite).

Curing for one day at 60 °C revealed a zeolite free OPG synthesis from silica MS at elevated temperatures, by limiting the curing time. Possible alterations of the phases at ambient conditions need to be subject of further investigations. However, after curing at 80 °C (1d), no later alterations were observed [48]. With increasing curing

temperature, the overall composition of the crystalline reaction products shifted from zeolite A dominated to a HS dominated. The biggest change occurred by increasing the curing temperature from 70 °C to 80 °C. In general, the composites were zeolite A dominated for T < 80 °C and HS dominated for T ≥ 80 °C. The increased amount of HS in MS_2 at T ≥ 80 °C compared to MS_6 and the consumption of zeolite A at the highest investigated temperature (90 °C) over the time fits into the previously described observations (XRD, SEM) and the literature, where increasing sodium content, here increasing SA content, enhances the formation of HS and transformation of zeolite A into heterogenous crystallites due to an increased supersaturation, accelerated by increasing reaction temperature [111, 116, 119, 120, 128, 149]. At 100 °C HS is the major crystalline phase in the system Na_2O-Al_2O_3-SiO_2-H_2O over a wide range of compositions and below specific water contents zeolites like zeolite A are unable to crystallize [120]. For the formation of zeolites with SiO_2/Al_2O_3 > 2 mol/mol the silica activity is of major importance and it is decreased by increasing hydroxide concentrations. Therefore, high silica zeolites correlate with low hydroxide concentration with respect to the silica content [120].

Low amounts of chabazite were observed at 80 °C and initially at 90 °C. The consumption of the chabazite phase at early ages suggests an increased silica content of the gel in the initial state of the reaction. However, only relatively low amounts of crystalline tectosilicates with increased silicon content occurred for silica MS, independent from the composition and the curing conditions, what also correlates with the high amount of hydroxide ions (pH > 14, Section 4.2.) in the fresh paste.

Fig. 4.17 presents the diffractograms of CR_6 after hardening at various temperatures. Independent from the curing temperature zeolite A was always the dominant and only detected crystalline aluminosilicate phase. A broadening of the hump indicated the formation of the geopolymer gel. For T ≥ 70 °C no changes occurred for curing times > 1d. No sodalite-type phase was detected. Quartz and calcite from silica CR remained after curing.

This shows, that those impurities of the feedstock do not participate the reaction at low degrees of reaction of silica CR. CR contained 1.4 wt.% Cl^- on average and the diffractograms of CR_6 identified low amounts of NaCl (halite, PDF # 00-005-0628) precipitated in CR_6. This results from the reaction of the chloride with the sodium of the highly alkaline activator solution.

After curing at 60 °C for one day (Fig. 4.18), CR_2 provided comparable state as MS_2. Accept traces of zeolite A, only an amorphous hump with two maximums and the new one at ≈ 28.9 °2θ was observed and the relative intensity of the second maximum was increased compared to the remaining silica. As for silica MS, a zeolite

free OPG synthesis with silica CR seems to be achievable, by further decrease of the curing time. On the other hand, possible alterations could occur and need to be considered in further experiments as well.

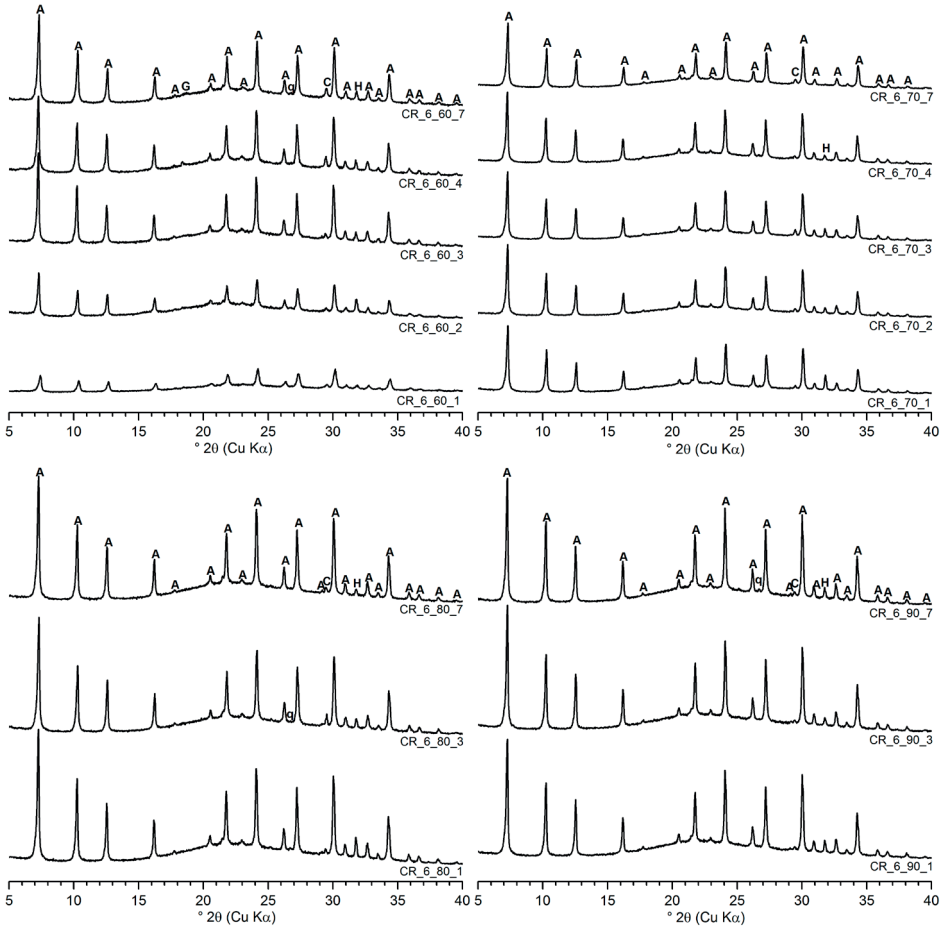

Figure 4.17: XRD diffractograms for the mix CR_6 after different curing temperatures (60 °C; 70 °C; 80 °C, 90 °C and 80% r.H.); A = zeolite A, H = halite, C = calcite, q = quartz, G = gibbsite.

However, after two days of curing zeolite A occurred and additionally, zeolite EMT and faujasite-type zeolite. The best fit for the faujasite-type zeolite was achieved with a specific zeolite Y ($Na_2Al_2Si_{4.5}O_{13}{\cdot}xH_2O$) reference (PDF # 00-043-0168) (Fig. 4.18). No changes occurred for CR_2 when cured > 2d at 60 °C. After curing at 70 °C zeolite A was already formed after one day and no major changes occurred for the phase assemblage for longer curing times, as also found for MS_2. Low amounts of EMT and zeolite Y formed again and the intensity of zeolite Y increased vs. EMT over the time (Fig. 4.18). In contrast to curing at 60 °C, traces of sodalite-type were

observed at later curing times, but no halite. Additionally, traces of zeolite P were found, that readily forms from aluminosilicate gels with high silica contents [120], as observed for MS_2 at after curing at 80 °C.

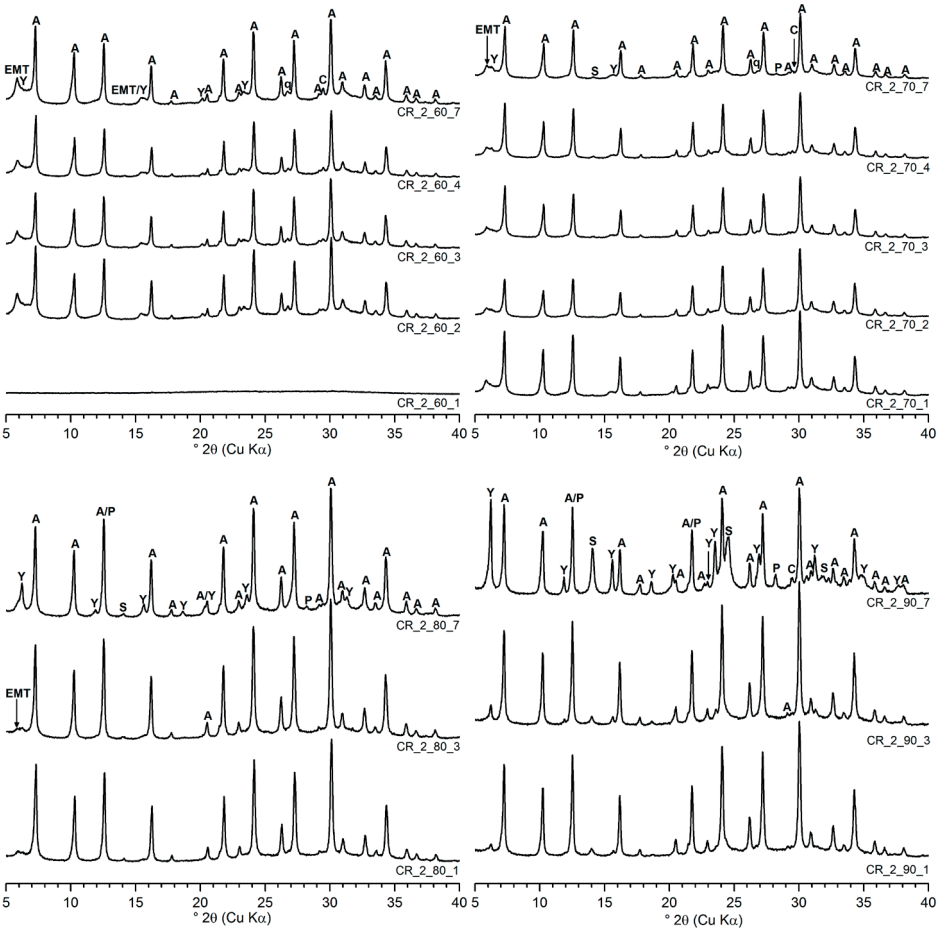

Figure 4.18: XRD diffractograms for the mix CR_2 after different curing temperatures (60 °C; 70 °C; 80 °C, 90 °C and 80% r.H.); A = zeolite A, EMT = zeolite EMT; Y = faujasite-type zeolite (zeolite Y), S = sodalite, P = zeolite P, C = calcite, q = quartz.

Curing at 80 °C led to the formation of the same qualitative phase assemblage as after curing at 70 °C for one day (Fig. 4.18). Especially between three days and seven days of curing, the intensities of the faujasite-type zeolite provided a major increase. Additionally, traces of zeolite P were observed. CR_2 provided the poorest reproducibility, with respect to the phase formation. Since CR is an industrial by-product, that is usually deposited, inhomogeneities of the properties, especially regarding the chemical composition are very common. No halite, but sodalite *sensu*

stricto, $Na_4Al_3Si_3O_{12}Cl$ (PDF # 00-037-0476) was found for CR_2 at T ≥ 80 °C. Thus, the chloride impurity has at least a partial influence on the OPG reaction at considerably high degrees of reaction and high curing temperatures.

The formation of zeolite Y was further enhanced at 90 °C, as well as the sodalite formation. Again, zeolite P was identified and the phase was more pronounced than for the lower temperatures (Fig. 4.18). As stated above, zeolite P forms from aluminosilicate gel with higher silica content, than for zeolite A, but below 150 °C and especially under non-hydrothermal conditions, the pure phase can be hardly synthesized and is usually dominated by zeolite A and faujasite [120]. The increase of zeolite P with increasing curing temperature, especially at 90 °C fits quite well into those observations of the literature. A moderate excess in sodium and silicon basically leads to an exaggeration of the third zeolite A peak [119] whereas in systems with higher amounts of available silica zeolite P is formed [120].

The deviations of the 80 °C samples (CR_2) in the phase formation compared to other samples with the same composition and related high degrees of reaction of the silica, indicate lower reproducibility with the CR feedstock. The chemical composition of different batches of the feedstock CR provides moderate differences [40, 51, 136, 137]. High degrees of reaction of the feedstock, *i.e.* when virtually the whole amount of silica and impurities is dissolved, lead to the decreased reproducibility. Whereas the calcite and quartz impurities remain stable, e.g. the chloride either precipitates as sodium chloride (low degree of reaction) or participates the main reaction to form chloride containing tectosilicates, *i.e.* sodalite. In addition, the OPG synthesis with silica CR, including high amount of various impurities (cf. Section 2.2.2.; Tab. 2.1), led to the formation of various zeolites at different temperatures. Thus, the feedstock, as well as the MS feedstock with more limitations, can be also a promising starting material for technical zeolite synthesis under non-hydrothermal conditions. First results on a controlled zeolite synthesis with CR, with less variation of the kind of tectosilicates have been published [136]. Depending on template (like metal ions or organic ions) various zeolites can be synthesized from almost equal chemical compositions [118].

Fig. 4.19 presents the results for the compressive strength testing of MS_6 after different curing (60-90 °C). The samples cured at 60 °C and 70 °C provided very similar strength development. For both curing temperatures, the compressive strength reached 31 MPa. Increasing the temperature to 80 °C and 90 °C led to a higher initial strength (22 MPa). After one day of curing at both temperatures virtually no further increase of the strength (23 MPa) occurred. Besides the higher

initial strength, the final strength decreased by > 25% when the curing temperature was increased above 70 °C.

Regarding the lowest initial strength of MS_6 at 60 °C, this fits into the XRD results, being the only temperature with observable changes, regarding the major reaction products, between one and two days of curing, *i.e.* when also a significant increase of the strength occurred (cf. Fig. 4.15 and Fig. 4.19). This was a result of the decreased hardening speed at this temperature. The increasing initial strength, up to 80 °C is a sign of the increased speed of the hardening reaction. A simultaneous increased formation of HS up to 90 °C correlates with an increased nucleation tendency [150, 151]. This leads to an increased amount of structural interphases and agglomeration of small crystallites, expressed as very broad shaped peaks [150] when transferred to geopolymer systems [117, 126, 140, 141] and enhances the particulate microstructure of the geopolymer-zeolite composites (Fig. 4.9).

Fig. 4.19 presents the results of the compressive strength development at different curing temperatures for MS_2. In general, the achieved compressive strengths were much lower than for the MS_6 at all investigated curing temperatures. The initial strength was always < 5 MPa (2.2 MPa – 4.0 MPa) and the maximum strength was always < 7 MPa (Fig. 4.19). The main reason for the considerably high standard deviations is the excessive expansion of the pastes during hardening. As discussed before, this expansion is mainly related to the silicon impurity of silica MS. The high degree of reaction of this formulation, at least at 80 °C a virtually full reaction was observed (Section 4.2.2.), provides a high amount of released hydrogen from the impurity and a fast reaction. This results in foaming and cracking of the samples, causing the low strength and the high standard deviation of the deformed specimens. The foaming also leads to a material and related density decrease of the actual cubes, since the material is removed from the initial volume. However, no significant change of the expansion was observed, when decreasing the curing temperature from 80 °C to 60 °C, but a further significant increase of the expansion occurred when the temperature was raised to 90 °C. Low strength was found for conventional MK- and FA-based GP with high aluminum content, *i.e.* low SiO_2/Al_2O_3-ratios, and a related high amount of pores and rather loose connection of the reaction products [117, 140, 141], MS-based formulations provided comparable microstructure (Section 4.2.2.), as observed by SEM, and especially high alumina MS_2 mixes [29], but the overlapping expansion is considered to be even more important in the present case.

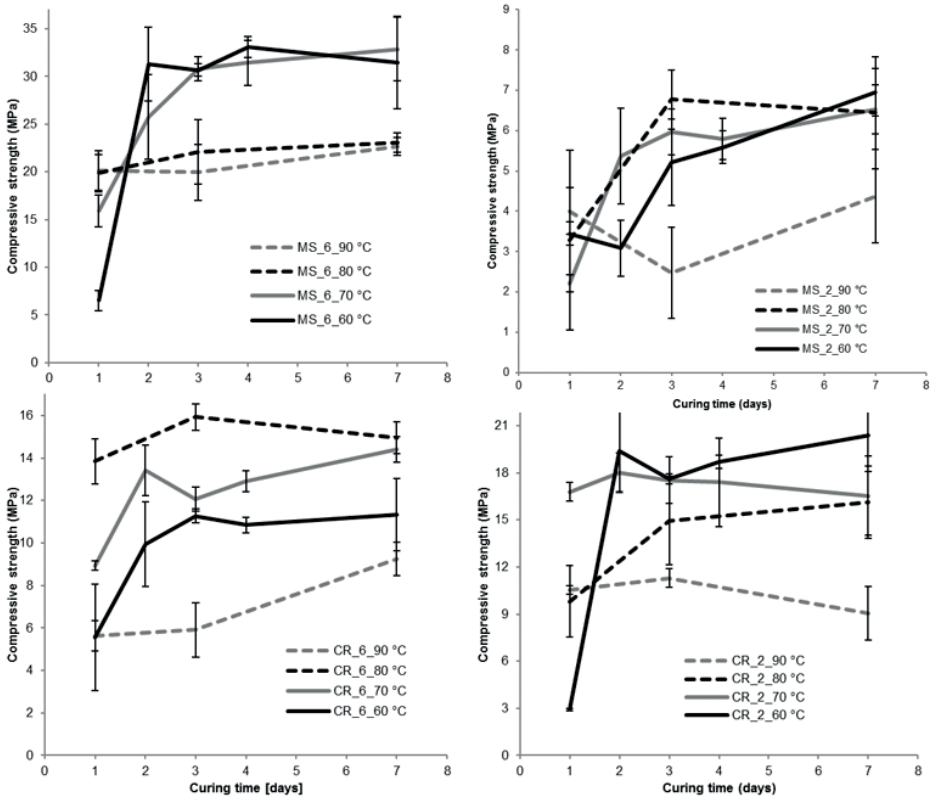

Figure 4.19: Compressive strength development of MS_6; MS_2; CR_6 and CR_2 after curing at different temperatures (60 °C; 70 °C; 80 °C; 90 °C and 80% r.H.). The error bars represent one standard deviation in each direction.

A trend of increasing initial strength and maximum strength with increasing temperature from 60 °C (≈ 11 MPa) to 80 °C was observed for CR_6, whereas the samples cured at 90 °C reached the lowest strength (≈ 9 MPa). This strength decrease at 90 °C is in line with all other series. The maximum strength of CR_6 was only ≈ 50% of the maximum strength of MS_6 (60 °C, 70 °C). The main reason for the considerably low strength in case of CR_6 is not the distinctive expansion, as observed for MS_2, but the very poor workability of the pastes. The main reasons for the much poorer workability of the OPG derived from CR, at any paste composition is the higher BET surface resulting in agglomeration and increasing water demand of the particles in the fresh pastes. As for the high strength MS_6 mix, samples cured at 60 °C (≈ 20 MPa) and 70 °C (≈ 19 MPa) reached higher strength than samples that were cured at 80 °C (≈ 16 MPa) and 90 °C (≈ 11 MPa), respectively. Curing at 90 °C led to the lowest compressive strength.

In summary, the curing at 60-90 °C provided only minor differences in the qualitative phase assemblage of CR_6 and MS_6. Zeolite A was always the dominant crystalline phase. Above 60 °C additionally HS formed for MS_6. The main part of the phase formation ceased already after one day of curing, indicating no major changes of the reaction kinetics at higher temperatures. The low silica MS_2 and CR_2 samples provided virtually zeolite-free reaction systems after one day of curing at 60 °C. Besides zeolite A, zeolite EMT and zeolite Y formed and with increasing curing temperature and curing time the relative zeolite Y content increased versus EMT for CR_2. Besides the occurrence of the latter zeolites, much less sodalite structures formed in CR_2 compared to MS_2. The general increase of tectosilicates with $SiO_2/Al_2O_3 > 2$ at higher temperatures suggests a general acceleration of the reaction kinetics, leading to a fast formation of the zeolites with increased Si content from a silica enriched gel and an enhanced sodalite formation with increasing supersaturation with respect to sodium at later ages due to the reaction progress and the physical release of water in the oven (r.H. = 80%).

Lower temperatures (60 °C and 70 °C) led to higher compressive strengths for the high strength specimens (MS_6 and CR_2) and the best compromise between initial and maximum strength was observed for 70 °C, with respect to the applied specimen geometry. Curing at ≥ 80 °C did not provide significant further strength improvement after one day but lower final strength. The decrease at 80 °C correlated with initial HS formation, indicating an increased nucleation tendency (further increased at 90 °C) and thus an increased reaction speed, resulting in faster hardening (increased initial strength). Curing at 90 °C provided the lowest strength results in general. Besides an increased expansion, especially for highly reactive MS-based mixes, an alteration of the reaction products and a related more particulate microstructure is assumed in this context. The increased temperature, provides further nucleation. Another effect occurs from an increased introduction of cracks due to increased water evaporation (80% r.H.) [38]. Regardless potential strength decreases, curing for longer than 24 hours at elevated temperatures is economically not reasonable.

4.5. Modelling of the OPG composition after curing

Based on the results presented in the previous sections, a simplyfied model for the prediction of the expected phase assemblage of the MS-based and RHA(1)-based pastes after curing at 80 °C and 80% r.H. will be conducted in this section.

For these calculations the cement chemistry shorthand notation will be used (N = Na_2O,A = Al_2O_3,S = SiO_2 and H = H_2O). The relative amounts of HS ($N_3A_3S_6H_4$) and zeolite A ($N_6A_6S_{12}H_{27}$) were set to 100% $N_3A_3S_6H_4$ for MS_2; to ~100% $N_6A_6S_{12}H_{27}$ for MS_6 and to ~50% $N_3A_3S_6H$ and ~50% $N_6A_6S_{12}H_{27}$ for MS_3.5. As described in Section 4.2., small amounts of $N_3A_3S_6H_4$ are actually forming in MS_6 and of $N_6A_6S_{12}H_{27}$ in MS_2. However, they form only in minor amounts and in addition their chemical compositions differ only in the water content of the hydrated phases, meaning that error introduced by this simplification will be minor.

The fraction of SiO_2 in the geopolymeric gel in the MS-based OPG composites is unknown from the results presented above. However, this value was determined for the mix CR_3.5 by means of ^{29}Si MAS NMR to be ~18% [48], referred to as the total SiO_2 fraction in the reaction products (*i.e.* excluding reacted SiO_2). Other values may occur for different starting SiO_2/Al_2O_3 ratios and for MS-based pastes, but due to the lack of additional data, the value of 18% will be used for all MS-based pastes. In support of the use of this value for all pastes it can be noted that all presented XRD results are in accord with this value, meaning it can be assumed that the deviations from this value are not exceedingly high. Since CR and MS react very comparable (Section 4.2.), the results presented below for MS can be considered to be applicable for the medium (CR_3.5) and high (CR_6) silica CR-based mixes too. For CR_2 the zeolite formation is more complex (*i.e.* it differs significantly from MS_2; Section 4.4), and thus the results may not be transferable to this paste.

The calculations are made for samples, that have been cured for 1d at 80 °C and 80% r.H., because no significant further reaction progress is expected after this curing time (cf. ss. 4.2. and 4.4.). Because of the slightly biased results for the chemical dissolution method (cf. Sections 4.2. and 4.3.), the calculations in the present section are based on the degree of reactions, that were determined by quantitative ^{29}Si MAS NMR (α[NMR]) for MS- [51] and RHA(1)-based OPG systems [70]. The water contents were taken from the LOI of the OPG samples for the chemical determination of the degree of reaction (Sections. 2.1;. 4.2. and 4.3.). The chemical composition of the MS-based OPG for the calculations was taken from section 4.2. (Tab. 4.1) and normalized to Na_2O, Al_2O_3, SiO_2 and H_2O (sum = 100%) as reaction system, *i.e.* excluding the impurities. This simplification can be made, since the chemical compositions of the silica feedstocks are always highly dominated by SiO_2 (e.g. Section 2.2., Tab. 2.1) Based on the chemical composition of the feedstocks (Section 2.2., Tab. 2.1), the fresh paste composition (e.g. Section 4.2., Tab. 4.1) and the water content of the samples after curing at 80 °C, the global chemical composition of the hardened pastes is known.

The molar concentration of the reacted SiO_2 ($C(S)_{reacted}$) and the unreacted SiO_2 from the silica ($C(S)_{unreacted}$) can be then calculated from α[NMR] and the global molar concentration of SiO_2 ($C(S)$)in the formulation

$$C(S)_{unreacted} = (1 - \alpha[NMR]) \cdot C(S) \quad (4.1)$$

$$C(S)_{reacted} = C(S) - C(S)_{unreacted} \quad (4.2a)$$

or

$$C(S)_{reacted} = \alpha[NMR] \cdot C(S) \quad 4.2b)$$

The evaporated water content ($C(H)_{evaporated}$) was calculated from the initial water content ($C(H)_i$) of the fresh pastes and the LOI based water content $C(H)_{LOI}$) of the vaccum dried hardened pastes (cf. comparison s. 2.1.).

$$C(H)_{evaporated} = C(H)_i - C(H)_{LOI} \quad (4.3)$$

In what follows, the following assumptions have been made: (1) As described above, the molar fraction of SiO_2 in the geopolymeric gel, referred to the total SiO_2 in the reaction products (*i.e.* excluding SiO_2 from unreacted silica feddstock), S_{NMR} is assumed to be 18%. (2) Since the overall molar SiO_2/Al_2O_3 ratio was found to be ~2 mol/mol, for all MS- and CR-based pastes, and the molar SiO_2/Al_2O_3 ratio of the major crystalline reaction products (HS and zeolite A) is exactly 2 mol/mol, this value is also applied to the geopolymeric gel [51]. The traces of chabazite and zeolite P in the mix MS_2 after curing at 80 °C (cf. ss. 4.2. and 4.4.), that have different molar SiO_2/Al_2O_3 ratios, are excluded in these general calculations. (3) Because of the necessity of charge balancing in the geopolymeric gel, the molar Na_2O/ Al_2O_3 ratio is assumed to be 1 mol/mol (as for HS and zeolite A). Thus, the overall dry composition of the geoploymeric gel is assumed to be NAS_2. It is noted, since the dominating crystalline aluminosilicates HS ($N_3A_3S_6H_4$) and zeolite A ($N_6A_6S_{12}H_{27}$) provide the same molar N/A/S ratios as the gel, all major reaction products have the same chemical compositions, in the dry state.

Based on these assumptions, the molar SiO_2 concentration in the geopolymeric gel ($C(S)_{GP}$) can be calculated as:

$$C(S)_{GP} = C(S) \cdot \alpha[NMR] \cdot S_{NMR} \quad (4.4)$$

The molar Na_2O and Al_2O_3 concentrations in the gel are then:

$$C(N)_{GP} = 0.5 \cdot C(S)_{GP} \quad (4.5a)$$

$$C(A)_{GP} = 0.5 \cdot C(S)_{GP} \quad (4.5b)$$

Based on $C(S)_{GP}$, the remaining SiO_2 of the reacted SiO_2 is then assigned to the crystalline aluminosilicates ($C(S)_z$)

$$C(S)_z = C(S)_{reacted} - C(S)_{GP} \tag{4.6}$$

The Na_2O ($C(N)_z$) and Al_2O_3 ($C(A)_z$) concentrations in the crystalline aluminosilicates are then:

$$C(N)_z = 0.5 \cdot C(S)_z \tag{4.7a}$$

$$C(A)_z = 0.5 \cdot C(S)_z \tag{4.7b}$$

With these values and the overall Na_2O ($C(N)$) and Al_2O_3 ($C(A)$) concentrations, the excess Na_2O ($C(N)_e$) and Al_2O_3 ($C(A)_e$) concentrations can be calculated as follows:

$$C(N)_e = C(N) - C(N)_{GP} - C(N)_z \tag{4.8}$$

$$C(A)_e = C(A) - C(A)_{GP} - C(A)_z \tag{4.9}$$

Applying the above-mentioned assumptions about the relative abundance of HS and zeolite A in the pastes (100% HS in MS_2; ~50% HS and ~50% zeolite Ain MS_3.5; and 100% zeolite A in MS_6), and with the given stoichiometry (HS = $N_3A_3S_6H_4$ and zeolite A $N_6A_6S_{12}H_{27}$) and thus the H_2O/SiO_2 ratios of these phases, the amount of water of hydration in the crystalline aluminosilicates ($C(H)_z$)can be calculated:

$$C(H)_z = C(H)_{HS} = \frac{4}{6} \cdot c(S)_z \approx 0.666 \cdot C(S)_z \quad \text{for MS\_2} \tag{4.10a}$$

$$C(H)_z = C(H)_{zeolite\ A} = \frac{27}{12} \cdot c(S)_z = 2.25 \cdot C(S)_z \quad \text{for MS\_6} \tag{4.10b}$$

For the intermediate case MS_3.5 (~50% HS and ~50% zeolite A), an average water content in terms of H_2O/SiO_2 ratio of the crystalline aluminosilicates was assumed

$$C(H)_z \approx 1.458 \cdot C(S)_z \qquad \text{for MS\_3.5} \tag{4.11}$$

It is further assumed that any excess Al_2O_3 will precipitate as alumina gel, which may further crystallize to gibbsite ($Al(OH)_3$; $Al_2O_3 \cdot 3H_2O$ or AH_3). The water bound in the excess alumina ($C(H)_{AH}$) is thus:

$$C(H)_{AH} = 3C(A)_e \tag{4.12}$$

All remaining water is then assigned to the geopolymeric gel, based on the initial water content of the fresh paste ($C(H)_i$):

$$C(H)_{GP} = C(H)_i - C(H)_{evaporated} - C(H)_z - C(H)_{AH} \tag{4.13}$$

With these equations all molar concentrations are known for the samples after the hardening at 80 °C. From the molar concentrations and molar masses of the components (M(S); M(A); M(N); M(A); M(H)), the relative mass fractions of the phases (F(GP), F(z), $F(N)_e$, $F(A)_e$, $F(S)_{unreacted}$) in the hardened pastes were calculated.

$$F(GP) = C(S)_{GP} \cdot M(S) + C(N)_{GP} \cdot M(N) + C(A)_{GP} \cdot M(A) + C(H)_{GP} \cdot M(H) \quad (4.14a)$$

$$F(z) = C(S)_z \cdot M(S) + C(N)_z \cdot M(N) + C(A)_z \cdot M(A) + C(H)_z \cdot M(H) \quad (4.14b)$$

$$F(S)_{unreacted} = C(S)_{unreacted} \cdot M(S) \quad (4.14c)$$

$$F(N)_e = C(N)_e \cdot M(N) \quad (4.14d)$$

$$F(AH) = C(A)_e \cdot M(A) + C(H)_{AH} \cdot M(H) \quad (4.14e)$$

$$F(H)_{evaporated} = C(H)_{evaporated} \cdot M(H) \quad (4.14f)$$

where M(S) = 60.084 g/mol; M(N) = 61.979 g/mol; M(A) = 101.961 g/mol; and M(H) = 18.015 g/mol.

To obtain the relative mass fractions of the phases ($F_n(i)$, where i is GP, z, AH, …), the above values were divided by the total mass of the paste (F_n(SUM)) (including the evaporated water):

$$F_n(SUM) = F(GP) + F(z) + F(N)_e + F(AH) + F(S)_{unreacted} + F(H)_{evaporated} \quad (4.15)$$

$$F_n(GP) = \frac{F(GP)}{F_n(SUM)} \quad (4.16a)$$

$$F_n(z) = \frac{F(z)}{F_n(SUM)} \quad (4.16b)$$

$$F_n(S)_{unreacted} \frac{F(S)_{unreacted}}{F_n(SUM)} \quad (4.16c)$$

$$F_n(N)_e = \frac{F(N)_e}{F_n(SUM)} \quad (4.16d)$$

$$F_n(AH)_e = \frac{F(AH)}{F_n(SUM)} \quad (4.16e)$$

$$F_n(H)_{evaporated} = \frac{F(H)_{evaporated}}{F_n(SUM)} \quad (4.16f)$$

For the RHA(1) based OPG specimen RHA_3.5, the calculations followed the same route. However, no crystalline aluminosilicates occurred in RHA_3.5, *i.e.* the concentrations of Na_2O, Al_2O_3 and SiO_2 in crystalline aluminosilicates are zero in this case and, thus, all reacted SiO_2 is in the geopolymeric gel. Quantitative data on the degree of reaction of silica RHA(1) and the SiO_2/Al_2O_3 ratio of the geopolymeric gel, determined by ^{29}Si MAS NMR and ^{29}Si{^{27}Al} TRAPDOR NMR experiments,

were taken from ref. [70]: α[NMR] = 89.1%; $(SiO_2/Al_2O_3)_{GP}$ = 3.78 mol/mol. The results obtained from these calculations are presented in Fig. 4.20.

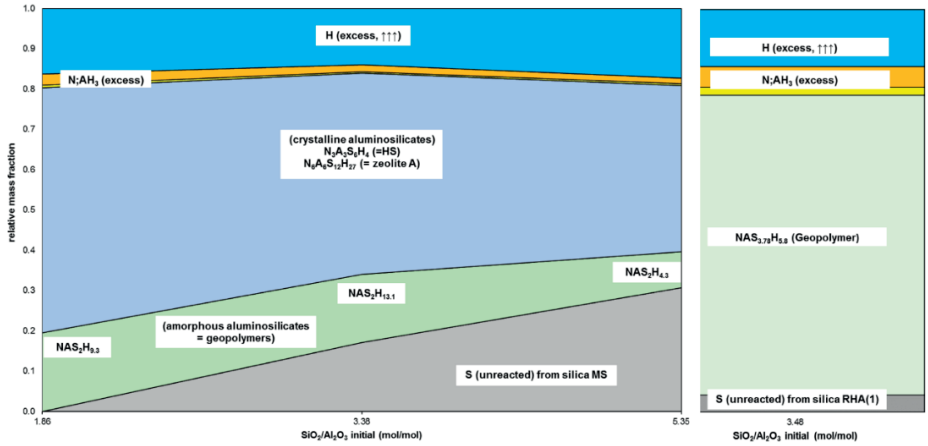

Figure 4.20: Modelling results of the phase assemblage of the MS-based OPG pastes in dependence of the initial composition (left), and of the intermediate RHA(1)-based mix RHA_3.5 (right).

Figure 4.20 highlights general trends, that were observed for the reaction of the MS-based composites. With increasing starting silica content, more of the according feedstock remains unreacted and at the highest starting SiO_2/Al_2O_3 ratio ~30% of the sample consisted of residual SiO_2 from unreacted silica MS. Simultaneously, the relative amounts of geopolymeric gel and crystalline aluminosilicates decreased from ~81% to ~50% and the total amount of the gel decreased from ~20% to ~9%.

The calculated water contents of the gel are considerably increased compared to the zeolites and vary from 9.3 mol/mol to 13.1 mol/mol (Fig. 4.20). This can be assigned to the porous nature of the gel (*cf.* ref. [48]) and the corresponding rather low degree of condensation and rather high surface area. The increased water content of the intermediate composition (MS_3.5) may possibly be a reason for the slight strength decrease for curing times longer than 3 days at 80 °C, by causing increased microcracking on removal of water. The calculations furthermore revealed that low amounts of excess Na_2O and Al_2O_3 remained after the hardening. This fits into the partially observed low amounts of hydrated sodium carbonate and aluminum hydroxide in the samples (Sections. 4.2.-4.4.).

The RHA(1)-based mix with an initial SiO_2/Al_2O_3 = 3.5 mol/mol provides a different composition after curing at 80 °C/ 80% R.H., compared to MS_3.5 (Fig. 4.20), as was previously observed by XRD and SEM (s. 4.3.). Most importantly, crystalline by-products were absent, and the SiO_2/Al_2O_3 ratio of the geopolymeric gel was

significantly higher. In addition, somewhat more Na_2O and $Al_2O_3{\cdot}3H_2O$ occurred and the incomplete incorporated alumina is a main reason for the increased SiO_2/Al_2O_3 ratio of the hardened paste (3.78 mol/mol) compared to the fresh pastes (3.5 mol/mol). In contrast to the complementary mix MS_3.5, only minor amounts of SiO_2 from the silica feedstock remained unreacted, leaving only ~3.8% SiO_2 in the overall composition (Fig. 4.20). The dominating phase (~75%) is the amorphous aluminosilicate gel (geopolymer) with an approximate composition of $NAS_{3.78}H_{5.8}$. Judging from the previous results (Section 3.3.) and the calculations of the present section, for the RHA(1)-based OPG formulations with SiO_2/Al_2O_3 < 3.5 mol/mol in the fresh paste, most likely comparable or even higher degrees of reaction of the silica can be assumed, while the alumina excess presumably will increase. The possible formation of crystalline tectosilicates must be considered in this context too. Therefore, especially formulations with further increased silica content should be considered more detailed to decrease the amount of excess alumina, with respect to commercial interests.

The molar mass of the predicted geopolymeric gel (M(GP)) can be calculated from the molar SiO_2/Al_2O_3 ratio of the gel, the molar H_2O/Na_2O ratio and the molar masses of the components. As stated above, the molar ratios of Al_2O_3/Na_2O was assumed to be 1 for the calculations.

$$M_{GP} = \frac{C(\mathrm{S})_{\mathrm{GP}}}{C(\mathrm{A})_{\mathrm{GP}}} \cdot M(\mathrm{S}) + M(\mathrm{N}) + M(\mathrm{A}) + \frac{C(\mathrm{H})_{\mathrm{GP}}}{C(\mathrm{N})_{\mathrm{GP}}} \cdot M(\mathrm{H}) \tag{4.17}$$

With the molar masses of the of the aluminosilicate reaction products the molar concentrations in the hardened pastes can be calculated, *i.e.* geopolymeric gel (C(GP) and crystallites (C(z)).

$$C_{GP} = \frac{F(\mathrm{GP})}{M(\mathrm{GP})} \tag{4.18a}$$

$$C_{GP} = \frac{F(\mathrm{z})}{M(\mathrm{z})} \tag{4.18b}$$

Considering only the aluminosilicate reaction products of the hardened pastes, excluding the excess Na_2O, Al_2O_3, the evaporated H_2O, and the unreacted SiO_2, a theoretical minimum w/b (w/b_{min}) by mass for fully hydrated geopolymeric gel and crystallites, if they could be obtained at all (but see below), can be estimated with the molar H_2O/Na_2O ratios of the gel (= molar water content, Fig.4.20) and the molar water content of the crystallites:

$$w/b_{\mathrm{min}} = \frac{\left(\frac{C(\mathrm{H})_{\mathrm{GP}}}{C(\mathrm{N})_{\mathrm{GP}}} \cdot C(\mathrm{GP}) \cdot M(\mathrm{H}) + 4 \cdot C(\mathrm{z}) \cdot M(\mathrm{H})\right)}{(C(\mathrm{GP}) \cdot M(\mathrm{GP}) + C(\mathrm{z}) \cdot M(\mathrm{z})) - \left(\frac{C(\mathrm{H})_{\mathrm{GP}}}{C(\mathrm{N})_{\mathrm{GP}}} \cdot C(\mathrm{GP}) \cdot M(\mathrm{H}) + 4 \cdot C(\mathrm{z}) \cdot M(\mathrm{H})\right)} = 0.18 \text{ for MS\_2} \tag{4.19a}$$

$$w/b_{\min} = \frac{\left(\frac{C(\mathrm{H})_{GP}}{C(\mathrm{N})_{GP}} \cdot C(\mathrm{GP}) \cdot M(\mathrm{H}) + 27 \cdot C(\mathrm{z}) \cdot M(\mathrm{H})\right)}{(C(\mathrm{GP}) \cdot M(\mathrm{GP}) + C(\mathrm{z}) \cdot M(\mathrm{z})) - \left(\frac{C(\mathrm{H})_{GP}}{C(\mathrm{N})_{GP}} \cdot C(\mathrm{GP}) \cdot M(\mathrm{H}) + 27 \cdot C(\mathrm{z}) \cdot M(\mathrm{H})\right)} = 0.28 \text{ for MS\_6} \quad (4.19b)$$

$$w/b_{\min} = \frac{\left(\frac{C(\mathrm{H})_{GP}}{C(\mathrm{N})_{GP}} \cdot C(\mathrm{GP}) \cdot M(\mathrm{H}) + \frac{4+27}{2} \cdot C(\mathrm{z}) \cdot M(\mathrm{H})\right)}{(C(\mathrm{GP}) \cdot M(\mathrm{GP}) + C(\mathrm{z}) \cdot M(\mathrm{z})) - \left(\frac{C(\mathrm{H})_{GP}}{C(\mathrm{N})_{GP}} \cdot C(\mathrm{GP}) \cdot M(\mathrm{H}) + \frac{4+27}{2} \cdot C(\mathrm{z}) \cdot M(\mathrm{H})\right)} = 0.33 \text{ for MS\_3.5} \quad (4.19c)$$

$$w/b_{\min} = \frac{\left(\frac{C(\mathrm{H})_{GP}}{C(\mathrm{N})_{GP}} \cdot C(\mathrm{GP}) \cdot M(\mathrm{H})\right)}{(C(\mathrm{GP}) \cdot M(\mathrm{GP})) - \left(\frac{C(\mathrm{H})_{GP}}{C(\mathrm{N})_{GP}} \cdot C(\mathrm{GP}) \cdot M(\mathrm{H})\right)} = 0.27 \text{ for RHA\_3.5} \quad (4.19d)$$

For the considered samples, the calculated w/b_{min} varied from 0.18 (MS_2) to 0.33 (MS_3.5). This is readily explained by the increased relative zeolite A content in MS_3.5 and MS_6, with zeolite A having a higher water content in the fully hydrated state compared to HS, and the increased water content of the predicted gel (Fig. 4.20).

The estimated minimum w/b for RHA_3.5 is 0.27. Especially the latter w/b of the virtually fully reacted RHA_3.5 mix and the w/b of MS_2 give hints for the theoretic water demand of highly reactive formulations. Because of the different water contents of the main reaction products both values differ considerably, but both are significantly lower than the actual applied w/b (w/b = 0.5 by mass). Due to the above discussed fresh paste properties, the predicted minimum w/b cannot be applied, however.

Calculation of the volume fractions of the phases in the hardened pastes (as has been done for pure and blended cement pastes [177; 228-231] and for alkali-activated slag pastes [176] could in principle be done by dividing the relative mass fractions of the phases by their respective densities, and referring the obtained values to the total volume of the paste:

$$V(i) = \frac{F_n(i)}{\varrho(i)} \quad (4.20a)$$

$$V(\mathrm{SUM}) = \sum i \; V(i) \quad (4.20b)$$

$$V_n(i) = \frac{V(i)}{V(\mathrm{SUM})} \quad (4.20c)$$

where $V_n(i)$ is the relative volume fraction of phase or component i, $\varrho(i)$ is the density of phase or component i (in g/cm^3), and i = GP, z, AH, …. This kind of calculation would also allow to compute the chemical shrinkage and, thus, the porosity of the hardened pastes [176, 177, 228-231].

However, though the densities of gibbsite, hydrosodalite and zeolite A can be retrieved from the literature or crystallographic databases, no data on the density of

pure geopolymeric gel is available in the open literature. Measurement of this density is not an easy task, as (1.) the density can be expected to vary strongly with composition (SiO_2/Al_2O_3 ratio), which means that many different measurements would have to be obtained; and, more importantly, (2.) it seems to be virtually impossible to obtain pure geopolymeric gels, as even in the highly reactive metakaolin-waterglass system residual feedstocks always remain [232]. Furthermore, because of the swelling and the necessary evaporation of excess water of the open containers during curing at 80 °C and 80% r.H. in the oven measurements of autogenous shrinkage are hardly possible. Despite losing a considerable mass of water, the volume always increases at least slightly during hardening. Sealed containers hinder the condensation reaction and the hardening of the specimens. In general, the relative humidity of the ambience plays an important role for the hardening and strengthening of the OPG, as will be discussed in Chapter 7. Further (long term) investigations of the pure pastes at ambient hardening conditions have to take into account the likely different phase formation that will occur (cf. e.g. Section 4.4.)

The above calculations of the composition and the mass fractions of the phases in the OPG pastes summarize the previous results of Chapter 4 and may be used to interpolate the phase assemblage of intermediate compositions (SiO_2/Al_2O_3 ratios), as indicated in Fig. 4.20. However, any extrapolation to SiO_2/Al_2O_3 ratios outside the studied range should be regarded as a first estimation of the actual phase assemblage at best. Further refinement and extension of the model can be achieved by gathering additional ^{27}Al and ^{29}Si MAS NMR data and quantitative phase analysis from XRD results (e.g. Rietveld method). The latter would also help to clarify the zeolite contents in formulations with more complex deviations of the phases (e.g. CR_2). Further improvements of the dissolution method (α[HCl]), e.g. by adjusting the concentration of the acid, may lead to more reliable results especially for reaction systems with high silicon content in the aluminosilicate network. In this case the molar SiO_2/Al_2O_3 ratios of the reaction products could be estimated from a chemical analysis of the dissolved species in the acid solution. Furthermore, the reactive part of silica feedstocks with a considerable amount of inert SiO_2 (e.g. RHA(2)) needs to be figured out, e.g. by chemical, spectroscopic or again by quantitative XRD analysis. Nevertheless, the above presented results are considered to be applicable for the estimation of the reaction systems of other silica sources with comparable properties to the model silica feedstocks MS, CR and RHA(1).

5. HIGH-TEMPERATURE RESISTANCE*

Chapter 3 showed, that for comparable mass based w/b the silica based OPG fresh pastes provide higher viscosities than OPC pastes. The hardening of the OPG (Chapter 4) strongly depends on the chemical composition of the according pastes, the reactivity of the silica feedstock, the curing conditions and the resulting microstructure, besides overlapping effects (e.g. expansion due to gas forming agents in the silica feedstocks).

Geopolymers are generally known for their gentle behavior at elevated and high temperatures. Nevertheless, certain systems are e.g. also known for significant shrinkage during thermal dehydration, what strongly depends on the state of water in the according systems. This Chapter studies the high-temperature resistance of the geopolymer-zeolite composites and the zeolite-free OPG mixes up to 1000 °C. The OPG pastes of this Chapter have been synthesized from MS(1), CR, RHA(2) and SA(2) and SA(3).

5.1. Introduction

Properly designed geopolymers provide gentle properties at high temperatures [9-15]. This makes them particularly interesting for fire-resistant coatings and refractories [7, 66, 152, 153], and also for production of ceramics [138, 139, 154, 155]. Especially the decomposition of portlandite causes sudden major structural changes and significant loss of the residual mechanical strength in OPC-based pastes above 400 °C, whereas AAM can provide thermal stability even above 600 °C [12, 13, 50, 156, 157]. However, some MK- and FA-based geopolymer systems exhibit significant shrinkage and cracking during dehydration even at ambient temperature due to the release of water (e.g. Ref. [38, 158]), and provide strength loss in the thermal dehydration range [11], which is a problem in construction and high-temperature applications. The thermal shrinkage of FA- and MK-based geopolymers was improved by limiting the SiO_2/Al_2O_3 ratios and adding fillers [14, 155].

In general, the predicted times until the flash over occurs in fire events are excellent for geopolymers, compared to other conventional fire protective materials, such as engineering thermoplastics, phenolics or advanced thermosets [159]. Recent research also focusses on the intumescence of geopolymers, regarding the applica-

* The MS and CR related results of Chapter 4, have been published in Sturm et al: The effect of heat treatment on the mechanical and structural properties of one-part geopolymers-zeolite composites. Thermochimica Acta, Vol. 635, p. 41-58 (2016).

tion as reactive fire-resistant steel-coatings. In general, promising results have been obtained, especially for MS- and MK-based geopolymers [160]. Compared to conventional "two-part" geopolymers, much less is known about the high-temperature behavior of OPG. Therefore, the next Section considers the properties of the silica-based OPG in terms of residual compressive strength and structural development at elevated to high-temperature treatment up to 1000 °C.

5.2. Experimental program

The CR- and MS-based OPG have been prepared with SA(2) at a nominal water/binder-ratio (w/b) by mass of 0.5. The sample composition is given in Tab. 5.1., compared to the MS- and CR-based OPG of Chapters 3 and 4., slight adjustments of the chemical composition have been conducted. The RHA(2)- and SA(3)-based formulations were produced at a nominal w/b of 0.4 by mass and had the same composition and mixing regimes as presented in Section 4.3.1. (Tab. 4.3). Pastes were mixed as described in the same Section and immediately casted into 20 mm × 20 mm × 20 mm cube molds. Subsequently the samples were cured at 80 °C and 80% r.H. for three days (MS- and CR- based OPG) or one day (RHA(2)-based OPG).

Table 5.1: Mix-designs of the MS- and CR-based OPG for the high-temperature investigations.

Sample	Na_2O/Al_2O_3	SiO_2/Al_2O_3	H_2O/Al_2O_3
	(mol/mol)	(mol/mol)	[mol/mol]
CR_2	0.92	2.02	8.54
CR_3.5	0.88	3.51	11.35
CR_6	0.82	6.01	16.04
MS_2	0.98	2.02	8.37
MS_3.5	0.98	3.52	11.05
MS_6	0.98	6.02	15.51

Cube specimens were used for compressive strength testing in the initial (as-cured) state and for the residual strength after further temperature-treatment. After the complete curing at 80 °C, the samples were stored 1-7 days at 23 °C and 50% r.H in a climate chamber until required for testing or heating. After heating and strength testing fracture pieces for the structural investigations were stored in a desiccator over dry silica gel at ambient temperature. TG measurements were conducted to analyze the dehydration behavior and to fix temperature points of interest for further investigations. Additionally, XRD, ATR FT-IR, SEM and high-temperature

dilatometry investigations were performed to characterize the OPG during heat-treatment. Grinding was done manually with mortar and pestle (agate) to provide a preparation as gently as possible, in particular for samples that were not fully dehydrated.

5.3. Results and discussion

5.3.1. Structural analysis of the MS and CR based OPG

The results of the XRD analysis of the 3d cured composites were very similar to the results from Section 4.2.2 (Fig. 4.1). This supports the observations, that curing times for longer than one day at 80 °C are not necessary. However, slight differences of the phase content occurred. Zeolite A and HS were the dominant crystalline phases of the MS-based OPG. In addition, the MS_2 mix contained residual amounts of chabazite. Zeolite A was always the crystalline main phase for CR-based OPG, but CR_2 provided more faujasite-type related peaks, as also observed in Section 4.4.2. The reproducibility of the phase content of CR-based OPG, especially at high degrees of reactions of the silica, appears to be generally lower than for MS-based OPG (cf. Section 4.4.2). Deviations in the phase assemblage are further attributed to the differences in chemical composition compared to the samples of Section 4.2.2. (Tab. 4.1).

Since zeolite A was the dominating crystalline phase in many of the considered samples, TG analysis was also performed on a reference zeolite A sample (Henkel AG & Co. KGaA, Düsseldorf, Germany). The average crystallite size of the reference zeolite A was ≈1 μm (as observed with SEM; results not shown), and it contained only traces of a sodalite-type impurity (PDF # 00-040-0101), checked by XRD (Fig. 5.1). After heating at 1000 °C zeolite A had transformed into a mix of carnegieite ($NaAlSiO_4$; PDF # 01-081-2081) and hexagonal nepheline ($NaAlSiO_4$; PDF # 00-035-0424), as typical for sodium A-type zeolites [119]. A HS reference was not available.

Its dehydration behavior was compared to those of the cured composites, and selected temperature points were determined for additional structural and mechanical investigations (Fig. 5.2). Mass loss for both, the quasi-pure zeolite A and the geopolymer-zeolite composites, ran quite similar with different absolute amounts. At 400 °C the major part of the dehydration was completed. The initial thermal dehydration of the composites occurred at ≈ 65 °C.

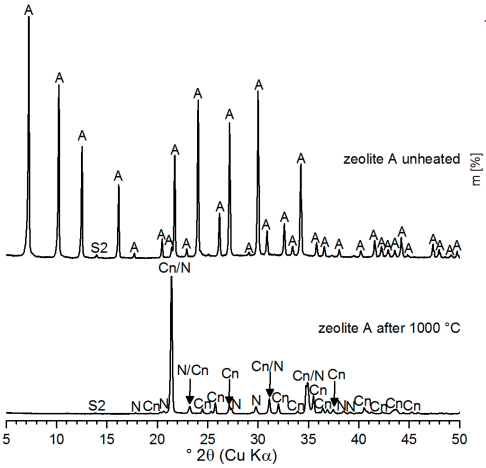

Figure 5.1: XRD results for the zeolite A reference before and after heating at 1000 °C (A = zeolite, S2 = anhydrous sodalite-type, Cn = carnegieite, N = nepheline).

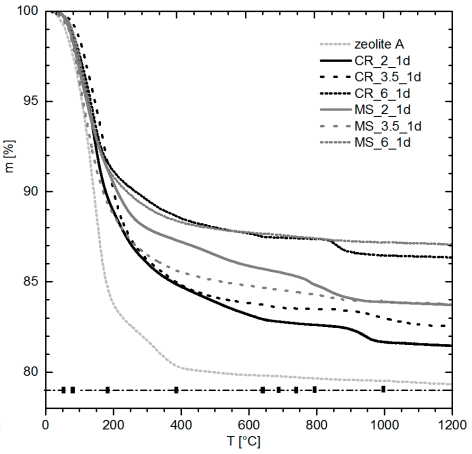

Figure 5.2: TG curves of the MS- and CR-based OPG composites after 3 days of curing at 80 °C and 80% r.H., respectively. Squares represent temperatures, chosen for XRD investigations and residual compressive strength testing.

Zeolite A exhibited a stepwise dehydration behavior with a steep loss up to ≈ 200 °C and a second step with lower slope between 200 °C and 400 °C. The geopolymer-zeolite composites exhibited a rather continuous behavior with the TG curve flattening due to a slower water release with increasing temperature. However, the MS_2 specimen exhibited a multiple-step mass loss at higher temperatures, most likely due to several incorporated HS, including hydroxy-types (see below). The final, reaction products related mass loss was thus shifted to higher temperatures compared to all other samples, giving hints for dehydroxylation.

Up to 100 °C a mass loss of 1.5–4.0 wt.% occurred (Tab. 5.2, Fig. 5.2). For all composites the most significant mass loss of 6.2–8.4 wt.% followed between 100 °C and 200 °C (for comparison: zeolite A: 12.3 wt.%), *i.e.* in the main dehydration range. A further significant mass loss of 2.5-5.3 wt.% (zeolite A: 3.7 wt.%) followed between 200 °C and 400 °C. This dehydration range furthermore correlates quite well with reported TG data for zeolite A and hydrosodalites [120, 161-163].

In general, in each class of geopolymer-zeolite composites (*i.e.* CR-based or MS-based), the final mass loss at 1200 °C decreased with increasing SiO_2/Al_2O_3 ratio. This is related to the fact that only in the low-silica samples (SiO_2/Al_2O_3 = 2) the silica feedstocks reacted virtually completely, while in the mixes with higher SiO_2/Al_2O_3 ratios the silica reacted only partly (cf. Section 4.2.). In general, the high-silica mixes with lower fraction of porous reaction products (zeolites and geopolymeric gel) and correspondingly lower total water content, provided lower mass losses, due

to the higher amount of inert silica filler. For medium and low silica samples, with generally more reaction products the trend was less pronounced.

Deviating from the general trend of the temperature dependent mass loss, the MS_2 sample exhibited a peculiar behavior in that its mass loss up to ca. 900 °C was lower than the mass loss of MS_3.5 (and virtually the same at 1200 °C). In this context zeolite A can include more water per unit cell (≤ 12 mol H_2O) than HS (≤ 8 mol H_2O) thus more water is included when more zeolite A is provided than HS and MS_2 contained only minor amounts of zeolite A but major amounts of HS.

Felsche and Luger [163] reported a double-step dehydration (two overlapping DTG peaks) of fully hydrated non-basic hydrosodalite ($Na_6(AlSiO_4)_6{\cdot}8H_2O$) in the range of ca. 60-340 °C and a multiple-step dehydration and dehydroxylation of basic hydrosodalite ($Na_8(AlSiO_4)_6OH_2{\cdot}4H_2O$) in the range of ca. 80-810 °C. In a subsequent study [161] the result for $Na_6(AlSiO_4)_6{\cdot}8H_2O$ was confirmed (double-step dehydration in the range of 100-350 °C), but it was found that basic HS, $Na_8(AlSiO_4)_6OH_2{\cdot}2H_2O$, exhibits a double-step dehydration (two overlapping DTG peaks) in the range of ca. 530-700 °C. The study furthermore proved that basic HS with more than 2 moles hydration water ($Na_8(AlSiO_4)_6OH_2{\cdot}2H_2O$) are actually a mix of basic and non-basic hydrosodalites. The TG curve of MS_2 is comparable to the curve presented in Ref. [163] for "$Na_8(AlSiO_4)_6OH_2{\cdot}4H_2O$", which was found later to be a mix of basic and non-basic hydrosodalites [161]. Taking also into account the XRD peak shapes (Fig. 5.4), it is tentatively concluded that this sample contained, besides non-basic hydrosodalite of intermediate water content, also smaller amounts of basic hydrosodalite and possibly non-basic hydrosodalites of different water content, as preliminary suggested in Section 4.2.2. and 4.4.2, respectively.

In this context also a dehydroxylation of hydroxide containing geopolymers up to 750 °C was found [158]. All CR-based samples exhibited a distinct step around 850-1000 °C. This step initially started at lower temperatures for higher silica contents (CR_6). This is related to the impurities in the CR-based systems, that contained calcite from the silica feedstock, which decomposes in that temperature range.

TG showed that release of most of the water in the samples occurred between ca. 100 °C and 200 °C, which is the typical dehydration range of geopolymers [11, 14, 15, 20–22, 55], and some additional, water loss occurred at 200-400 °C. Comparison with the TG curve of an almost pure zeolite A (Fig. 5.2) and consideration of the IR spectra of the heated samples (Figs. 5.9 and 5.10) as well as the thermal deformation behavior (Fig. 5.11) leads to the conclusion that most of this water is adsorbed (free) or of zeolitic character, and in particular related to zeolite A and/or

HS and only minor amounts of interstitial water in the gel. Above 400 °C generally only minor mass losses occurred, particularly for CR mixes, caused by escaping CO_2 from incorporated calcite. In contrast to other geopolymer systems [11, 13–15, 20–23, 43, 55], the geopolymer-zeolite composites investigated in the present work did not exhibit pronounced shrinkage in the main dehydration range < 200 °C (Fig. 5.11), because the released water is mainly "zeolitic" water; instead, thermal shrinkage occurred rather continuously from ambient to ca. 700 °C (< 3 %). The zeolites acted as kind of fillers/aggregates, improving the deformation behavior.

Table 5.2: Residual masses of the CR- and MS-based OPG during TG analysis.

Sample	m_r (100 °C) (wt.%)	m_r (200 °C) (wt.%)	m_r (400 °C) (wt.%)	m_r (650 °C) (wt.%)	m_r (700 °C) (wt.%)	m_r (750 °C) (wt.%)	m_r (1000 °C) (wt.%)
CR_2	97.2	88.9	84.8	82.9	82.8	82.7	81.7
CR_3.5	98.5	90.1	84.8	83.7	83.5	83.5	83.0
CR_6	97.6	91.1	88.5	87.5	87.5	87.4	86.5
MS_2	96.7	90.5	87.2	85.7	85.5	85.3	83.9
MS_3.5	96.1	88.7	85.5	84.7	84.5	84.4	83.9
MS_6	97.3	90.8	88.3	87.7	87.6	87.5	87.2
zeolite A	96.3	84.0	80.3	79.8	79.8	79.7	79.5

XRD was conducted on the MS and CR based OPG to identify structure changes and phase transformations during the dehydration (main part up to 400 °C), up to the "breakdown" of the structures between 650 °C and 750 °C and the new phase formation up to 1000 °C. Since the samples cooled down to ambient in the furnace, retrograde phase formation cannot be fully excluded. Up to specific temperatures, at least 650 °C, no major phase transformations were observed. Above this temperature completely new structures occurred with significant differences between the different composites (Figs. 5.3–5.10). Equally composed mixes (*i.e.* mixes produced from different silica feedstocks but with identical SiO_2/Al_2O_3 ratio) exhibited comparable behavior.

Fig. 5.3 presents the XRD results of CR_2 after heating to specific temperatures. Up to 400 °C, except the disappearance of faujasite and a decrease of the third zeolite A peak at 12.47° 2θ, no significant changes could be observed by XRD. Other small changes of the absolute intensities in the range of moderate temperature treatment are not regarded due to the influence of the preparation with mortar and pestle. At 650 °C first significant structure transformations occurred. Only zeolite A from the initial crystalline phases remained, all peak intensities decreased and the FWHM of

the peaks increased, attributed to commencing of structural breakdown. A new peak occurred (21.4° 2θ), indicating the initial formation of a new phase.

At 700 °C this "metaphase" and nepheline, $NaAlSiO_4$ (PDF # 00-035-0424), were the new crystalline main phases. Most peaks of the pattern were matched with the nepheline reference, but the reflection of maximum intensity located at 21.4° 2θ was exaggerated. At 700 °C all peak intensities were increased and FWHM decreased compared to 650 °C. Several studies [119, 155, 164] found low carnegieite, $NaAlSiO_4$, as a metaphase during the transformation of geopolymers and A-type zeolites to stuffed tridymite structures (nepheline), and reported the position of the diagnostic main peak to be in the same 2θ-range as the observed exaggerated peak at 21.4° 2θ. However, with the available carnegieite references this peak could not be matched satisfyingly. Since the composition of stuffed silica structures is variable [165, 166], a carnegieite-type phase of intermediary composition is assumable instead. In addition to the aforementioned phases, sodalite *sensu stricto*, $Na_8(SiAlO_4)_6Cl_2$, (PDF # 00-037-0476) was observed in the heated CR_2 samples (chloride provided by the silica feedstock CR). Only residues of zeolite A remained in the sample. At 750 °C nepheline was clearly the crystalline main phase, and the exaggeration of the main peak at 21.4° 2θ decreased. Sodalite, which is known to coexist with nepheline [167], remained in the system, but no zeolite A related peaks remained. At 800 °C the system was almost equal to that at 750 °C, only the intensity to background ratio increased, as a sign for probably increased crystallinity and exaggeration of the peak at 21.4° 2θ further decreased.

After exposure to the highest investigated temperature of 1000 °C the position of the main peak slightly shifted to lower diffraction angle (21.19° 2θ), thus nepheline matched only the shoulder of that peak. Thompson and co-workers [165, 166] reported several silicates of carnegieite structure, synthesized at high temperatures and noted the problem of reaching equilibrium below 1300 °C because of slow reaction kinetics. However, one of the reported intermediary structures ($Na_{1.45}Al_{1.45}Si_{0.55}O_4$, PDF # 00-049-0002) [165] matches the two diagnostic peaks of CR_2 after 1000 °C at 21.10° 2θ and 34.83° 2θ (Fig. 5.3). This is in line with previous studies on the high-temperature behavior of geopolymers [155, 164], which reported the formation of dominating hexagonal nepheline and carnegieite type phases above 800 °C. A further diagnostic peak, with low related intensity occurred after 1000 °C at ≈ 28.2° 2θ and is related to monoclinic trinepheline. No signs for amorphous phase occurred and the sample appeared virtually fully crystalline.

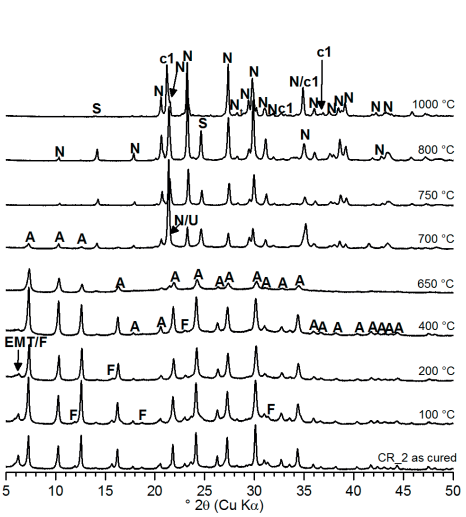

Figure 5.3: XRD results of temperature-treated CR_2. (A = zeolite A; F = faujasite, EMT = zeolite EMT; N = hexagonal nepheline; N_t = monoclinic trinepheline, S = sodalite *sensu stricto*, c1 = intermediary carnegieite structure; U = unidentified metaphase).

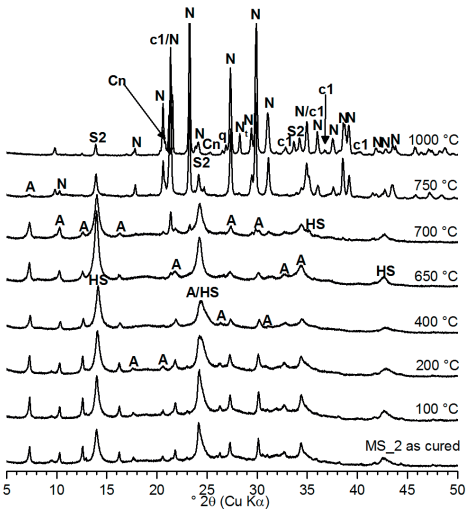

Figure 5.4: XRD results of temperature-treated MS_2. (A = zeolite A, HS = hydrosodalite, N = nepheline; N_t = monoclinic trinepheline; S2 = anhydrous sodalite-type; c1 = intermediary carnegieite structure; Cn = carnegieite).

Fig. 5.4 shows the evolution of phase content of MS_2. Except the decrease of the third zeolite A peak, up to 650 °C no major changes were observed for this phase. The relative intensity of the main peak of HS, located at ≈ 24.7° 2θ, decreased compared to the second diagnostic peak at 13.97° 2θ after exposure at > 400 °C, *i.e.* after the main part dehydration as proven by TG (Fig. 5.2). The XRD observations giving further hints for the presence of different HS, partially with hydroxy-types, and possibly also low amounts of the initial aluminosilicate gel that dehydroxylate up to 750 °C [158].

Felsche and Luger [162] reported a water-free sodalite-type, $Na_6(SiAlO_4)_6$, (PDF # 00-040-0101), the one that gave the best match for the residual peak of the HS impurity in the zeolite A reference (Fig. 5.1), that exhibits the same "reversed" intensities as observed in the diffractograms of MS_2. The zeolite A peaks underwent no visible changes up to 700 °C but above 200 °C no chabazite remained.

At 750 °C a phase transformation was observed. Nepheline appeared as the new crystalline main phase. The main peak was again exaggerated, but less intensive as for CR_2. Only minor peaks of zeolite A and the supposed water-free sodalite remained. A small reflection appeared at 9.75° 2θ, which could not be assigned to a phase. The pattern at 1000 °C appeared quite similar to the one at 750 °C, al-

though few additional small peaks occurred that can be matched with the proposed intermediate stuffed silica phase. In contrast to CR_2, small amounts of pure low carnegieite (PDF # 96-101-0954) were identified at the final temperature (1000 °C), as also found in Refs. [155, 164]. Again, monoclinic trinepheline was present as additional phase; the unassigned reflection at 9.75° 2θ disappeared.

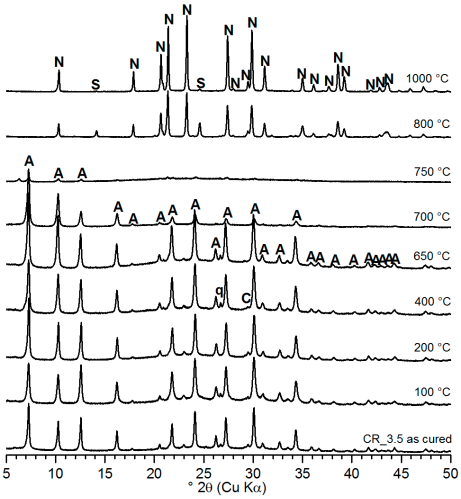

Figure 5.5: XRD results of temperature-treated CR_3.5. (A = zeolite A, N = nepheline, S = sodalite *sensu stricto*).

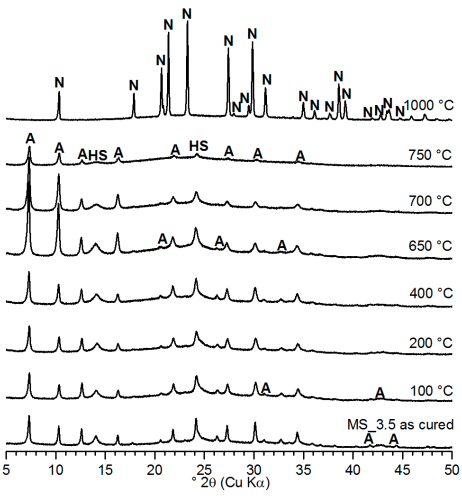

Figure 5.6: XRD results of temperature-treated MS_3.5. (A = zeolite A, N = nepheline, HS = hydrosodalite).

For sample CR_3.5 (Fig. 5.5) no significant changes were observed up to 650 °C except the diminishment of the third zeolite A peak at 12.48° 2θ. At 700 °C the first significant changes occurred. The intensity of the peaks started to decrease, eventually leading to an almost complete structure breakdown at 750 °C, and thus comparable to the behavior of almost stoichiometric zeolite A, but at a slightly lower temperature [119]. Only residues of zeolite A remained as well as a very small not identified peak at the position of faujasite's main peak; the rest of the diffraction pattern displayed just an amorphous hump. At 800 °C the mix recrystallized with nepheline as main phase and minor amounts of sodalite *sensu stricto*; probably including chloride and providing no reversed intensities. At 1000 °C XRD indicated almost pure nepheline phase and additionally some residues of the previously introduced sodalite.

Fig. 5.6 shows the XRD results for MS_3.5. As for the CR_3.5 mix, virtually no changes occurred for zeolite A up to 650 °C, except a noticeable maximum of the signal to background ratio at that temperature and the diminishment of the peak at 12.48° 2θ. At 700 °C a breakdown of the initial phases commenced, and at 750 °C almost the whole sample appeared X-ray amorphous. Zeolite A residues remained

as well as small amounts of HS. After exposure to 1000 °C XRD indicated only hexagonal nepheline.

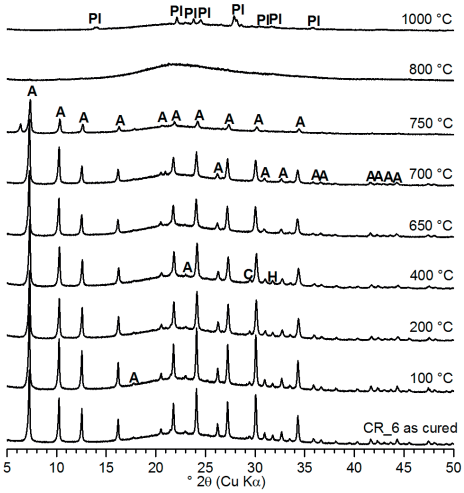

Figure 5.7: XRD results of temperature-treated CR_6. (A = zeolite A, Pl (plagioclase) = albite, q = quartz, C = calcite, H = halite).

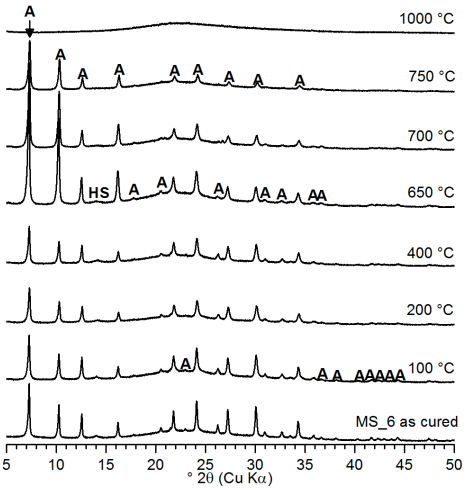

Figure 5.8: XRD results of temperature-treated MS_6. (A = zeolite A, HS = hydrosodalite).

Fig. 5.7 shows the XRD patterns of the sample CR_6. Almost no changes occurred up to a temperature of 700 °C. At 750 °C a large fraction of zeolite A had been transformed into amorphous phase. Besides the remaining zeolite, like for CR_3.5 again a single reflection, matching the main peak of faujasite structures occurred at 6.25° 2θ. After treatment at 800 °C the sample was almost completely amorphous. The unassigned peak at 6.25° 2θ disappeared. After 1000 °C the sample remained mainly amorphous, but some albite (PDF # 00-010-0393) appeared. This means that, in contrast to the previously discussed mixes, a feldspar phase with an elemental formula of $Na(Si_3AlO_8)$ was formed. This can be explained by the increased amount of silicon in the CR_6 mix (SiO_2/Al_2O_3 = 6).

The results for MS_6 are displayed in Fig. 5.8. Up to 650 °C this composite exhibited the same behavior as the previously discussed medium- and high-silica mixes. No major changes could be identified by XRD. At 700 °C the sample stayed quite crystalline, although first signs of structural breakdown were observed. No HS was left. After treatment at 1000 °C the sample appeared X-ray amorphous and no albite formed. The maximum of the hump shifted back, indicating the incorporation of more silicon to the network.

For sample CR_3.5 additional ATR FT-IR measurements were conducted on the heat-treated samples. In particular the region between 3000 cm^{-1} and 4000 cm^{-1}

(Fig. 5.9) is of interest for the consideration of the thermal dehydration, since in that range the characteristic stretching vibration centres of water and hydroxyl groups appear. After 100 °C almost no change was observed. After treatment at 150 °C, *i.e.* in the region of the most significant dehydration (Fig. 5.2), the intensity reduced by almost 50 %, which fits the TG results quite well. After heating at 400 °C almost the entire band disappeared, again in line with the TG results. Above 400 °C no water band remained.

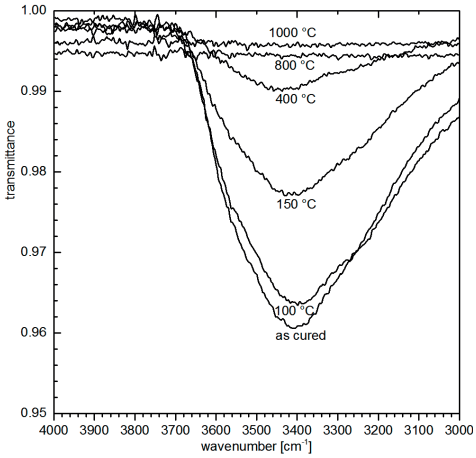

Figure 5.9: ATR FT-IR spectra of selected temperature-treated CR_3.5 samples between 3000 cm^{-1} and 4000 cm^{-1}.

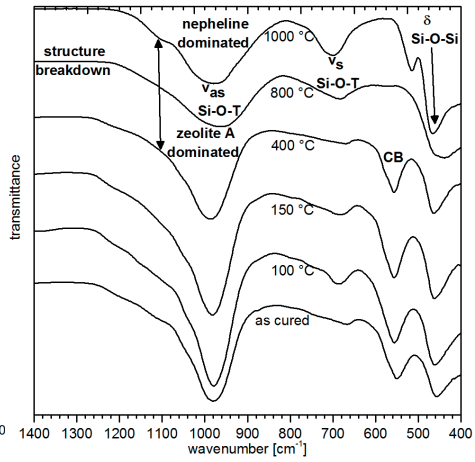

Figure 5.10: ATR FT-IR spectra of selected temperature-treated CR_3.5 samples between 400 cm^{-1} and 1400 cm^{-1}. (T = Si or Al, $\nu_{as,s}$ = asymmetric and symmetric stretching vibration, CB = complex band; δ = bending vibration)

The IR spectra below 1400 cm^{-1} (Fig. 5.10) fits into the results of the other investigations as well. Up to 400 °C no significant changes occurred since the structure remained largely stable despite dehydration. At 800 °C the IR spectrum indicated a breakdown of the original structure, as shown by the disappearance of absorption band at ≈ 550 cm^{-1}, characteristic of zeolite A [168]. Previous Investigations [90, 133] have found this band in A-type zeolites to be a complex band (CB) occurring from stretching vibrations (ν_s Si-O-Si) and bending vibrations (δ O-Si-O) of higher order. After heating to 1000 °C four new absorption centres (982 cm^{-1}, 702 cm^{-1}, 514 cm^{-1} and 465 cm^{-1}) occurred, which fit quite well the IR spectra of nepheline presented in Ref. [87], again in accordance with the observed diffraction patterns (Fig. 5.5).

In summary, depending on the starting mix-design, phase transformations started between 400 °C and 750 °C. Except for the high-silica mixes MS_6 and CR_6, the materials transformed to stuffed silica structures of nepheline-type (MS_3.5 and

CR_3.5) or a mix of nepheline and carnegieite-type structures (MS_2 and CR_2). This behavior parallels previous reports about aluminosilicate precursors transforming into various stuffed silica structures [18, 21, 39, 44, 45]. With increasing content of unreacted silica partial melting increased (see dilatometry) and MS_6 and CR_6 turned into completely amorphous or formed traces of albite on heating at 1000 °C (Figs. 5.7 and 5.8), respectively, the latter being a behavior that has already been reported for geopolymers with SiO_2/Al_2O_3 = 6 [18].

The high-temperature dilatometry experiments indicated only minor deformations in the dehydration range up to 400 °C (Fig. 5.11). Except MS_3.5 ($\Delta l/l \approx 2\%$) all mixes exhibited a relative linear shrinkage of $\Delta l/l \leq 1.5\%$ up to this temperature. At 650 °C a relative shrinkage of only 1.5% was observed for CR_6, while the other mixes exhibited somewhat higher deformations ($\Delta l/l \leq 3$ %). Up to this temperature the deformations proceeded almost linear over the complete temperature range. At ca. 700 °C the deformation-temperature curves of all samples became significantly steeper, and consequently the shrinkage increased to values of 4.2% (CR_6) to 9.5% (CR_3.5) at 800 °C. This behavior is in line with the observed deformation behavior of the cubes for the residual compressive strength tests and it correlates with the observed phase transformations above 650 °C (Figs 5.3–5.10).

At temperatures above ca. 700 °C a sudden increase in shrinkage occurred. This sudden "softening" is generally attributed to viscous sintering or densification/ crystallization/ partial melting in the geopolymers [11, 13, 15, 20–22, 55]. The rather uniform shrinkage of the specimens up to this temperature is an advantage in high-temperature applications. Above ca. 800 °C the various samples behaved quite different. The low-silica mixes yielded the lowest maximum shrinkage (CR_2 = 9.8% and MS_2 = 9.5 %), while CR_3.5 reaches a maximum shrinkage of 23% at 860 °C. The CR_6 mix showed basically the same tendency but at slightly higher temperatures and with lower maximum shrinkage ($\Delta l/l$ = 16.2 %). This is readily explained by the lower content of pores in the initial state. Medium- and high-silica MS-based mixes exhibited a differing behavior. Both had comparable shrinkage maxima ($\Delta l/l_{max}$(MS_3.5) = 17% at 840 °C and $\Delta l/l_{max}$(MS_6) = 18% at 850 °C), but with further increasing temperature the samples started to expand (MS_6: + 6% and MS_3.5: + 18 %). In contrast to MS_2 both mixes incorporated remaining silica MS from the starting mix.

The peculiar behavior of MS_3.5 and MS_6 observed by high-temperature dilatometry indicated a maximum shrinkage for medium- and high-silica MS-based mixes (MS_3.5 and MS_6) around 850 °C, followed by a sharp expansion at higher temperatures. A rapid expansion at temperatures around 600-800 °C has been

observed previously for some fly ash-based geopolymers and was attributed to silica gel-like products of the employed sodium silicate activating solutions [13, 15, 56]. In addition, Fletcher et al. [57] observed swelling of metakaolin-based geopolymers, comprising high amounts of silica (Aerosil), at temperatures of 100–300 °C. Since in the present study only samples with remaining MS after curing (in MS_2 the silica is virtually completely reacted) showed sharp high temperature swelling, this behavior seems to be mainly caused by the residual MS. The CR-based samples did not exhibit extensive swelling up to the maximum measured temperature of 900 °C, which is considered to be an advantage over the MS-based mixes.

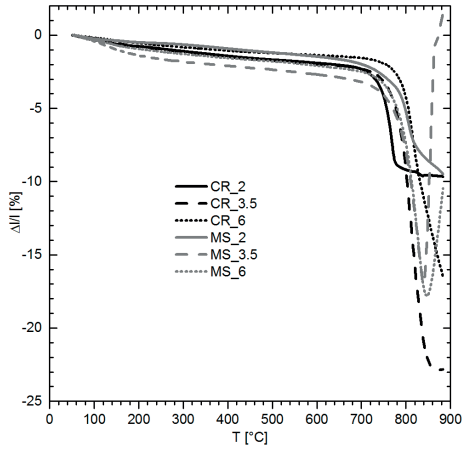

Figure 5.11: Relative shrinkage of the MS- and CR-based OPG during high-temperature dilatometry measurements.

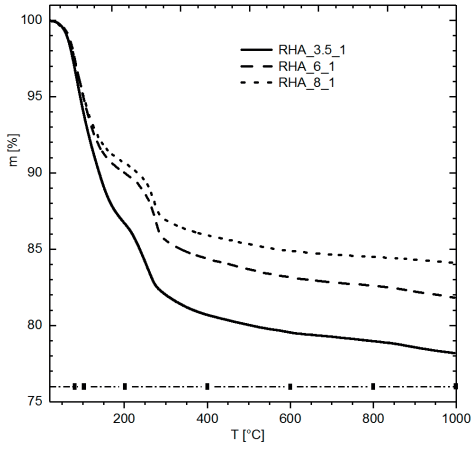

Figure. 5.12: TG curves of RHA_3.5_1, RHA_6_1 and RHA_8_1, prepared with RHA(2) and cured at 80 °C and 80% r.H. (1d) up to 1000 °C. Squares represent temperatures chosen for XRD and residual compressive strength testing.

5.3.2. Structural analysis of the RHA(2) based OPG

Fig. 5.12 presents the results of the TG experiments on the RHA(2)-based OPG RHA_3.5_1, RHA_6_1 and RHA_8_1. The temperature dependent mass losses of all OPG mixes occurred in the same temperature range. On the other hand, the absolute mass losses of the curves differed with changes of the SiO_2/Al_2O_3-ratio of the formulations. Up to 100 °C the OPG lost ≤ 5.8 wt.% of their starting mass (Tab. 5.3), where the initial dehydration temperature was ≈ 59 °C. Up to 200 °C the samples lost ≤ 13.3 wt.% (Tab. 5.3). In this context the mass losses of the high silica mixes were lower (≤ 10 wt.%) than for RHA_3.5_1. The extrapolated end temperature of the first dehydration step was 148 °C for RHA_3.5_1 and 126 °C for RHA_6_1 and RHA_8_1, respectively. The IR spectrum of RHA_3.5_1 (Fig. 5.13) after 200 °C fitted into the TG results, indicating a decrease of the water

hump, but remaining hydroxide bands from the gibbsite impurity. Thus, the mass loss up to 200 °C was mainly attributed to water from the OPG pastes.

There was no point of zero slope between both dehydration steps due to overlapping reactions, enhanced by the dynamic heating. The midpoint temperature between the first step and the second step was 178 °C – 185 °C. The second dehydration step started at 220 °C (RHA_3.5_1) or 245 °C (RHA_6 and RHA_8). The end of the second step was situated at 290 °C and 307 °C. Up to 300 °C the samples lost ≤ 18 wt.% of their starting mass, whereas the high silica formulation lost only < 14.5% (RHA_6_1). and 13.1% (RHA_8_1). The second step included the dehydroxylation of the gibbsite impurity [169] as proved by IR (Fig. 5.13) and XRD (Fig 5.14).

TG measurements indicated only slight differences of the mass loss due to thermal dehydration for RHA_6 and RHA_8, whereas significantly more mass loss occurred in RHA_3.5, fitting into the general observed trends of the MS- and CR-based OPG (Fig. 5.2). All samples provided slight further continuous mass loss after the dehydration up to the final temperature (1000 °C).

Table 5.3: Residual masses of the RHA(2)-based OPG during TG analysis.

Sample	$m_{r(100\,°C)}$	$m_{r(200\,°C)}$	$m_{r(400\,°C)}$	$m_{r(600\,°C)}$	$m_{r(800\,°C)}$	$m_{r(1000\,°C)}$
	(wt.%)	(wt.%)	(wt.%)	(wt.%)	(wt.%)	(wt.%)
RHA_3.5_1	94.2	86.7	80.7	79.5	79.0	78.2
RHA_6_1	95.1	90.0	84.4	83.1	82.6	81.8
RHA_8_1	95.2	90.6	85.9	84.9	84.5	84.1

The IR spectrum of the as-cured RHA_3.5_2 sample (Fig. 5.13) revealed typically broad and overlapping asymmetric and symmetric stretching vibration (ν1 and ν3) of incorporated water between 3500 cm^{-1} and 3200 cm^{-1}, as observed for CR_3.5 (Fig. 5.9). Furthermore, three signals occurred at around 3525 cm^{-1} (1), 3458 cm^{-1} (2) and 3386 cm^{-1} (3). They represent the stretching vibrations of the hydroxide groups in gibbsite [88, 170], that was identified by XRD (Section 4.3.2; Fig. 4.10 and Fig. 5.14). The IR spectrum of the 100 °C sample revealed more pronounced gibbsite related hydroxide vibration. This is a result of the decreased water hump. The hump further decreased with increasing temperature and after 400 °C (Fig. 5.13) the hump disappeared, deviating from the composite CR_3.5, that provided low intensity remaining water bands at 400 °C (Fig. 5.9) due to the zeolitic character of the included water. The hydroxide related bands of the former gibbsite phase disappeared as well. Thus, can be concluded at ≥ 400 °C the specimens were virtually

free from water and hydroxides. The diffractograms of the samples after exposure to 400 °C indicated the disappearance of the gibbsite impurity (Fig. 5.14) as well.

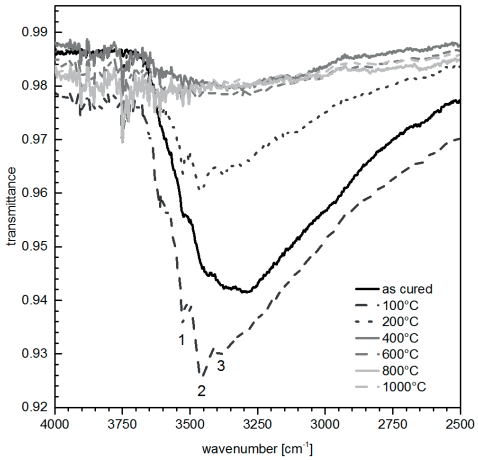

Figure 5.13: ATR FT-IR spectra of RHA_3.5_2 after exposure to specific temperatures (1, 2, 3 = ν(OH)).

The XRD results of the high-temperature treated RHA(2)-based OPG are shown in Fig. 5.14. The diffractogram of the geopolymer-zeolite composite RHA_3.5_1 provided an apparent decrease of the hydrated zeolite A phase from the as-cured state to after the exposure to 100 °C. No further major changes of the zeolite A related peaks occurred from 100 °C to 400 °C and the previous investigations of this Chapter showed the zeolite A phase in the geopolymer-zeolite composites was stable even above 400 °C (e.g. Figs. 5.5 and 5.6). At 400 °C, traces of sodalite-type phase were observed but disappeared again at the next higher temperature (600 °C). However, the 600 °C sample provided a decrease of the zeolite A related peaks, *i.e.* at lower temperatures as for equally composed composites based on CR and MS. The disappearance at 800 °C was also observed (Figs. 5.5; 5.6 and 5.14).

Furthermore, the cristobalite related peaks from the silica feedstock RHA(2) decreased, compared to 600 °C. Nepheline occurred as a new phase and the initial phases virtually disappeared, fitting into the observations of CR_3.5 and MS_3.5. After exposure to 1000 °C cristobalite fully disappeared and nepheline decreased. The dominating hump indicates the partial melting of the sample. Compared to the as-cured sample, the maximum of the hump shifted back to lower diffraction angles (≈ 23.5 °2θ, indicating a silica enrichment of the glassy phase, due to the incorporation of the SiO_2 from the former cristobalite.

The relative temperature dependent development of the phase assemblage of RHA_3.5_2 was quite comparable. No major changes after exposure to 100 °C

occurred and after 400 °C the gibbsite impurity disappeared. At 800 °C a major decrease of cristobalite was found, as well as the formation of nepheline. Nepheline was the only remaining crystalline phase, after exposure to 1000 °C major parts of the samples were amorphous, providing a back shifted diffraction maximum (≈ 23.1 °2θ) as well. The initial hump of the as-cured mix decreased up to 400 °C (Fig. 5.15). This was related to the dehydration of the initial aluminosilicate N-A-S(-H) gel, fitting into TG (Fig. 5.12) and IR (Fig. 5.13) investigations.

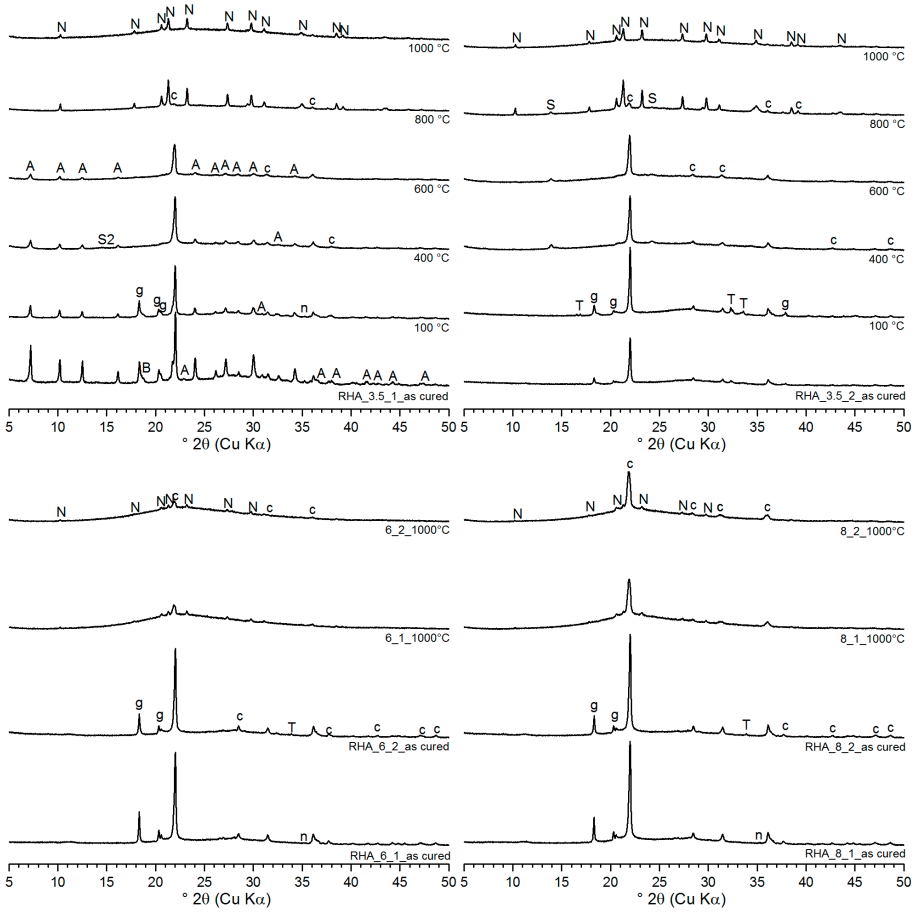

Figure 5.14: XRD results of temperature-treated RHA_3.5_1 (top left), RHA_3.5_2 (top right), RHA_6_1 (bottom left), RHA_8_1 (bottom right) (A = zeolite A; G = gibbsite; B = bayerite; n = natrite; T = thermonatrite; c = cristobalite; N = nepheline S2 = anhydrous sodalite-type).

The diffractograms of the RHA_6 samples were characterized by a hump after exposure to 1000 °C (Fig. 5.14). The hump was shifted back to smaller diffraction angles (≈ 22.6 °2θ) as well. Traces of nepheline have been detected. In contrast to the RHA_3.5 mixes also residues of the cristobalite remained in the system. The dif-

fractograms of the RHA_8 samples after exposure to 1000 °C (Fig. 5.14) provided only minor differences to RHA_6. Samples where characterized by a hump, with its maximum shifted back to lower diffraction angles (≈ 22.0 °2θ). Traces of nepheline were found and parts of the cristobalite remained in the system.

SEM micrographs of the high-temperature treated composite RHA_3.5_1 (Fig. 5.16) after exposure to 800 °C were characterized by a matrix of glassy phase and low amount of phenocrysts. Taking into account the XRD results (Fig. 5.14), the crystalline structures in the micrographs likely correspond to nepheline and residual cristobalite. The matrix provided less interfaces than in the as cured state (Section 4.3.2; Fig. 4.11). Furthermore, the sample included a significant volume of pores. Those pores had various sizes of ≤ 40 µm and irregular shapes. Besides spherical pores, also pores with elongate shapes were found. All pores provided smooth interfaces as a consequence of partial melting.

After exposure to 1000 °C, even less interfaces in the glassy matrix remained, indicating further melting at the higher temperature, what fits into the XRD observations (Fig. 5.14). Few phenocrysts remained in the matrix. The pore shapes and sizes became more homogenous. The major part of the pores provided sperical shapes. Furthermore the amount of the smaller pores (≤ 10 µm) decreased from 800 °C to 1000 °C and the pore sizes became more homogenous. The microstructure was macroscopicaly expressed by a strong expansion, leading to the formation of foams. In this context the foaming effect was much more pronounced for the high silica mixes (RHA_6 and RHA_8), i.e the mixes with more unreacted silica, as also observed by high-temperature dilatometry of MS_3.5 and MS_6 (Fig. 5.11).

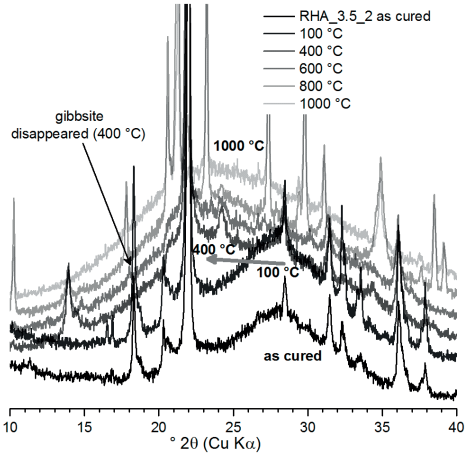

Figure. 5.15: XRD results of the zeolite free mix RHA_3.5_2 after heating at various temperatures. The grey arrow indicates the backshift of the hump within thermal dehydration.

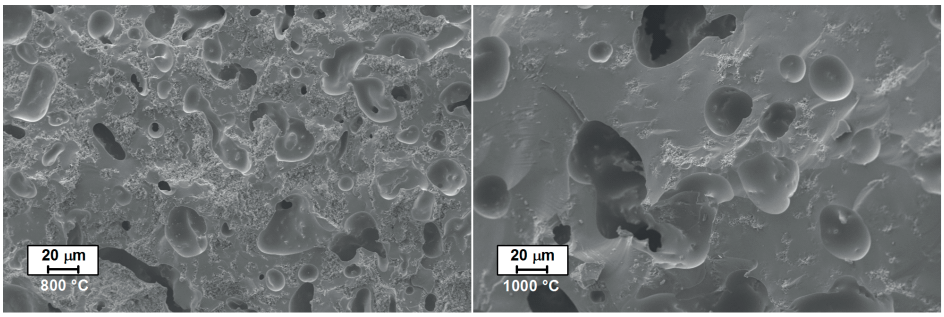

Figure. 5.16: SE SEM micrographs of crack surfaces of RHA_3.5_1 after exposure to 800 °C (left side) and 1000 °C (right side).

5.3.3. Residual compressive strength development

The (residual) compressive strength of the MS- and CR-based OPG increased after thermal treatment at moderate temperatures (200-400 °C), compared to the strength after curing (Fig. 5.17). The only exception was MS_2, which had the lowest strength after curing and no strength increase after thermal treatment as well. Although no visual changes occurred for MS_2, after treatment at ≥ 400 °C the MS_2 samples could be crumbled manually, *i.e.* strength was virtually zero. The peculiar behavior of MS_2, *i.e.* its decreased strength after thermal treatment at 100 °C and 200 °C and its complete loss of strength at 400 °C, may be related to the fact that the major crystalline phase in the specimens was HS. Some authors [40, 41] reported an increase of the volume of the unit cell of HS during thermal dehydration and assigned this behavior to destruction of the hydrogen bonding between hydrate water and the sodalite framework. Expansion of HS in MS_2, restrained by shrinking zeolite A and other compounds, probably led to excessive crack formation in these samples. This assumption is supported by the dilatometry results (Fig. 5.11), where MS_2 exhibited the lowest shrinkage of all mixes up to ca. 500 °C.

The strength of MS_3.5 reached a maximum after heating at 400 °C (23 MPa). Except for a drop at 650 °C, the performance stayed almost constant up to 700 °C. At 750 °C the compressive strength decreased below the starting value. With almost 28 MPa after a treatment at 200 °C, the MS_6 specimens yielded the highest strength but with further increasing temperature the compressive strength decreased. After heating at 650 °C the strength value decreased below the starting value, and at 750 °C large deformations occurred (Fig. 5.11). MS_3.5 and MS_6 mixes reached a maximum relative compressive strength of about 150% of the starting values (Fig. 5.17). While the performance of MS_6 continuously diminished after reaching the

maximum at 200 °C, MS_3.5 retained its performance over a larger temperature range. Both mixes had residual strength of only 10 MPa (MS_3.5) and 5 MPa (MS_6) after a treatment at 750 °C.

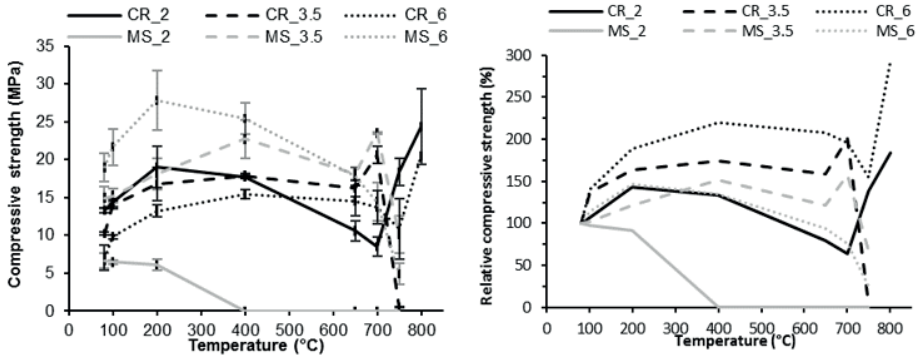

Figure 5.17: Absolute (left) and relative (right) residual compressive strengths of the MS- and CR-based OPG after 3 days of curing and residual strength after exposure at specified temperatures. Error bars represent one standard deviation in each direction.

The CR-based mixes increased in residual strength at least up to 200 °C, including the low-silica mix CR_2 that did not contain increased HS contents. These latter composites reached a maximum of 19 MPa after treatment at 200 °C (Fig. 5.17). Above 200 °C, the strength of CR_2, comparable to MS_2, decreased successively with higher treatment temperatures down to a minimum of 8.5 MPa at 700 °C (≈ 65% of the starting value). A further temperature increase above 700 °C resulted in a regain of strength, reaching the overall maximum for this series of almost 25 MPa at 800 °C. This is equivalent to 183% of the starting strength and represents the highest compressive strength of all experiments on CR-based mixes.

Since already increased shrinkage occurred at this temperature (Fig. 5.11), the initial phase assemblage started to transform and virtually no amorphous high-temperature phase formed (Fig. 5.3), most likely initial sintering reaction enhanced the density and thus the residual strength at this temperature. CR_6 reached a maximum of 15 MPa at 400 °C. CR_3.5 exhibited similar behavior as MS_3.5, *i.e.* strength decreased slightly at 650 °C, but re-increased to 21 MPa after heating at 700 °C. This value corresponds to 195% of the strength after curing. Increasing the temperature to 750 °C resulted in massive deformations and nearly total loss of strength (Fig. 5.17). CR_6 reached a relative compressive strength of 220% after heating to 400 °C. After treatment at 750 °C the strength was significantly reduced by 65% compared to the former maximum. After heating to 800 °C, a re-increase of ≈ 140% of the value measured at 750 °C was observed. At this point CR_6 reached an average strength of 20.3 MPa or 292% of the starting value. This is the highest relative

increase of all considered composites caused by the thermal treatment. Remarkable is a rather ductile behavior, in line with the XRD results and dilatometry results, but nevertheless crack inducing shrinkage (volume decrease) between 750 °C and 800 °C.

Summarizing, in all cases except for MS_2, thermal treatment at temperatures up to 200-400 °C caused the (residual) compressive strength of the MS- and CR based OPG to increase. Up to these temperatures no changes in phase assemblage and only subtle changes in crystallinity of the samples could be observed (Figs. 5.3–5.9). However, it has been previously established (Section 4.2.2) that virtually no further geopolymerization occurs in the investigated mixes after one day of curing at 80 °C. Thus, the increases in strength are probably mainly related to the subtle changes in crystallinity or to other changes, not observable with XRD. The gentle thermal shrinkage (densification) also had a positive effect on the residual strength. Significant changes in compressive strength could be observed after heating to temperatures that also caused significant changes in phase assemblage of the composites, particularly at temperatures of 700 °C and higher. The behavior at these temperatures varied considerably, depending on the silica feedstock (MS or CR) and the SiO_2/Al_2O_3 ratio of the composites. MS_3.5 and CR_3.5 exhibited a strength increase on going to a treatment temperature of 700 °C and a sharp decrease afterwards (at 750 °C). For MS_6 only a small strength increase, followed by continuous strength deterioration was observed. On the contrary, CR_2 and CR_6 exhibited a more moderate strength loss after heating to 700 °C or 750 °C, and strength regain afterwards (800 °C). For CR_2 the strength gain can be mainly attributed to sintering effects, while with CR_6 the strength increase is attributed to sintering and partial melting. Although a strength decrease was observed for MS_3.5, CR_3.5 and MS_6 in the range 700-800 °C, their residual strength evolution, *i.e.* the absence of an abrupt strength decrease up to 700 °C, is beneficial in high-temperature applications.

Fig. 5.18 shows the absolute and relative development of the residual compressive strengths of the RHA(2)-based OPG and CEM III/B after heat treatment at various temperatures up to 1000 °C. At slightly elevated temperatures (100 °C) all OPG formulations provided an increase of the initial (as-cured) compressive strength. The absolute strength of RHA_6_2 (65 MPa) was the highest in this context. This was a relative increase to 118% of the initial strength. RHA_8_1 and RHA_6_1 provided a relative increase of > 50% and > 40 %, respectively. The absolute strength of both (50 MPa and 53 MPa) was significantly lower than the one of RHA_6_2. The RHA_6 formulations provided increase up to 200 °C and remained constant within the standard deviations up to 600 °C (74 MPa), except a local maximum of RHA_6_2 and a local minimum of RHA_6_1 at 400 °C. However, RHA_6_2

remained the OPG mix with the highest residual strength at each considered temperature up to 600 °C. The absolute and relative residual strength of RHA_6_1 between 200 °C and 600 °C was always lower than RHA_6_2, but higher than the rest of the OPG specimens, indicating an optimum of the chemical composition of the regarded samples with respect to the thermal strength development. Between 200 °C and 600 °C the RHA_8 formulations provided the second highest compressive strength of the OPG formulations.

After exposure to 100 °C the geopolymer-zeolite composite RHA_3.5_1 remained the formulation with the lowest compressive strength (36 MPa) but remained constant up to 400 °C. In contrast to the composite, the zeolite free RHA_3.5_2 mix showed a decrease of the residual strength up to 400 °C (33 MPa). After 600 °C the composite provided a further slight improvement to 39 MPa, whereas the zeolite free mix remained virtually constant within the standard deviations (32 MPa), *i.e.* after the thermal dehydration ended. Thus, the absolute residual strength of the composite passed the latter one (Fig. 5.18).

The obviously increased degree of melting at ≥ 800 °C, as observed by XRD (Fig. 5.14), SEM (Fig. 5.16) and visual soft expansion/foaming enhanced an irregular specimen shape. Therefore, no compressive strength was measured for the 1000 °C samples. All OPG specimens showed dramatical decrease of the residual strength at 800 °C, except RHA_3.5_2 (Fig. 5.18). The latter mix provided a re-increase to 44 MPa and thus, it was the mix with the highest residual strength, by far. The residual strength of the other mixes varied between 8 MPa and 20 MPa. The occurring high-temperature expansion/deformation at 1000 °C was somehow lower for RHA_3.5_2 and the residual strength was thus determined to 18 MPa.

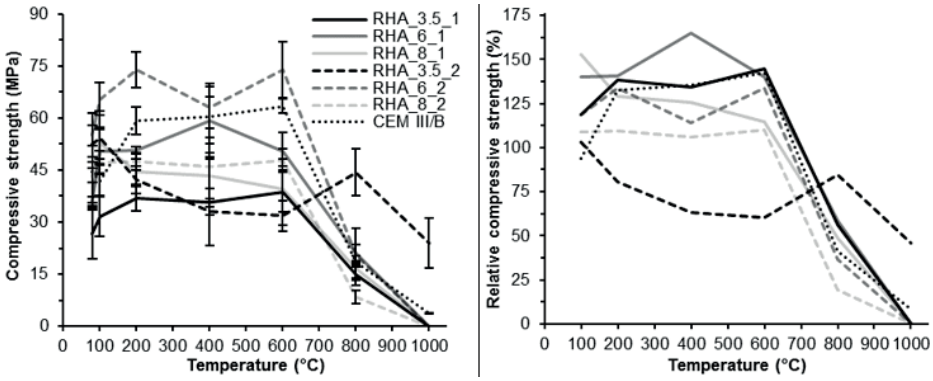

Figure 5.18: Absolute (left side) and relative (right side) residual compressive strength of the RHA(2)-based OPG specimens after exposure at specified temperatures. Error bars of the absolute strength values represent the standard deviation in each direction.

CEM III/B showed a strong increase of the compressive strength between 100 °C and 200 °C (59 MPa), and remained virtually constant up to 600 °C, providing slight further improvement (63 MPa). This was 87% of the strength of RHA_6_2 after exposure to the same temperature. Like for the OPG samples, after 800 °C also a dramatical strength decrease was observed for CEM III/B (18 MPa). The final, residual compressive strength after 1000 °C was only 4 MPa (Fig. 5.18) and extensive shrinkage occurred above 600 °C as well.

Both RHA_3.5 mixes contained the highest amount of reaction products and thus, the highest amount of water containing phases. RHA_3.5_1 contained zeolitic water, besides structural water from the amorphous geopolymer, whereas RHA_3.5_2 contained only the latter one. The zeolitic water is reversible removable without the occurrence of major structural changes of the aluminosilicate network. In contrast to that, there is a fundamental necessity of interstitial water for the structural integrity of aluminosilicate networks of C-A-S-H and N-A-S-H gels, to avoid structural alteration and decrease of the mechanical strength [38, 146, 147, 158].

RHA_6 seems to be an optimum formulation with respect to the residual strength after thermal treatment up to the high-temperature phase formation ($\geq$ 600 °C). A molar SiO_2/Al_2O_3 ratio of 6 was also the optimum regarding the relative development of the residual strength after thermal treatment up to 400 °C for MS based OPG. However, no values exist for an exposure to 600 °C (Fig. 5.17). Unreacted silica works as an inert filler until the introduction of new phase formation. Thus, lower amounts of water containing reaction products, as shown by TG (Fig. 5.2 and Fig. 5.12), mean lower effects on the overall structure due to thermal dehydration. After exposure to 800 °C the OPG specimens as well as CEM III/B underwent partial melting and/or sintering. The residual compressive strength of all OPG specimens dramatically decreased and at 750 °C for the MS- and CR-based OPG (no testing at 750 °C was conducted for the RHA(2)-based OPG). The relative development of the residual strength was quite similar to commercial CEM III/B (Fig. 5.18) and therefore the OPG of Chapter 5 can be an alternative for CEM III/B applications with respect to the thermal properties.

6. WORKABILITY OF THE MORTARS

In Chapter 3 the general fresh paste behavior of the OPG was investigated and in as well as their hardening and high-temperature resistance in Chapters 4 and 5. Since many applications of building materials include the incorporation of aggregates, this Chapter considers the general transferability of the fresh paste behavior to the fresh mortars, derived from them. Furthermore, adjustments of the workability of the fresh mortars via the composition, without the use of superplasticizers is considered.

The OPG mortars of this Chapter were produced from MS(2), CR, SA(3) and the two different aggregates RS (≤ 2 mm) and S1 (≤ 1 mm).

6.1. Experimental program

The workability of the mortars was studied by the spread flow method. In the first step, OPG mortars have been produced in accordance with DIN EN 196-1: 2005 [72] and the spread flow was determined using the Hägermann table [69]. The spread flows of a low silica mortar (MS_2), a medium silica mix (MS_3.5) and a high silica mix (MS_6), at w/b = 0.5 were determined to see whether the relative behavior of the fresh mortars is similar to those of the pure fresh pastes. After the investigation of the general comparability of pastes and mortars, further series regarding the mixing procedure, the water content and the paste content were conducted.

6.2. Results and discussion

The results of the spread flow experiments on the reference OPG mortars MS_2, MS_3.5 and MS_6 are presented in Tab. 6.1. In general, the relative behavior of the MS-based OPG fresh mortars was comparable to those of the pure pastes. At equal paste contents (by volume) and equal w/b (by mass) the spread flow decreased with increasing silica content (Tab. 6.1). MS_2 (192 mm) provided the largest spread flow and MS_6 (150 mm) the lowest, whereas the value of MS_3.5 (175 mm) was in between the values of the others. This fits quite well into the observations of the previously discussed pure pastes (cf. Section 3.2.2). In summary, the more SA included, the more the binder immediately dissolves after the addition of water, and the less low-density silica (2.21-2.26 g/cm³; Section 2.2., Tab. 2.1) included, a resulting higher volume based liquid to solids ratio is achieved. Thus, at equal paste and water contents low silica mortars provide better workability than high silica fresh mortars, as well as the fresh pastes.

Table 6.1: Composition and spread flows of the MS-based OPG reference mortars.

sample	w/b	Water (wt.%)	paste (wt. %)	paste (V %)	spread flow (mm)
MS_2	0.5	11.5	30.9	41.9	192
MS_3.5	0.5	11.4	30.7	41.9	175
MS_6	0.5	11.3	30.5	41.9	150

An MS_6-based, modified mortar with slightly decreased binder content and decreased w/b (0.4) was used for further investigations on the influence of the mixing procedure. The effect of the mixing time on the workability of the MS_6_0.4_0.9_RS mortar was investigated by comparing the spread flow of the mortar, mixed in accordance to DIN EN 196: 2005, to mortars where step by step additional three minutes (up to 5 × 3 min) at the high rotation speed were added after the standard mixing procedure. The results are shown in Fig. 6.1. Although the MS-based pastes provided no hardening at room temperature under the applied cube specimen geometry in a reasonable time, there was a clear negative trend for the MS_6_0.4_0.9_RS mortar that with increasing mixing time up to + 15 min the spread flow decreased linear from 127 mm (DIN EN 196-1) to 105 mm (DIN EN 196-1 + 15 min at high rotation speed). Additionally, an increase of the viscosities and yield stresses were observed for the pastes within one hour (cf. Section 3.2.2). Furthermore, the hardening of the OPG mortars at room temperature is accelerated compared to the pastes, as will be discussed below (cf. Section 7.2.). However, the following results are based on this mixing design (DIN EN 196-1 + 3 min), since a slight increase occurred for the shortest extend time.

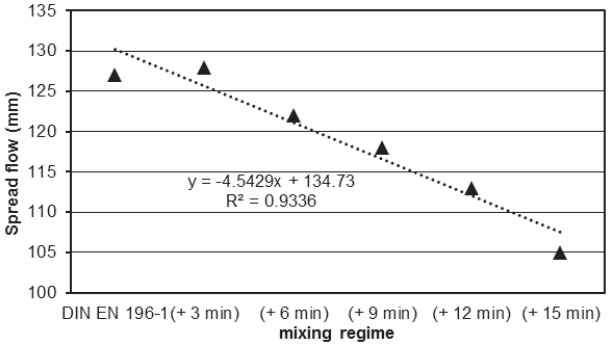

Figure 6.1: Influence of the mixing time on the spread flow of the OPG mortar MS_6_0.4_0.9_RS. The values represent the average of the measurements of two samples each.

Fig. 6.2 shows the influence of the two different sand aggregates on the spread flow of MS_6-based mortars. Due to its higher specific surface area and the accordingly

increased water demand of the S1 aggregates, for equal composed mortars, the spread flow of samples with S1 was significantly lower than with the coarse RS sand.

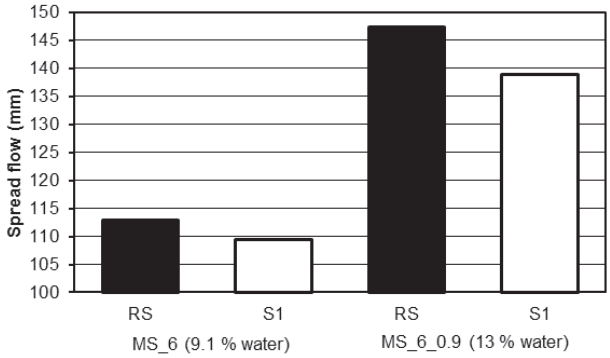

Figure 6.2: Influence of the sand aggregates RS and S1 on the spread flow of MS_6-based OPG mortars.

The presented results are representative for all other mortars. Since the spread flows of the mortars with S1 are lower but the PSD of the sand is very common in the industry, the following investigations have been conducted with the fine sand (S1). All presented spread flows can be expected to be higher if RS aggregates would be used.

Tab. 6.2 and Fig 6.3 present the spread flows of MS_6 with S1 aggregates at different water contents and constant binder content (22.8% of the solid's mass; Tab. 6.3). By increasing the water content from 9% to 16% and simultaneous increase of the paste content, the spread flow increased linearly (R^2 = 0.951) from 104 mm to 155 mm (Fig. 6.3), *i.e.* by one third (≈ 33%).

Table 6.2: Results of the spread flow measurements on MS_6 at low constant binder content with S1 aggregates (m = over all mass; s = solid's mass; b = binder mass, w= water mass, p = paste mass).

aggregates	S1	S1	S1	S1	S1	S1	S1	S1
water content w/s (wt. %)	9.1	10.0	11.0	12.0	13.0	14.0	15.0	16.0
water content w/m (wt. %)	8.4	9.1	9.9	10.7	11.5	12.3	13.0	13.8
w/b (by mass)	0.40	0.44	0.48	0.53	0.57	0.61	0.66	0.70
binder content b/s (wt. %)	22.8	22.8	22.8	22.8	22.8	22.8	22.8	22.8
binder content b/m (wt. %)	20.9	20.7	20.5	20.3	20.2	20.0	19.8	19.6
paste content p/m (wt. %)	29.2	29.8	30.4	31.1	31.7	32.3	32.9	33.4
spread flow (mm)	104	111	127	134	142	149	151	155

Tab. 6.3 and Fig 6.4 present the results of the spread flow investigations on a high binder content mortar MS_6 (49.6 wt.% of solid's mass; Tab. 6.3) with S1 ag-

gregates, *i.e.* more than double as the results presented above, and thus comparable to the binder content of the reference mortar CAC_REF (cf. Sections 2.2. and 7.2.), at different water contents ($0.30 < w/b \leq 0.40$). Again, a linear trend ($R^2 = 0.997$) of decreasing spread flows with decreasing water contents was observed from 158 mm (w/b = 0.4) to 118 mm (w/b = 0.3; Fig. 6.4). Therefore, it can be concluded that independent from the binder content there is a linear trend between the water content and resulting paste content or w/b of an OPG mortar and its workability. For the low paste OPG mortar (Fig. 6.3) the water content could be reduced to 9.1 wt.%, with respect to the solid's mass, whereas the water content could be only reduced to 13 wt.% for the high paste OPG mortar (Fig. 6.4). Furtermore, it is concluded that the higher the binder content of the dry OPG mortar, the more water is needed to provide workable consistencies, due to dominating properties of the fresh pastes. Pure MS_6 fresh pastes with w/b = 0.4 provide no reasonable workability.

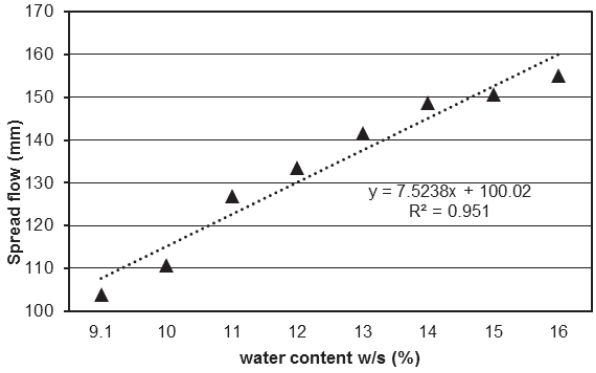

Figure 6.3: Spread flows of MS_6 mortar with S1 aggregates and low constant binder content (b/s = 22.8 wt. %) and different water contents (w/s).

Table 6.3: Results of the spread flow measurements on MS_6 with a high constant binder content and S1 aggregates (m = over all mass; s = solid's mass; b = binder mass, w= water mass, p = paste mass).

aggregates	S1	S1	S1	S1
water content w/s (wt. %)	15.0	16.1	17.5	19.8
water content w/m (wt. %)	13.0	13.9	14.9	16.6
w/b (by mass)	0.30	0.325	0.35	0.40
binder content b/m (wt. %)	49.6	49.6	49.6	49.6
binder content b/s (wt. %)	43.1	42.7	42.2	41.4
paste content p/m (wt. %)	56.2	56.6	57.1	57.9
spread flow (mm)	118	129	141	158

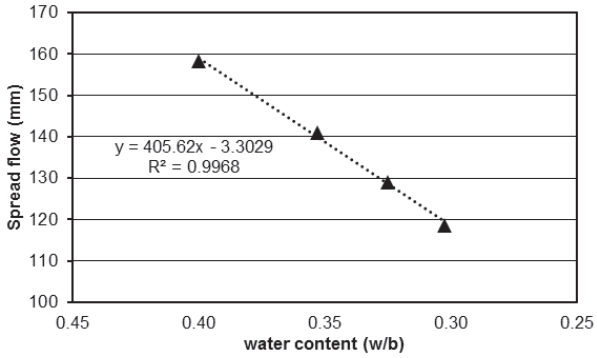

Figure 6.4: Spread flows of MS_6 mortars with S1 aggregates and constant high binder content (49.6 wt. %) and different w/b.

Tab. 6.4 and Fig. 6.5 present the results of the spread flow investigations on the MS_6 with S1 at equal water contents (11 wt. %) and different paste contents. For constant water contents and decreasing paste or binder contents the spread flow decreased linearly from 127 mm to 111 mm (R^2 = 0.9988), although the w/b ratio increased simultaneously from 0.48 to 0.67 by mass. The mortars provided very low paste contents and by further decreasing below 30.4 wt.% (Tab. 6.4). The spread flows decreased because of increasing mechanical interactions of the sand aggregates. No further decrease of the paste content was investigated, because at the lowest considered amount (24.7 wt.%) the MS_6-based fresh mortar became crumbly.

Table 6.4: Results of the spread flow measurements on MS_6-based OPG mortars, produced with S1 aggregates and 11% water (m = over all mass; s = solid's mass; b = binder mass, w = water mass, p = paste mass).

aggregates	S1	S1	S1	S1
water content w/s (wt. %)	11.0	11.0	11.0	11.0
water content w/m (wt. %)	9.9	9.9	9.9	9.9
w/b (by mass)	0.48	0.53	0.59	0.67
binder content b/m (wt. %)	20.5	18.7	16.8	14.8
binder content b/s (wt. %)	22.8	20.8	18.7	16.4
paste content p/m (wt. %)	30.4	28.6	26.7	24.7
spread flow (mm)	127	121	116	111

The investigations on the workability of the OPG fresh mortars revealed comparable relative behavior to the MS-based OPG fresh pastes (cf. Section 3.2.2.), *i.e.* with increasing silica MS content the spread flows decreased (Tab. 6.1). Mortars, prepared with the coarser RS aggregates provided, higher spread flows than mortars

prepared with the finer S1 aggregates, due to its lower specific surface area and higher specific mass. The experiments further revealed linear trends for decreasing water/ paste contents and decreasing spread flows. High paste content mortars need more water to provide a reasonable consistence, due to the increased influence of the paste properties. Thus, the aggregates provide an improvement of the workability up to a certain extent. At very low paste contents, *i.e.* when a high amount of aggregates is provided, the spread flows decreased, even when the w/b of the paste was simultaneously increased (Tab. 6.4, Fig. 6.5), since more mechanical interactions of the aggregates occur, finally resulting in a crumbly consistency.

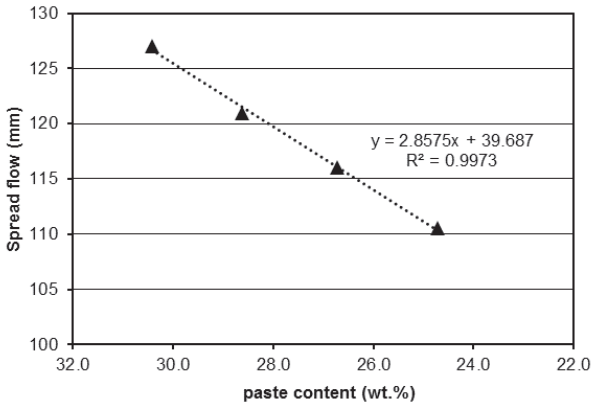

Figure 6.5: Spread flows of MS_6 mortars with S1 aggregates and 11 wt.% water, at different low paste contents.

The very different behavior of the fresh mortars was further tested *in-situ* at the head quarter of the project partner '*HERMES Technologie*'. It was found, that manual application dry mortars with rather low binder contents provide better properties. Since low paste OPG mortars are less sticky, it can be applied in various layer thicknesses (Fig. 6.6) with conventional trowels. A clean and moist trowel improves the adjustment of the surface, because a thin soapy film interface forms.

High binder contents are beneficial for spray applications (Fig. 6.6) and skidding (Fig. 6.6). A high paste content, including high amounts of silica MS, provides gentle pumping properties (Fig. 6.6) as well. Layers were built up to > 25 mm. Small grain sizes of the aggregates improved the stability of the applied layers. The mortars for the *in-situ* experiments have been initially produced with S1 aggregates (≤ 1 mm) and were further tested with even finer aggregates from a commercial supplier (grainsize distribution unknown).

Figure 6.6: Photographs of the *in-situ* application test of MS_6-based OPG fresh mortars, including: hand application (top left); skidding of a manhole (top right), spraying (bottom left) and pumping (bottom right).

7. HARDENING OF THE MORTARS

Chapter 6 showed, that the general behavior of the fresh pastes is transferable to the behavior of the fresh mortars and the workability/ applicability can be adjusted by changing the w/b and the relative amounts of pastes and the aggregates. This Chapter studies the transferability of the hardening properties to the mortars in addition to the fresh paste properties. Ground granulated blast furnace slag (SL) was used as a potential accelerator to study the influence of CaO supply to the reaction systems at elevated and ambient temperature curing.

The samples of this Chapter were produced with MS(2), CR, RHA(2), SA(3), SL and RS aggregates.

7.1. Experimental program

Preliminary experiments have been conducted on the compressive strength evolution of MS- and CR-based mortars to evaluate the transferability of the results of the previously described strength investigations of the OPG pastes (cf. Chapter 4.) to the mortars. Therefore, reference mortars with different molar SiO_2/Al_2O_3- ratios (2; 3.5; 6) were produced in accordance with DIN EN 196-1:2005 with CEN standard sand (RS) at a nominal w/b of 0.5 by mass. CR_2 and CR_3.5 were prepared equally. Only the high silica CR_6 mortar was prepared at w/b = 0.8. The reason was its poor workability, that was already observed for the pure pastes. The testing of the compressive and flexural strengths was carried out in accordance with DIN EN 196-1:2005.

Based on the results of the strength evolution of the pastes at different temperatures (cf. Section 4.4.2), it was decided to perform the first experiment on the strength of the mortars at 70 °C. It was shown, that most of the pastes provided the best compromise between early strength and final strength at 70 °C. Furthermore, the phase content showed no significant changes after one day of curing, contrary to lower (60 °C) or significantly higher (90 °C) temperatures. A relative humidity of 80% was chosen for the curing. Due to the high energy consumption related to the curing at elevated temperatures, the curing time was strictly limited to 24 hours for all considered mortars that were cured at elevated temperatures (t (50-80 °C) = 24 h).

Further considerations were conducted on the initial hardening of specific MS_6 and RHA_6-based OPG mortars, including slag containing formulations, at different elevated temperatures. Long term hardening at ambient temperature (23

°C) and different humidities (50% or ≈ 100%) with and without initial elevated temperature curing was considered up to 182 days.

7.2. Results and discussion

Fig. 7.1 presents the compressive strength results of the CR and MS-based OPG reference mortars after curing for one day at 70 °C and 80% r.H., respectively. For the MS-based mortars, the trend fits into the trend of the pure pastes. The low silica MS_2 mortar achieved the lowest strength (8 MPa), followed by the intermediate MS_3.5 mix (15 MPa) and the MS_6 mix (17 MPa). MS_2 provided higher strength than its respective paste at the same temperature, mainly due to the much less pronounced expansion of the mortar, compared to the pure paste. Compared to the pastes the strength differences of the different chemical compositions were less pronounced. The mortar prisms (40 mm Îmm 40 Î 160 mm) generally showed much less expansion during elevated temperature curing, than the respective paste cubes (20 mm Î 20 mm Î 20 mm). This is regarded to be a main reason for the lower differences. Due to the sand aggregates, the relative amount of binder is always reduced compared to the pure pastes. Low silica CR_2 (25 MPa) mortars achieved the highest strength after one day of curing at 70 °C, but CR_3.5 reached only slightly lower strength (24 MPa). Both mortars achieved significantly higher strength than the best MS-based mortars. The CR_6 mortar achieved virtually no compressive strength (0.3 MPa). This is readily explained by the significantly higher water content (w/b = 0.8) of this mortar to make it workable.

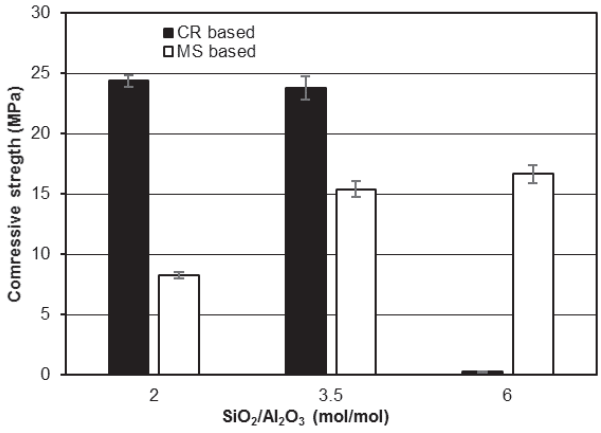

Figure 7.1: Compressive strength of the MS- and CR-based OPG reference mortars, produced in accordance with DIN EN 196-1 and cured for one day at 70 °C and 80% r. H., respectively. Samples were prepared at w/b = 0.5 (by mass), except CR_6 (w/b = 0.8). The values represent the average of three prisms (six samples) each and error bars represent one standard deviation in each direction.

The CR_3.5 mortar was investigated for its resistance against sulfuric acid attack (cf. Section 9.3) and provided the lowest resistance of all considered SL free OPG mortars. For CR_2 even less acid resistance is expected (for explanation see Section 9.3) and thus all CR formulations were excluded from further investigations. The decreased swelling of MS_2 in the mortar stage resulted in a significant strength gain but still the material showed considerable expansion. The expectable introduction of (micro)cracks has a potentially negative influence on the acid resistance, additionally to the phase content as for CR_2. Since the CR_3.5 mix showed only moderate acid resistance, a comparable behavior was expected for MS_3.5. Since a high acid resistance was a main aim of this work, the mix was also excluded. Thus, it was decided to do the further experiments only on MS_6-based OPG mortars. Furthermore, besides generally low paste contents, high MS content in the mortars is economical beneficial as $NaAlO_2$ is more expensive.

Fig. 7.2 shows the flexural and compressive strengths of different MS_6-based mortars (MS_6_1.3_RS; MS_6_1.4_RS) at w/b = 0.4 after curing at various temperatures for one day. Compared to the preliminary investigations the w/b was decreased and the paste contents have been slightly increased to 1.3 and 1.4, respectively. First experiments on slag containing mixes (10 wt.% CaO in the dry binder) were conducted (MS_6_SL_1.2_RS) at w/b = 0.37.

The two MS_6-based mortars showed comparable behavior. After curing for one day at 60 °C and 80% r.H. the mortars achieved 26 MPa (1.3) and 22 MPa (1.4). This was already significantly higher than the compressive strength of the reference MS_6 mortar (w/b = 0.5) that was cured at 70 °C (17 MPa, Fig. 7.1). Curing of those mortars at 70 °C led to an increase of the compressive strength to 32 MPa (1.3; ≈ 23%) and 30 MPa (1.4; ≈ 39%). Thus, the compressive strength of both mixes was almost double as the respective reference mortar, cured at the same temperature (Fig. 7.1). The difference between both adjusted mortars decreased compared to the lower curing temperature. By increasing the curing temperature to 80 °C an even more pronounced strength gain was observed. The compressive strength increased to 48 MPa (1.3) and 49 MPa (1.4). This was an increase of 82% (1.3) and 126% (1.4) compared to 60 °C. After curing at 80 °C the compressive strength of the mortar with higher binder content (1.4) closed in the values of the lower binder content (1.3). The same trends were observed for the evolution of the flexural strength. The flexural strength of the MS_6_1.3_RS mortar increased from 3.7 MPa (60 °C), over 4.3 MPa (70 °C), to 5.1 MPa (80 °C). This is equal to a relative strength gain of ≈ 38% from 60 °C to 80 °C. For MS_6_1.4_RS the flexural strength increased from 3.1 MPa (60 °C) to 5.3 MPa (80 °C), what is equal to a relative strength gain of ≈ 71% in the applied temperature range. Similarly, regarding the compressive

strength, the mortar with the higher binder content (1.4) closed in the values of the mortar with lower binder content after curing at 80 °C. The observed behavior is a result of the higher paste volume that needs to be reacted and with increasing temperature, more volume can react in shorter times. From 60 °C to 80 °C the ratio of flexural to compressive strength decreased from 0.14 to 0.06 (1.3) and from 0.23 to 0.11 (1.4), indicating higher relative flexural strength for higher paste content and occurring microcracks at higher curing temperature (cf. Section 8.2.3).

The slag containing mortar (MS_6_SL_1.2_RS) was investigated in the range from 50 °C to 80 °C (Fig. 7.2). After curing at 50 °C for one day, the mortar reached a compressive strength of 33 MPa, which was as high as the values of the slag free systems cured at 70 °C (Fig. 7.2). Increasing the curing temperature to 60 °C led to a gain in compressive strength of ≈ 60% to 52 MPa. This strength was higher than the maximum values of the slag free systems at 80 °C. A further increase of the curing temperature did not provide further improvements (52 MPa = 70 °C; 52 MPa = 80 °C). The flexural strength of the specimens, cured at 50 °C (4.0 MPa), was comparable to the values of the slag free mortars that were cured at 70 °C. Curing at 60 °C led to an increase of ≈ 70% (6.8 MPa). A further increase of the curing temperature had no positive effect (6.8 MPa = 70 °C; 6.7 MPa = 80 °C). The observed flexural strength at 60 °C was significantly higher than all values of the slag free systems.

The investigations showed that the slag containing mixes achieved significantly higher mechanical strength at lower curing temperatures. Curing of the slag containing mortars above 60 °C was not reasonable. The CaO rich slag works as an accelerator of the hardening and likely forms a considerable amount of C-(A)-S-H. However, with increasing curing temperature the differences of the strength performance between slag containing and slag free system decreased. The compressive strength of slag containing mortars was double as for the slag free system after curing at 60 °C. After curing at 80 °C the compressive strength of slag free mortars reached more than 90% and the flexural strength more than 80% of the slag containing mortars. Thus, the slag introduced acceleration of the hardening can be almost compensated by increasing the curing temperatures for slag-free mortars.

The following results were part of a bigger investigation series. The regarded mortars have not only been investigated for the evolution of their compressive and flexural strength but also for the shrinkage under ambient curing conditions (cf. Section 8.1.3,), their bond behavior (cf. Section 8.2.3.) and the resistance against sulfuric acid attack (cf. Section 9. 3.). Therefore, the mortars were produced using the Zyklos mixer. Tab. 7.1 and in more detail Tab. 9.1 (Section 9.2) present the composition of the mortars.

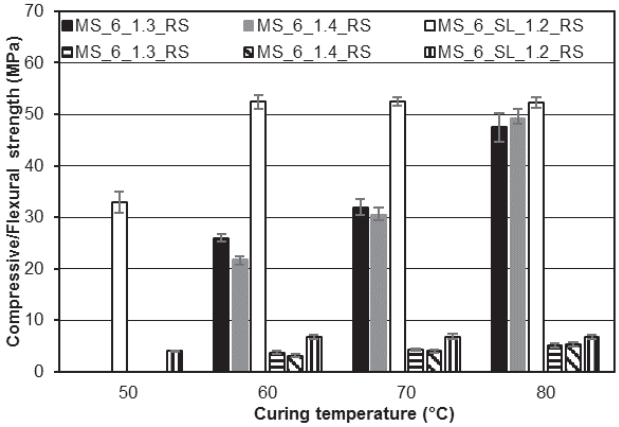

Figure 7.2: Compressive strength and flexural strength of MS_6- and MS_6_SL-based OPG mortars, cured for one day at various elevated temperatures and 80% r.H., respectively.

Table 7.1: Mix design and curing conditions of the OPG mortars and CAC_REF. The slag content provides 10 wt.% CaO in the dry binder mass.

Sample	w/b	Slag content (wt.%)	1d curing (°C/% r.H.)
MS_6_1.3_RS	0.40	-	80/80
MS_6_SL_0.9_RS	0.38	22.2	60/80
RHA_6_1.3_RS	0.40	-	80/80
RHA_6_SL_1.3_RS	0.38	21.3	60/80
CAC_REF	16% H_2O		23/25

Fig. 7.3 and 7.4 show the flexural strength and compressive strength of the OPG mortars and CAC_REF one day after the production and curing at the specific temperatures (Tab. 7.1). The previously discussed MS_6_1.3_RS mortar achieved comparable flexural strength (4.8 MPa) but considerably lower compressive strength (40 MPa) than the samples produced with the standard mortar mixer (5.1 MPa; 49 MPa). The modified slag mortar (MS_6_SL_0.9_RS) achieved 6.1 MPa flexural strength and 49 MPa compressive strength. The values were slightly lower than the ones of the preliminary mix with MS_6_SL_1.2_SL, produced with the mortar mixer. The mechanical strength of the RHA(2)-based mortars was significantly below the strength of the MS-based mortars (Fig 7.3 and 7.4). The slag-free mortar reached 4.5 MPa flexural strength and 30 MPa compressive strength and the slag-containing mortar achieved 2.8 MPa and 20 MPa, respectively. Contrary to the MS-based slag containing mortar, the acceleration and improvement of the early mechanical strength was less pronounced. An additional test on the slag containing RHA-based mortar was conducted at a curing temperature of 80 °C. In contrast

to the MS-based SL containing mortars (Fig. 7.2), there was a strength gain to 3.4 MPa flexural strength and 22 MPa compressive strength but this was only a slight improvement. Thus, it was decided to keep the lower curing temperature.

Remaining specimens were transferred to two different curing regimes (23 °C/ 50% r.H. and 23 °C/ above water (aW)) to study the further evolution of the mechanical strength at ambient temperatures but different humidity. The relative humidity aW reached virtually 100% within a short period of time (cf. Section 8.1.2.; Fig 8.1). Figs. 7.3 and 7.4 present the result of the compressive and flexural strength measurements at ambient temperature after initial curing at elevated temperature (Tab. 7.1).

After initial curing at elevated temperatures and further curing at 23 °C/ 50% r.H., the MS_6 mortar provided a compressive strength gain up to 60 MPa at an age of 28 days. For longer curing times the improvement decreased. After 91 days the final observed strength was 67 MPa (+ 68% of the initial value). For the flexural strength a comparable trend was observed. After 28 days the flexural strength improved to 6.9 MPa. The final strength after 91 days of curing was 8.1 MPa. During the curing at 23 °C/ 50% r.H., the flexural strength improved by ≈ 69%, which was almost equal to the evolution of the compressive strength.

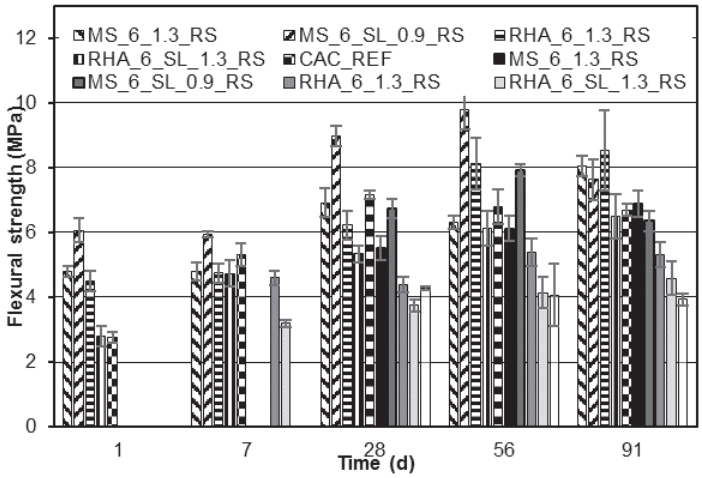

Figure 7.3: Flexural strength of the OPG mortars of Tab. 7.1, cured for one day at various conditions and CAC_REF after further curing at 23 °C/ 50% r.H. (dashed columns) or 23 °C/ aW (≈ 100% r.H.).

The MS_6_SL mortar reached 70 MPa after 28 days at 23 °C/ 50% r.H., but the final strength after 91 days significantly decreased to 62 MPa. Compared to the starting value this was still a relative improvement of ≈ 28%. A very comparable trend was observed for the flexural strength. After 28 days of curing 9.0 MPa and

after 91 days 7.6 MPa was detected. Thus, the final strength was ≈ 25% higher than the initial value after one day of curing at 60 °C. To study the reproducibility of the strength evolution at 23 °C/ 50% r.H. of the slag containing MS-based mortar and the decrease after 56 days, the series was repeated (Fig. 7.2.7). The maximum difference occurred after 56 days of curing. The first MS_6_SL_0.9_RS mortar provided a local maximum of all investigated mortars (72 MPa), whereas the MS_6_SL_0.9_RS_b mortar provided 65 MPa. After 91 days the difference in the average compressive strength finally decreased to 3 MPa. Again, a decrease was observed (59 MPa), but this decrease was much less pronounced than in the first series. The flexural strength (8.8 MPa) even passed the values of the first series and showed a further improvement between 56 days and 91 days. Thus, the compressive strength increased by ≈ 40% and the flexural strength increased by ≈ 42% during the investigations. The exorbitant difference of the strength between 28 days and 56 days is probably related to statistical errors due to inhomogeneity, since it was also the first experience with the large scale Zyklos mixer. The second series suggests a main part of the strength evolution at 23 °C/ 50% r.H. during the first 28 days, afterwards no significant changes besides a slight increase in flexural strength and a slight decrease in compressive strength was observed. After 140 days of curing at 23 °C/ 50% r.H. no further trend of decreasing compressive strength was observed but a slight re-increase to 8.3 MPa flexural strength and 62 compressive strength, indicating its general stabilization (Fig. 7.5).

RHA_6_1.3_RS showed a more continuous evolution of the compressive strength when cured at 23 °C/ 50% r.H. 7 days after production and after 6 days of curing at 23 °C and 50% r.H., the mortar reached a compressive strength of 37 MPa. After 28 days it increased to 47 MPa, after 56 days to 55 MPa and after 91 days to 65 MPa. Over the course of time the strength increased by 115%. This was by far the highest relative increase of all considered mortars. The relative development of the flexural strength was quite similar to that of the MS_6-based mortar. There was a significant increase up to 28 days (6.2 MPa) and a further increase up to 8.5 MPa after 91 days occurred. Thus, RHA_6_1.3_RS provided an increase of the flexural strength of ≈ 89%. After seven days of curing 23 °C/ 50% r.H. the compressive strength of the slag containing RHA_6_SL_1.3_RS mortar, increased by 50% to 31 MPa. With further curing time no additional major improvement occurred (33 MPa after 91 days). In contrast to this the flexural strength improved more continuously to 4.7 MPa after 7 days, 5.4 MPa after 28 days and slowing down at later ages up to 91 days (Fig. 7.3). Thus, the relative improvement compared to the initial strength was ≈ 132%. This was the biggest increase of the flexural strength of all considered systems.

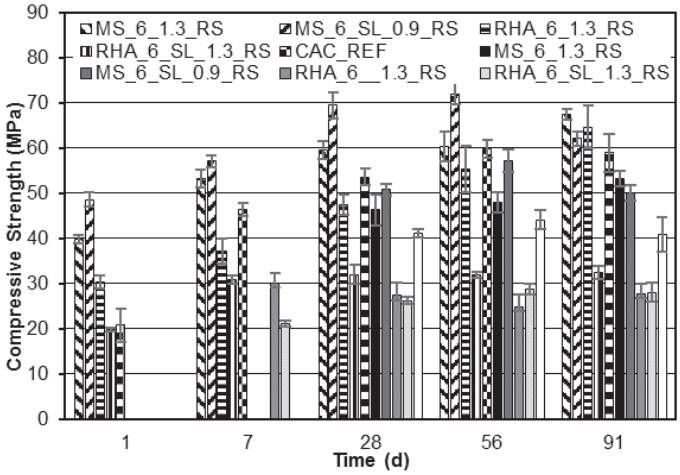

Figure 7.4: Compressive strength of the OPG mortars of Tab. 7.1, cured for one day at various conditions and CAC_REF after further curing at 23 °C/ 50% r.H. (dashed columns) or 23 °C/ aW (≈ 100% r.H.).

Curing at 23 °C/ aW (≈ 100% r.H.) led to less strength gain for all OPG mortars (Fig. 7.3 and 7.4). The time dependent strength development of the MS_6 based mortar was comparable to the less moist regime (23 °C/ 50% r.H.) but at a significant lower level. After 91 days of curing the compressive strength reached 53 MPa, what was ≈ 20% below the final strength of the drier regime. The flexural strength reached 6.9 MPa, which was ≈ 15% below the level of the 23 °C/ 50% r.H. regime.

Compared to the initial compressive strength of the slag containing MS_6_SL mortar only an improvement of ≈ 3%, to 50 MPa and regarding the flexural strength only ≈ 5% occurred. Thus, the final observed was below the strength of the slag free mix. RHA_6_1.3_RS reached 28 MPa at an age of 91 days after curing at 23 °C/ aW. This is ≈ 9% less than after curing for one day at 80 °C. No improvement of the compressive strength, but a slight decrease within the standard deviation was found. In contrast to that, the flexural strength increased by ≈ 18% to 5.3 MPa. RHA_6_SL_1.3_RS provided a compressive strength increase of ≈ 41% and reached 28 MPa after 91 d of curing. This was equal to the final strength of the slag free mix when dried above water. The flexural strength increased to 4.6 MPa (≈ 64%). The more humid conditions generally decelerated the further hardening, since the condensation reaction is constrained, without a drying effect. The respective specimens increased their mass during the storage above water (c.f. 8.1.2.).

Fig. 7.5 shows the evolution of the mechanical strength of the MS_6_SL_0.9_RS_RT (RT = room temperature = 23 °C/ 50% r.H.) when not initially cured at 60

°C for one day. No mechanical strength could be measured after one day of curing at 23 °C, because the specimens did not provide a sufficient hardening. After two days, the specimens were carefully removed from the containers and after three days the observation of the strength evolution started, providing 1.1 MPa flexural strength and 3 MPa compressive strength. After 28 days the compressive strength improved to 62 MPa and the flexural strength improved to 7.1 MPa. After 56 days the compressive strength further increased to 73 MPa. At later ages only a slight further increase was observed up to 182 days (77 MPa). This was the highest final strength of all considered mortars, as well as after 91 days, and thus higher as for all samples, that have been initially cured at elevated temperatures. As for CAC_REF and the elevated temperature cured OPG mortars, the main part of the strength evolution occurred within the first 28 days (Figs. 7.3–7.5). The main part of the evolution of the flexural strength occurred within the first 28 days as well (7.1 MPa; Fig. 7.5), reaching the strength level of the slag containing OPG samples that have been initially cured at 60 °C. This behavior was very similar to the compressive strength evolution, but a more pronounced further relative increase up to 182 days (11.6 MPa) was detected. The final observed flexural strength was the highest of all considered mortars, as well as after 91 days, as observed for the compressive strength. Especially the avoidance of expansion cracking (cf. s. 8.2.3.; Fig. 8.7) due to the lower reaction speed were the main reasons for the different strength development.

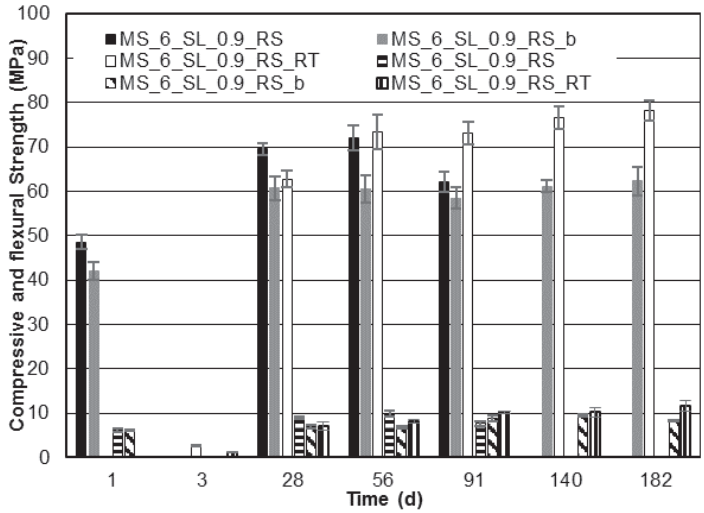

Figure 7.5: Compressive strength (colored columns) and flexural strength (dashed columns) of OPG mortars, cured for one day at 60 °C/ 80% r.H. or 23 °C/ 50% r.H (= RT). and further cured at 23 °C/ 50% r.H., respectively.

The slag free MS_6 mortar provided slower strength development at 23 °C/ 50% r.H., without initial curing at 80 °C. Samples could be carefully removed from

the molds after 4 days. The initially determined values after 7 days included 1.6 MPa for the flexural strength and 8 MPa for the compressive strength. As for the slag containing system a strong increase of the mechanical strength occurred after 28 days (25 MPa and 4.6 MPa) and after 56 days a further significant increase to 39 MPa for the compressive strength and 6.1 MPa for the flexural strength was detected, what matches the initial strength of the 80 °C sample (Fig. 7.4). After 56 days, the strength improvement decreased and after 91 days a final flexural strength of 6.9 MPa and compressive strength of 42 MPa was measured.

The investigation on the initial compressive strength of the OPG-based mortars after curing at elevated temperature (70 °C) revealed a comparable behavior to the pure pastes, with respect to the chemical composition (*i.e.* the SiO_2/Al_2O_3 ratio). For MS-based OPG mortars the differences were much lower than for the pure pastes. The main reason was the much lower expansion during hardening. CR-based OPG mortars with high silica content (CR_6) could not be prepared below w/b = 0.8 and the mortar provided almost no strength after curing. In contrary to the pastes, the slag free MS_6-based mortars provided sufficient hardening also at ambient conditions (23 °C/ 50% r.H.) in reasonable times. A major reason are the included aggregates, that work as nucleation sites and thus accelerate the hardening. Increasing the curing temperature to 80 °C resulted in a major increase of the initial mechanical strength of slag free mortars compared to 60 °C and 70 °C. The sample volume of a mortar prism is 12 times higher than of the paste cubes and thus much more volume must be cured. The sample geometry by means of surface to volume ratio further influences the hardening speed and the resulting properties after elevated and ambient temperature curing. As will be seen below for the bond behavior, the mortar coatings for the investigation of the bond behavior provided even faster hardening than the prisms. The addition of slag, in order to provide a total CaO content of 10 wt.%, led to a major increase of the initial strength compared to the slag-free MS_6 mortar, even below 80 °C. Samples cured for one day at 60 °C provided comparable and slightly higher initial strength than the MS_6 mortar after curing at 80 °C, likely due to the formation of additional C-(A)-S-H phases.

Without elevated temperature curing, slag-containing specimens could be removed from the containers after 2 days, whereas the slag-free mortars could not be removed until an age of 4 days. After 182 days of curing at ambient conditions the slag-containing MS_6_SL-based mortar provided the highest mechanical strength of all considered OPG mortars. The main part of the strength evolution occurred within the first 28 days, with and without initial elevated temperature curing (Figs. 7.3-7.5). For the samples, that were initially cured at elevated temperatures, the further strength evolution was much less pronounced. The main reasons therefore

are the much higher initial strength because of the further reacted specimens at early ages. For the RHA(2)-based mortars much lower initial strength after curing at elevated temperatures was observed and a much less pronounced effect of the slag addition was observed. Especially the slag-free mortars also provided a much more pronounced increase of the mechanical strength during further curing at 23 °C and 50% r.H., ending up at equal final levels as the slag free MS_6 mortar after 91 days. The observed compressive strength of the initially elevated temperature cured OPG mortars (up to > 60 MPa) and only ambient temperature cured (up to > 70 MPa) after 91 days matches the strength levels of many conventional geopolymer systems (cf. e.g. [16, 171-174]). For the more humid conditions at 23 °C and above water (≈ 100% r.H.) much lower or even no further strength gain occurred. This highlights the importance of the release of at least certain amounts of water for the strengthening, since the reaction is mainly a condensation (geopolymers), whereas the hardening reaction of hydraulic cements or alkali-activated slags is mainly a hydration reaction and this reaction is only minor represented in the slag-containing OPG mortars.

8. SHRINKAGE AND BOND BEHAVIOR OF THE MORTARS

Chapters 6 and 7 proved the general transferability of the properties of the fresh and hardened pastes to the mortar state and showed additionally that curing without elevated temperatures can have a positive effect on the mechanical strength at later ages, because the introduction of microcracks is decreased. For possible applications, such as as acid-resistant or heat-resistant coatings or repair mortars, not only the absolute strength but also the shrinkage/ expansion behavior and the bond behavior are of major importance, especially for the durability of the applied systems. Therefore, this Chapter studies the deformation behavior of the OPG mortars at different storage conditions and the bond behavior in dependence of the composition and the curing conditions.

The OPG mortars of this Chapter were produced with MS(2), RHA(2) and SA(3), as well as RS or S1 aggregates.

8.1. Shrinkage

8.1.1. Introduction

The shrinkage of AAM is a complex issue. In this context many studies have been conducted on the shrinkage of alkali-activated slags (AAS) and fly ash-based geopolymers or composites [62-65, 147, 175-180], as well as geopolymers derived from metakaolin or other pozzolans [146, 158, 181] at ambient temperature. When compared to OPC-based pastes, mortars or concretes, AAM often show significantly higher shrinkage [62-65]. Especially AAS were found to be strongly affected from shrinkage in some cases [65, 180]. In SL-FA-based composites the shrinkage was found to increase with increasing slag content [64]. Cracking due to shrinkage is considered to be a major reason for the rather low longterm strength evolution of specific FA-based geopolymers [147]. A few promissing shrinkage retarding agents (SRA), such as polypropylene glycol-based SRA were proposed, that where able to reduce the shrinkage of AAS up to 85% without affecting the mineralogical composition of the reaction products [178]. Others found a positive effect of TiO_2 for the shrinkage behavior of AAS [179]. Chi et al. reported an improvement of the shrinkage behavior of AAS mortars by increasing the sand to slag ratio [62].

Many authors observed a dependence of the shrinkage on the nature and the content of the activator solution. With increasing activator concentration, the degree of reaction, the initial compressive strength as well as the deformation due to shrinkage

increased [64, 146, 158]. A significant increase in shrinkage often correlates with an increase of alkalis in the system, whereas potassium seems to have less negative effects than sodium [146, 147, 158, 180]. A reason may be the lower charge density associated with potassium, resulting in a less strongly bond hydration sphere and thus a more stable bond to the aluminum sites than with sodium [158]. Different observations have been made on the Si/Na modulus of activator solutions. While some authors found a degradation of the shrinkage behavior with increasing Si/Na modulus [146, 158], another study observed a contrary trend [147]. An increasing shrinkage was attributed to an increased gel formation and thus a larger amount of structural (interstitial) water needed to avoid shrinkage [158]. Few authors found no negative effect of the water content of the fresh pastes on the critical content of structural water, necessary to avoid shrinkage due to moisture loss [158], while others found a degradation [146, 147]. The total porosity and especially the amount of mesopores with a diameter of 1.25–25 nm (IUAPC, [63]) are often a significant difference between AAM and OPC. Whereas the relative content of mesopores of comparable designed concretes was found to be only about 36% for OPC, it ranged from 60 to 80% for FA-SL composites. A higher related cappilar stress due to the loss of moisture was conlcuded to be an important reason for the more pronounced shrinkage compared to OPC [63, 180].

A very important role for the shrinkage of alkali-activated materials is attributed to the curing conditions. Curing at elevated temperatures was found to have a positive effect [62, 146, 147, 175, 181]. Significant improvements for alkali-activated FA and FA-SL composites have been achieved by increasing the curing temperature from RT to 40–80 °C [147, 175]. By increasing the curing temperature, the time to achieve no further shrinkage at ambient conditions can be decreased [175]. A very positive effect was found from hydrothermal treatment. The very early shrinkage of pumice-type pozzolan-based geopolymers was increased, but the rate decreased to virtually zero after a short time [146]. Besides a decrease of the shrinkage, curing at elevated temperatures usually improves the mechanical strength as well [62, 147, 175, 181]. The improvement of the shrinkage behavior of MK-based geopolymers, not only by curing at elevated temperature, but also by exchange of MK with a CaO-rich parawood ash was observed by Tonayopas et al. [181]. A very low relative humidity (11 %) was found to cause less drying shrinkage, although more moisture loss occurred than under more humid curing conditions but a significant part of the drying effect was reversible. The authors assumed that under dry conditions interlayer water is reversibly removed, whereas curing under high humidity led to a structural reorganization of the gel in AAS [180].

The literature review shows that shrinkage of AAM is a very complex topic. Many factors are influencing the shrinkage, that is usually more pronounced than for conventional OPC-based systems. Depending on the reaction system several adjustments can help to improve the behavior. Much less is known about the ambient temperature shrinkage of silica-based OPG. Therefore the following Section presents general results on the shrinkage of the considered OPG-based mortars.

8.1.2. Experimental program

The composition (Sections 7.2.; Tab. 7.1; and 9.2.; Tab. 9.1), mixing (Zyklos mixer) and curing of the OPG mortars was similar to that presented in Section 7.2. The measurement of the shrinkage/expansion at ambient temperatures was conducted on standard mortar prisms (40 mm Î 40 mm Î 160 mm). OPG samples cured at ≤ 60 °C have been transferred into polyvinyl chloride (PVC) based containers without necessity of coating it with scotch tape but only with formwork oil to avoid bonding between container and mortar. Through holes at the face side, pins (penetration depth = 5 mm) for the later shrinkage measurements were introduced before the filling of the fresh mortars. Mortars that were cured at 80 °C were cast into conventional steel containers that were coated with scotch tape and additionally covered with formwork oil. The pins have been glued to the face sides after the initial elevated temperature curing (24 h), using a two-component adhesive. CAC_REF specimens were prepared as described for OPG mortars that were cured at 60 °C. OPG were initially cured for one day at 80 °C (slag free OPG) or 60 °C (slag containing OPG) and 80% r.H., respectively. CAC_REF was cured at 23 °C/aW for one day.

Subsequently the initial length was measured, *i.e.* at an age of ≈ 25 hours, and afterwards the mortars were transferred to the two different curing regimes 23 °C/ 50% r.H. in a chamber with climate conditioning or 23 °C/ aW in the same chamber but in sealed plastic boxes until an age of 91 days, similar to the conditions of the long term strength investigations in Section 7.2 (Figs. 7.3 and 7.4). The relative humdity for the aW storage was found to be stabalized above 99% (≈ 100 %). The relative humidity was documented over more than 10 days using a Ahlborn Almemo® 2590 device and an Ahlborn Almemo 2890-9 device (introduced after 135 hours of start of the measurement) to provide reliable results (Fig. 8.1).

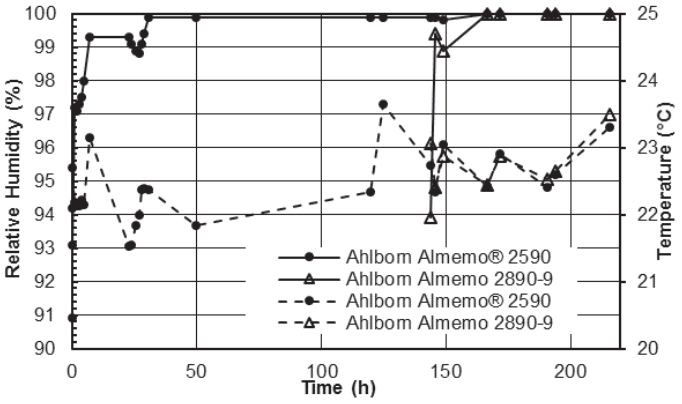

Figure 8.1: Relative humidity (full lines) above water (aW). Dashed lines refer to the additionally documented development of the ambient temperature. Ahlborn Almemo 2890-9 was additionally introduced after a measurement time of ca. 135 hours for verification.

8.1.3. Results and discussion

The OPG mortars and CAC-REF showed significantly different behavior in the different humidities (Figs. 8.2 and 8.3). CAC_REF provided the most significant shrinkage when stored at a relative humidity of 50%. After 91 days a final shrinkage of 1.94 mm/m was detected and over the time vertical shrinkage cracks were introduced, visuable at the surface of the prisms. The pronounced shrinkage is a major reason for its comparably low bond strength (Section 8.2.; Fig. 8.7) and probably also for the slight decrease of the flexural strength over the time at the same curing conditions (Section 7.2; Fig. 7.3). The final observed shrinkage of CAC_REF at 23 °C and 50% r.H. was more than double the maximum shrinkage, observed for the OPG mortars. After 91 days of curing at 50% r.H. the slag free MS_6_1.3_RS mortar provided a shrinkage of 0.90 mm/m (Fig. 8.2). All other OPG mortars provided even less shrinkage under the same conditions. MS_6_SL_0.9_RS provided a shrinkage of only 0.19 mm/m and the absolute shrinkage of the RHA-based mortars was negligible (Fig 8.3).

All OPG mortars achieved the requirements of the *„Richtlinie für die Prüfung von Mörteln für den Einsatz im Sielbau"* of < 0.9 m/mm at an age of 28 days [182], when cured at 23°C and 50% r.H., respectively. The mortars also achieved the requirements of the DAfStb guidline "*Schutz und Instandsetzung von Betonbauteilen*" (RiliSIB) [183] of < 0.9 mm/m when cured at 21±2 °C and 60±10% with respect to Appendix A in DIN EN 12617-4:2002 [73]. Even after 91 days no OPG exceeded a shrinkage of 0.9 m/mm. The requirements for the various repair mortars reported

in DIN 19573 "*Mortars for construction and rehabilitation of drains and sewers outside buildings*" reach from ≤ 2 mm/m to ≤ 4 m/mm after 91 days at 20 °C/ 65% r.H. [76]. This means even under the considered warmer and less moist conditions (23 °C/ 50% r.H.), all OPG mortars remained significantly below the shrinkage requirements. The main part of the shrinkage of the OPG mortars, except the RHA_6-based mortar, occurred within the first 21 days, afterwards the shrinkage slowed down and reached a plateau. In contrast to that RHA_6_1.3_RS provided a continous shrinkage over the time of 91 days, but at negligible low niveau as (Fig 8.3). The mix also provided a more continous gain in compressive strength (cf. Section 7.2; Fig. 7.4) at the same conditions, compared to the other OPG mortars.

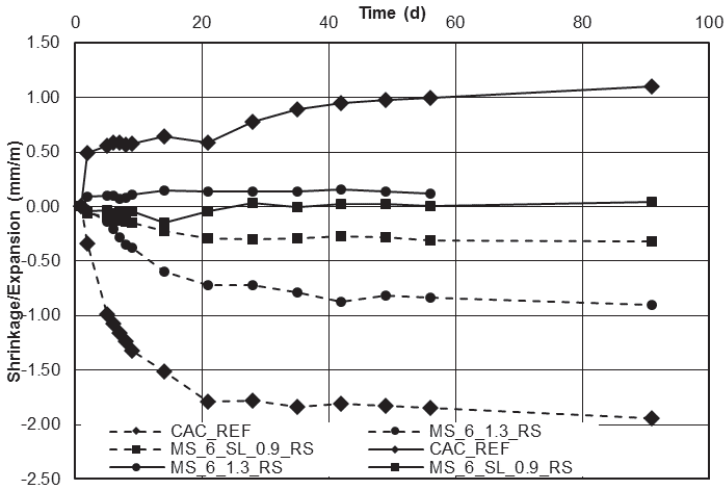

Figure 8.2: Shrinkage/ expansion of the investigated MS-based OPG mortars and CAC_REF under different curing conditions (full lines = 23/aW; dashed lines = 23 °C/ 50% r.H.) until an age of 91 days.

Curing under more moist conditions (23 °C/ aW) resulted in an inverse trend (Fig. 8.2 and 8.3). All mortars provided expansion but the expansion was less pronouncend than the shrinkage at the lower relative humidity. After 91 days CAC_REF reached an expansion of 1.10 mm/m. This was more than eight times higher than the maximum expansion detected for the OPG mortars. MS_6_1.3_RS reached 0.12 m/mm expansion after 56 days (last measurement). The slag containing MS_6_SL-based mortar provided an expansion of only 0.04 mm/m after 91 days of storage and after 28 days almost no further changes occurred. Like the shrinkage under the dry storage conditions, the expansion under moist conditions was negligible for the RHA_6 and RHA_6_SL-based mortars (Fig. 8.3). After 91 days the expansion of slag free and slag containing RHA-based mortars was less than 1×10^{-4} mm/m. All mortars achieved the requirements of DIN 19573, that demands

an expansion of < 1 mm/m for repair mortars at an age of 91 days [76]. Furthrmore, all GPM fitted into the requirements of Rili-SIB, which demands an expansion of < 0.3 mm/m after 28 days [183]. Even after 91 days, again all OPG fullfilled the 28 days requirements by far.

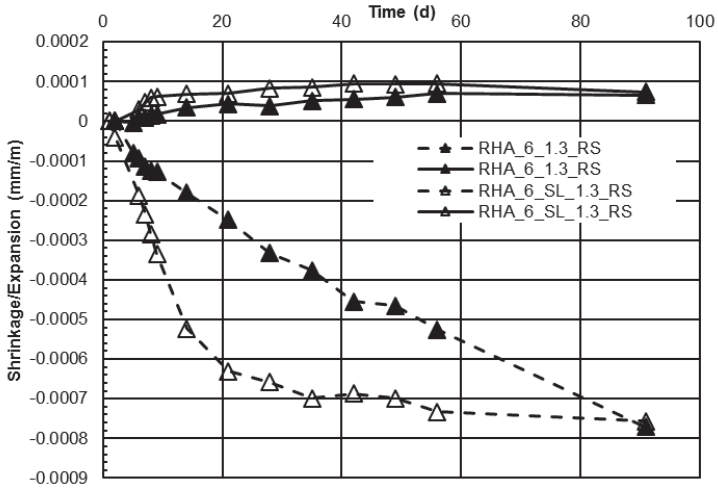

Figure 8.3: Shrinkage/ expansion of the investigated RHA(2)-based OPG mortars at different curing conditions (full lines = 23/aW; dashed lines = 23 °C/ 50% r.H.) until an age of 91 days.

Fig. 8.4 shows the deformation (shrinkage/expansion) of the mortars in dependence of the change in mass. All specimens that were stored at 23 °C/ 50% r. H. provided mass loss, whereas all specimens showed a mass gain when cured aW. After reaching a mass loss of more than 1.5 wt.%, the shrinkage of the CAC_REF strongly increased. By removing another wt.% (= 2.5 wt.%), the shrinkage increased more than four times (≈ 1.5 mm/m). In contrast to that, the absolute shrinkage of the OPG mortars was significantly lower but the mass changes were more pronounced (Fig. 8.4). The MS-based mortars, both slag-free and slag-containing system, at a comparable mass loss (≈ 1.5 wt.%) provided a shrinkage of < 0.10 mm/m. By increasing the mass loss up to 2.5 wt.% shrinkage of < 0.15 mm/m was measured, one tenth of CAC_REF at the same mass loss. At a mass loss of ≈ 3.5 wt.%, the shrinkage increased to ≈ 0.7 mm/m. An increase of the shrinkage rate of MS_6_SL_0.9_RS was observed at an even higher mass loss. By increasing the drying mass loss above 3.2 wt.% the shrinkage increased from 0.14 m/mm to 0.22 mm/m (- 3.5 wt.%). Comparable trends have been observed for the very low shrinkage of the RHA-based specimens but at negligible shrinkage of only ≈ 8×10^{-4} m/mm (≈ -3.8 wt.%).

When stored aW (≈ 100% r.H.), CAC_REF provided a dramatical increase of expansion especially at low mass gain and corresponding low curing times. Up to

a mass increase of ≈ 0.35 wt.%, the specimens expanded on average ≈ 0.8 mm/m. With further increasing moisture gain the expansion curve flattened. The final observed moisture gain was equal to a mass increase of 1.35 wt.% (1.10 mm/m). This was by far the most significant expansion but the lowest mass gain of all considered mortars. In contrast to that, MS_6_1.3_RS provided an expansion of 0.15 mm/m (+ 2 wt. %) and with further mass gain up to 3 wt.% no further increased expansion occurred. MS_6_SL_0.9_RS showed expansion especially at low mass changes up to a moisture gain of ≈ 0.25 wt.% (= 0.03 mm/m). By further increasing moisture content up to the maximum observed mass gain (= 1.75 wt.%) the expansion remained almost constant. Only a small further increase to 0.04 mm/m was detected. For the RHA-based mortars the most pronounced expansion occurred up to a moisture gain of ≈ 1 wt.%. Up to the maximum observed moisture gain of 2.96 wt.%, only a slight furtherer increase of the expansion was observed for the mortar RHA_6_SL_1.3_RS. RHA_6_1.3_RS provided a maximum moisture increase of 2.75 wt.% in the respective period. As mentioned above the absolute expansion was negligible compared to all the other considered mortars.

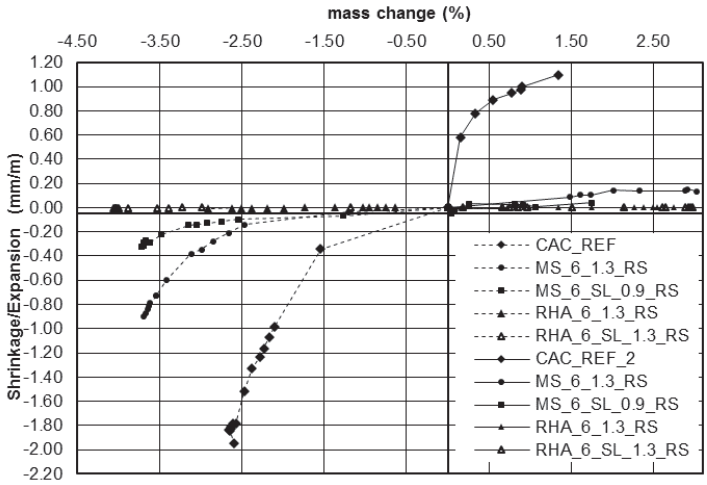

Figure 8.4: Shrinkage/ expansion of the investigated OGP mortars and CAC_REF in dependence of the mass change (full lines = 23/aW; dashed lines = 23 °C/ 50% r.H.).

The low shrinkage of the OPG mortars under the dry conditions, connected with the increased mass loss compared to CAC_REF suggests the main part was atributed to physically bond water [155, 158]. Much more water was released from the OPG mortars, with much less pronounced shrinkage. Apart from the slag-free RHA-based OPG mortar, all specimens reached a plateau, *i.e.* the further shrinkage became virtually zero. This suggests no further significant shrinkage at 23 °C and 50 % r.H. after 91 days, with the exception of the RHA_6-based mortar. For the

other OPG mortars the main part of the shrinkage occurred within the first 21 days after the production. As reported in Section 7.2, the respective specimens for the investigation of the compressive strength provided the most significant strength gain up to an age of 28 days (Figs. 7.3 and 7.4), when cured for one day at elavated temperatures.

Furthermore, the results fit quite well into the observations of the thermal dehydration (cf. Section 5.3.). In the dehydration range (up to 400 °C), the MS-based OPG pastes showed only low shrinkage (Section 5.3.; Fig. 5.11). This was attributed to the loss of physically bound water from the significant amount of zeolites in the reaction products of the geopolymer-zeolite composites and the filler function of unreacted silica in specific formulations. The low paste contents of the OPG mortars (< 38 wt. %) compared to CAC_REF (> 50 wt.%) is another factor that contributes to the excellent deformation behavior, since the aggregates (quartz) are not affected from shrinkage. In this context the slag-containing MS-based mortar (≈ 30 wt.%) provided the lowest paste content, which may have also contributed to its further improved shrinkage behavior compared to MS_6_1.3_RS, as well as the lower applied w/b ratio of 0.38 compared to 0.40 (Section 7.2, Tab. 7.1). The comparably high content of aggregates also provides economic benefits.

Curing under the more humid conditions (23 °C/ aW) resulted in mass gain and expansion of all mortars. All OPG mortar specimens reached a plateau, i.e the expansion became virtually constant after a certain time. This suggests no further significant expansion under the regarded conditions after a certain time. The main part of the shrinkage occurred within the first 10 days after the production. The expansion at the humid conditions was even less pronunced than the drying shrinkage under the dry conditions and the increase in mass is mainly attributed to the incorporation of physically bound water. Also the gain in compressive strength was lower than for the dry conditions (Section 7.2.; Fig. 7.3 and 7.4).

8.2. Bond behavior

8.2.1. Introduction

As reported before, the steel containers for the preparation of standard mortar prisms needed to be covered with adhesive tape to avoid the formation of an irreversibly bond composite of the OPG mortars and the containers during hardening, especially at elevated temperature. These observations are supported by few authors that reported on promising bond behavior between AAM and steel reinforcements like

beams and bars, as the bond strength exceeded those of conventional cementitious materials [184-187].

In context of the bond behavior of AAM to conventional cementitious substrates, Zhang et al. reported high bond strength up to 3 MPa for MK- and FA-based GPM to OPC-based substrates at ambient temperature and remarkable residual strengths up to 300 °C [18]. Alanazi et al. found excellent bond behavior (3.8 MPa) between MK GPM and fresh cementitious substrate, even above the bond strength of Ultra High Performance Concrete (UHPC), which makes the materials promising as repair mortars. When applied to a deteriorated substrate that was exposed to HCl, the bond strength was degraded and failure occurred in the interface layer [17]. Kahlid et al. [188] investigated the bond behavior of fibre-reinforced (FR) FA-SL composite concretes to FR polymers with different epoxy adhesives interfacial layers and found no positive effects of fibre-reinforcement to the bond strength of the composites. Tamburini et al. [189] reported on excellent adhesion strength of FA-SL composites based grouts on soft mud bricks and extruded clay bricks, investigated by pull-off tests. Furthermore, a negative effect of fibre-reinforcement, with respect to the bond strength was observed. Song et al. [190] found promising bond strengths of GP mortars derived from FA, SL and RHA up to 1.6 MPa, where the increase of the RHA content had a positive effect on the bond strength.

This shows, that AAM can provide good bond behavior. No literature was found for the bond behavior of OPG on conventional concretes. As the application of the considered OPG, e.g. as repair mortars, requires good bond strength on concrete substrates too, the general bond behavior, will be studied in the following Section.

8.2.2. Experimental program

For the determination of the bond strength the mortars were applied on standard MC 0.40 (w/b= 0.40) concrete specimens or MC 0.90 (w/b = 0.90) concrete specimens with a maximum grain size of the aggregates of 8 mm and a cement content of 410 kg/m^3 (MC 0.40) and 210 kg/m^3 (MC 0.90), respectively, in accordance with DIN EN 1766:2017 [75]. To investigate the applicability of the mortars under different conditions, specific samples were applied on horizontally oriented concrete specimens (marked with "1") and additionally on vertically oriented specimens ("2"). No reference number in the graphics means only the horizontally oriented specimens were used for application of the mortars. The fresh mortars were applied to a thickness of 8 mm.

The composition of the mortars is similar to that presented in Section 7.2. (Tab. 7.1) and Section 9.2 (Tab. 9.1). Additionally, a sample from the workability investigations (Section 6.2; (w/b = 0.59) Tab. 6.4), referred to MS_6_0.87_S1, was prepared. Because of the moderate amount of needed material, all OPG mortars were produced with the Eirich Intensive Mixer (Type RV02) as described in Section 2.3.4. CAC_REF was produced in accordance with the instructions of the supplier.

No additional bridging agents or adjustments of the fresh mortars for the application of the initial interlayer were conducted to exclude further effects. Depending on the consistency of the mortars, the interlayer was applied manually either by hand or with a brush. The rest of the material was applied with conventional trowels. The surface of the fresh mortars was adjusted with a steel ruler. After a specified time (2–4 hours) the specimens were removed from the molds and either transferred to an oven with climate control (60 °C or 80 °C; 80% r.H.) or stored in accordance with DIN EN 1542:1999 at 23 °C, covered with plastic film (Appendix A.1.2 [74]). After 24 hours the specimens that were cured at elevated temperatures have been removed from the oven. All specimens were then sealed with plastic foil and stored for further two days at 23 °C as suggested in DIN EN 19542:1999 (Appendix A.1.2). At an age of three days after the production, the specimens were removed from the plastic film and further stored at 23 °C/ 50% r.H. or 20 °C/ 65% r.H. in a climate chamber until testing, respectively.

8.2.3. Results and discussion

Fig. 8.5 present the results of the pull-off tests for various OPG mortars, cured at elevated temperatures for one day and further cured at 23 °C and 50% r.H., at an age of 28 days after production. For all MS_6-based mortars, that were cured at 80 °C for one day, 100% of the failure occurred in the mortar. Pull-off strengths of 0.55–0.60 MPa were measured for MS_6_1.3_RS, although the mortar provided ≈ 60 MPa compressive strength in the same age (28 days), as shown in Section 7.2. (Fig. 7.4). By changing the sand (S1), decreasing the binder content and increasing the water content (MS_6_0.87_S1) the bond strength decreased to virtually zero (Fig. 8.5). MS_6_SL_0.9_RS provided bond strengths of 1.10–1.25 when cured for one day at 60 °C. This was double the values for the slag free MS-based mortar when cured at 80 °C temperatures. Similarly, for the slag-free mix, 100% of the failure occurred in the mortar. Thus, the actual bond strength between OPG mortar and MC 0.40 concrete was always higher than the detected pull-off strength.

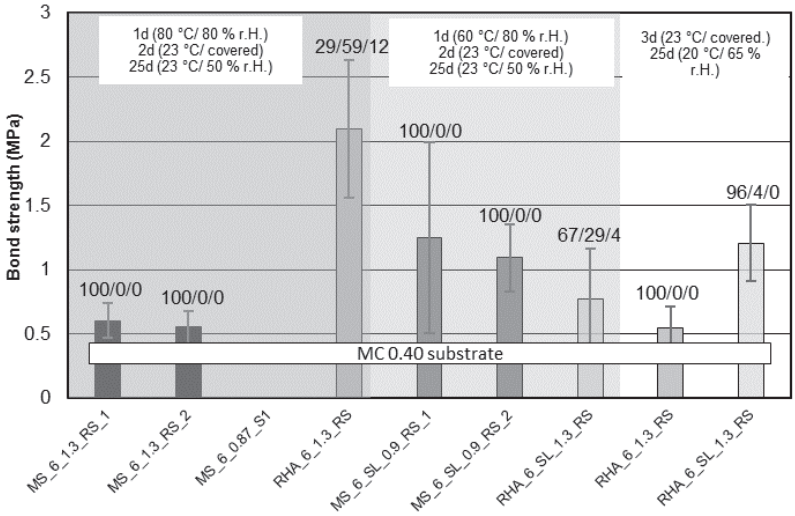

Figure 8.5: Results of the pull-off tests of different OPG mortars on MC 0.40 concrete, after initial curing at elevated temperatures. The values X/Y/Z refer to the percentage of the failure origin (X = OPG mortar/ Y = between X and Z; Z = concrete). Each column represents the average of four pull-off tests and error bars represent one standard deviation in each direction.

In the contrary, RHA_6_1.3_RS reached almost 2.1 MPa after initial elevated temperature curing. The main part of the failure (≈ 60 %) occurred in the interface between substrate and mortar, about 30% occurred in the mortar and about 10% in the substrate (Fig. 8.5). It was the only OPG mortar with a dominating failure occurrence in the interface. The detected bond strength of the slag containing RHA(2)-based mix (RHA_6_SL_1.3_RS) provided 0.77 MPa, when cured for one day at 60 °C. This was significantly below the values of the slag containing MS-based mix but still higher than the values of the pure MS-based mix. Similarly, for the slag-free RHA(2)-based mix, parts of the failure occurred in the interlayer, but only ≈ 30%. The main part of the failure (≈ 67%) occurred in the mortar.

Fig. 8.6 presents the results for the OPG specimens and CAC_REF that were only cured at 23 °C and 50% r.H., respectively. The pull-off strength of MS_6_1.3_RS increased more than 400% to 2.85–3.12 MPa compared to specimens that were initially cured at 80 °C, although the mortar only provided 39 MPa (two thirds of the strength of the sample, that was initially cured at 80 °C at the same age). Still 100% of the failure occurred in the mortar. The pull-off strength of MS_6_SL_0.9_RS increased to 3.15–3.67 MPa. This was an increase of more than 300% compared to the sample that was initially cured at 60 °C for one day. In this case virtually 100% of the failure occurred in the concrete specimen. This means the actual bond strength between OPG mortar and concrete was still higher, than the observed

values and the bond strength between MS_6_SL_0.9_RS and concrete was higher than the ultimate tensile strength of the concrete specimens (MC 0.40).

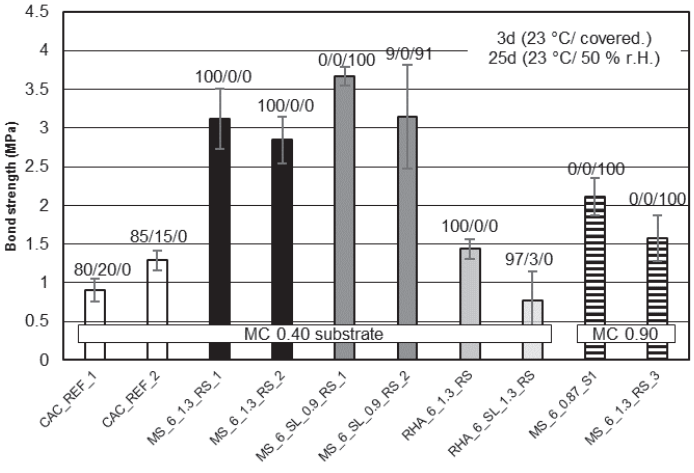

Figure 8.6: Results of the pull-off tests of different OPG mortars and CAC_REF on MC 0.40 and MC 0.90 concrete, after only curing at 23 °C and 50% r.H., respectively. The values X/Y/Z refer to the percentage of the failure origin (X = OPG mortar/ Y = between X and Z/Z = concrete).

In contrast to the previous mixes, the pull-off strength of RHA_6_1.3_RS decreased (1.43 MPa) without initial elevated temperature curing. The pull-off strength of RHA_6_SL_1.3_RS was equal to the values observed after curing at 80 °C. In both cases, virtually 100% of the failure occurred in the mortar.

CAC_REF provided between 0.90 MPa and 1.29 MPa after curing at 23 °C/ 50% r.H. and the main part of the failure occurred in the mortar but 15–20 % of the failure occurred in the interface between mortar and substrate. The determined bond strength of CAC_REF under the conditions 23 °C/ 50% r.H. was lower than for all considered OPG mortars, except the slag-containing RHA_6_SL-based mortar (Fig. 8.6).

Specific specimens of the RHA(2)-based series were stored at 23 °C for three days and further cured at 20 °C and 65% r.H. until testing. This led to a significant decrease of the bond strength for RHA_6_1.3_RS to 0.55 MPa. RHA_6_SL_1.3_RS reached even higher bond strength (1.20 MPa) than the according specimen that was cured at 60 °C for one day. In both cases the failures virtually occurred only in the mortars. Additional tests were conducted for MS_6_1.3_RS and MS_6_0.86_S1 on MC (0.90) concrete specimens (Fig. 8.6). For MS_6_0.87_S1 the biggest increase of the pull-off strength of all considered samples was detected. After curing at 80 °C the bond strength was virtually zero (Fig. 8.5), but after curing only at 23 °C the

average detected bond strength was > 2.10 MPa. 100% of the failure occurred in the substrate, because the mechanical strength of MC (0.90) concrete is lower than of MC (0.40) concrete. For MS_6_1.3_RS also 100% of the failure occurred in the concrete.

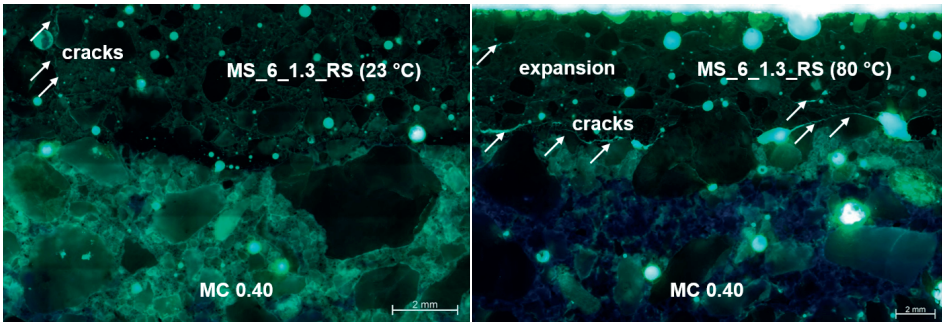

Figure 8.7: Micrographs of MS_6_1.3_RS mortars on MC 0.40 concrete specimens after initial curing at 80 °C/ 80% r.H. (top) and only curing at 23 °C/ 50% r.H. (bottom), investigated by optical microscopy under UV-light.

Fig. 8.7 shows micrographs of the interface zone of sample MS_6_1.3_RS on MC 0.40 concrete after curing at 80 °C for one day and 27 days at 23 °C and after curing only at 23 °C. The samples were treated with a fluorescent resin, thus areas of low density, e.g. cracks or pores, appear lighter in the micrographs when considered under UV-light (Fig. 8.7). The sample that was cured for one day at 80 °C (Fig. 8.7) displays horizontal cracks in the mortar coating. Those structures are considered to be a main reason for the lower pull-off strength of the MS-based samples that were cured at elevated temperatures (Fig. 8.5). The cracks occurred from expansion during hardening of the specimens. As reported in Chapter 4, the expansion is mainly caused by a silicon impurity in MS. MS_6_0.87_S1 showed no bond strength after curing at 80 °C. Since the paste content was decreased and the water content was increased compared to MS_6_1.3_RS, the viscosity of the paste was significantly decreased. Therefore, the gas formation had a worse effect during hardening, than on the fresh mortars with higher paste content and higher viscosity. Visible bubbles were identified on the surface of this specimen. The reasons for the higher pull-off strengths of MS_6_SL_0.9_RS after curing at elevated temperatures was the lower total MS content, due to the exchange of the pure MS_6 formulation with slag, to provide 10% CaO (≈ 22 wt.% slag) and the lower initial curing temperature (60 °C), besides the generally improved mechanical strength (cf. Section 7.2.).

Regarding the interface zone between MS_6_1.3_RS and MC 0.40 concrete without initial curing at 80 °C (Fig. 8.7; bottom), no significant expansion cracks were

observed. On the other hand, also no major vertical cracks due to shrinkage have been observed and thus all MS-based OPG mortars provided significantly increased pull-off strength. In case of the slag-containing MS-based mortar, the pull-off strength was higher than the ultimate tensile strength of the concrete specimen. As reported above, for MS (+ SL)-based OPG mortars the actual bond strength was always higher than the detected pull-off strength.

For both, slag-free and slag-containing MS-based OPG mortars, the detected pull-off strengths failed to achieve the requirements of DIN 19573: 2016 and Rili-SIB (Tab. 8.1) after initial curing at 80 °C or 60 °C, respectively. The main reason for the lower bond strength is the introduction of cracks due to expansion, related to the release of hydrogen from the silicon impurity of the MS feedstock. The observed values for the slag containing mortar were considerably higher, because the MS content and initial curing temperature was decreased compared to the slag-free mortar.

Table 8.1: Classification of the bond-strength of the OPG mortars in terms of DIN 19573 [76] and Rili-SIB [183] after curing at elevated temperatures for one day and 23 °C for 27 days.

	DIN 19573					**Rili-SIB**		
	repair mortar		**coating mortar**		**injection mortar**	**M1**	**M2**	**M3**
	B1	**B2**	**B1**	**B2**				
requirement (MPa)	**-**	**1.5**	**1.5**	**2.0**	**1.5**	**-**	**2.0**	**2.0**
MS_6_1.3_RS		-	-	-	-		-	-
*MS_6_0.87_S1 **		-	-	-	-		-	-
MS_6_SL_0.9_RS		-	-	-	-		-	-
RHA_6_1.3_RS		+	+	+	+		+	+
RHA_6_SL_1.3_RS		-	-	-	-			

*…on MC (0.90) concrete

On the other hand, all MS-based OPG mortars, cured only at 23 °C provided excellent bond strength, in line with literature [17, 18, 189]. All MS (+ SL)-based OPG achieved the requirements of DIN 19573 for repair mortars (class B2), coating mortars (class B1 and B2) and injection mortars (Tab. 8.2). Furthermore, the requirements of Rili-SIB for all three exposition classes (M1, M2, M3) were achieved, as well. Even the MS_6_0.87_S1 (w/b = 0.59) achieved all requirements of the standard, when not initially cured at 80 °C. No significant expansion cracks were observed by optical microscopy, as well as no major shrinkage cracks. Compared to mortar prisms, the geometry of the specimens for the measurement of the bond strength supports a faster hardening at ambient temperature as well. Since only a thin layer of mortar is applied to the concrete (≈ 8 mm), the surface/ volume ratio is

significantly higher than for the prisms. The specimens for the bond strength were removed from the molds already after 2-4 hours, in a not hardened state. This fits into the previous observations of the *in-situ* applications, where various mortars with different consistencies were successfully applied in thicknesses up to 2 cm (cf. Section 6.2.; Fig. 6.6).

Table 8.2: Classification of the bond-strength of the OPG mortars in terms of DIN 19573 [76] and Rili-SIB [183] after curing at 23 °C for 28 days.

	DIN 19573					Rili-SIB		
	repair mortar		coating mortar		injection mortar	M1	M2	M3
	B1	B2	B1	B2				
requirement (MPa)	**-**	**1.5**	**1.5**	**2.0**	**1.5**	**-**	**2.0**	**2.0**
MS_6_1.3_RS		+	+	+	+		+	+
*MS_6_0.87_S1 **		+	+	+	+		+	+
MS_6_SL_0.9_RS		+	+	+	+		+	+
RHA_6_1.3_RS		-	-	-	-		-	-
RHA_6_SL_1.3_RS		-	-	-	-		-	-
CAC_REF		-	-	-	-		-	-

*…on MC (0.90) concrete

For the RHA(2)-based OPG mortars only one sample fulfilled the requirements of DIN 19573 and Rili-SIB. Compared to the MS-based samples, the slag-containing RHA(2)-based mortars provided lower maximum bond strength. The accelerating and strength improving function of the slag was less pronounced for the RHA(2) feedstock compared to the MS feedstock, as reported in Section 7.2, and goes along with a generally lower strengthening speed with this silica feedstock. Further investigations on RHA_6_SL_1.3_RS at higher curing temperatures need to be conducted for a sufficient evaluation. No negative, but a positive effect on the bond strength of curing at elevated temperatures was observed. The pure pastes showed also significant expansion, with decreasing silica content, *i.e.* with increasing degree of reaction of the RHA feedstock. Since this RHA(2) batch tends to decelerate the hardening and strength development compared to the MS feedstock, the temperature (80 °C) is considered to be necessary to reach a sufficient degree of reaction in a possibly short time. There was a clear degradation for RHA_6_1.3_RS from curing at 80 °C for one day (≈ 2.09 MPa), over curing only at 23 °C (≈ 1.43 MPa), to curing at 23 °C for three days and at 20 °C for further 25 days (0.55 MPa). Finally, the bond strength should be measured at later times if further investigations are conducted, to see if the strength level reaches the values of the MS-based mixes, as found for the

compressive strength (cf. Section 7.2). A decrease of the bond strength at later ages due to shrinkage or expansion is not expected (cf. Section 8.1.).

9. SULFURIC ACID RESISTANCE OF THE OPG*

Besides the variable adjustability of the workability for specific applications (e.g. manual application or spraying; Chapter 6) and the excellent mechanical strength up to 77 MPa compressive strength and 11.6 MPa flexural strength (Chapter 7), it was shown that the OPG mortars provide excellent shrinkage/ expansion and bond behavior at ambient temperature and varying relative humidity (Chapter 8), as well as gentle deformation behavior during thermal dehydration for the pastes (Chapter 5). Chapter 9 focuses the resistance of the OPG pastes and mortars against sulfuric acid attack, since biogenic acid corrosion is one of the most important degradation processes of conventional concrete structures in various fields (e.g. sewers or digestion sites).

In this Chapter the OPG are produced with MS(2), RHA(2), SA(3) and RS aggregates.

9.1. Introduction

The long term chemical durability of concrete structures is of major importance for sustainable civil engineering, and is often heavily affected by acidic attacks. Especially sewers play an important role for the infrastructure and the national economy of modern nations. Due to the specific conditions, sewers are often affected by concrete corrosion [191]. A main reason for that is the biogenic *in-situ* formation of sulfuric acid from the metabolism of sulfur oxidizing bacteria. Therefore, the attack is also called "biogenic sulfuric acid attack". Warm and moist climates enhance this biogenic corrosion process of conventional concretes [191].

Due to the microbial degradation of sulfates and sulfur containing amino acids under reducing conditions at the bottom of sewers, H_2S and volatile organic sulfides (e.g. dimethyl sulfide = $(CH_3)_2S$ and methyl mercaptan = CH_3SH) form in the first step. Above the reducing zone, together with oxygen from the air and possibly due to further microorganisms, the volatile sulfides are oxidized to sulfur. This sulfur is a substrate for various organisms of the species of Thiobacillus bacteria, that live on the moist surface of the sewer concretes. These bacteria transform the sulfur to sulfuric acid (Fig. 9.1). The most efficient acid producing member of the species

* The results of Chapter 9 are published in Sturm et al: Sulfuric acid resistance of one-part alkali-activated mortars. Cement and Concrete Research, Vol. 109, p. 54-63 (2018).

is the so called Thiobacillus thiooxidans, in the past also known as the "concrete feeder" [191, 192].

Above pH = 12, virtually no member of these corrosion causing Thiobacilla exists. By decreasing the pH below 9, e.g. due to carbonation, several members of the Thiobacillus bacteria start to increase its population significantly. Due to the acid production of the bacteria, the pH continues to decrease. By decreasing the pH below 5, the Thiobacillus thiooxidans enters the field [193]. Besides the pH, also the temperature plays an important role. At 29 °C Thiobacillus thiooxidans provides its maximum activity. In conventional cementitious materials this threatens especially the highly soluble portlandite ($Ca(OH)_2$) in the first case, followed by C-S-H and sulfate phases [191]. Recent studies propose another participating bacterium (Acidithiobacillus ferrooxidans) and proved their occurrence also in strongly deteriorated, partially anaerobic layers. Furthermore, it was proposed, thiooxidans dominates oxygen rich areas close to the surface, while ferrooxidans dominates the inner parts with lack of oxygen [194].

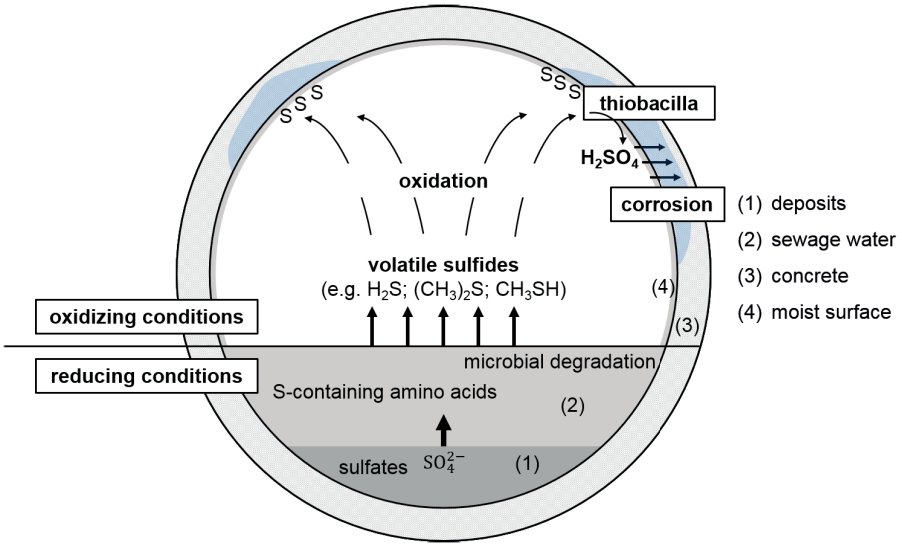

Figure 9.1: General process of the biogenic sulfuric acid attack in a sewer (adapted from Stark & Wicht [191]).

Due to the alteration of sewers, in Germany alone investments of approximately 58 Mrd € (status 2008) are necessary for the maintenance of urban sewer systems [195]. Many approaches are conducted to save the original structures, like avoiding backwater by increasing the slopes of the pipes, avoiding of turbulences, air conditioning (oxygen supply), cleaning procedures or limiting the ambient temperature to < 20 °C [191]. Those procedures mainly affect the production of H_2S, since it is

necessarily related to an exclusion of oxygen and already low oxygen concentrations have a strong limitation effect, but the production of organic sulfides was found to be not inhibited sufficiently. Usually the organic and inorganic sulfides (H_2S) are detected together in sewers, and thus a high degree of contribution is assumed for the organics [192]. The acid resistance of conventional concretes can be slightly improved by increasing its density (lowering the w/b) and decreasing the portlandite content by passivation of the substrate with coatings [191].

In this context, a recent approach is the use of AAM as protective coatings. Well designed, AAM can provide significantly higher durability under acidic conditions compared to OPC, as the majority of authors observed [30, 196-203] and compared to Portland Pozzolana Cement Concrete (PPCC) [204]. Nevertheless, Lloyd et al. presented results, showing much less acid resistance of low-Ca GP compared to OPC and CAC with respect to the corrosion depth [205]. Zhang et al. found no significant benefits of FA and red mud-based GP compared to OPC regarding the leaching of heavy metals from the matrix in sulfuric acid [206].

The most critical aspect with respect to the chemical stability against acid attack of OPC and AAM is the CaO content. Especially the high CaO content in OPC is problematic. Usually the transformation of portlandite leads to the formation of gypsum [196, 198, 199, 201, 207]. The formation of gypsum was also observed for FA (class-C) where portlandite was formed during the hydration. Furthermore, the occurrence of ettringite was detected due to the reaction with released Al from the GP matrix [208]. In this context it was shown, that the acid resistance of low calcium FAs (class-F) was higher than of high calcium FA (class-C) [205]. MS was found to have a positive impact on the acid resistance of AAM [202, 207]. Furthermore, the formation of gypsum in OPC blended FA GP could be avoided by the addition of MS [207].

Regarding the type of alkalis, only few literature statements were found. Compared to sodium, potassium seems to decrease the acid resistance of MK-based GP with respect to HCl [209] and of FA-based GP with respect to H_2SO_4 and organic acetic acid (CH_3COOH) [30]. The decrease of the chemical stability was attributed to bigger pore sizes occurring from potassium activation [30]. The latter also reported on a positive effect of crystalline aluminosilicates on the acid resistance of AAM. In this context, mixes with the highest crystallite content (hydrosodalite) provided the best properties by far. The authors concluded an increasing resistance to acid attack by increasing the long-range order in the reaction products [30].

Hartman et al. [124, 125] investigated the dissolution behavior of different zeolites (A-type, Y-type, ANA-type) in HCl ($pH \leq 1$) and found congruent dissolution be-

havior of 1:1 (Si:Al) zeolites (A-type) and incongruent dissolution behavior for X:1 (X>1) zeolites. The dissolution of 1:1 types led to the formation of a proposed new aluminosiliceous gel phase, whereas the dissolution of X>1 types led to the selective removing of Al from the structures, related to an Si enrichment and amorphization of the residual structure. The higher the Si/Al ratio of the framework, the more of the structure remained intact after acid attack [125]. The treatment of A-type zeolites with H_2SO_4 at pH = 4 was found to have no major effects on the structure. At pH ≤ 2 dealumination was observed. Highly soluble sodium sulfate formed and was diluted. Almost no remaining sodium and sulfate was observed after the treatment and it was concluded dealumination of A-type zeolites is not substantially affected by the acid anion [142]. The preliminary investigations on the degree of reaction of the geopolymer-zeolite composites (Section 4.2.2.) showed comparable dissolution behavior under HCl-treatment, *i.e.* a virtually fully dissolution of the reaction products when the molar SiO_2/Al_2O_3 of the reaction products was ≈ 2, especially when the feedstocks fully reacted (MS_2), in accordance with NMR [70], whereas SiO_2/Al_2O_3 > 2 mol/mol led to significantly too low calculated reactivity, probably due to the contribution of remaining, silica enriched reaction products (Section 4.3.2.).

The following Section studies the effects of sulfuric acid on the OPG, in terms of the residual strength of OPG mortars after acid exposure and the structural changes of the respective pastes to evaluate their general acid resistance and potential use asprotective repair coatings for sewer concretes, in addition to the observed good applicability of the fresh mortars (cf. Section 6.2.) and shrinkage/bond behavior (cf. Sections 8.1. and 8.2.).

9.2. Experimental program

The sample compositions of the OPG mortars and CAC_REF are given in Tab. 9.1. Besides the considered mortars of the investigations on the mechanical strength development (Section 7.2.), the shrinkage behavior (Section 8.1.) and the bond behavior (Section 8.2.), preliminary investigations have been conducted on MS_6_RS (w/b = 0.4) and CR_3.5_RS (w/b = 0.5). As stated before, CR_6-based mortars could not be prepared below w/b = 0.8, because of the poor workability and the according mortar provided virtually no strength after curing (Section 7.2; Fig. 7.1). The increased SiO_2/Al_2O_3 ratios of the slag containing formulations to provide 10 wt.% CaO in the binder is due to the high silica content of the slag. The low amount of HS (1 wt.% CaO) in MS_6_SL_1.3_RS did not change the SiO_2/Al_2O_3 ratio.

Table 9.1: Composition of the OPG mortars. Produced with MS, CR and RHA(2) and CAC_REF for the investigations on the resistance against sulfuric acid attack.

Sample	SiO_2/Al_2O_3 (mol/mol)	w/b (g/g)	Paste content (wt.%)	Na_2O/CaO (mol/mol)	$H_2O/(Na_2O+CaO)$ (mol/mol)
MS_6_RS	6.03	0.4	31.5	10.66	11.44
MS_6_1.3_RS	6.03	0.4	37.4	10.66	11.44
MS_6_SL_0.9_RS	6.31	0.38	30.0	0.80	6.74
MS_6_SL_1.3_RS	6.03	0.4	37.3	10.19	10.85
RHA_6_1.3_RS	6.05	0.4	37.6	12.4	11.30
RHA_6_SL_1.3_RS	6.38	0.38	38.2	0.80	6.67
CR_3.5_RS	3.52	0.5	30.7	6.36	11.10
CAC_REF			> 50		

The investigation of the resistance against sulfuric acid was conducted in accordance with DIN 19573: 2016-03, Appendix A [76], with moderate adjustments of the curing conditions, to avoid dilution of the activator solution in early ages (Tab. 9.2) before acid-treatment, as stated more detailed in Section 2.1.2.2. After preparation of the mortar specimens (40 mm × 40 × 160 mm) in accordance to DIN EN 196-1: 2005, the OPG mortars were subsequently transferred to an oven with climate condition and cured for 24 hours at a certain temperature and relative humidity, at 23 °C/ 50% r.H for the following 25 days, and at 23 °C under water at an age of 26 days (Tab. 9.2). At an age of 28 days half of the cut prisms were transferred to sulfuric acid (pH = 1) and the other half remained under water.

Table 9.2: Curing conditions of the OPG mortars and CAC_REF during the investigation of the acid resistance (uW = under water storage).

Sample	Curing before acid-treatment			H_2SO_4	Ending
MS_6_RS	1d (80 °C/ 80% r.H.)	25d (23 °C/ 50% r.H.)	2d (23 °C/ uW)	70d (23 °C/ pH 1) or 70d (23 °C/ uW = REF)	2d (23 °C/ 50% r.H.)
MS_6_1.3_RS	1d (80 °C/ 80% r.H.)				
MS_6_SL_0.9_RS	1d (60 °C/ 80% r.H.)				
MS_6_SL_1.3_RS	1d (60 °C/ 80% r.H.)				
RHA_6_1.3_RS	1d (80 °C/ 80% r.H.)				
RHA_6_SL_1.3_RS	1d (60 °C/ 80% r.H.)				
CR_3.5_RS	1d (80 °C/ 80% r.H.)				
CAC_REF	1d (23 °C/ 98% r.H.)				

Besides the evaluation of the sulfuric acid attack of the OPG mortars, the according pastes MS_6, MS_6_SL (10 wt.% CaO) as well as RHA_6 and RHA_6_SL were additionally investigated for their structural changes, by XRD, ^{29}Si single pulse NMR, ICP-OES and SEM. Therefore, the pastes have been produced at the same w/b as the discussed mortars (Tab. 9.2.), using the planetary centrifugal mixer at a rotation speed of 1200^{-min} for 3 minutes. Subsequently the pastes were casted into 20 mm × 20 mm × 20 mm cube molds. The following treatment was equal to those of the mortars until removing from the acid bath. MS_6_SL and RHA_6_SL have been transferred to separate beakers (V = 400 ml) after 2 weeks under acid because the observed expansion led to a destruction of the cubes and the loss of material. The acid bath of the beaker was renewed once a week, as well. MS_6 and RHA_6 remained mechanically stable and were treated together with the mortars for the whole investigation time. After the acid-treatment, the pastes were washed with deionized water and dried in an oven (40 °C) for 2 days. In the following, the samples were ground manually using mortar and pestle (agate) and all particles passed through a sieve with 0.063 mm mesh widths. Until the further testing, the samples were stored in a desiccator above dry silica gel.

9.3. Results and discussion

The results of the investigations on the acid resistance of the OPG mortars are presented in Tab. 9.3. MS_6_RS provided a residual compressive strength of 72% of the water reference and an effective corrosion depth of 3.1 mm. This was close to the requirements of DIN 19573: 2016 of > 75% residual strength and a related corrosion depth of < 2.7 mm. For MS_6_1.3_RS with equal w/b of the paste but increased total paste content (Tab. 9.1), the relative residual strength increased to 77.1 %, and thus fitting into the requirements of DIN 19573: 2016, for resistant mortars after sulfuric acid-treatment (70 d, pH 1) [76]) and the requirements for “class II” acid resistant mortars (> 75 %) of Rili-SIB [182].

The absolute strengths of MS_6_1.3_RS, with and without acid-treatment, was below MS_6_RS. This is related to the higher binder content of MS_6_1.3_RS what resulted in a slower strength development and the wet conditions did not enhance further strengthening at later ages, as can be seen from Section 7.2., thus no expectable significant further strength improvement occurred also for the under water stored samples after 28 days. Almost no visible alterations occurred on the surfaces after the specimens were removed from the acid. Even the initial colored marks have been still on the specimen surface. The brushing scratched traces off the surface. However, the core of the specimens was visually indicated as a more or less

sharp line between the big core (uncorroded) and the shell (corroded). Remarkably, the shell was not dissolved through the acid attack and still a discrete part of the structure, a beneficial observation for all OPG mortars, as the representative pictures of Fig. 9.2. reveal.

The relative residual strength of RHA_6_1.3_RS mortar during the acid-treatment was quite equal, indicating a comparable acid resistance. A residual strength of 77.9% of the reference was observed. On the other hand, the absolute strengths (water = 32.0 MPa; acid = 25.0 MPa) were lower than for MS_6_1.3_RS (water = 41.0 MPa; acid = 31.6 MPa), fitting into the observation of the slower related strength development of the RHA(2)-based OPG mortars, especially under moist conditions (cf. Section 7.2; Figs. 7.3 and 7.4).

Table 9.3: Residual compressive strengths of the mortars after treatment with sulfuric acid (pH 1). The bold, cursive values of the residual strength achieve the requirements of DIN 19573: 2016 (Appendix A) [76].

Sample	R_{water} (N/mm²)	R_{acid} (N/mm²)	$R_{residual}$ (%)	$X_{f,D}$ (mm)	*Requirement* ($R_{residual}$, $X_{f,D}$)
MS_6_RS	58.0 ± 4.5	41.7 ± 4.7	72.0	3.1	≥ 75/ < 2.7
MS_6_1.3_RS	41.0 ± 0.8	31.6 ± 1.1	***77.1***	***2.5***	
MS_6_SL_0.9_RS	53.6 ± 5.3	33.5 ± 1.6	62.5	4.2	
MS_6_SL_1.3_RS	45.6 ± 1.1	34.6 ± 1.8	**75.8**	**2.6**	
RHA_6_1.3_RS	32.0 ± 4.1	25.0 ± 0.6	***77.9***	***2.4***	
RHA_6_SL_1.3_RS	30.3 ± 1.3	17.3 ± 0.9	57.2	5.0	
CR_3.5_RS	48.7 ± 0.7	25.8 ± 1.6	52.9	5.6	
CAC_REF	63.6 ± 3.2	35.4 ± 2.2	55.7	5.1	

CR_3.5_RS provided lower resistance to sulfuric acid attack. The residual strength of the acid stored specimens was only 52.9% of the reference and the calculated corrosion depth ($X_{f,D}$) was 5.6 mm (Tab. 9.3). This was the lowest relative residual strength of all considered OPG mortars. On the other hand, like for the other OPG mortars no major visual changes have been observed after removing the samples from the acid bath. The main reasons for the lower resistance of the CR_3.5 mix are the necessarily higher water content to make it workable and the lower molar SiO_2/Al_2O_3-ratio (Tab. 9.3), as will be discussed below.

MS_6_SL_0.9_RS reached a residual strength of 62.5% of the reference and an effective corrosion depth of 4.2. mm. In contrast to the afore mentioned specimens, the SL modified mortar underwent expansion during the acid-treatment, which

is the main reason for the lower residual strength. Still huge parts of the corroded layer remained a structural part of the specimens (Fig. 9.2). On the other hand, the formulation with only 1 wt.% CaO (MS_6_SL_1.3_RS) showed no expansion and a residual strength of 75.8 %. The absolute residual strength of both SL containing MS-based mortars after acid treatment was equal (Tab. 9.3). Both samples were initially cured at 60 °C. The main part of the strength gain occurs within this period of elevated temperature curing (cf. Section 7.2.) and the lower CaO content of the latter formulation decreased the accelerating function of SL in the system. No further significant strength gain under water (t > 28 d) is expected (cf. Section 7.2.). RHA_6_SL_1.3_RS had lower acid resistance than the SL free RHA_6 mortar, as well. The mortar reached 57.2% of the reference sample after the acid-treatment. The increased paste content of the RHA_6_SL (10 wt.% CaO) based mortar compared to MS_6_SL (10 wt.% CaO), *i.e.* the higher absolute SL content and the lower as-cured strengths are the main reasons for the lower relative residual strength.

CAC_REF exhibited a residual strength of 55.7% and an effective corrosion depth of 5.1 mm. Unlike the OPG mortars, the sulfuric acid attack led to dissolution of the corroded layer during the acid-treatment. This means an ongoing process of acid attack would lead to a fully dissolution of a protective coating after a certain time, thus the *in-situ* substrate would fully loose its protection. The remaining of the corroded part is a clear advantage of the OPG mortars in this context.

Pure pastes (MS_6, MS_6_SL (10 wt.% CaO); RHA_6 and RHA_6_SL (10 wt.% CaO)) have been investigated by XRD. The results of the XRD analyses are presented in Fig. 9.3. The obtained diffractogram of the water stored MS_6 paste, fits quite well into the former results for equal samples cured at 80 °C (Sections 4.2.2; 4.4.3 and 5.3). Besides gel and unreacted MS feedstock, zeolite A was the dominant crystalline phase besides small amounts of HS, as observed for curing of the mix at 80 °C without further curing under wet conditions, indicating a considerable stability of the phase content also when stored under water.

After treatment with H_2SO_4 (pH 1) all primary crystalline reaction products disappeared (Fig. 9.3). Furthermore, the asymmetric broadening of the hump, indicating the geopolymers, disappeared. The insoluble residue looked very much like the MS feedstock (Fig. 9.3). Additionally, low amounts of a hydrated silica $H_2Si_{14}O_{29}{\cdot}xH_2O$ (PDF # 00-045-0423) were observed as secondary reaction product. The hump was slightly broadened compared to silica MS, indicating more scattering. Parts of the silicon carbide impurity of the silica MS remained, whereas the silicon traces disappeared due to the reaction during the hardening and the related hydrogen formation (cf. Sections 4.2.–4.4.). No sulfates were identified. The results fit well

into the previous studies, where it has been shown that after hydrochloric acid attack virtually only the unreacted silica, *i.e.* the insoluble residue, remained for the geopolymer-zeolite composites MS_6 (Section 4.2.2.).

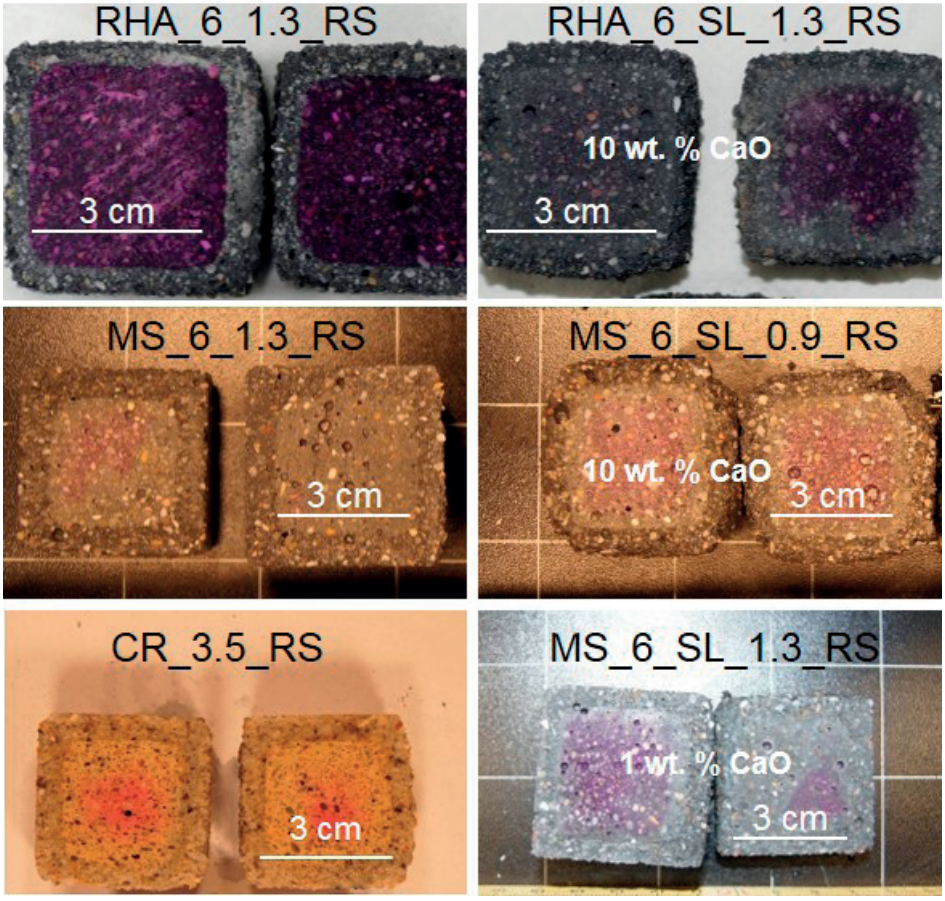

Figure 9.2: Cross sections of the OPG mortars RHA_6_1.3_RS (top, left), RHA_6_SL_1.3_RS (top, right), MS_6_1.3_RS (middle, left), MS_6_SL_0.9_RS (middle, right), CR_3.5_RS (bottom, left) and MS_6_SL_1.3_RS (bottom, right) after exposure to sulfuric acid (pH 1; 70 d).

The qualitative crystalline phase content of the water stored slag containing paste (MS_6_SL) with 10 wt.% CaO in the binder looked quite like the slag free MS_6 mix (Fig. 9.3). Significant amounts of hydrated zeolite A occurred. Since the cations are exchangeable, probably a mixture of zeolite 4A (Na-type) and 5A (Ca-type) formed. In contrast to pure MS_6, no traces of HS were observed and no portlandite formed. This shows that the major phase formation does not underwent significant changes at least up to a total CaO content of 10 wt. %. Still geopolymer-zeolite composites were formed and parts of the MS feedstock remained unreacted, as also

observed as Q^4(0Al) sites in the ^{29}Si NMR spectrum, but with less intensity than for pure MS_6 (Fig. 9.4), indicating an increased degree of reaction of the silica feedstock. This fits into the observed accelerated hardening and increased early strength (cf. Section 7.2.) of the slag containing Ms-based formulations.

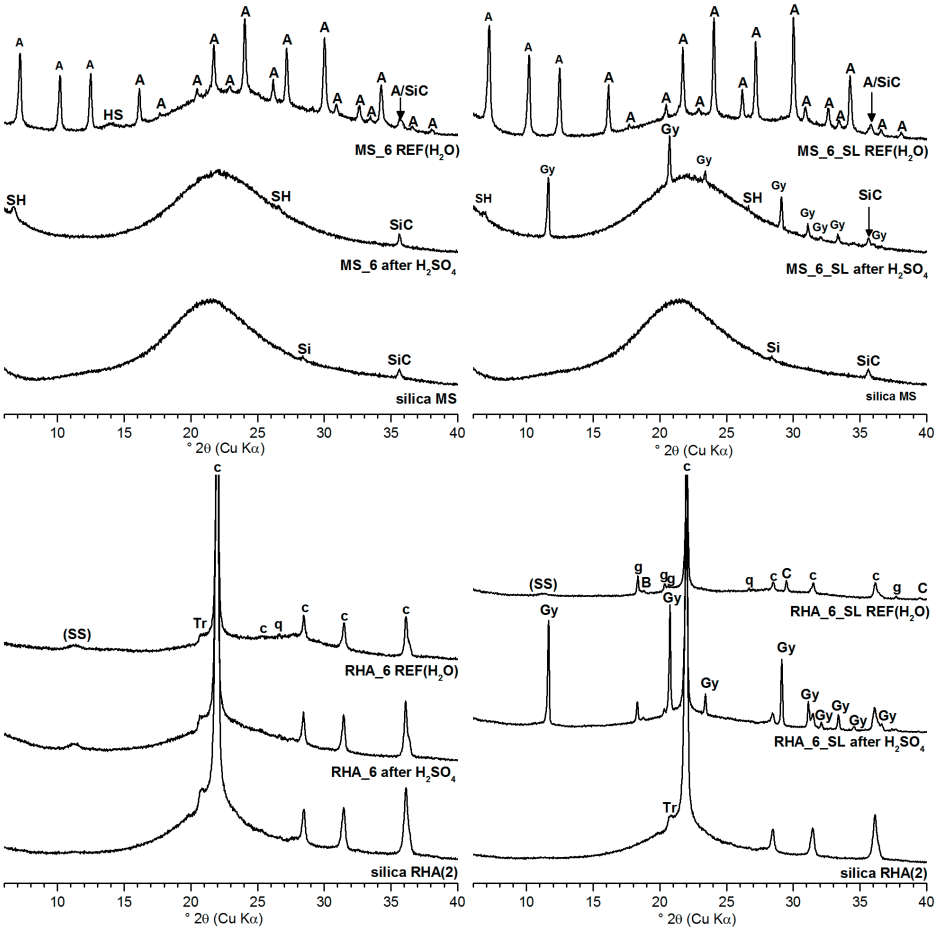

Figure 9.3: XRD results of the pastes MS_6 (top. left side), MS_6_SL with 10 wt.% CaO in the binder (top, right side) RHA_6 (bottom. left side) and RHA_6_SL with 10 wt.% CaO in the binder (bottom, right side) after reference storage (H_2O) and after sulfuric H_2SO_4-treatment (pH 1; 70 d) as well as pure silica MS and RHA(2) (A = zeolite A; HS = hydrosodalite; SiC = silicon carbide; Si = silicon; SH = hydrated silicic acid, G = gibbsite; B = bayerite; C = calcite; Gy = gypsum; (SS) = sodium silicate).

After the acid-treatment, like for the slag free mix, the primary reaction products disappeared. No zeolite A remained, the residual hump was very similar to silica MS and again low amounts of the hydrated silicic acid have been detected (Fig. 9.4). As the main difference to MS_6, additionally, significant amounts of gypsum (PDF #

00-033-0311) were identified. This is attributed to the increased CaO content (10 wt.% of the binder) of MS_6_SL, as also observed for class-C FA, OPC and SL blended FA composites [207, 208]. This further fits into the visual observations of the according mortar MS_6_SL_0.9_RS after acid attack, where the samples underwent significant expansion. The expansion was attributed to the gypsum formation. The related introduction of cracks further decreased the residual strength and the decreased residual acid resistance of the altered mortars (Tab. 9.3). In case of the pure paste it resulted in a fully destruction of the cubes.

It can thus be concluded, that the slag content, i.e. the increased CaO content, has a negative impact on the acid resistance of the regarded OPG systems, although the initial dissolution rate of Na_2O at low pH in multioxide silicates is higher than of CaO [143]; also, sodium or aluminum sulfates provide a very high solubility under the acidic conditions and won't precipitate [142]. Pure slag-based AAM in the literature also formed gypsum and expanded [196, 205]. The formation of gypsum and a related expansion in AAM with significant slag content when treated with sulfuric acid is well known [197, 198, 205, 207]. No increased expansion occurred in the MS_6_SL-based mortars with only 1 wt.% total CaO in the binder and the samples achieved promising acid resistance. Thus, it can be concluded the CaO content of the mixes must be limited for the regarded systems, in terms of the resistance against sulfuric acid attack.

Fig. 9.4 presents the results of the single pulse ^{29}Si MAS NMR experiments on MS_6 with and without acid-treatment. The observations of the NMR measurements fit quite well into the XRD results. Without acid-treatment, the spectrum includes Q^3 and Q^4 sites that are related to unreacted MS (Q^4(0Al)) and partially dissolved surface layer (Q^3(0Al)) of MS. The sharp Q^4(4Al) signal at -89.2 ppm is related to zeolite A products, and the low intense shoulder around -85 ppm is attributed to the gel. Since no silicon sites with different aluminum environments occurred an overall $SiO_2/Al_2O_3 \approx 2$ mol/mol is indicated for the reaction products. After the treatment with sulfuric acid, the Q^4(4Al) sites disappeared, *i.e.* the aluminosilicate reaction products were decomposed. Only Q^4(0Al) and Q^3(0Al) sites remained. The ^{29}Si NMR spectra, as well as the XRD results of the MS-based OPG are in good agreement with the previous results for HCl treatment to determine the degree of reaction of the silica feedstock and only the insoluble residue, *i.e.* the unreacted silica remained after the acid attack (cf. Section 4.2.2) and no Q^4(4Al) sites remained [51].

The ^{29}Si NMR spectrum of MS_6_SL without acid-treatment indicates Q^3 and Q^4 sites from the silica feedstock and Q_4(4Al) sites from the reaction products. Less

unreacted silica remained, indicating a higher degree of reaction of the silica. In this context it must be mentioned that less silica was included, since it was partially exchanged with SL. In the present case the slag (CaO), provided increased reactivity, as also expressed through higher initial strength at lower curing temperatures and faster hardening (cf. Section 7.2), to go along with a decreased $H_2O/(Na_2O+CaO)$ ratio compared to pure MS_6 (Tab. 9.1). After the acid-treatment, the $Q^4(4Al)$ signals disappeared, indicating the dissolution of the primary aluminosilicate reaction products. Like for the pure MS_6 mix, only the Q^3 and Q^4 sites from the silica feedstock remained.

The ^{29}Si MAS NMR spectrum of RHA_6 without acid storage showed significant amounts of $Q^4(0Al)$ sites with a sharp maximum at -108.9 ppm. The latter signal is related to the crystalline cristobalite [210] of silica RHA(2). The results indicate the incomplete reaction of the feedstock, in accordance with the XRD results (Fig. 9.3). In contrast to MS_6 (without acid-treatment), the spectrum does not contain a sharp $Q^4(4Al)$ peak from aluminum related sites in zeolites, but instead a broad hump, including signals from silicon sites with different aluminum environment. The signal at ca. -100.6 ppm most likely also includes $Q^3(0Al)$ from the partially reacted silica RHA(2), as observed for MS_6. The RHA_6 spectrum indicates the formation of more aluminosilicate gel, compared to MS_6, and the inclusion of more silicon into the network ($Q^4(mAl)$; $m \leq 4$), in line with the observed glassy microstructure of the formulation (cf. Section 4.3.2., Fig. 4.9 and Fig. 4.11). After acid-treatment the aluminum-related sites disappeared. The exception was a low signal at -91.6 ppm (Fig. 9.4), that possibly occurred from traces of $Q^4(3Al)$. The same traces are assumed for the MS based OPG, but the in even lower quantity (*i.e.* close to the detection limit). As for MS_6 after acid-treatment, the spectrum mainly consists of $Q^4(0Al)$ and $Q^3(0Al)$ signals, indicating the dissolution of the primary aluminosilicate reaction products.

The spectrum of RHA_6_SL, is generally comparable to RHA_6 (Fig. 9.4), but in contrast to the former one, the signals in the region between -90 ppm and -102 ppm are less intense. This suggests a relatively decreased content of the suggested silicon environments. The hump starts at higher shifts (ca. -65 ppm). In silicates, signals between -80 ppm and -60 ppm are usually assigned to Q^1 (sorosilicates) and Q^0 (nesosilicates) sites [211]. The occurrence in the presented spectrum is possibly related to monomers, that formed during the curing reaction but have not been incorporated into the aluminosilicate network, and, more likely, to silicate dimers in minor amounts of calcium (alumino)silicate hydrates (C-A-S-H), formed due to the supply of CaO from the slag. After the acid-treatment, the according spectrum appeared virtually identical to RHA_6 after the same procedure. The aluminosilicates

virtually fully dissolved and virtually only Q^4(0Al) and Q^3(0Al) sites remained. The slightly increased aluminum content of the according sample (≈ 2.4 wt.%, Tab. 9.4) would be an explanation for the signal at -91.6 ppm. In addition, the results fit well into the observations, made for the MS based formulations, as also found for XRD and residual strength (Tab 9.3, Fig. 9.3). The spectra after treatment with H_2SO_4 further support the proposed precipitation of a silica-rich secondary gel, that protects the remaining reaction products and decelerates the further corrosion process.

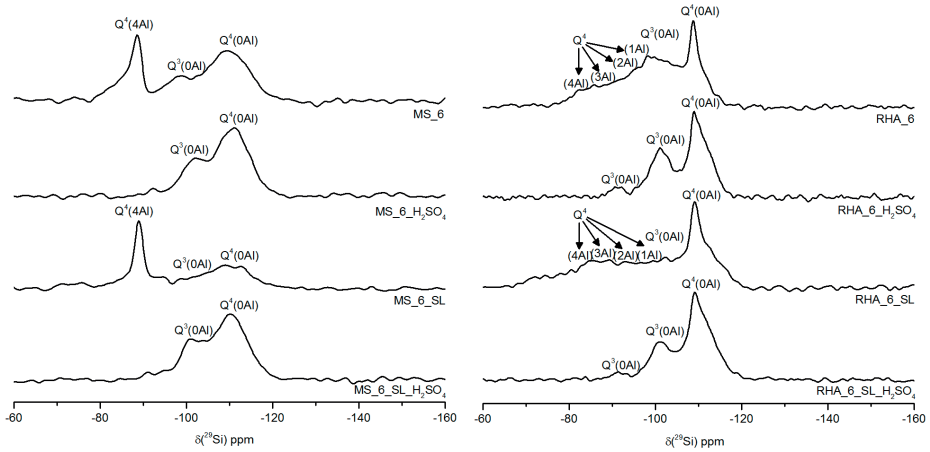

Figure 9.4: Left: ^{29}Si single pulse MAS NMR Spectra of the samples MS_6 and MS_6_SL (10 wt.% CaO) after treatment with H_2SO_4 and the reference under water storage. Right: ^{29}Si single pulse MAS NMR Spectra of the samples RHA_6 and RHA_6_SL (10 wt.% CaO) after treatment with H_2SO_4 and the reference under water storage.

Tab. 9.4 shows the main chemical composition of the OPG pastes after treatment with sulfuric acid, investigated by ICP-OES. The residue contained ≈ 85 wt.% SiO_2 and only ≈ 1 wt.% Al_2O_3, *i.e.* huge parts of the aluminum have been dissolved, whereas huge parts of the silica remained. The high LOI is related to the water content of the samples after drying and may be related to hydrated secondary reaction products (e.g. hydrated silica (rich) phases). The LOI free composition of the sample, including 95.1 wt.% SiO_2, was virtually equal to silica MS (94.6 wt.% SiO_2, Section 2.2.2.; Tab. 2.1). The results are in very good agreement to the ^{29}Si NMR experiments, where no remaining signals for aluminum related silicon sites (Si^4 (4Al)) and virtually only Q^4(0Al) and Q^3(0Al) sites (Fig. 9.4) remained. RHA_6 had virtually no remaining aluminum and a LOI corrected SiO_2 content of 96.57 (77.3 wt.% without LOI), close to the composition of RHA(2) (cf. Section 2.2.2.; Tab. 2.1), as well. Only a low, but slightly increased content of Al remained

in RHA_6_SL (Tab. 9.4) and again the main component was SiO_2 (65.8 wt.%). Additionally, CaO (6.0 wt.%), introduced by the slag, remained and sulfate (6.7 wt.%) was identified. These components mainly represent the gypsum impurity. The chemical analysis and fits quite well into the XRD investigations (Fig. 9.3). After the structural investigations, too less MS_6_SL material remained for a chemical analysis.

Table 9.4: Chemical composition the OPG after sulfuric acid-treatment (pH 1). Too less MS_6_SL remained for a chemical analysis.

Oxide	MS_6 (wt.%)	RHA_6 (wt.%)	RHA_6_SL (wt.%)
SiO_2	84.62	77.34	65.84
Al_2O_3	1.13	0.53	2.38
CaO	0.54	< 0.01	6.03
Na_2O	0.62	0.24	0.37
SO_3	0.72	0.34	6.70
LOI^*	11.03	19.92	16.62

LOI...loss on ignition at 1000 °C

Fig. 9.5 presents the micrographs of the RHA_6 paste with and without acid-treatment. The sample without acid-treatment provided a homogenous gel network, with interfaces mainly at boundaries of the pores. The pores provided quite irregular shapes with smooth borders, indicating the partial dissolution of the porous RHA feedstock and the inclusion of partly reacted silica (Q^3 (0Al), Q^4 (0Al) sites) into the network. For more detailed description of the as-cured RHA(2)-based OPG see Section 4.3.2. The micrograph of RHA_6 after acid-treatment (Fig. 9.5) indicated a less dense network. The sample showed more interfaces of smaller and partly more granular shaped particles. The small granular particles looked like "debris" and represented probably the silica (rich) residues and the holes, the removed parts of the primary reaction products, *i.e.* the amorphous geopolymers (no zeolites occurred for the mix, cf. Section 4.3.2.). The network appeared more particulate structured and the increased surface provided a high amount of irregular shaped pores and fractured or agglomerated residues. The observed microstructure is in line with the published literature of AAM with observed dissolution of the primary reaction products and related increase of the pore volume and formation fractured particulate networks, including BA and FA-based geopolymers and slag or OPC blended FA geopolymers (e.g. [30, 203, 206, 207, 212]) after sulfuric acid attack or MK-based geopolymers (pH 2) [209] and sodium containing zeolites [125] after HCl attack.

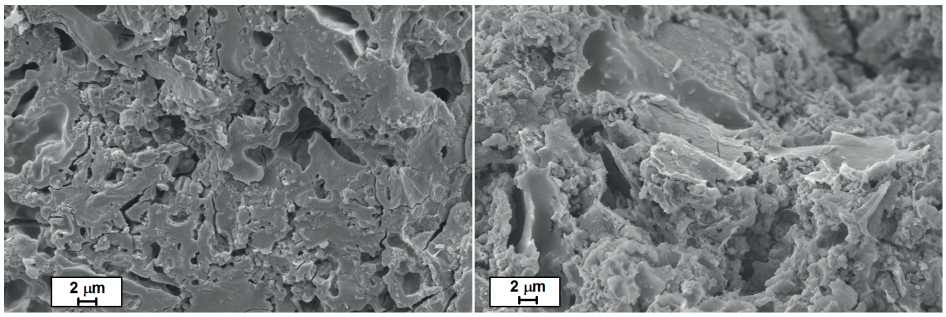

Figure 9.5: SEM micrographs of the RHA_6 reference sample after under water storage (left side) and RHA_6 after treatment with sulfuric acid (right side).

In general, MS- and RHA(2)-based mortars provided a promising acid resistance, regarding the requirements of DIN 19573: 2016. The RHA(2)-based mortar with the same composition as MS_6_1.3_RS (≈ 77 %) provided quite comparable relative residual strength (≈ 78 %). For the regarded, slag free geopolymer mortars, equally composed samples provided equal acid resistance in terms of relative residual strength. CR_3.5 provided the lowest relative residual strength of all considered OPG mortars. One reason was the increased water content, that led to an increased pore volume compared to the OPG mortars with lower applied water contents (Tab 9.1). The lower SiO_2/Al_2O_3 ratio led to a higher degree of reaction, and thus to an increased amount of soluble reaction products. For all OPG mortars, huge parts of the corroded layer were not dissolved and remained an inherent part of the structure.

MS_6_SL and RHA_6 SL-based OPG mortars, where parts of the binder were exchanged with slag, to provide an absolute CaO binder content of 10 wt.%, did not achieve the requirements of DIN 19573:2016. Due to the higher paste content, and lower absolute strength, the relative residual strength of RHA_6_SL_1.3_RS was even slightly lower than for MS_6_SL_0.9_RS. By decreasing the total CaO content of the binder to 1 wt.% (MS_6_SL_1.3_RS), expansion, due to significant gypsum formation was avoided and the residual strength reached > 75% of the water reference, achieving the requirements of DIN 19573:2016. Therefore, the results of the slag containing OPG mortars suggest a limitation of the CaO content for applications with high required acid resistance. More dissolution was observed but still huge parts of the corroded layer remained inherent.

The promising observed acid resistance of the OPG is in line with the results of previous studies of the acid resistance of conventional geopolymers and geopolymer mortars of [16, 30, 173, 196, 199-201, 203]. For the considered OPG of this work, it is thus interpreted that the precipitation of silica enriched gel at the acid-geopolymer interface is a major mechanism responsible for the high acid resistance of the

studied mortars. Hints for this in the XRD results are the occurrence of a hydrated silica after the acid-treatment of the MS-based OPG, the increased scattering of the hump of the insoluble residue and the high water content of the samples after drying. Furthermore, the observed acid consumption (Fig. 9.6) for the adjustment of the pH value was increased at early times.

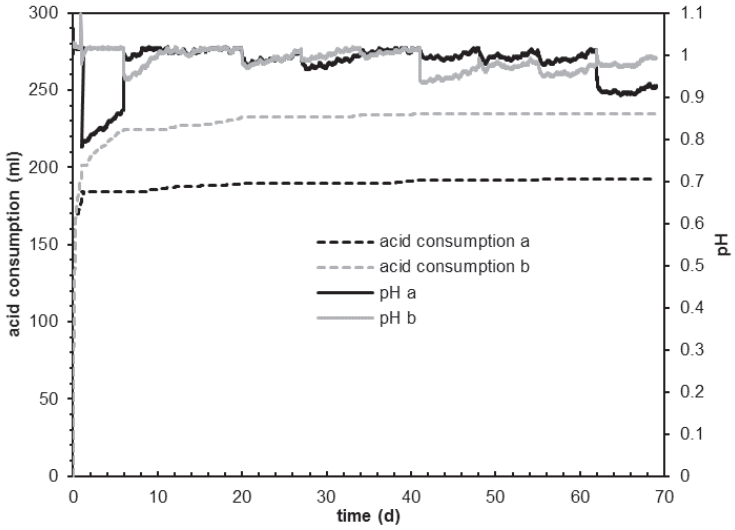

Figure 9.6: Development of the pH value and the acid consumption for sample MS_6_SL_1.3_RS (= 1 wt.% CaO). Box a contained 2 prisms and box b contained 3 prisms.

This was mainly caused by the reaction of the acid with the alkaline pore solution and the solid aluminosilicate reaction products. After a certain time (< 7d) the acid consumption, to hold the pH at 1 decreased and became virtually constant. This further supports a deceleration of the acid corrosion process, due to the proposed precipitation of secondary silica rich reaction products, that protect the remaining aluminosilicates from fast further dissolution.

As proposed for HCl attack [124, 125], the dissolution of zeolite A and other zeolites in acid occurs from leaching of the charge balancing non-framework cations Na^+ (Ca^{2+}), exchanging with H_3O^+ in the case of zeolite A, or Na^+ in the case of HS. Sodalite-cages (β-cage) are structural parts of zeolites, as 8 sodalite cages, connected through 12 double 4 rings (D4R) form zeolite A, with its included α-cage and a thus increased inner surface. The denser crystal structure may decrease the dissolution rate of HS compared to zeolite A under acidic conditions and Bakharev [30] reported the best sulfuric acid resistance of FA-based GP with the highest included HS content. However, the removing of the charge balancing non-framework cations

is followed by the removal of Al from the framework by hydrolysis and a subsequently hydrolyses of Si–O–Si bonds [124, 125, 142, 143], whereas the hydrolysis of the latter ones decreases with increasing silicon content of the initial framework [124, 125]. For A-type zeolites the removal of Al from the framework, already leads to the complete destruction of the framework, since due to SiO_2/Al_2O_3 = 2 mol/mol (Si/Al = 1 mol/mol) and virtually complete adherence to the Loewenstein rule [213] each Si site is bonded to four Al sites via Si–O–Al bonds. Since at low pH the solubility of SiO_2 is low [214], it can be expected that most of the dissolved Al is retained in solution, while dissolved silica will precipitate as (hydrated) silica, as partially observed by XRD as hydrated silicic acid (Fig. 9.3), at the acid-paste interface [173]. The gel covers the surface of the exposed mortar and decreases further dissolution, which explains the high acid resistance of both, the mortars based on geopolymer-zeolite composites and on geopolymers. In addition, any unreacted silica in the OPG will act as insoluble filler in the matrix [125], improving the acid resistance. Regarding the biogenic sulfuric acid attack, it can be expected that the high concentration of dissolved Al will probably inhibit the activity of sulfuric acid-producing bacteria as found for CAC-based mortars [215]. That would further increase the durability of the OPG mortars under the natural conditions prevailing in sewer structures. For increased CaO contents, the general process remains the same, but the additional precipitation of $CaSO_4 \cdot 2H_2O$ (gypsum) weakens the acid resistance, due to expansion and related cracking. Sodium sulfate will not precipitate on the other hand, due to its much higher solubility under the acidic conditions [142].

10. INFLUENCE OF LI AND ADDITIVE MANUFACTURING*

Additive manufacturing is nowadays widely used in various economic fields but it is still a rather new approach in the building industry. For geopolymers only few studies are presented in the literature. Therefore, in this Chapter, the OPG of this work are investigated for their general potential for additive manufacturing, in addition to the properties with respect to the conventional applications. The OPG in this Chapter are produced with MS(2), SA(3), and LA.

10.1. Introduction

Additive manufacturing of ceramics and other materials can provide many advantages compared to conventional production processes [216, 217]. While various approaches have been extensively studied on ceramics, additive manufacturing of geopolymers was much less considered so far. Nevertheless, geopolymers were successfully produced via the powder printing method [218] and direct ink writing (DIW) [219], proving the general applicability of the material class for additive manufacturing. Since the hardening of geopolymers is generally a condensation reaction, Laser-induced slip casting (LIS) is a promising new method for the additive manufacturing of geopolymer fresh pastes with low viscosities, as has been shown for conventional MK- and FA-based geopolymers, as well as MS- and SA-based OPG [220, 221].

The following Chapter therefore presents the results of preliminary studies on additive manufacturing of the considered OPG via LIS, [216]. Besides the alkaline SA activator another alkali aluminate (lithium aluminate = LA) was used for the experiments. In the regarded silica-based OPG systems, LA provided generally different behavior than SA. Therefore, only in this Chapter the names of the formulations have an additional mark in brackets at the end, either (Na), (Li) or (Na+Li) for the indication of the used alkaline activators.

* Some results of the SA containing mixes have been published in Sturm et al: Additive Manufacturing of Geopolymers by Selective Laser Curing. 92nd DKG Annual Conference & Symposium on High-Performance Ceramics. March 20-22 (2017) and Sturm et al: Additive Manufacturing of Geopolymers by Selective Laser Curing. Proceedings of the 6th International Conference on Non-Traditional Cement & Concrete Brno, Czech Republic, ISBN 978-80-214-5507-8, p. 307 (2017)

10. 2. Experimental program

The preliminary investigations have been conducted on MS_2(Na) (w/b = 0.6), MS_3.5(Na) (w/b = 0.6), MS_3.5(Li) (w/b = 0.5) and MS_3.5(Li + Na) (w/b = 0.5). In the SA and LA containing formulations 50 wt.% of the SA content of the binder was exchanged by LA. In some samples quartz powder was added as a filler material. LIS experiments were performed either with a SP-200C-A-S6-A-A fiber laser device from SPI Lasers (200 W cw, λ = 1.07 µm) or a Rofin CO_2 Laser (λ = 10.6 µm, 100 W, 200 W cw) and a Hurricane scanner from Scanlab (F-Theta-Optics and focal length 300 mm).

For LIS a slurry (or paste) is provided in a hutch, covering a ground plate. The ground plate works as a fundament for the manufactured specimen. The preferred geometry and conditions for the laser curing is implemented via computer. After the laser-treatment, the next layer is adjusted and the procedure starts again [216]. Due to the laser-treatment, a local temperature increase is implemented that accelerates the hardening reaction. Besides LIS, specific OPG were produced conventionally and After preparation and Laser-induced slip casting, the according specimens ('greenstones') were transferred to the oven too. Specimens were cured at 80 °C in an oven, either sealed in plastic foil or at 80% r.H. for 24 h.

10.3. Results and discussion

XRD patterns of the OPG are presented in Fig. 10.1. LIS prepared MS_2(Na) showed that the feedstocks partially reacted and geopolymeric gel formed. Compared to the conventional cured specimens (Fig. 10.1; Sections 4.2.2., 4.4.2.; 5.3.) much less crystalline aluminosilicates formed. HS was observed, but no zeolite A. Significant amounts of bayerite and thermonatrite formed in the LIS sample, related to the experimental conditions. The samples were still wet after LIS and were washed with fresh water, leading to carbonation at the specimen surface. This is also in line with the observed incongruent dissolution behavior of SA, as typical for multioxide compounds [143], with increased initial dissolution of the sodium component and the proposed super saturation with respect to SA in the starting pore solution at high alumina contents (cf. Section 3.2.2.). This leads to the precipitation of alumina gel that crystallizes to aluminum hydroxide and to the carbonation of the sodium species to (thermo)natrite with CO_2 from the air (cf. Chapter 4.). In contrast to conventional curing at 80 °C, where virtually the whole MS feedstock reacted (cf. Section 4.2.2.), the initial hump partially remained. This fits to the observed bayer-

ite and thermonatrite impurities and indicates a lower degree of reaction, related to the very short reaction time compared to the conventional method.

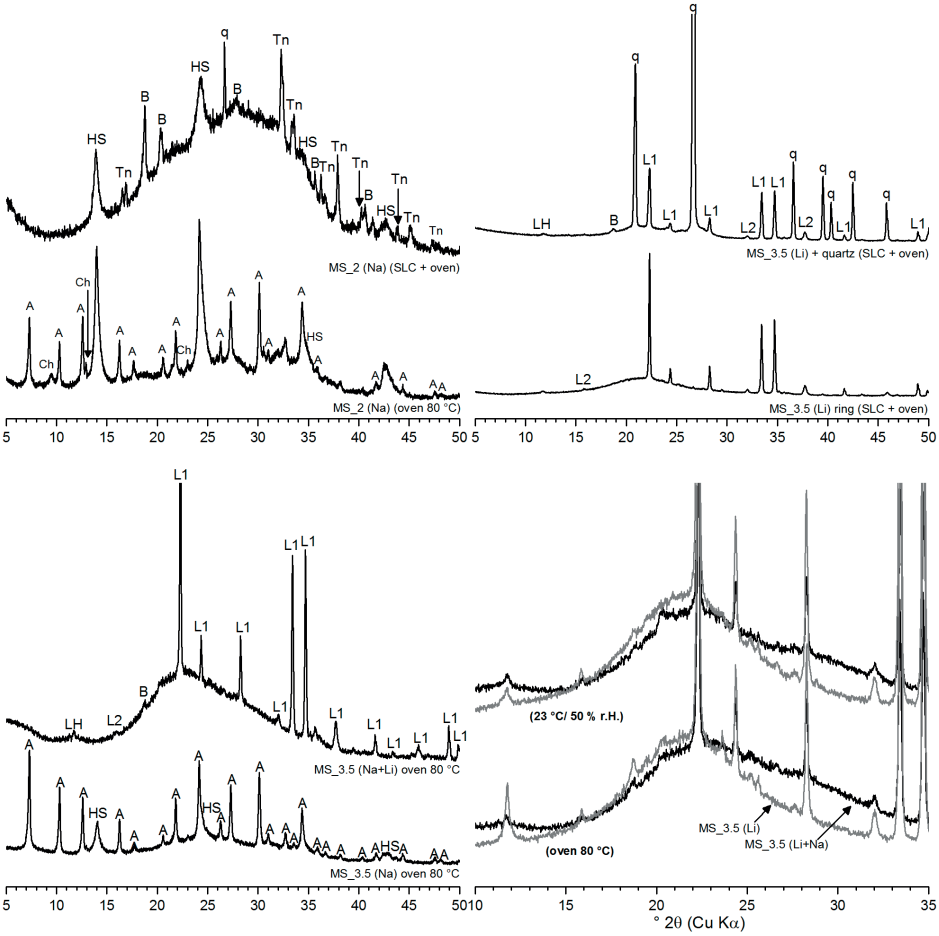

Figure 10.1: XRD results of the LIS experiments on the OPG: LIS of MS_2(Na) compared to conventional oven curing (top left); LIS of MS_3.5(Li), with and without quartz filler (top right); MS_3.5(Na) and MS_3.5(Na+Li) after oven curing (bottom left); MS_3.5(Na) and MS_3.5(Na+Li) after oven curing for 1d or curing at 23 °C/ 50% r.H. for 5d (bottom right); (L1 = $LiAlO_2$; L2 = $LiAl_5O_8$; LH = $LiAl_2(OH)_7{\cdot}2H_2O$; B = bayerite; T = thermonatrite; A = zeolite A; HS = hydrosodalite; q = quartz).

The diffractograms of MS_3.5(Li), with and without quartz filler, after LIS (Fig. 10.1) indicate a low reactivity of the formulation. No significant change of the silica hump occurred and the lithium aluminate related peaks (L1 and L2) remained. A main reason is the much lower solubility of LA compared to SA due to the different ratios of the ionic radii of alkali and aluminum ion, leading to lower distance

between lithium and aluminum ion and a resulting higher binding energy between both compared to sodium and aluminum [222]. This also resulted in almost no heat-development after adding water, whereas the SA-activated OPG pastes always provided temperature increase (up to 48 °C) because of the exothermic dissolution reaction of SA. Furthermore, the pH of the fresh pastes (pH ≈ 10.5) was lower than of the SA-activated pastes (pH > 13; Chapter 4.).

The L1 and L2 related peaks also remained in the MS_3.5(Na+Li) formulations (Fig. 10.1) after conventional oven curing, but the temperature of the fresh pastes increased very much compared to the pure LA formulation. In contrast to the pure MS_3.5(Na) formulation no zeolite A and no HS occurred. Asymmetric broadening of the original hump occurred, indicating partial reaction after oven curing, as well as after curing at 23 °C and 50 °C r.H. (5 days). The lack of zeolites after oven curing and the hardening of the pastes at room temperature reveals an accelerating function of LA as will be discussed below. Despite the acceleration under conventional curing conditions no increased amount of aluminum hydroxide and no thermonatrite were found.

Fig. 10.2 shows photographs of OPG that have been produced by LIS. MS_2(Na) provided a layer structure with huge space between the layers and white fillings of precipitated thermonatrite and bayerite. The observed expansion effect of MS_2(Na) was even more pronounced as for the conventional curing at elevated temperature between 60 °C and 80 °C (cf. Sections 4.2.2 and 4.4.2). Besides the hydrogen release local evaporation of water supported a layered structure as also observed by SEM for sodium activated MS_2, MK- and FA-based geopolymers, synthesized by LIS [220, 221]. The general LIS process worked, but no sufficient specimen geometries could be realized so far.

In contrast to that, a ring, synthesized from MS_3.5(Li) by LIS provided a dense structure and a well-formed geometry with sharp borders (Fig. 10.2). The ring was produced from pure MS_3.5(Li) paste and was affected from moderate shrinkage during curing. The shrinkage was decreased by adding ≈ 50 wt.% quartz powder filler and thus more complex structures, including bulges, for the additive manufacturing of facilities, e.g. for pipes could be realized (Fig. 10.2.). MS_3.5(Li) reached compressive strength of 22 MPa and a flexural strength of 11.6 MPa after LIS and additional oven curing (80 °C). The according mortar (50 wt.% quartz) provided 49 MPa and 6.3 MPa in the manufactured direction.

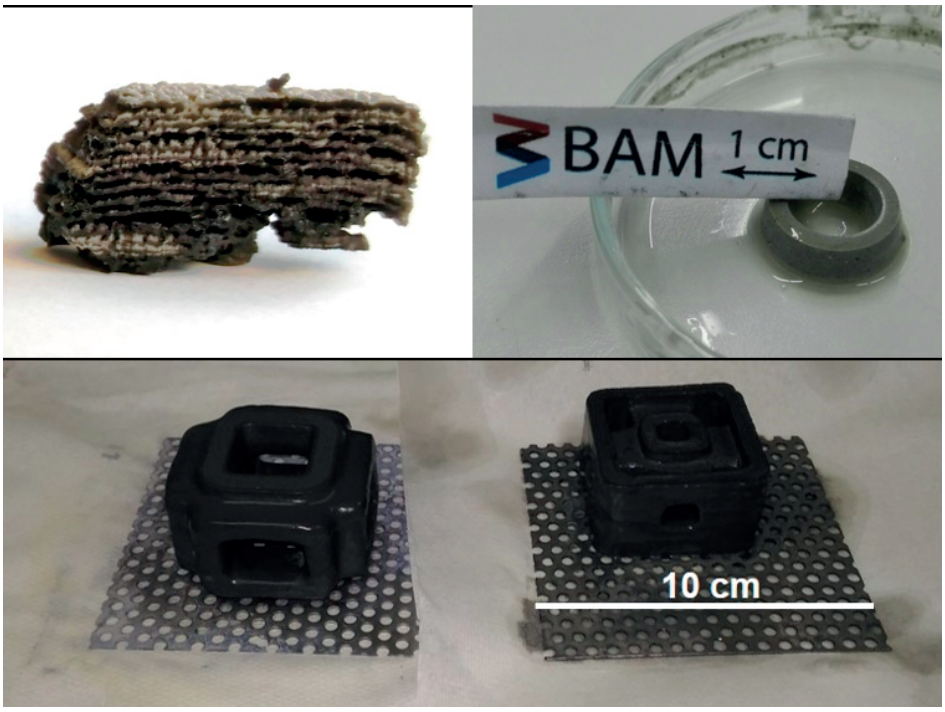

Figure 10.2: Photographs of OPG produced by LIS: MS_2(Na) (top left), a ring from MS_3.5(Li) (top right) and more complex structure for possible elements, synthesized from MS_3.5(Li) with quartz filler (bottom).

Additive manufacturing of MS- and SA-based OPG resulted in huge expansion, due to hydrogen release and local water evaporation. Likely a dense surface layer forms, that hinders the gas release. Furthermore, an increase of the adjusted surface temperature (< 100 °C) up to > 200 °C occurred. This is probably related to a total local dehydration (condensation reaction) and more pronounced coupling of the laser energy to the condensed aluminosilicate network. In contrast to conventional oven curing less HS and no zeolite A formed. In addition, with the partially remaining hump of silica MS, it can be concluded, that accelerated reaction kinetics occur with LIS and the reaction ceases at earlier state. This further correlates with the very fast hardening. The LIS process was always applied only for few seconds on each applied layer. The very fast hardening reaction is also the reason for the significant amounts of secondary bayerite and thermonatrite, due to incongruent dissolution of SA.

The exchange of SA with LA provided a change of the reaction route. This was mainly related to the lower solubility of the LA. No intensive heat-development occurred after the addition of water, opposite to the exothermic dissolution reaction of SA in the according pastes. The viscosity of the activator solution, that dominates

the fresh paste properties especially at low silica contents (= MS_2; cf. Section 2.2.2.); was thus much lower. This also correlated with lower pH values of the fresh pastes. The lower reactivity of LA decreased hydrogen formation during conventional curing and LIS and due to the formation of less dense surface layer hydrogen and evaporated water could be removed. On the other hand, shrinkage was an issue occurring with LA. Less of the water was consumed from the reaction, correlating with the above mentioned fresh paste properties and the release of the excess water during hardening resulted in shrinkage. The shrinkage was significantly decreased by adding quartz powder as filler. Furthermore, the quartz modified formulations could form complex structures, including bulges and moderate compressive strength by synthesis with the LIS method. The main part of the LA related peaks remained after curing and thus only a low amount of reacted material provided the formation of a strong network. The effect of the Li exchange on the microstructure needs to be conducted in further NMR and SEM experiments.

Exchanging 50 wt.% of SA with LA resulted in a further change of the reaction kinetics. In contrast to pure LA containing OPG, that provided no heat-development after the addition of water, a very strong temperature increase was observed for the SA and LA containing OPG fresh pastes and the viscosity strongly increased (above the viscosity of pure SA containing fresh pastes). Furthermore, a strong acceleration even at ambient conditions was observed. As previously mentioned, the pure MS- and SA-based OPG pastes provided no hardening in the cube molds, even after several weeks at room temperature. In contrast to that the hybrid mixes provided hardening in less than 5 hours at 23 °C and 50 °C r.H., respectively. No swelling occurred and due to the acceleration, no zeolites formed, even at 80 °C. The partial reaction of silica MS and formation of aluminosilicate gel was indicated by a broadening of the amorphous hump. No significant differences occurred in the diffractograms of MS_3.5(Na+Li) after ambient conditions or oven curing.

The solubility of alkali aluminates strongly depends on the binding energy between alkali cation and aluminate ion, based on the differences of the ion radii and is much lower for lithium aluminate, compared to aluminates with other alkali ions (Na, K, Rb, Cs) [222], the only disappearing phase of the LA feedstock after curing was always the Li_2CO_3 impurity. In high alumina cements LA, e.g. precipitated from lithium salts such as. Li_2CO_3, was found to be a strong accelerator [223-225] already at very low concentrations of 0.3 wt.% [223], due to the crystal seeds function as heterogenous nucleation substrates of the actual hydration products [223] and the supply of bridging oxygen ions into the aluminate network [224, 225]. The stronger accelerating function of the lithium compounds compared to other alkali metal salts from Na, K, Rb or Cs was attributed to the coordination of lithium with

hydroxyl groups [224]. The function as nucleation substrates of the unreacted or additionally formed lithium aluminate might be a reason for the strong acceleration in the regarded OPG systems too. Further studies are warranted to study the general reaction behavior of LA and LA + SA containing OPG, also regarding the acceleration of SA activated OPG at low LA contents. Further ^{29}Si NMR investigations will be conducted to study the state of the Q sites in the hardened OPG after LIS.

11. CONCLUSIONS AND RECOMMENDATIONS

11.1. Fresh paste behavior and workability of the mortars

The experiments on the fresh paste properties of the MS-based OPG pastes (cf. Chapter 3.) showed that at a comparable and even higher w/b by mass, OPG pastes are significantly stiffer than conventional OPC (CEM I 42.5 R) pastes. This is mainly caused by the high viscosity of the pore solution of the OPG pastes, based on the solubility/ reactivity of the alkaline activator (e.g. Na or Li (Chapter 10.)) and the physical properties of the silica feedstock (e.g. particle shapes, BET, PSD, porosity). This provides a generally increased water demand and a decreased volume related w/b (ρ CEM I > ρ SA > ρ MS/CR/RHA) at equal mass related w/b, whereas it is further decreased with increasing MS content. Lower amounts of mixing water and higher SiO_2/Al_2O_3-ratios led to an increase of yield stress and viscosity (except for viscosity of SiO_2/Al_2O_3 > 4.7 at w/b = 0.6, cf. Chapter 3.), due to the decrease of the w/b (by volume) and increasing SiO_2/Al_2O_3, *i.e.* the initial amount of MS particles.

The CR-based fresh pastes appeared stiffer than the MS-based fresh pastes, whereas the RHA(1)-based fresh paste was more flowable at equal composition. Especially the BET surface and particle shapes as well as the solubility rate of the silica are considered to be the main reasons for the different fresh paste behavior that occurred within the different silicas. CR-based pastes provided the poorest workability but provided comparable primary particle sizes as MS (Section 2.2.2.; Fig. 2.5), but a higher BET surface and resulting an increased agglomeration tendency and water adsorption. RHA(1) provided the highest BET surface by far (≈ 50 m^2/g) due to the angular shaped particles, but a significantly coarser PSD than MS and CR. The unground RHA(2) provided the coarsest PSD of all silicas by far and correlating the lowest BET surface (≈ 14 m^2/g). The technical grade RHA(2) provided uncommon workability at high silica contents. However, further investigations on the preparation of RHA(2), including grinding need to be conducted (see below) for an improvement of the RHA(2)-based fresh paste properties. As the investigations on the strength development revealed, high silica contents often correlate with improved properties in the hardened state. Thus, generally compromises must be made regarding the workability of the fresh pastes.

Additional investigations on the general influence of superplasticizers (PCE, NFS, LiS a) and LiS b)) have been conducted on MS-based and SL containing MS-based OPG pastes. PCE and NFS caused virtually no changes at the considered concen-

trations in the highly alkaline milieu. The lignin sulfonates instead provided more promising results. In this context LiS a) had a more pronounced effect in the slag free mix. The spread flow was increased up to 125% (Section 3.3.2). In the slag containing, *i.e.* CaO containing mix, both additives increased the spread flow to ≥ 130% (Section 3.3.2; Fig. 3.6) at a concentration of 0.75 wt.% of the binder mass.

The preliminary experiments with LA revealed much lower viscosities of the fresh pastes. This is mainly related to the lower solubility of lithium aluminate, leading to lower viscosity of the activator solution and lower dissolution rate of silica MS, correlating with lower measured pH values of the fresh pastes. Hybrid mixes with LA and SA provide a strong re-increase of the viscosity and strong heat-development, correlating with a significant acceleration of the hardening reaction. Preliminary interpretations suggest an enhanced nucleation of the actual reaction products due to the lithium aluminate seedings.

The experiments on the workability of the OPG mortars, revealed comparable behavior to the pure pastes. At equal paste and water contents, the workability of the mortars improved with decreasing silica content of the paste, *i.e.* with decreasing amount of solid silica and resulting increasing liquids to solids ratio by volume. At equal water contents, the spread flow of low paste content mortars increases with increasing paste content (= decreasing w/b) up to a certain point, since the aggregate interactions increase with decreasing paste content. Low paste content OPG mortars provide good manual applicability by trowel as observed by *in-situ* experiments (Section 6.2.; Fig. 6.6), due to the less pronounced sticky character of the fresh pastes and mortars with a rather low binder content are cheaper than the ones with high paste contents. For spray and skidding applications with included pumping activities, promising *in-situ* experiments were performed on high paste content MS-based mortars (Section 6.2.; Fig. 6.6). The high MS content provided very good pumping properties and initial bonding behavior (Section 6.2.; Fig. 6.6) of the sticky mortars in various layer thicknesses at vertical walls and manholes. In addition, the generally long processing time at room temperature compared to established commercial systems, without the necessity of adding retarding additives, is further benefit for real live applications.

11.2. Structure and hardening

After curing at elevated temperatures (60–90 °C) between one and seven days OPG, synthesized from MS or CR and SA led to the formation of geopolymer-zeolite composites. At 80 °C, the composites contained zeolite A and HS as major crystal-

line reaction products, as well as geopolymeric gel and depending on the chemical composition, remaining silica feedstock. Both crystalline main phases provide molar SiO_2/Al_2O_3 ratios of 2. For the MS-based OPG, the amount of HS increased with decreasing amount of silica content, *i.e.* with increasing degree of reaction, whereas the amount of zeolite A was more constant over the investigated range of the starting composition (SiO_2/Al_2O_3: $2 \leq X \leq 6$ mol/mol, cf. Section 4.2.). For CR-based OPG certain amounts of faujasite-type, EMT and zeolite P formed at low silica starting contents (Tab. 11.2). With increasing silica content, the degree of reaction of the silica feedstock decreased and the reaction ceased when an SiO_2/Al_2O_3 of ≈ 2 mol/mol was reached for the reaction products (at 80 °C). When the chemical composition of the fresh paste was adjusted to SiO_2/Al_2O_3 of = 2 mol/mol, virtually the whole silica feedstock (CR or MS) reacted (cf. Section 4.2.).

Below 70 °C the formation of (hydro)sodalite-type phases was virtually avoided and at ≥ 80° C the HS formation was enhanced especially for MS-based OPG and at 90 °C also for CR-based OPG, indicating a significant acceleration of the reaction kinetics and nucleation tendency. At ≥ 70 °C and ≤ 90 °C no significant changes occurred for curing times > 24 hours, indicating the ceasing of the phase formation and no necessity of curing for longer times and the applied sample geometry (at 80% r.H.). The zeolite formation was virtually avoided for low silica CR- and MS-based OPG at 60 °C after 24 hours curing.

The degree of reaction of the MS- and CR-based composites, that only contain aluminosilicate reaction products with SiO_2/Al_2O_3 of = 2 can be estimated using a chemical method (dissolution in HCl). Judging from NMR quantification [70], the results of the dissolution method are lower than they actually are, in particular at lowered degrees of reaction (MS, CR). However, both methods clearly disclosed the same trends for changes of the degree of reaction, depending on the geopolymer formulation and curing time, making the dissolution method at least useful to follow these trends for the MS-based OPG and with limitation for CR-based geopolymer-zeolite composites (Section 4.2.). For RHA(1)-based OPG with SiO_2/Al_2O_3 > 2 mol/mol in the reaction products the dissolution method is inadequate as discussed above (cf. Section 4.3.), because silica enriched residues of the reaction products contribute to the residual overall mass.

In contrast to the MS and CR-based OPG, OPG based on RHA(1) provided the formation of zeolite free aluminosilicate gels. As shown in Section 4.3.2., the feedstocks almost completely reacted and transformed into amorphous geopolymer (N-A-S(-H) gel) for the formulation with an intermediary molar SiO_2/Al_2O_3 starting ratio of 3.5. The technical grade RHA(2) provided comparable behavior, *i.e.* the

absence of crystalline aluminosilicates, also at higher SiO_2/Al_2O_3 ratio ($3.5 < X \leq 8$) after curing at 80 °C. Considerable amounts of aluminum hydroxide precipitated. Because of the crystalline (unreactive) SiO_2 content (cristobalite) an SA excess was introduced. Tab. 11.1 shows the qualitative composition of the OPG, synthesized with the different silica sources at 80 °C.

Table 11.1: Summary of the qualitative phase assemblage of the OPG systems after curing at 80 °C and 80% r.H., respectively. The values in brackets refer to phases that did not occur in all samples.

SiO_2/Al_2O_3 (mol/mol)	MS	CR	RHA(1)	RHA(2)
2	gel, A, HS, (Ch), (MS)	gel, A, HS, S, F, EMT, (P), (CR)	-	
3.5	gel, A, HS, MS	gel, A, (F), CR	gel, RHA	gel, (A), RHA
6	gel, A, HS, MS	gel, A, CR	-	gel, RHA
8	-	-	-	gel, RHA
Impurities	(G), (T)	(H)	T	T, G, (B)

In general, the CR- and MS-based composites (cured at 80 °C) provided a particulate microstructure, with interconnected pores and lots of interfaces, especially for high alumina formulations. The denser microstructure of the RHA(1)- and RHA(2)-based formulations, with $SiO_2/Al_2O_3 > 2$ mol/mol in the reaction products, is considered to be a main reason for the higher compressive strength of the according pastes.

Differences in the mechanical properties of the geopolymers were related to the observed differences in the amount of remaining (non-reacted) silica, the phase assemblage and overlapping expansion. While the compressive strength of the MS-based geopolymers increased with increasing silica content, the opposite trend was observed for the CR-based OPG. A main reason for the decreasing strength of MS (and RHA(2)) based OPG with increasing SA content is the related increasing expansion (density decrease), cracking and foaming (MS_2). In general, the more of the silica feedstock reacted, the more expansion occurred. because the higher the degree of reaction of the silica, the more of the foaming agent (mainly Si) was released. The opposite strength trend, observed for the much less expanding CR-based OPG, revealed a considerable strength of highly reacted OPG without overlapping effects. Tab. 11.2 presents the compressive strength of OPG pastes after one day of curing at different elevated temperatures.

The relative compressive strength of the CR- and MS-based mortars was comparable to those of the pure OPG pastes. For MS-based mortars the initial compressive strength after curing at elevated temperature increased with increasing MS content.

The swelling was less pronounced in general and in consequence the differences of the strength decreased for the different formulations.

Table: 11.2: Summary of the compressive strength of the OPG pastes after one day of curing at various elevated temperatures and 80% r.H., respectively.

Sample	w/b	1d Compressive strength (MPa)			
		60 °C	70 °C	80 °C	90 °C
MS_2	0.5	3	2	3	4
MS_3.5	0.5	-	-	8	-
MS_6	0.5	7	15	20	20
CR_2	0.5	3	17	10	10
CR_3.5	0.5	-	-	10	-
CR_6	0.5	6	9	14	6
RHA(1)_3.5	0.5	-	-	30	-
RHA(2)_3.5	0.4	-	-	14-56	-
RHA(2)_6	0.4	-	-	22-40	-
RHA(2)_8	0.4	-	-	20-24	-

The initial (1d) strength of the MS-based mortars provided a continuous increase with increasing curing temperature from 60 °C to 80 °C. The most significant increase occurred between 70 °C and 80 °C. This is the result of a scaling factor. The bigger mortar specimens (40 mm × 40 mm × 160 mm) contained higher volume of material and thus a higher temperature is needed to attract the volume in a comparable time (cf. Section 7.2). Furthermore, mortars with higher paste volume need a higher curing temperature to achieve comparable strength in comparable times. The necessary temperature for high initial strength can be decreased by exchanging parts of the MS-based formulation with a CaO containing slag. Up to 80 °C the differences to the slag free mix decrease. Thus, by adding 10 wt.% CaO, the curing temperature can be decreased by 20 °C to provide comparable or even higher initial strength (1d). Tab. 11.3 presents the compressive strength of OPG mortars after one day of curing at different elevated temperatures.

The further strength development of the OPG mortar at ambient temperature (23 °C) depends on the relative humidity of the ambience (Tab. 11.4). Curing at 50% r.H. provided always higher final strength after 91 days, than curing above water (≈ 100% r.H.) and the main part of the strength gaining occurs up to 28 days. The exception is the slag free RHA(2)-based mortar, that provide the lowest initial strength, but a continuous increase of the mechanical strength up to 91 days.

Table: 11.3: Summary of the flexural and compressive strength (flex/comp) of the OPG mortars, produced with RS aggregates, after one day of curing at various elevated temperatures and 80% r.H., respectively.

Sample	w/b	1d Flexural and compressive strength (MPa)			
		50 °C	60 °C	70 °C	80 °C
MS_2	0.5	-	-	2.0/ 8	
MS_3.5	0.5	-	-	2.7/ 15	-
MS_6_RS	*0.5*	-	-	2.7/ 17	-
CR_2	*0.5*	-	-	3.4/ 24	-
CR_3.5	0.5	-	-	3.3/ 23	2.8/ 20
CR_6	0.8	-	-	0/ 0	-
MS_6	*0.4*	-	3.1-3.8/ 22-26	4.0-4.3/ 30-32	4.8-5.3/ 40-50
MS_6_SL	0.38	3.8-4.0/ 31-33	6.1-6.5/ 42-49	6.8/ 52	6.7/ 52
RHA_6	*0.4*	-	-	-	4.5/ 30
RHA_6_SL	*0.38*	-	2.8/ 20	-	5.3/35

When only cured at 23 °C and 50% r.H., the finally observed compressive strength (78 MPa) and flexural strength (11.6 MPa) of MS_6_SL were the maximum values of all considered samples of this work (Tab. 11.4). The slag free MS-based mortars reached a compressive strength of 42 MPa and the flexural strength 6.9 MPa after 91 days. Curing of the OPG mortars above water (r.H. ≈ 100 %) provided much less improvement of the mechanical strength, because the necessary release of water for further increasing condensation and precipitation is decelerated.

Summarizing, the hardening and strength development of the OPG depends on the degree of reaction of the used silica source and thus the reactivity of the silica also determines the achievable amount of the silicon for the reaction products. Increased silicon contents in the reaction products support higher degrees of condensation, the avoidance of zeolite formation and a resulting denser microstructure. Due to impurities, the actual strength of a hardened OPG mix can be overlapped by expansion, especially at high degrees of reaction of the according silica. The hardening is significantly accelerated by the addition of CaO containing slag, providing increased Na_2O+CaO/H_2O ratios. The activation of the slag, thus enhances the activation of the mix. Curing at ambient temperature is enhanced by lowering the relative humidity from ≈ 100% to 50%, due to enhancing of the polycondensation. The addition of sand aggregates as nucleation sites, further accelerates the hardening process.

Table: 11.4: Summary of the flexural and compressive strength (flex/comp) development of the OPG mortars, produced with RS aggregates, after initial curing at elevated temperatures and further curing at 23 °C and 50% r.H. or 23 °C and ≈ 100% r.H., respectively. Samples marked with "RT" were produced without initial curing at elevated temperature. Samples marked with "SL" were initially cured at 60 °C for 1d. Samples without RT or SL were initially cured at 80 °C for 1d.

Sample	w/b	Flexural and compressive strength (MPa)			
		28 d	56 d	91 d	182 d
		Curing at 23 °C and 50% r.H.			
MS_6_1.3_RS	0.4	6.9/ 60	6.3/ 60	8.1/ 67	-
MS_6_1.3_RS_RT	0.4	4.5/ 25	6.1/ 39	6.9/ 42	-
MS_6_SL_0.9_RS	0.38	7.0-8.9/ 61-70	6.9-9.8/ 60-72	7.6-8.8/ 58-62	8.3/ 62
MS_6_SL_0.9_RS_RT	0.38	7.1/ 63	8.1/ 73	10.2/ 73	11.6/ 77
RHA_6_1.3_RS	0.4	6.2/ 47	8.1/ 55	8.5/ 65	-
RHA_6_SL_1.3_RS	0.38	5.4/ 32	6.1/ 32	6.5/ 33	-
		Curing at 23 °C above water (≈ 100% r.H.)			
MS_6_1.3_RS	0.4	5.5/ 46	6.1/ 48	6.9/ 53	-
MS_6_SL_0.9_RS	0.38	6.7/ 50	7.9/ 57	6.4/ 50	-
RHA_6_1.3_RS	0.4	4.4/ 27	5.4/ 25	5.3/ 28	-
RHA_6_SL_1.3_RS	0.38	3.7/ 26	4.1/ 29	4.6/ 28	-

11.3. High-temperature resistance

The thermal dehydration of the MS and CR and RHA(2)-based OPG started at approximately 60 °C (cf. Chapter 5.). While the major part of the dehydration occurred at < 200 °C. The final temperature could be hardly identified by TG. RHA(2)-based OPG provided a more distinct two-step dehydration than the MS and CR-based OPG. Depending on the sample composition the first and bigger dehydration step, occurring from the loss of free (adsorbed) water ended between 125 and 150 °C. The second step, including the dehydroxylation of aluminum hydroxide, started at 178-185 °C and ended between 290 °C and 305 °C. IR indicated the disappearance of all water related bands after treatment at 400 °C. The observed results are in line with the reported dehydration behavior of geopolymers, as well as for hydrated zeolite A (Section 5.3.1; Fig 5.2) and HS in the reported literature (e.g. [9, 12, 14, 120, 138, 139, 155, 158, 161-163, 226]).

An approximately linear shrinkage was observed for the geopolymer-zeolite composites up to 700 °C, with the maximum shrinkage up to this temperature being ca. 2–3% and < 1.5% below 400 °C. No significant influence of the composition on the thermal deformation behavior was observed in the same temperature range.

This behavior differs from the behavior of MK- and FA-based geopolymers, known from the literature, with high amounts of N(-C)-A-S(-H) gel, *i.e.* rapid shrinkage in the dehydration range < 200 °C due to the release of "structural" water from the gel (e.g. [12, 14, 155, 157, 158]). This makes the investigated composites interesting for applications at moderate high temperatures. The observation lead to the conclusion (together with the TG results and the observed phase contents) that the incorporated water is more of zeolitic character for the investigated CR- and MS-based systems. Thermal-treatment at moderate temperatures (200–400 °C) led to a strength improvement. Heating above this range led to a moderate performance loss up to 700 °C.

The RHA(2)-based OPG provided an increase of the residual compressive strength up to ≤ 200 °C, *i.e.* in the range of the maximum dehydration and remained more or less constant up to 600 °C. The exception was the zeolite free RHA_3.5 mix. The mix provided a continuous decrease of the compressive strength up to 400 °C, due to the high amount of reaction products and correlating increased amount of structural important water. The zeolite containing mix provided an increase up to 200 °C and constant levels up to 600 °C, very similar to the previous described MS and CR-based geopolymer-zeolite composites. Thus, the performance of the former one is presumably attributed to the release of structural water, of the second thermal dehydration step and the formation of weakening cracks. Further dilatometer and SEM investigations need to be conducted for a final evaluation.

Above ca. 700 °C extensive shrinkage deformations occurred in all OPG mixes, independent from the silica feedstock. This behavior is caused by structural breakdown of the initial phases and sintering/densification and/or partial melting. Certain mixes with unreacted silica after curing provided extensive expansion at higher temperatures (≥ 750 °C), as also found for MS-based intumescent protective fire-coatings [160]. For example, SiC and Si are known as expanding agents at high temperatures. However, the expansion process at high temperatures of the regarded OPG of this work is not fully clear yet.

The MS- and CR-based low-silica and medium-silica specimens formed nepheline-type and/or carnegieite-type stuffed silica phases at 1000 °C, which are of some interest for the ceramic industry. The high-silica mixes formed mainly an amorphous phase at 1000 °C. Independent from the chemical composition ($3.5 < SiO_2/Al_2O_3 \leq 8$), for the RHA(2)-based OPG partial melting occurred at ≥ 800 °C, leading to virtually fully amorphous samples after exposure to 1000 °C with a back shifted maximum of the hump in the XRD patterns, due to the incorporation of the unre-

acted Si after curing and traces of nepheline. The studied OPG can be a promising alternative for CEM III/B for applications in the temperature range < 800 °C.

11.4. Shrinkage and bond strength

The shrinkage measurements on the initially elevated temperature cured OPG mortars revealed promissing behavior. The low shrinkage of the OPG mortars under ther more dry conditions, connected with the significant higher loss due to the drying effect suggests the moisture loss of the OPG mortars was mainly attributed to physically bond water. This fits into the observations of the thermal deformation in the dehydration range of the MS- and CR-based OPG pastes (cf. Section 5.3.). All OPG mortars fullfilled the requirements of DIN EN 12617-4, Rili-SIB and DIN 19573 after 28 days storage at 23 °C and 50% r.H. for allowed shrinkage by far and even after 91 days the requiremts for the 28 days shrinkage where still achieved. Except the slag free RHA(2)-based OPG mortar, who's absolute shrinkage was negligible all specimens reached a plateau, i.e the shrinkage became virtually constant and the main part of the shrinkage occurred withing the first 20 days. This fits into the periode of the most significant strength evolution (Sections 7.2. and 11.3.). However, for a final evaluation additional analyses of the portion of drying shrinkage and autogenous shrinkage have to be part of further studies.

The reaching of plateaus suggest no further significant shrinkage under this conditions. Storing under the more humid conditions (23 °C/ ≈ 100% r.H.) resulted in expansion for all considered OPG mortars. The expansion was even less pronuonced than the shrinkage, although a significant mass gain due to the wetting effect occured. This suggests the moisture gain of the OPG mortars was mainly attributed to physically bond water. All OPG mortars achieved the requirements of DIN EN 12617-4, Rili-SIB and DIN 19573 after 28 days for allowed expansion and even after 90 days, the 28 days requirements were fullfilled. As for the shrinkage under the more dry conditions, the OPG mortar specimens reached a plateau, i.e the expansion became virtually constant after a certain time. This suggests no further significant expansion under the regarded consitions. The general observed shrinkage/expansion behavior is a clear advantage of the regarded OPG mortars compared to other conventional geopolymers and alkali-activated slags from the literature (cf. e.g. [62, 63, 65, 180]).

The considerably low paste contents of the mortars (30-40 wt. %), e.g. compared to CAC_REF (> 55 wt.%) further contributed to the excellent shrinkage behavior. The general promissing shrinkage behavior of the OPG mortars is considerably attributed to the initial curing at elevated temperatures. The main part of the reaction and hardening of the OPG mortars occurs within the first 24 hours and the mortars

provided already moderate or high mechanical strength after that time (cf. Section 7.2.). Furthermore, already considerable amounts of (excess) water are removed (80% r.H.). The observed benefits of elevated temperture curing fit into the observations of the reported literature [62, 146, 147, 175].

In contrast to that, for the MS-based mortars a negative effect on the absolute pull-off strength was found for specimens, that have been initially cured at elevated temperatures. The actual bond strength between mortars and substrate was always higher than the detected values. The main reason is the introduction of horizontal expansion cracks during hardening. On the other hand, MS-based OPG mortars (> 3 MPa) and MS- (+ SL) based (> 3.5 MPa) that were only cured at 23 °C and 50% r.H. achieved the requirements of DIN 19573, including repair mortars (class B1; B2), coating mortars (class B1; B2) and injection mortars. Furthermore, the requirements of Rili-SIB for all three exposition classes (M1; M2; M3) were achieved. No expansion cracks were found by optical microscopy. Compared to mortar prisms, the geometry of the specimens for the measurement of the bond strength further accelerates the hardening. This behavior is beneficial for a potential application as repair mortar (e.g. for sewer maintenance). For the RHA(2)-based samples an opposite trend was observed. A degradation of the pull-off strength was identified for decreasing curing temperatures. This fits into the generally slower hardening/ strengthening speed of the RHA(2)-based mortars and may lead to further increased pull-off strength at later ages.

11.5. Acid resistance

For all OPG mortars, huge parts of the corroded layer were not dissolved during treatment with H_2SO_4 (pH 1) and remained a structural part of the specimen, with the potential to still provide protection for a substrate. No major spalling of the surface was observed. MS and RHA(2)-based mortars reached 77% or 78% residual strength, and thus achieved the requirements of DIN 19573: 2016 (Appendix A; pH 1) and Rili-SIB (class II).

The microstructural investigations on the MS-based OPG pastes revealed a corrosion process that led to the dissolution of the of aluminosilicates, *i.e.* geopolymer gel and zeolites. As observed for the dissolution experiments in HCl, NMR, XRD and ICP-OES showed that after the treatment with H_2SO_4, the samples were virtually free of aluminum and aluminum related silicon sites. The ^{29}Si NMR single pulse spectrum contained only Q_4 (0Al) and Q_3 (0Al) sites, *i.e.* mainly the unreacted and partially dissolved silica MS, and probably a secondary precipitated silica rich

gel. The dissolution of the primary reaction products resulted in a more particulate microstructure, providing more interfaces, partially dissolved fracture pieces and presumably an increased pore volume, in line with the observations of the literature (e.g. FA- and MK-based GP [30, 197, 199, 201, 227]).

The promising observed acid resistance of the OPG is in line with the results of previous studies on geopolymers and geopolymer mortars [16, 30, 173, 196, 199-201, 203]. For the considered OPG of this work, it is thus interpreted that the precipitation of silica gel at the acid-geopolymer interface is a major mechanism responsible for the high acid resistance of the studied mortars. The gel covers the surface of the exposed mortar and decreases further dissolution, which explains the high acid resistance of both, the mortars based on geopolymer-zeolite composites and on geopolymers. In addition, any unreacted silica will act as insoluble filler in the matrix, further improving the acid resistance of the composites. Regarding the biogenic sulfuric acid attack, it can be expected that the high concentration of dissolved Al, will probably inhibit the activity of sulfuric acid-producing bacteria as found for CAC-based mortars [215]. Furthermore, the increased initial pH value of the pore solution (pH > 13) compared to many conventional cementitious repair mortars, provides an increased buffer function, since an increased formation of thiobacilla starts at pH < 9 and above pH 11 virtually none of these bacteria occurs *in-situ*.

OPG mortars with an absolute CaO binder content of 10 wt.% provided less acid resistance. A main reason for this was expansion, cracking and a related weakening of the structure, whereas again huge parts of the corroded layer did not dissolve. The general phase formation during hardening and the corrosion process remained the same for the slag containing OPG, but additionally precipitation of gypsum occurred in H_2SO_4, due to the increased calcium content and its reaction with the sulfate ions, whereas sodium sulfate will not precipitate due to its high solubility [142]. This gypsum is the main reason for the lower acid resistance of the slag containing MS-based systems. The precipitation of gypsum causes expansion, cracking and related lower sulfuric acid resistance of the mortars. Decreasing the CaO content to 1.0 wt.% resulted in much better acid resistance and a residual strength of > 75 %, achieving the requirements of DIN 19573. Therefore, the results of the slag containing OPG mortars suggest a limitation of the CaO content for applications with necessarily high as acid resistance.

11.6. Influence of Li and additive manufacturing

In general, promising results on additive manufacturing of the OPG by LIS were observed. LIS on MS- and SA-based OPG resulted in expansion, due to hydrogen release and local water evaporation together with a dense surface layer, contradicting the gas release. Due to the accelerated reaction kinetics the reaction ceases at earlier state. This further correlates with the very fast (flash) hardening. The very fast main reaction is also a major reason for the significant amounts of observed bayerite and thermonatrite.

The exchange of SA with LA provided much lower viscosity of the fresh pastes. This also correlated with lower pH values of the fresh pastes, revealing a lower reactivity of LA. The formulations are furthermore very good applicable with LIS. Exchanging 50 wt.% of SA with LA resulted in a very strong temperature development and viscosity increase of the fresh pastes. Furthermore, a strong acceleration was found for pure LA formulations and SA containing hybrid formulations. No swelling and no zeolites occurred, even for conventional curing at 80 °C. In high alumina cements LA was found to be a strong accelerator [223] Besides the good behavior of pure LA activated OPG, further studies on acceleration function in SA activated OPG at much lower LA concentration are of interest for the adjustment of the SA-activated OPG mortars at room temperature.

11.7. Future work

A major importance for the degree of reaction and the resulting microstructure (gel + zeolites + unreacted silica + pores) was the kind of silica source (e.g. crystallinity, BET, PSD, particle shapes, porosity, solubility). Future work should therefore focus on the processing of the technical RHA(2), including granulation with further feedstocks and additional grinding. First results show promising improvement of the OPG fresh pastes, even at high silica RHA(2) contents. Further feedstocks, such as bagasse ash, with SiO_2 contents up to > 70 wt.% and additional ingredients should be included as well. The superior goal for a contribution to a better sustainability at the very end would be the synthesis of OPG from various residues with regional dependency. In the context of sustainability, the reactivation of the OPG, e.g. after thermal-treatment, should be considered as well.

Further investigation on the protective function of the OPG coatings should be considered. In this context, a next step would be the exposure of OPG coated concrete specimens to sulfuric acid to study the residual bond strengths and the alteration of the substrate. Furthermore, concrete corrosion from organic acid attack

is a major issue with increasing importance, especially in the field of agriculture. Besides a further improvement of the additive manufacturing with LA, including necessary investigations of the microstructure, the accelerating function of LA can be used as fundament for an extended study on accelerators for the OPG systems besides the presented slag.

LIST OF FIGURES

LIST OF TABLES

REFERENCES

[1] H. Kühl: Slag Cement and Process of making the same, US patent 900,939 (1908), p. 2.

[2] H. Kühl: "Kolloide Zementerhärtung," Zement 19 (1930), pp. 262-264.

[3] V. D. Gluchovskij, "Alkalischlackebeton" Baustoffindustrie 17 (1974), pp. 9-13.

[4] J. L. Provis and J. S. J. Van Deventer, Alkali activated materials: State-of-the-art-report, RILEM TC 224-AAM, ed. Dordrecht: Springer, 2014.

[5] J. Davidovits: Synthesis of new high-temperature geopolymers for reinforced plastics/composites, in: Pactec'79, Society of Plastic Engineers, (1979), pp. 151-154.

[6] J. Davidovits: Geopolymers: inorganic polymeric new materials Journal of Thermal Analysis and Calorimetry 37 (1991), pp. 1633-1656.

[7] J. Davidovits, M. Davidovics: Geopolymer: room-temperature ceramic matrix for composites, Ceramic Engineering and Science Proceedings 9 (1988), pp. 835-841.

[8] J. Davidovits: Geopolymers and Geopolymeric Materials, Journal of Thermal Analysis and Calorimetry 35 (1989), pp. 429-441.

[9] V.F.F. Barbossa, K.J.D. MacKenzie: Thermal behaviour of inorganic geopolymers and composites derived from sodium polysialate, Materials Research Bulletin 38 (2003), pp. 319-331.

[10] A. Fernández-Jiménez, A. Palomo: New Cementitious Materials Based on Alkali-Activated Fly Ash: Performance at High Temperatures, Journal of the American Ceramic Society 91 (2008), pp. 3308-3314.

[11] W.D.A. Rickard, G.J.G. Gluth, K. Pistol: In-situ thermo-mechanical testing of fly ash geopolymer concretes made with quartz and expanded clay aggregates , Cement and Concrete Research 80 (2016), pp. 33-43.

[12] W.D.A. Rickard, C.S. Kealley, A. van Riessen: Thermally Induced Microstructural Changes in Fly Ash Geopolymers: Experimental Results and Proposed Model, Journal of the American Ceramic Society 98 (2015), pp. 929-939.

[13] W.D.A. Rickard, J. Temuujin, A. van Riessen: Thermal analysis of geopolymer pastes synthesised from five fly ashes of variable composition, Journal of Non-Crystalline Solids 358 (2012), pp. 1830-1839.

[14] L. Vickers, W.D.A. Rickard, A. van Riessen: Strategies to control the high temperature shrinkage of fly ash based geopolymers, Thermochimica Acta 580 (2014), pp. 20-27.

[15] L. Vidal, E. Joussein, M. Colas, J. Absi, S. Rossignol: Effect of the addition of ammonium molybdate on metakaolin-based geopolymer formation: Shrinkage and crystallization, Powder Technology 275 (2015), pp. 211-219.

[16] C. Montes, E.N. Allouche: Evaluation of the potential of geopolymer mortar in the rehabilitation of buried infrastructure, Structure and Infrastructure Engineering 8 (2012), pp. 89-98.

[17] H. Alanazi, M. Yang, D. Zhang, Z. Gao: Bond strength of PCC pavement repairs using metakaolin-based geopolymer mortar, Cement & Concrete Composites 65 (2016), pp. 75-82.

[18] H.Y. Zhang, V. Kodur, S.L. Qi, B. Wu: Characterizing the bond strength of geopolymers at ambient and elevated temperatures, Cement & Concrete Composites 58 (2015), pp. 40-49.

[19] P. Duxon, J.L. Provis, G.C. Lukey, A. Palomo, J.S.J. van Deventer: The role of inorganic polymer technology in the development of 'green concrete', Cement and Concrete Research 37 (2007), pp. 1590-1597.

[20] P. Duxon, A. Fernández-Jiménez, J.L. Provis, G.C. Lukey, A. Palomo, J.S.J. Van Deventer: Geopolymer technology: the current state of the art, Journal of Materials Sciences 42 (2007), pp. 2917-2933.

[21] E. Gartner: Industrially interesting approaches to “low-CO2” cements, Cement and Concrete Research 34 (2004) 1489-1498.

[22] C. Le Quéré, G. Peters, R. Andrew, B. Andres, T. Boden, T. Conway, S. Houghton, J. House, G. Marland, G. van der Werf, A. Ahlström, L. Bopp, P. Caanadell, P. Ciais, S. Doney, C. Enright, P. Friedlingstein, C. Huntingford, A. Jain, C. Jourdain, E. Kato, R. Keeling, K. Klein Goldewijk, S. Levis, P. Levy, M. Lomas, B. Poulter, M. Raupach, J. Schwinger, S. Stich, B. Stocker, N. Viovy, C. Wilson, S. Zaehle, N. Zeng, Global Carbon Budget 2012, (2013).

[23] R.M. Andrew: Global CO2 emissions from cement production, Earth System Science Data Discussions (2017).

[24] J. Davidovits, Geopolymer chemistry and sustainable Development. The Poly(sialate) terminology: a very useful and simple model for the promotion and understanding of green-chemistry, in: World Congress Geopolymer, 2005.

[25] J.L. Provis, J.S.J. van Deventer: Geopolymerisation kinetics. 2. Reaction kinetic modelling, Chemical Engineering Science 62 (2007), pp. 2318-2329.

[26] V.F.F. Barbossa, K.J.D. MacKenzie, C. Thaumaturgo: Synthesis and characterisation of materials based on inorganic polymers of alumina and silica: sodium polysialate polymers, International Journal of Inorganic Materials 2 (2000), pp. 309-317.

[27] A. Palomo, S. Alonso, A. Fernández-Jiménez: Alkaline Activation of Fly Ashes: NMR Study of the Reaction Products, Journal of the American Ceramic Society 87 (2004), pp. 1141-1145.

[28] H. Rahier, B. van Mele: Low-temperature synthesized aluminosilicate glasses Part I Low-temperature reaction stoichiometry and structure of a model compound, Journal of Materials Sciences 31 (1996), pp. 71-79.

[29] J.L. Provis, G.C. Lukey, J.S.J. van Deventer: Do Geopolymers Actually Contain Nanocrystalline Zeolites? A Reexamination of Existing Results, Chemistry of Materials 17 (2005), pp. 3075-3085.

[30] T. Bakharev: Resistance of geopolymer materials to acid attack, Cement and Concrete Research 35 (2005), pp. 658-670.

[31] W.M. Kriven, J.L. Bell, M. Gordon, Microstructure and microchemistry of fully-reacted geopolymers and geopolymer matrix composites, in: N.P.S. Bansai, J. P.; Kriven, W. M.; Schneider, H. (Ed.) Advances in Ceramic Matrix Composites, vol 153, The American Ceramic Society, Nashville, (2003), pp. 227-250.

[32] J.L. Bell, P. Sarin, P.E. Driemeyer, R.P. Haggerty, P.J. Chupas, W.M. Kriven: X-Ray pair distribution function analysis of a metakaolin-based, KAlSi2O6·5.5H2O inorganic polymer (geopolymer), Journal of Materials Chemistry 18 (2008), pp. 5974-5981.

[33] J.L. Bell, P. Sarin, J.L. Provis, R.P. Haggerty, P.E. Driemeyer, P.J. Chupas, J.S.J. van Deventer: Atomic Structure of a Cesium Aluminosilicate Geopolymer: A Pair Distribution Function Study, Chemistry of Materials 20 (2008), pp. 4768-4776.

[34] P. Duxon, J.L. Provis, G.C. Lukey, F. Separovic, J.S.J. van Deventer: 29Si NMR Study of Structural Ordering in Aluminosilicate Geopolymer Gels, Langmuir 21 (2005), pp. 3028-3036.

[35] A. Fernández-Jiménez, A. Palomo, I. Sobrados, J. Sanz: The role played by the reactive alumina content in the alkaline activation of fly ashes, Microporous and Mesoporous Materials 91 (2006), pp. 111-119.

[36] W. Loewenstein: The Distribution of Aluminum in the Tetrahedra of Silicates and Aluminates, American Mineralogist 39 (1954), pp. 92-96.

[37] G.Y. Kovalchuk, A. Fernández-Jiménez, A. Palomo: Alkali-activated fly ash: Effect of thermal curing conditions on mechanical and microstructural development – Part II, Fuel 86 (2007), pp. 315-322.

[38] J.G.S. van Jaarsveld, J.S.J. van Deventer, G.C. Lukey: The effect of composition and temperature on the properties of fly ash- and kaolinite-based geopolymers, Chemical Engineering Journal 89 (2002), pp. 63-73.

[39] D.R.M. Brew, K.J.D. MacKenzie: Geopolymer synthesis using silica fume and sodium aluminate, Journal of Materials Science 42 (2007), pp. 3990-3993.

[40] G.J.G. Gluth, C. Lehmann, K. Rübner, H.-C. Kühne: Geopolymerization of a silica residue from waste treatment of chlorosilane production, Materials and Structures 46 (2013), pp. 1291-1298.

[41] A. Hajimohammadi, J.L. Provis, J.S.J. van Deventer: One-Part Geopolymer Mixes from Geothermal Silica and Sodium Aluminate, Industrial & Engineering Chemistry Research 47 (2008), pp. 9396-9405.

[42] A. Hajimohammadi, J.L. Provis, J.S.J. van Deventer: The effect of silica availability on the mechanism of geopolymerisation, Cement and Concrete Research 41 (2011), pp. 210-216.

[43] P. Duxon, J.L. Provis: Designing Precursors for Geopolymer Cements, Journal of the American Ceramic Society 91 (2008), pp. 3864-3869.

[44] D. Feng, J.L. Provis, J.S.J. Deventer: Thermal Activation of Albite for the Synthesis of One-Part Mix Geopolymers, Journal of the American Ceramic Society 95 (2012), pp. 565-572.

[45] A. Hajimohammadi, J.L. Provis, J.S.J. Van Deventer: Effect of Alumina Release Rate on the Mechanism of Geopolymer Gel Formation, chemistry of Materials 22 (2010), pp. 5199-5208.

[46] D. Koloušek, J. Brus, M. Urbanova, J. Andertova, V. Hulinsky, J. Vorel: Preparation, structure and hydrothermal stability of alternative (sodium silicate-free) geopolymers , Journal of Materials Science 42 (2007), pp. 9267-9275.

[47] T. Luukkonen, Z. Abdollahnejad, J. Yliniemi, P. Kinnunen, M. Illikainen: One-part alkali-activated materials: A review, Cement and Concrete Research (2018), pp. 21-34.

[48] S. Greiser, P. Sturm, G.J.G. Gluth, M. Hunger, C. Jäger: Differentiation of the solid-state NMR signals of gel, zeolite phases and water species in geopolymer-zeolite composites, Ceramics International 43 (2017), pp. 2202-2208.

[49] P. Sturm, G.J.G. Gluth, H.J.H. Brouwers, H.-C. Kühne: Synthesizing one-part geopolymers from rice husk ash, Construction and Building Materials 124 (2016), pp. 961-966.

[50] P. Sturm, G.J.G. Gluth, S. Simon, H.J.H. Brouwers, H.-C. Kühne: The effect of heat treatment on the mechanical and structural properties of one-part geopolymer-zeolite composites, Thermochimica Acta 635 (2016), pp. 41-58.

[51] P. Sturm, S. Greiser, G.J.G. Gluth, C. Jäger, H.J.H. Brouwers: Degree of reaction and phase content of silica-based one-part geopolymers investigated using chemical and NMR spectroscopic methods, Journal of Materials Science 50 (2015), pp. 6768-6778.

[52] X. Ke, S.A. Bernal, N. Ye, J.L. Provis, J. Yang: One-Part Geopolymers Based on Thermally Treated Red Mud/NaOH Blends, Journal of the American Ceramic Society 98 (2015), pp. 5-11.

[53] S.J. O'Connor, K.J.D. MacKenzie: Synthesis, characterisation and thermal behaviour of lithium aluminosilicate inorganic polymers, Journal of Materials Science 45 (2010), pp. 3707-3713.

[54] A. Hajimohammadi, J.S.J. Deventer: Solid Reactant-Based Geopolymers from Rice Hull Ash and Sodium Aluminate, Waste and Biomass Valorization 8 (2016); pp. 2133-2140.

[55] G. Chagas Cordeiro, R. Dias Toledo Filho, L.M. Tavares, E. de Moraes Rego Fairbairn, S. Hempel: Influence of particle size and specific surface area on the pozzolanic activity of residual rice husk ash, Cement & Concrete Composites 33 (2011), pp. 529-534.

[56] G. Rodríguez de Sensale: Effect of rice-husk ash on durability of cementitious materials, Cement & Concrete Composites 32 (2010), pp. 718-725.

[57] V.-T.-A. Van, C. Rößler, D.-D. Bui, H.-M. Ludwig: Rice husk ash as both pozzolanic admixture and internal curing agent in ultra-high performance concrete, Cement & Concrete Composites 53 (2014), pp. 270-278.

[58] J. He, Y. Jie, J. Zhang, Y. Yu, G. Zhang: Synthesis and characterization of red mud and rice husk ash-based geopolymer composites, Cement & Concrete Composites 37 (2013), pp. 108-118.

[59] U.H. Heo, K. Sankar, W.M. Kriven, S.S. Musil, Rice Husk Ash as a Silica Source in a Geopolymer Formulation, in: D.Z. Waltraud M. Kriven, Kyoung Il Moon, Taijin Hwang, Jingyang Wang, Charles Lewinsohn and Yanchun Zhou (Ed.) Developments in Strategic Materials and Computational Design V: A Collection of Papers Presented at the 38th International Conference on Advanced Ceramics and Composites January 27-3, 2014 Daytona Beach, Florida, American Ceramic Society, (2015), pp. 87-101.

[60] J.M. Meija, R. Mejia de Gutierrez, F. Puertas: Rice husk ash as a source of silica in alkali-activated fly ash and granulated blast furnace slag systems, Materiales de Construcción 63 (2013), pp. 361-375.

[61] S.A. Bernal, E.D. Rodriguéz, R. Mejia de Gutierrez, J.L. Provis, S. Delevasto: Activation of Metakaolin/Slag Blends Using Alkaline Solutions Based on Chemically Modified Silica Fume and Rice Husk Ash, Waste and Biomass Valorization (2012), pp. 99-108.

[62] M.-c. Chi, J.-j. Chang, R. Huang: Strength and Drying Shrinkage of Alkali-Activated Slag Paste and Mortar, Advances in Civil Enigineering (2012), pp. 1-7.

[63] F. Collins, J.G. Sanjayan: Effect of pore size distribution on drying shrinkage of alkali-activated slag concrete, Cement and Concrete Research 30 (2000), pp. 1401-1406.

[64] N.K. Lee, J.G. Jang, H.K. Lee: Shrinkage characteristics of alkali-activated fly ash/slag paste and mortar at early ages, Cement & Concrete Composites 53 (2014), pp. 239-248.

[65] A.A. Melo Neto, M.A. Cincotto, W. Repette: Drying and autogenous shrinkage of pastes and mortars with activated slag cement, Cement and Concrete Research 38 (2008), pp. 565-574.

[66] P.V. Krivenko, G.Y. Kovalchuk: Directed synthesis of alkaline aluminosilicate minerals in a geocement matrix, Journal of Materials Science 42 (2007), pp. 2944-2952.

[67] C. Montes, D. Zang, E. Allouche: Rheological behavior of fly ash based geopolymers with the addition of superplasticizers, Journal of Sustainable Cement-Based Materials 1 (2012), pp. 179-185.

[68] N. Roussel, C. Stefanie, R. Leroy: From mini-cone test to Abrams cone test: measurement of cement-based materials yield stress using slump tests, Cement and Concrete Research 35 (2005), pp. 817-822.

[69] DIN EN 1015-3: Methods of test for mortar for masonry – Part 3: Determination of consistence of fresh mortar (by flow table), Deutsches Institut für Normung, Beuth Verlag GmbH, Berlin; GER, (2007), p. 11.

[70] S. Greiser, NMR-Untersuchungen zum Reaktionsprozess von One-part Geopolymeren, Mathematisch-Naturwissenschaftlichen Fakultät, Doctoral Thesis, Humboldt-Universität, Berlin; GER, (2018), p. 133.

[71] A. Fernández-Jiménez, A.G. de la Torre, A. Palomo, G. López-Olmo, M.M. Alonso, M.A.G. Aranda: Quantitative determination of phases in the alkaline activation of fly ash. Part II: Degree of reaction, Fuel 85 (2006), pp. 1960-1969.

[72] DIN EN 196-1: Methods of testing cement Part 1: Determination of strength in: Beuth Verlag GmbH, Berlin; GER, (2005), p. 33.

[73] DIN EN EN 12617-4: Products and systems for the protection and repair of concrete structures Test methods Part 4: Determination of shrinkage and expansion, Deutsches Institut für Normung, Beuth Verlag GmbH, Berlin; GER, (2002), p. 14.

[74] DIN EN 1542: Products and systems for the protection and repair of concrete structures — Test methods —Measurement of bond strength by pull-off, Deutsches Institut für Normung, Beuth Verlag GmbH, Berlin; GER, (1999), p. 11.

[75] EN 1766:2017: Products and systems for the protection and repair of concrete structures – Test methods – Reference concretes for testing, Deutsches Institut für Normung, Beuth Verlag GmbH, Berlin; GER, (2017), p. 13.

[76] DIN 19573:2016-03: Mortar for construction and rehabilitation of drains and sewers outside buildings, Deutsches Institut für Normung, Beuth Verlag GmbH, Berlin; GER, (2016), p. 52.

[77] R. Snellings: Assessing, Understanding and Unlocking Supplementary Cementitious Materials, RILEM Technical Letters (2016), pp. 50-55.

[78] J. He: Synthesis and Characterization of Geopolymers for Infrastructural Applications, Department of Civil and Environmental Engineering, Dissertation, Louisiana State University, USA, (2012), p. 105.

[79] Statistical Yearbook World Food and Agriculture: Food and Agriculture Organization of the United Nations, Rome: ITA, (2013), p. 289.

[80] D. Koteswara Rao, P.R.T. Pranav, M. Anusha: Stabilization Of Expansive Soil With Rice Husk Ash, Lime And Gypsum – An Experimental Study, International Journal of Engineering Science and Technology 3 (2011), pp. 8076-8085.

[81] G. Abood Habeeb: Study on Properties of Rice Husk Ash and Its Use as Cement Replacement Material, H. Bin Mahmud, Materials Research 13 (2010), pp. 185-190.

[82] S. Chanddrasekhar, K.G. Satyanarayana, P.N. Pramada: Processing, properties and applications of reactive silica from rice husk—an overview, Journal of Materials Science 38 (2003), pp. 3159-3168.

[83] D.V. Reddy, M. Alvarez: Marine Durability Characteristics of Rice Husk Ash-Modified Reinforced Concrete, in: International Latin American and Caribbean Conference for Engineering and Technology, vol 4, Mayagüez, Puerto Rico, 2006.

[84] Y. Shinohara, N. Kohyama: Quantitative Analysis of Tridymite and Cristobalite Crystallized in Rice Husk Ash by Heating, Industrial Health 42 (2004), pp. 277-285.

[85] DIN EN 197-1: Cement – Part 1: Composition, specifications and conformity criteria for common cements, Deutsches Institut für Normung, Beuth Verlag GmbH, Berlin; GER, (2011), p. 42.

[86] N.P.G. Roeges: A Guide to the Complete Interpretation of Infrared Spectra of Organic Structures, A Guide to the Complete Interpretation of Infrared Spectra of Organic Structures, John Wiley & Sons, (1995), p. 340.

[87] H.W.H. Moenke: Silica, the Three-dimensional Silicates, Borosilicates and Beryllium Silicates, in: V.C. Farmer (Ed.) The infrared spectra of minerals, Mineralogical Society, London; GB, (1974), pp. 365-382.

[88] N.V. Chukanov: Infrared spectra of mineral species, Springer, vol 1, (2014), p. 1726.

[89] S. Jakobbson: Determination of Si/Al Ratios in Semicrystalline Aluminosilicates by FT-IR Spectroscopy, Applied Spectroscopy 56 (2002), pp. 797-799.

[90] W. Mozgawa, W. Jastrębski, M. Handke: Vibrational spectra of D4R and D6R structural units, Journal of Molecular Structure 744-747 (2005), pp. 663-670.

[91] A. Hajimohammadi, J.S.J. van Deventer: Dissolution behavior of source materials for synthesis of geopolymer binders: a kinetic approach, International Journal of Mineral Processing 153 (2016), pp. 80-86.

[92] D.G. Nair, A. Fraaij, A.A.K. Klaassen, A.P.M. Kentgens: A structural investigation relating to the pozzolanic activity of rice husk ashes, Cement and Concrete Research 38 (2008), pp. 861-869.

[93] D.M. Ibrahim, S.A. El-Hemaly, F.M. Abdel-Kerim: Study of Rice-Husk Ash Silica by Infrared Spectroscopy, Thermochimica Acta 37 (1980), pp. 307-314.

[94] D.M. Ibrahim, M. Helmy: Crytallite Growth of Rice Husk Ash Silica, Thermochimica Acta 45 (1981), pp. 79-85.

[95] DIN EN 933-1:2021: Tests for geometrical properties of aggregates –Part 1: Determination of particle size distribution –Sieving method, Deutsches Institut für Normung, Beuth Verlag GmbH, Berlin; GER, 2012, p. 19.

[96] R. Bhattacharjee, A.I. Laskar: Rheological Behavior of Fly Ash based Geopolymer Concrete, in: Conference on our World in Concrete & Structures, vol 35, Singapore, (2010), p. 7.

[97] M. Criado, A. Palomo, A. Fernández-Jiménez, P.F.G. Banfill: Alkali activated flay ash: effect of admixtures on paste rheology, Rheologica Acta 48 (2009), pp. 447-455.

[98] A. Favier, J. Hot, G. Habert, J.-B. d´Espinose de Lacaillerie: Rheology of Geopolymer: Comparative Study between Portland Cement and Metakaolin based Geopolymer, in: N.R.a.H. Bessaies-Bey (Ed.) 1st RILEM International Conference on Rheology and Processing of Construction Materials., RILEM Publications s.a.r.l., Paris: France, (2013), pp. 49-56.

[99] A. Poulesquen, F. Frizon, D. Lambertin: Rheological behavior of alkali-activated metakaolin during geopolymerization, Journal of Non-Crystalline Solids 357 (2011), pp. 3565-3571.

[100] H. Rahier, B. Van Mele: Low-temperature synthesized aluminosilicate glasses - Part II Rheological transformations during low-temperature cure and high-temperature properties of a mode/compound, Journal of Materials Science 31 (1996), pp. 80-85.

[101] M. Romagnoli, C. Leonelli, E. Kamse, M. Lassinantti Gualtieri: Rheology of geopolymer by DOE approach, Construction and Building Materials 36 (2012), pp. 251-258.

[102] A. Palomo, P.F.G. Banfill, A. Fernández-Jiménez, D.D. Swift: Properties of alkali-activated fly ashes determined from rheological measurements, Advances in Cement Research 17 (2005), pp. 143-151.

[103] A. Favier, G. Habert, J.-B. d´Espinose de Lacaillerie, N. Roussel: Mechanical properties and compositional heterogeneities of fresh geopolymer pastes, Cement and Concrete Research 48 (2013), pp. 9-16.

[104] M. Palacios, P.F.G. Banfill, F. Puertas: Rheology and setting of alkali-activated slag pastes and mortars: effect of organic, ACI Materials Journal 105 (2008), pp. 140-148.

[105] J.L. Provis, P. Duxon, J.S.J. van Deventer: The role of particle technology in developing sustainable construction materials, Advanced Powder Technology 21 (2010), pp. 2-7.

[106] P. Sturm, G. J. G. Gluth, W. Schmidt, A. Astorg, H.-C. Kühne, and H. J. H. Brouwers, "Rheological properties of microsilica and sodium aluminate based one-part geopolymers compared to ordinary portland cement," in 5th International Conference on Non-Traditional Cement & Concrete, Brno, Czech Republic, (2014), pp. 241-244.

[107] R.V. Lundquist, H. Leitch: Solubility Characteristics of Sodium Aluminate, U. S. Dept. of the Interior, Bureau of Mines (1964), pp. 1-19.

[108] Specification for Sodium Aluminate used for potable Supply, in: SAJ Holdings Sdn Bhd, Quality Assurance Department (2002), pp. 1-5.

[109] C. Misra: sodium aluminate, in: Industrial Alumina Chemicals, American Chemical Society, Washington, DC: USA, (1986), p. 153.

[110] E. Königsberger, P.M. May, G. Hefter: Comprehensive Model of Synthetic Bayer Liquors. Part 3. Sodium Aluminate Solutions and the Solubility of Gibbsite and Boehmite, Monatshefte für Chemie 137 (2006), pp. 1139-1149.

[111] B. Zhang, K.J.D. MacKenzie, I.W.M. Brown: Crystalline phase formation in metakaolinite geopolymers activated with NaOH and sodium silicate, Journal of Materials Science 44 (2009), pp. 4668-4676.

[112] M.M.J. Treacy, J.B. Higgins, Collection of Simulated XRD Powder Patterns for Zeolites, International Zeolite Association, (2001), p. 586.

[113] M.M.J. Treacy, D.E.W. Vaughan, K.G. Strohmaier, J.M. Newsam: Intergrowth segregation in FAU-EMT zeolite materials, Procedings of the Royal Society A 452 (1996), pp. 813-840.

[114] J. Weitkamp, R. Schumacher, U. Weiß: Hydrothermalsynthese und Charakterisierung von Zeolith EMT, Chemie Ingenieur Technik 64 (1992), pp. 1109-1112.

[115] D. Gao, A. Duan, X. Zhang, Z. Zhao, H. E, Y. Qin, C. Xu: Synthesis of CoMo catalysts supported on EMT/FAU intergrowth zeolites with different morphologies and their hydro-upgrading performances for FCC gasoline, Chemical Engineering Journal 270 (2015), pp. 176-186.

[116] B. Subotić, D. Škrtić, I. Šmit: Transformation of Zeolite A into Hydroxysodalite - I. An approach to the mechanism of transformationand its experimental evaluation, Journal of Crystal Growth 50 (1980), pp. 498-508.

[117] P. Duxon, J.L. Provis, G.C. Lukey, S.W. Mallicoat, W.M. Kriven, J.S.J. van Deventer: Understanding the relationship between geopolymer composition, microstructure and mechanical properties, Colloids and Surfaces A: Physicochemical and Engineering Aspects 269 (2005), pp. 47-58.

[118] M. Zaarour, B. Dong, I. Naydenova, R. Retoux, S. Mintova: Progress in Zeolite Synthesis Promotes Advanced Applications, Microporous and Mesoporous Materials 189 (2014), pp. 11-21.

[119] A. Radulović, V. Dondur, P. Vulić, Z. Miladinović, G. Ćirić-Marjanović, R. Dimitrijević: Routes of synthesis of nepheline-type polymorphs:An influence of Na-LTA bulk composition on its thermal transformations, Journal of Physics and Chemistry of Solids 74 (2013), pp. 1212-1220.

[120] D.W. Breck: Zeolite Molecular Sieves, John Wiley & Sons, New York; USA, (1974), p. 771.

[121] A.R. Brough, C.M. Dobson, I.g. Richardson, G.W. Groves: A study of the pozzolanic reaction by solid-state 29Si nuclear magnetic resonance using selective isotopic enrichment, Journal of Materials Science 30 (1995), pp. 1671-1678.

[122] G. Sun, A.R. Brough, J.F. Young: 29Si NMR study of the hydration of Ca3SiO5 and β-Ca2SiO4 in the presence of silica fume, Journal of the American Ceramic Society 82 (1999), pp. 3225-3230.

[123] A. Leemann, G. Le Saout, F. Winnefeld, D. Rentsch, B. Lothenbach: Alkali-Silica Reaction: the Influence of Calcium on Silica Dissolution and the Formation of Reaction Products, Journal of the American Ceramic Society 94 (2010), pp. 1243-1249.

[124] R.L. Hartman, S.H. Fogler: Reaction Kinetics and Mechanisms of Zeolite Dissolution in hydrochloric acid, Industrial & Engineering Chemistry Research 44 (2005), pp. 7738-7745.

[125] R.L. Hartman, S.H. Fogler: Understanding the dissolution of zeolites, Langmuir 23 (2007), pp. 5477-5484.

[126] M. Gougazeh, J.-C. Buhl: Conversion of Natural Jordanian Kaolin into Zeolite A without Thermal Preactivation, Zeitschrift für Anorganische und Allgemeine Chemie 640 (2014), pp. 1675-1679.

[127] E. Grujic, B. Subotic, L.A. Despotovic: Transformation of zeolite A into hydroxysodalite. III The influence of the temperature, Zeolites (1989), pp. 261-270.

[128] B. Subotić, L. Sekovanić: Transformation of Zeolite A Into Hydrosodalite - II. Growth kinetics of hydroxysodalite microcrystals, Journal of Crystal Growth 75 (1986), pp. 561-572.

[129] M.Y. Khalil, E. Merz: Immobilisation of intermediate-level wastes in geopolymers, Journal of Nuclear Materials 211 (1994), pp. 141-148.

[130] J.E. Oh, J. Moon, M. Mancio, S.M. Clark, P.J.M. Monteiro: Bulk modulus of basic hydrosodalite, Na8[AlSiO4]6(OH)2_2H2O, a possible zeolitic precursor in coal-fly-ash-based geopolymers, Cement and Concrete Research 41 (2011), pp. 107-112.

[131] E. Prud`homme, P. Michaud, E. Joussein, C. Peyratout, A. Smith, S. Arrii-Clacens, J.M. Clacens, S. Rossignol: Silica fume as porogent agent in geo-materials at low temperature, Journal of the European Ceramic Society 30 (2010), pp. 1641-1648.

[132] W.B. White: The carbonate minerals, in: V.C. Farmer (Ed.) The infrared spectra of minerals, Mineralogical Society, London; GB, (1974), pp. 227-284.

[133] W. Mozgawa, M. Król, K. Barczyk: FT-IR studies of zeolites from different structural groups, Chemik (2011), pp. 671-674.

[134] V.C. Farmer, Vibrational Spectroscopy in Mineral Chemistry, in: V.C. Farmer (Ed.) The Infrared Spectra of Minerals, Mineralogical Society, London; GB, (1974), pp. 1-10.

[135] P.V. Krivenko, G.Y. Kovalchuk, Fly-ash based zeolite cements, in: R.K. Dhir, P.C. Hewlett, L. Csetenyi (Eds.), Innovations and Developments in Concrete Materials and Construction, Thomas Telford, London, 2002, pp. 123-132.

[136] A. Hartmann, V. Petrov, J.-C. Buhl, K. Rübner, M. Lindemann, C. Prinz, A. Zimathies: Zeolite Synthesis under Insertion of Silica Rich Filtration Residues from Industrial Wastewater Reconditioning, Advances in Chemical Engineering and Science 4 (2014), pp. 120-134.

[137] T. Herbst, K. Rübner, M. Seidemann: Utilization of siliceous filter residues in mineral building materials, ZKG INTERNATIONAL 66 (2013), pp. 58-65.

[138] J.L. Bell, P.E. Driemeyer, W.M. Kriven: Formation of ceramics from metakaolin-based geopolymers: part I—Cs-based geopolymer, Journal of the American Ceramic Society 92 (2009), pp. 1-8.

[139] J.L. Bell, P.E. Driemeyer, W.M. Kriven: Formation of Ceramics from Metakaolin-Based Geopolymers. Part II: K-Based Geopolymer, Journal of the American Ceramic Society 92 (2009), pp. 607-615.

[140] M. Steveson, K. Sagoe-Crentsil: Relationships between composition, structure and strength of inorganic polymers - Part I Metakaolin-derived inorganic polymers, Journal of Materials Science 40 (2005), pp. 2023-2036.

[141] M. Steveson, K. Sagoe-Crentsil: Relationships between composition, structure and strength of inorganic polymers - Part 2 Fly ash-derived inorganic polymers, Journal of Materials Science 40 (2005), pp. 4247-4259.

[142] H.L. Jamieson, H. Yin, A. Waller, A. Khosravi, M.L. Lind: Impact of acids on the structure and composition of Linde Type A zeolites for use in reverse osmosis membranes for recovery of urine-containing wastewaters, Microporous and Mesoporous Materials 201 (2015), pp. 50-60.

[143] E.H. Oelkers: General kinetic description of multioxide silicate mineral and glass dissolution, Geochimica et Cosmochimica Acta 65 (2001), pp. 3703-3719.

[144] A. Fernández-Jiménez, A.G. de la Torre, A. Palomo, G. López-Olmo, M.M. Alonso, M.A.G. Aranda: Quantitative determination of phases in the alkali activation of fly ash. Part I. Potential ash reactivity, Fuel 85 (2006), pp. 625-634.

[145] J.L. Provis, S.A. Bernal: Geopolymers and Related Alkali-Activated Materials, Annual Review of Materials Research 44 (2014), pp. 299-327.

[146] E.N. Kani, A. Allahverdi: Investigating Shrinkage Changes of Natural Pozzolan based Geopolymer Cement Paste, Iranian Journal of Materials Science & Engineering 8 (2011), pp. 50-60.

[147] C. Ridtirud, P. Chindaprasirt, K. Pimraksa: Factors affecting the shrinkage of fly ash geopolymers, International Journal of Minerals, Mettallurgy and Materials 18 (2011), pp. 100-104.

[148] P. Sturm, G.J.G. Gluth, M. Lindemann, S. Greiser, C. Jäger, H.J.H. Brouwers: Structural Investigations on One-Part Geopolymers after different Drying Regimes, in: S.A. Bernal, J.L. Provis (Eds.), Conference on Cement and Concrete Science, vol 34, Sheffield; GB, (2014), pp. 37-40.

[149] B. Subotić, N. Mašić, I. Šmit: Analysis of Particulate Process During the Transformation of Zeolite A into Hydrosodalite, Zeolites (1985), pp. 207-214.

[150] C.S. Cundy, P.A. Cox: The Hydrothermal Synthesis of Zeolites: Precursors, Intermediates and Reaction Mechanism, Microporous and Mesoporous Materials 82 (2005), pp. 1-78.

[151] C.S. Cundy, P.A. Cox: The Hydrothermal Synthesis of Zeolites: History and Development from the Earliest Days to the Present Time, Chemical Reviews 103 (2003), pp. 663-701.

[152] P.V. Krivenko, J.K. Pushkavera, M.V. Sukhanevich, S.G. Guziy: Fireproof coatings on the basis of alkaline aluminum silicate systems, in: T. Ohji, A. Wereszczak (Eds.), Developments in strategic materials. Ceramic engineering and science proceedings, vol 29(10), Wiley, (2009), pp. 129-142.

[153] D.C. Comrie, W.M. Kriven: Composite cold ceramic geopolymer in a refractory application, Advances in Ceramic Matrix Composites 153 (2003), pp. 211-225.

[154] J.L. Bell, M. Gordon, W. Kriven: Use of geopolymeric cements as a refractory adhesive for metal and ceramic joins, in: D. Zhu, K. Plucknett (Eds.), Advances in ceramic coatings and ceramic-metal systems. Ceramic engineering and science proceedings, vol 26(3), American Ceramic Society, Westerville: USA, (2005), pp. 407-413.

[155] C. Kuenzel, L.M. Grover, L. Vandeperre, A.R. Boccaccini, C.R. Cheeseman: Production of nepheline/quartz ceramics from geopolymer mortars, Journal of the European Ceramic Society 33 (2013), pp. 251-258.

[156] H.M. Khater: Studying the effect of thermal and acid exposure on alkali activated slag Geopolymer, MATEC Web of Conferences (2014).

[157] W.D.A. Rickard, C.D. Borstel, A. van Riessen: The effect of pre-treatment on the thermal performanceof fly ash geopolymers, Thermochimica Acta 573 (2013), pp. 130-137.

[158] C. Kuenzel, L.J. Vandeperre, S. Donatello, A.R. Boccaccini, C. Cheeseman: Ambient Temperature Drying Shrinkage and Cracking in Metakaolin-Based Geopolymers, Journal of the American Ceramic Society 95 (2012), pp. 3270-3277.

[159] R.E. Lyon, P.N. Balaguru, A. Foden: Fire Resistant Aluminosilicate Composites, Fire and Materials 21 (1997), pp. 67-73.

[160] M.-B. Watolla, G.J.G. Gluth, P. Sturm, W.D.A. Rickard, S. Krüger, B. Schartel: Intumescent Geopolymer-Bound Coatings for Fire Protection of Steel, Journal of Ceramic Science and Technology 8 (2017), pp. 351-364.

[161] G. Engelhardt, J. Felsche, P. Sieger: The Hydrosodalite System Na6+x[SiAl04]6(OH)x*nH20: Formation, Phase Composition, and De- and Rehydration Studied by 1H, 23Na, and 29Si MAS-NMR Spectroscopy in Tandem with Thermal Analysis, X-ray Diffraction, and IR Spectroscopy, Journal of the American Chemical Society 114 (1992), pp. 1173-1182.

[162] J. Felsche, S. Luger: Structural Collapse or Expansion of the Hydro-Sodalite Series Na8[AlSiO4]6(OH)2·nH2O and Na6[AlSiO4]6·nH2O Upon Dehydration, Berichte der Bunsengesellschaft für physikalische Chemie 90 (1986), pp. 736-742.

[163] J. Felsche, S. Luger: Phases and Thermal Decomposition Characteristics of Hydrosodalites Na6+x[AISiO4]6(OH)x·nH2O, Thermochimica Acta 118 (1987), pp. 35-55.

[164] A. Buchwald, M. Vicent, R. Kriegel, C. Kaps, M. Monzó, A. Barba: Geopolymeric binders with different fine fillers — Phase transformations at high temperatures, Applied Clay Science 46 (2009), pp. 190-195.

[165] J.G. Thompson, A. Melnitchenko, S.R. Palethorpe, R.L. Withers: An XRD and Electron Diffraction Study of Cristobalite-Related Phases in the NaAlO2–NaAlSiO4 System, Journal of Solid State Chemistry 131 (1997), pp. 24-37.

[166] J.G. Thompson, R.L. Withers, A. Melnitchenko, S.R. Palethorpe: Cristobalite-Related Phases in the NaAlO2±NaAlSiO4 System. I. Two Tetragonal and Two Orthorhombic Structures, Acta Crystallographica B 54 (1998), pp. 531-546.

[167] M. Okrusch, S. Matthes, Mineralogie: Eine Einführung in die spezielle Mineralogie, Petrologie und Lagerstättenkunde, Springer, (2014), p. 728.

[168] E.M. Flanigen, H. Khatami, H.A. Szymanski: Infrared Structural Studies of Zeolite Frameworks, in: F.E. M., L.B. Sand (Eds.), Molecular sieve zeolites, American Chemical Society, Washington DC; USA, (1971), pp. 201-229.

[169] M. Földvári, Handbook of thermogravimetric system of minerals and its use in geological practice: Geological Institute of Hungary, (2011), p. 180.

[170] E. Balan, M. Lazzeri, G. Morin, M. Mauri: First-principles study of the OH-stretching modes of gibbsite, American Mineralogist 91 (2006), pp. 115-119.

[171] E. Atlan, T. Erdoğan: Alkali activation of a slag at ambient and elevated temperatures, Cement and Concrete Research 34 (2012), pp. 131-139.

[172] D. Demie, M.F. Nuruddin, N. Shafiq: Effects of micro-structure characteristics of interfacial transition zone on the compressive strength of self-compacting geopolymer concrete, Construction and Building Materials 41 (2013), pp. 91-98.

[173] A. Fernández-Jiménez, I. Garcia-Lodeiro, A. Palomo: Durability of alkali-activated fly ash cementitious materials, Journal of Materials Science 42 (2007), pp. 3055-3065.

[174] K.-H. Yang, J.-K. Song, A.F. Ashour, E.-T. Lee: Properties of cementless mortars activated by sodium silicate, Construction and Building Materials 22 (2008), pp. 1981-1989.

[175] A. Castel, S.J. Foster, T. Ng, J.G. Sanjayan, R.I. Gilbert: Creep and drying shrinkage of a blended slag and low calcium fly ash geopolymer Concrete, Materials and Structures 49 (2016), pp. 1619-1628.

[176] W. Chen, H.J.H. Brouwers: The hydration of slag, part 1: reaction models for alkali-activated slag, Journal of Materials Science 42 (2007), pp. 428-443.

[177] W. Chen, H.J.H. Brouwers: The hydration of slag, part 2: reaction models for blended cement, Journal of Materials Science 42 (2007), pp. 444-464.

[178] M. Palacios, F. Puertas: Effect of shrinkage-reducing admixtures on the properties of alkali-activated slag mortars and pastes, Cement and Concrete Research 37 (2007), pp. 691-702.

[179] L.Y. Yang, Y.M. Jia, Y.M. Zhang, J.G. Dai: Effects of nano-TiO2 on strength, shrinkage and microstructure of alkali activated slag pastes, Cement & Concrete Composites 57 (2015), pp. 1-7.

[180] H. Ye, A. Radlińska: Shrinkage mechanisms of alkali-activated slag, Cement and Concrete Research 88 (2016), pp. 126-135.

[181] D. Tonnayopas, A. Hawa, W. Prachasaree, P. Taneerananon: Effect of Parawood Ash on Drying Shrinkage, Compressive Strength and Microstructural Characterization of Metakaolin-based Geopolymer Mortar, Key Engineering Materials 594-595 (2013), pp. 411-415.

[182] L. Franke, M. Oly, S. Witt: Richtlinie für die Prüfung von Mörteln für den Einsatz im Sielbau, Technische Universität Hamburg - Harburg (2001), p. 10.

[183] Schutz und Instandsetzung von Betonbauteilen - Instandsetzungsrichtlinie, Deutscher Ausschuss für Stahlbeton, (2001), p. 216.

[184] Z. Dahou, A. Castel, A. Noushini: Prediction of the steel-concrete bond strength from the compressive strength of Portland cement and geopolymer concretes, Construction and Building Materials 119 (2016), pp. 329-342.

[185] R.M. Doguparti: A Study on Bond Strength of Geopolymer Concrete, International Journal of Civil, Environmental, Structural, Construction and Architectural Engineering 9 (2015), pp. 355-358.

[186] P.K. Sarker: Bond Strengths of Geopolymer and Cement Concretes, Advances in Science and Technology 69 (2010), pp. 143-151.

[187] P.K. Sarker: Bond strength of reinforcing steel embedded in fly ash-based geopolymer concrete, Materials and Structures 44 (2011), pp. 1021-1030.

[188] H.R. Kahlid, S.K. Ha, S.M. Park, G.M. Kim, H.K. Lee: Interfacial bond behavior of FRP fabrics bonded to fiber-reinforced geopolymer mortar, Composite Structures 134 (2015), pp. 353-368.

[189] S. Tamburini, M. Natali, E. Garbin, M. Panizza, M. Favaro, M.R. Valluzzi: Geopolymer matrix for fibre reinforced composites aimed at strengthening masonry structures, Construction and Building Materials 141 (2017), pp. 542-552.

[190] L. Song, Z. Li, P. Duan, M. Huang, X. Hao: Novel low cost and durable rapid-repair material derived from industrial and agricultural by-products, Ceramics International (2017), pp. 14511-14516.

[191] J. Stark, B. Wicht: Dauerhaftigkeit von Beton, Springer, Berlin Heidelberg; GER, (2013), p. 479.

[192] W.A. König, M. Aydin, M. Rinken, S. Sievers: Schwefelverbindungen als Verursacher von Betonkorrosion, Tiefbau Ingenieurbau Straßenbau 7 (1983), pp. 434-435.

[193] E. Bock: Biologische Korrosion, Tiefbau Ingenieurbau Straßenbau (1984), pp. 240-250.

[194] C. Grengg, F. Mittermayr, G. Koraimann, F. Konrad, M. Szabó, A. Demeny, M. Dietzel: The decisive role of acidophilic bacteria in concrete sewer networks: A new model for fast progressing microbial concrete corrosion, Cement and Concrete Research 101 (2017), pp. 93-101.

[195] T. Bracher, B. Grabow, S. Schneider, A. Seidel-Schulze, M. Reidenbach: Investitionsrückstand und Investitionsbedarf der Kommunen: Ausmaß, Ursachen, Folgen, Strategien, Deutsches Institut für Urbanistik, Berlin, GER, (2008), p. 468.

[196] M. Albitar, M.S.M. Ali, P. Vistin, M. Drechsler: Durability evaluation of geopolymer and conventional concretes, Construction and Building Materials 136 (2017), pp. 374-385.

[197] A. Allahverdi, F. Škvára: Sulfuric Acid Attack on hardened Paste of Geopolymer Cements Part 1. Mechanism of Corrosion at relatively high Concentrations, Ceramics - Silikáty 49 (2005), pp. 225-229.

[198] A. Allahverdi, F. Škvára: Sulfuric Acid Attack on hardened Paste of Geopolymer Cements Part 2. Corrosion Mechanism at mild and relatively low Concentrations, Ceramics - Silikáty 50 (2006), pp. 1-4.

[199] M.A.M. Ariffin, M.A.R. Bhutta, M.W. Hussin, M.M. Tahir, N. Aziah: Sulfuric acid resistance of blended ash geopolymer concrete, Construction and Building Materials 43 (2013) pp. 80-86.

[200] P. Duan, C. Yan, W. Zhou, W. Luo, C. Shen: An investigation of the microstructure and durability of a fluidized bed fly ash–metakaolin geopolymer after heat and acid exposure, Materials & Design 74 (2015), pp. 125-137.

[201] A. Mehta, R. Siddique: Sulfuric acid resistance of fly ash based geopolymer concrete, Construction and Building Materials 146 (2017), pp. 136-143.

[202] F.N. Okoye, S. Prakash, N.B. Singh: Durability of fly ash based geopolymer concrete in the presence of silica fume, Journal of Cleaner Production 149 (2017), pp. 1062-1067.

[203] V. Sata, S. A, P. Chindaprasirt: Resistance of lignite bottom ash geopolymer mortar to sulfate and sulfuric acid attack, Cement & Concrete Composites 34 (2012), pp. 700-708.

[204] N.P. Rajamane, M.C. Nataraja, N. Lakshmanan, J.K. Dattatreya, D. Sabitha: Sulphuric acid resistant ecofriendly concrete from geopolymerisation of blast furnace slag, Indian Journal of Engineering & Materials Sciences 19 (2012), pp. 357-367.

[205] R.R. Lloyd, J.L. Provis, J.S.J. van Deventer: Acid resistance of inorganic polymer binders. 1. Corrosion rate, Materials and Structures 45 (2012) pp. 1-14.

[206] M. Zhang, M. Zhao, G. Zhang, D. Mann, K. Lumsden, M. Tao: Durability of red mud-fly ash based geopolymer and leaching behavior of heavy metals in sulfuric acid solutions and deionized water, Construction and Building Materials 124 (2016), pp. 373-382.

[207] P.S. Deb, P.K. Sarker, S. Barbhuiya: Sorptivity and acid resistance of ambient-cured geopolymer mortars containing nano-silica, Cement & Concrete Composites 72 (2016), pp. 235-245.

[208] P. Chindaprasirt, U. Rattanasak, S. Taebuanhuad: Resistance to acid and sulfate solutions of microwave-assisted high calcium fly ash geopolymer, Materials and Structures 46 (2013), pp. 375-381.

[209] X.X. Gao, P. Michaud, E. Joussein, S. Rossignol: Behavior of metakaolin-based potassium geopolymers in acidic solutions, Journal of Non-Crystalline Solids 380 (2013), pp. 95-102.

[210] K.J.D. MacKenzie, M.E. Smith: Multinuclear Solid-State NMR of Inorganic Materials, Elsevier Science, Camebridge; UK, (2002), p. 727.

[211] M. Mägi, E. Lippmaa, A. Samoson: Solid-State High-Resolution Silicon-29 Chemical Shifts in Silicates, Journal of Physical Chemistry 88 (1984), pp. 1518-1522.

[212] R. Gopalakrishnan, C. Komarasamy: Durability of Alumina Silicate Concrete based on Slag/Fly-Ash Blends against Acid and Chloride Environments, Materials and technology 50 (2016), pp. 929-937.

[213] C.A. Fyfe, J.M. Thomas, J. Klinowski, G.C. Gobbi: Magic-Angle-Spinning NMR (MAS-NMR) Spectroscopy and the Structure of Zeolites, Angewandte Chemie International Edition 22 (1983), pp. 259-336.

[214] J. Šefčík, A.V. McCormick: Thermochemistry of Aqueous Silicate Solution Precursors to Ceramics, AIChE Journal 43 (1997), pp. 2773-2784.

[215] J. Herisson, M. Guéguen-Minerbe, E.D. van Hullebusch, T. Chaussadent, Water Science & Technology 69 (2014) pp. 1502-1508.

[216] P. Sturm, J. Lüchtenborg, P. Hlavaček, G.J.G. Gluth, H.-C. Kühne, J. Günster: Additive Manufacturing of Geopolymers by Selective Laser Curing, in: V. Bilek, Z. Keršner, H. Šimonová (Eds.), 6th International Conference on Non-Traditional Cement & Concrete, Brno, Czech Republic, (2017), pp. 307.

[217] P. Sturm, J. Lüchtenborg, P. Hlavaček, J. Günster, H.-C. Kühne, G.J.G. Gluth, Additive Manufacturing of Geopolymers by Selective Laser Curing, in: 92nd DKG Annual Conference & Symposium on High-Performance Ceramics, Berlin; GER, (2017).

[218] T. Mühler, J. Heinrich: Slurry-Based Additive Manufacturing of Ceramics, Journal of Applied Ceramic Technology 12 (2015), pp. 18-25.

[219] A. Zocca, P. Colombo, C.M. Gomes, J. Günster: Additive Manufacturing of Ceramics: Issues, Potentialities, and Opportunities, Journal of the American Ceramic Society 98 (2015), pp. 1983-2001.

[220] M. Xia, J. Sanjayan: Method of formulating geopolymer for 3D printing for construction applications, Materials & Design 110 (2016), pp. 382-390.

[221] G. Franchin, P. Scanferla, L. Zeffiro, H. Elsayed, A. Baliello, G. Giacomeello, M. Pasetto, P. Colombo: Direct ink writing of geopolymeric inks, Journal of the European Ceramic Society 37 (2017), pp. 2481-2489.

[222] T. Matsuo, K. Kobayashi, K. Tago: Estimation of the Solubility Dependence of Aluminate Salts of Alkali Metals on Ion Radii of Alkali Metals by LDF Molecular Orbital Calculations, Journal of Physical Chemistry 100 (1996), pp. 6531-6542.

[223] M. Niziurska, J. Malolepszy, G. Malata: The influence of lithium carbonate on phase composition of calcium aluminate cement paste, Procedia Engineering 108 (2015), pp. 363-370.

[224] T. Matsunović, M. Čurlin: Lithium Salts as Set Accelerators for High Alumina Cement, Cement and Concrete Research 23 (1993), pp. 885-895.

[225] T. Matsunović, M. Čurlin: Alkali Metal Salts as Set Accelerators for High Alumina Cement, Cement and Concrete Research 23 (1993), pp. 177-186.

[226] V.F.F. Barbossa, K.J.D. MacKenzie: Synthesis and thermal behaviour of potassium sialate geopolymers, Materials Letters 57 (2003), pp. 1477-1482.

[227] M. Jin, Z. Zheng, Y. Sun, L. Chen, Z. Jin: Resistance of metakaolin-MSWI fly ash based geopolymer to acid and alkaline environments, Journal of Non-Crystalline Solids 450 (2016), pp. 116-122.

[228] H.J.H. Brouwers: The work of Powers and Brownyard revisited: Part 1, Cement and Concrete Research 34 (2004), pp. 1697-1716.

[229] H.J.H. Brouwers: The work of Powers and Brownyard revisited: Part 2, Cement and Concrete Research 35 (2005), pp. 1922-1936.

[230] H.J.H. Brouwers: The work of Powers and Brownyard revisited: Part 3, in: 12th International Congress on the Chemistry of Cement, Montréal, Canada (2007).

[231] H.J.H. Brouwers: A hydration model of Portland cement, Eindhoven University of Technology, Eindhoven, 2011.

[232] R.P. Williams, R.D. Hart, A. van Riessen: Quantification of the extent of reaction of metakaolin-based geopolymers using X-ray diffraction, scanning electron microscopy, and energy-dispersive spectroscopy, Journal of the American Ceramic Society 94 (2011) pp. 2663-2670.

LIST OF ABBREVIATIONS AND SYMBOLS

Abbreviations

AAM	alkali-activated material(s)
AAS	alkali-activated slag
ANA	analcime-type
ATR FT-IR	attenuated total reflection Fourier transform infrared spectroscopy
aW	stored above water (r.H. ≈ 100 %)
BA	bottom ash
BET	specific surface area, determined by N_2-sorption
$c_{silica,dried}$	total amount of silica in the dry powder
$c_{silica,paste}$	total amount of silica in the paste
CAC_REF	commercial, CAC-based repair mortar
C-A-S-H	calcium aluminosilicate hydrate
CB	complex band
CEM III/B	blast furnace cement
CEM I	Portland cement
CEN	European Committee for Standardization
cf.	see for
CP	cross polarization (NMR)
CR	silica rich residue of the chlorosilane production
d	tricalcium aluminate (C_3A)
d_0	average edge length of the cross section before the acid-treatment
D4R	double 4 rings
DIN	German Institute for Standardization/ German Standard
DIN EN	European Standard
DIW	direct ink writing
DTG	differential thermogravimetry
e.g.	for example
$F_{D,acid}$	failure load for the acid stored specimens
$F_{D,water}$	failure load for the water stored specimens
FA	fly ash
Fig.	Figure
fs	feedstock
FR	fiber-reinforced
FWHM	full width at half maximum
GP	geopolymer(s)
GPM	geopolymer mortar
GSD	grain size distribution

h	height
HT	high-temperature
ICP-OES	inductively coupled plasma optical emission spectrometry
IR	insoluble residue
l	length
l_{max}	original length of the dilatometry samples (= maximum length)
i.e.	id est
LIS	Laser-induced slip casting
LOI	loss on ignition
m	mass
m_r	residual mass
MC (0.X)	standard concrete specimens (X = w/b = 0.90 or 0.40)
MK	metakaolin
MS	microsilica/ silica fume
MAS NMR	magic angle spinning nuclear magnetic resonance spectroscopy
OPC	Ordinary Portland Cement
OPG	one-part geopolymer(s)
OPG-SL	ground granulated blast furnace slag containing OPG
OPG_{mortar}	OPG-based mortar
$OPG\text{-}SL_{mortar}$	slag containing OPG_SL-based mortar
PPCC	Portland Pozzolana Cement Concrete
PSD	particle size distribution
q_1; q_2	mass factors for the calculation of OPG-SL
q_n	quotient for the determination of slag mass in OPG-SL
r.H.	relative humidity
REF	reference
RHA	rice husk ash
Rili-SIB	DAfStb Guideline "*Schutz und Instandsetzung von Betonbauteilen*"
R_s	remaining silica
RS	CEN standard sand
RT	room temperature (20 – 23 °C)
R_{acid}	compressive strength after storage in sulfuric acid
$R_{residual}$	relative residual compressive strength after storage in sulfuric acid
R_{water}	compressive strength after under water storage
RWTH	Rheinisch-Westfälische Technische Hochschule (Aachen)
SE	secondary electrons
SEM	scanning electron microscopy
SL/GBSL	ground granulated blast furnace slag
SRA	shrinkage retarding agent

Si^n (mAl)	silicon sites of ^{29}Si MAS NMR with different (aluminum) environments
Tab.	Table
TC	total carbon content
TG(A)	thermogravimetric analysis
UHPC	Ultra High Performance Concrete
UV	ultra violette (light)
uW	stored under water
V	volume
wt.(%)	relative mass content
w_{dried}	water content of the dry powder
w_{paste}	water content of the paste
w/b	water/ to binder ratio
w/s	water/ to solids ratio
$X_{f,D}$	effective strength related corrosion depth
XRD	X-ray diffraction

Symbols

α	corundum (α-Al_2O_3)
α[HCl]	degree of reaction of the silica, based on the dissolution method
λ	wavelength
ρ	density (g/cm³)
Δm	change in length
Δl	change in length
°2Θ	diffraction angle (XRD)

Chemical components and phases

A	zeolite A
a	alite (C_3S; tricalcium silicate)
Al	aluminum
Al_2O_3	aluminum oxide
$Al(OH)_3$	aluminum hydroxide
An	anhydrite ($CaSO_4$)
Ar	argon
B	bayerite ($Al(OH)_3$)
b	belite (C_2S; dicalcium silicate)
C	calcite ($CaCO_3$)
c	cristobalite (SiO_2)
c1	intermediary carnegieite

CA	monocalcium aluminate
CAC	calcium aluminate cement
CaO	calcium oxide
$Ca(OH)_2$	calcium hydroxide
Ch	chabazite
Cn	carnegieite
CO_2	carbon ddioxide
EMT	zeolite EMT
F	fauyasite-type zeolite (including zeolite Y)
f	brownmillerite (C_4AF; tetracalcium aluminate ferrite
Fe_2O_3	iron oxide
g	gehlenite
G	gibbsite
Gy	gypsum ($CaSO_4 \cdot 2H_2O$)
H	halite
HC	hydroxysodalite
H_2SO_4	sulfuric acid
HCl	hydrochloric acid
HS	hydrosodalite
K_2O	potassium oxide
L1	lithium aluminate ($LiAlO_2$)
L2	lithium aluminate ($LiAl_5O_8$)
LA	lithium aluminate
LC	lithium carbonate (Li_2CO_3)
LH	lithium aluminate hydroxy hydrate ($LiAl_2(OH)_{7} \cdot {}_2H_2O$)
LiS	lignin sulfonate
M	mullite
Me	merwinite
MgO	magnesium oxide
N	nepheline
n	natrite
N_2	nitrogen
N_t	monoclinic trinepheline
Na_2O	sodium oxide
NaOH	sodium hydroxide
N-A-S(-H)	sodium aluminosilicate (hydrate)
NFS	naphthalenesulfonate
P	potassium magnesium phosphate/ zeolite P
p	portlandite ($Ca(OH)_2$; CH)

P_2O_5	phosphor pentaoxide
PCE	polycarboxylate ether
Pl	plagioclase (= albite)
PVC	polyvinyl chloride
q	quartz
S	sodalite *sensu stricto*
S1	fine sand
S2	anhydrous sodalite-type
SA	sodium aluminate
SAH	sodium aluminate hydrate
SH	hydrated silicic acid
Si	silicon
SiC	silicon carbide
SiO_2	silicon oxide
SS	sodium silicate/ waterglass
T	thermonatrite
TiO_2	titanium oxide
Tr	tridymite

SUMMARY

In this work, one-part geopolymers were synthesized by mixing solid silica and sodium aluminate with water. Two industrial silicas, a microsilica and a residue of the chlorosilane production, as well as two differing batches of biogenic silica (rice husk ash) have been used as silica feedstocks (Chapter 2). The alumina feedstock incorporated the alkaline activator, thus, just water must be added to start the reaction. Therefore, the handling and alteration of highly alkaline activator solutions, such as sodium hydroxide solutions or sodium silicate solutions is avoided on site.

Viscometer and spread flow tests have been conducted on the one-part mixes to evaluate the general rheological properties of the OPG pastes and mortars. The fresh pastes appeared to be stiffer than OPC-based pastes, even when higher water-binder ratios (w/b by mass) were applied to the OPG pastes. This is mainly attributed to the viscosity of the pore solution and the lower densities of the solid feedstocks. At equal w/b by mass, the viscosity of the OPG fresh pastes increased with increasing silica content up to a certain content, while the yield stresses increased continuously due to the simultaneous decrease of the w/b by volume (Chapter 3). Several superplasticizers were tested and promising results were found for lignin sulfonates. The workability of the OPG fresh mortars is very variable by adjusting the paste content. Depending on the paste content the fresh mortars can be applied manually or by spraying in various layer thicknesses (Chapter 6).

Pastes were cured at elevated temperatures (60–90 °C) and relative humidity (r.H.) of 80–98 %. After curing the pastes at 80 °C and 80% r.H for one day, the reaction virtually ceased. No significant further changes of the phase assemblage have been observed for longer curing times. For MS- and CR-based OPG, the reaction ceased, when a SiO_2/Al_2O_3-ratio of ~2 mol/mol was reached in the reaction products, i.e. in MS/CR-based OPG mixes with an initial SiO_2/Al_2O_3 > 2 mol/mol, always a fraction of the silica feedstock remained unreacted. CR- and MS-based OPG mixes formed geopolymer- zeolite composites. Zeolite A and hydrosodalite were the dominant crystalline phases. Depending on the molar SiO_2/Al_2O_3 ratio of the starting mixes their relative amounts varied. For CR-based mixes, zeolite A was always the dominant crystalline phase and more diverse zeolites formed. In contrast to that, RHA-based OPG achieved higher degrees of incorporation of silicon into the aluminosilicate network and can provide zeolite free geopolymeric gel formation, depending on the pre-treatment of the silica feedstock. The compressive strength of the geopolymer-zeolite composites was lower as the compressive strength of a pure geopolymer (Chapter 4), mainly due to a significantly denser and glassy microstructure with less interfaces.

The major part of the thermal dehydration occurred between 60 °C and 200 °C. Up to 700–800 °C only minor changes of the phase assemblage have been observed for the composites. Furthermore, only low to moderate linear thermal shrinkage was observed. The samples gained compressive strength and stayed above 100% of the as-cured state. At higher temperatures, the samples underwent new phase formation. That was connected to partial melting, sintering and the loss of the mechanical strength. Depending on the paste composition either ceramic or amorphous phases from during exposure to 1000 °C (Chapter 5).

MS-based mortars provided a significantly faster hardening than the pure pastes (Chapter 7), due to the induced nucleation sites from the aggregates. By adding CaO up to a certain content the hardening can be further accelerated, without a fundamental change of the forming reaction products. Compared to other AAM, very low ambient drying/wetting shrinkage/expansion was observed for the mortars (Chapter 8). This is mainly attributed to the initial curing at elevated temperatures and the mainly physical bond water in the composites (zeolitic water).

Regarding the very promising bond behavior between mortars and concrete substrate, curing only at ambient temperatures can be beneficial. Depending on the processing of the silica feedstock, gas forming agents can be included as traces in the silica feedstocks. Depending on the curing temperature and the correlating reaction speed, those gas forming agents can introduce microcracks. In such a case the bond between OPG mortar and concrete is stronger than the actual tensile strength of the OPG mortar.

The figure below gives a summary of the general relationships of the factors influencing the properties of the considered OPG, synthesized with silica and SA and thus excluding the additive manufacturing.

General relationships, observed in this work, for the properties of silica-based OPG pastes and mortars, activated with SA. Big black arrows represent major influences, whereas, grey arrows represent minor influences.

The OPG mortars provide very high resistance against sulfuric acid (pH 1) and provided residual compressive strengths up to > 77 % of the reference. The acid initially attacks parts of the paste and a secondary silica gel precipitates at the acid-mortar interface. This gel protects the remaining reaction products and decreases the further corrosion speed. Furthermore, huge parts of the corroded layer are not dissolved from the specimen and can still provide protection for a potential substrate. In terms of sulfuric acid resistance, above a critical CaO content from potential

additives, the formation of gypsum is introduced. This causes expansion, cracking and the decrease of the sulfuric acid resistance. (Chapter 9).

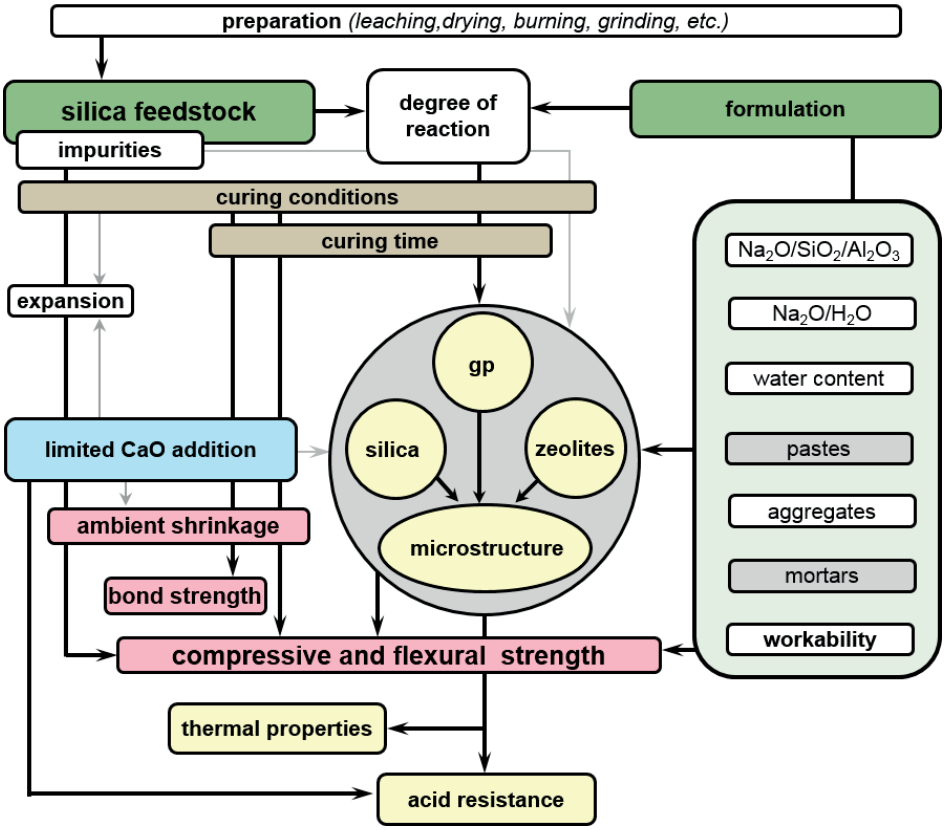

First investigations on the additive manufacturing by LIS revealed promising behavior. In this context lithium aluminate revealed significantly lower viscosities of the fresh pastes and the possible manufacturing of complex structures (Chapter 10).

ZUSAMMENFASSUNG

In dieser Arbeit wurden einkomponentige Geopolymere aus verschiedenen Silkas (Mikrosilika, Filterrückstand der Chlorosilanherstellung, Reisschalenasche) und Natriumaluminat synthetisiert. Der alkalische Aktivator ist im Aluminat enthalten und so muss nur noch Wasser zugefügt werden, um die Reaktion zu starten. Dadurch wird der Umgang mit hochalkalischen Aktivatorlösungen im Baubereich vermieden. Die rheologischen Untersuchungen zeigten grundsätzlich steifere Konsistenzen der Geopolymerleime im Vergleich zu konventionellen CEM I basierten Leimen. Ursächlich dafür sind vor allem die hohe Viskosität der Aktivatorlösung und die geringeren Dichten der Ausgangsstoffe, weshalb bei gleichen massebezogenen Wassergehalten immer geringere volumenbezogene Wassergehalte resultieren (Kapitel 3).

Für eine zügige Erhärtung wurden die Leime bei erhöhten Temperaturen (60–80 °C) für maximal 7 Tage wämebehandelt. Nach einem Tag (80 °C) ist der Hauptteil der Reaktion abgeschlossen. In Abhängigkeit der eingesetzten Silka kommt es dabei zur Bildung von zeolithhaltigen Kompositen (Mikrosilika und Filterrückstand) oder reinem Geopolymergel (Reisschalenasche). Die Komposite zeichnen sich dabei durch ein SiO_2/Al_2O_3 Verhältnis von ≈ 2 mol/mol in den Reaktionsprodukten aus und überschüssige Silika bleibt unreagiert zurück, wohingegen die zeolithfreien Formulierungen $SiO_2/Al_2O_3 > 2$ in den Reaktionsprodukten ermöglichen. Die resultierende, dichtere Mikrostruktur begünstigt höhere mechanische Festigkeiten der entsprechenden Formulierungen, wenn überlappende Effekte ausgeschlossen werden können (Kapitel 4). Die thermische Entwässerung der Reaktionsprodukte beginnt ab 60 °C, wobei der Hauptteil bis 200 °C erfolgt und nach 400 °C alle Proben nahezu wasserfrei sind. Im Beriech der thermischen Entwässerung kommt es bevorzugt zum Festigkeitszuwachs der Proben. Dabei treten unterhalb von 700–800 °C keine signifikanten Phasenumwandlungen und nur moderates, lineares Schwinden auf. Bei noch höheren Temperaturen kommt es zum Sintern/Schmelzen und damit verbunden zur Bildung von neuen Hochtemperaturphasen, Verformungen und zum Verlust der mechanischen Festigkeit (Kapitel 5).

Vor allem durch die Funktion der Sandkörner als Kristallisationskeime, ist das Erhärten der Mörtel auch bei Raumtemperatur beschleunigt (Kapitel 7). Verglichen mit anderen AAM aus der Literatur wurde ein sehr gutes Schwindverhalten (Kapitel 8) bei Raumtemperaturlagerung dokumentiert. Darüber hinaus wurden exzellente Haftzugfestikeiten (Kapitel 8) erzielt, wobei höhere Haftzugfestigkeiten ohne initiale Wärmebehandlung (Expansion) erreicht wurden. Der Einsatz von Calcium beschleunigt die Erhärtung (Kapitel 7), aber verringert die Säurebeständigkeit.

Oberhalb von einem krittischen Gehalt kommt es zur Gipsbildung beim Kontakt mit Schwefelsäure (Kapitel 9).

Durch den Einsatz von Lithiumaluminat kommt es zur Änderung der Reaktionskinetig und die entsprechenden Leime zeigen ein sehr vielversprechendes Verhalten im Sinne der additiven Fertigung (Kapitel 10).

CURRICULUM VITAE

Personal data

Name:	Patrick Sturm
Date of birth:	August 22, 1986
Place of birth	Lutherstadt Eisleben, German Democratic Republic

Education

2009–2012	Martin-Luther-Universität Halle-Wittenberg, Germany Master thesis (in Applied Geosciences): ´Metal benzoate-hydrates: Synthesis, characterization and influence on the hydration of cements´ (in German), supervised by Prof. Dr. Dr. H. Pöllmann.
2006–2009	Martin-Luther-Universität Halle-Wittenberg, Germany Bachelor thesis (in Applied Geosciences): ´Comparison of methods for the Characterization of the loading capacity´ (in German), supervised by Prof. Dr.-Ing. C. Lempp.
1999–2006	Paul-Gerhardt-Gymnasium, Gräfenhainichen, Germany

PhD research/ work

2013–present	BAM Federal Institute for Materials Research and Testing, Berlin Division 7.4 Technology of Construction Materials researcher in the field of geopolymers; maintenance
2013-present	Eindhoven University of Technology, The Netherlands Department of the Built Environment PhD student in the field of geopolymers
2012–2013	IBG-Krüger, Lutherstadt Wittenberg, Germany surveys for the evaluation of building grounds, monitoring of construction areas and factory sites

PUBLICATIONS

Journals

1. Sturm, P.; Gluth, G.J.G.; Jäger, C.; Brouwers, H.J.H.; Kühne, H.-C.: Sulfuric acid resistance of one-part alkali-activated mortars, *Cement and Concrete Research*, Vol. 109, p. 54-63 (2018).

2. Watolla, M.-B.; Gluth, G.J.G.; Sturm, P.; Rickard, W.D.A.; Krüger, S.; Schartel, B.: Intumescent Geopolymer-Bound Coatings for Fire Protection of Steel, *Journal of Ceramic Science and Technology*, Vol. 8, p. 351-363 (2017).

3. Greiser, S.; Sturm, P.; Gluth, G.J.G.; Hunger, M.; Jäger, C.: Differentiation of gel, zeolite phases and water species in geopolymer-zeolite composites, *Ceramics International*, Vol. 43, p. 2202-2208 (2017).

4. Sturm, P.; Gluth, G.J.G.; Brouwers, H.J.H.; Kühne, H.-C.: Synthesizing one-part geopolymers from rice husk ash. *Construction and Building Materials*, Vol. 124, p. 961-966 (2016).

5. Sturm; P.; Gluth, G.J.G.; Simon, S.; Brouwers, H.J.H.; Kühne, H.-C.: The effect of heat treatment on the mechanical and structural properties of one-part geopolymers-zeolite composites. *Thermochimica Acta*, Vol. 635, p. 41-58 (2016).

6. Sturm, P.; Greiser, S.; Gluth, G.J.G.; Jäger, C.; Brouwers, H.J.H.: Degree of reaction and phase content of silica-based one-part-geopolymers investigated using chemical and NMR spectroscopic methods. *Journal of Materials Science*, Vol. 50, p. 6768-6778 (2015).

Conferences

1. Sturm, P.; Gluth, G. J. G.; Greiser, S.; Jäger, C.; Brouwers, H.J.H.; Kühne, H.C.: Structure, acid-resistance and high-temperature behavior of silica-based One-Part geopolymers and geopolymer-zeolite composites. International Conference on Alkali Activated Materials and Geopolymers. Tomar, Portugal, May 27-June 1, (2018).

2. Gluth, G. J. G.; Sturm, P.; Greiser, S.; Jäger; C.; Kühne, H.-C. One-part geopolymers and geopolymer-zeolite composites based on silica: factors influencing microstructure and engineering properties. In Proceedings of the 42nd International Conference and Expo on Advanced Ceramics and Composites (eds xxx) Ceramic Engineering and Science Proceedings, Vol. xx, Issue xx, pp. xxx–xxx (Wiley, 2018).

3. Sturm, P.; Lüchtenborg, J.; Hlavacek, P.; Gluth, G.J.G.; Kühne, H.-C.; Günster, J.: Additive Manufacturing of Geopolymers by Selective Laser Curing. Proceedings of the 6th International Conference on Non-Traditional Cement & Concrete. Brno, Czech Republic, ISBN 978-80-214-5507-8, p. 307 (2017).

4. Sturm, P.; Gluth; G.J.G.; Greiser, S.; Jäger, C.; Brouwers, H.J.H.; Kühne, H.C.: Investigations on One-part Geopolymers Synthesized from different Silica Sources. *Proceedings of the 6th International Conference on Non-Traditional Cement & Concrete.* Brno, Czech Republic, ISBN 978-80-214-5507-8, p. 299-306 (2017).

5. Sturm, P.; Gluth; G.J.G.; Greiser, S.; Jäger, C.; Brouwers, H.J.H.; Kühne, H.C.: Properties of One-part Geopolymers Synthesized from different Silica Sources. *92nd DKG Annual Conference & Symposium on High-Performance Ceramics*. Berlin, March 20-22 (2017).

6. Sturm, P.; Lüchtenborg, J.; Hlavacek, P.; Günster, J.; Kühne, H.-C.; Gluth, G.J.G.: Additive Manufacturing of Geopolymers by Selective Laser Curing. *92nd DKG Annual Conference & Symposium on High-Performance Ceramics*. March 20-22 (2017).

7. Greiser, S.; Sturm, P.; Gluth, G.J.G.; Hunger, M.; Jäger, C.: ^{29}Si-^{27}Al NMR to Verify and Distinguish Q^n(mAl) Sites in Zeolites and Geopolymers. *57th Experimental Nuclear Magnetic Resonance Conference*, Wyndham Grand Hotel, Pittsburgh, Pennsylvania April 10–15, p. 109 (2016).

8. Sturm, P.; Gluth; G.J.G.; Brouwers, H.J.H.; Kühne, H.C.: Structural Investigations on one-part geopolymers with different chemical composition. *Tagung Ibausil*, Monographie Bd. 19 Weimar, Deutschland, p. 857-864 (2015).

9. Sturm, P.; Gluth; G.J.G.; Lindemann, M.; Greiser, S.; Jäger, C.; Brouwers, H.J.H.: Structural Investigations on One-Part Geopolymers after Different Drying Regimes. *Proceedings of the 34th Annual Cement and Concrete Science Conference*. Sheffield, England, p. 37-40 (2014).

10. Greiser, S.; Gluth, G.J.G.; Sturm, P.; Brouwers, H.J.H.: ^{27}Al-^{1}H and ^{27}Al-^{29}Si Double Resonance NMR of One-part Geopolymers. *Proceedings of the 5th International Conference on Non-Traditional Cement & Concrete*. Brno, Czech Republic, ISBN 978-80-214-4867-4, p. 91-94 (2014).

11. Sturm, P.; Gluth, G.J.G.; Schmidt, W.; Astorg, A.; Brouwers, H.J.H.: Rheological properties of microsilica and sodium aluminate based one-part geopolymers compared to ordinary Portland cement. *Proceedings of the 5th International*

Conference on Non-Traditional Cement & Concrete. Brno, Czech Republic, ISBN 978-80-214-4867-4, p. 241-244 (2014).

12. Pöllmann, H.; Sturm, P.; Kaden, R.: Hydration control of Portland cement and Calcium Aluminate cement using different earth alkali benzoate hydrates. *Proceedings of the 35th International Conference on Cement Microscopy.* Rosemont, Illinois, U.S.A. ISBN 1-930787-03-0; p. 302-356 (2013).

13. Sturm, P.; Pöllmann, H.: Der Einfluss von Metall-Benzoat-Hydraten auf die Hydratation von Tonerdezement und Portlandzementklinker. *GDCh-Tagung Bauchemie*. Dübendorf, Schweiz. ISBN 978-3-936028-72-0, Bd. 45, p. 250-255 (2012).

Patents

1. Sturm, P.; Gluth, G.J.G.; Kühne, H.-C.; Hermes, R.: Mörtel und Beton auf Basis von einkomponentigen Geopolymeren für den Kanalbau und die Kanalsanierung. *German patent application*, file number: 10 2017 120 798.8 (2017).

In terms of sustainable civil engineering, alkali-activated materials (AAM) attract steadily increasing attention since decades. In the past, especially the handling of the highly alkaline activator solutions limited their social and economic acceptance. By supplying the alkaline activator in solid form, those problems are avoided and only water has to be added to initiate the reaction to form so called One-Part Geopolymers (OPG).
The main purpose of this work is the basic understanding of silica-based OPG systems in terms of, reactivity, phase assemblage, microstructure and mechanical strength after curing at different conditions. The influence of industrial and biogenic silica feedstocks on the reactivity and the phase formation is of particular importance in this context.
Further objectives are the study of the high-temperature resistance and the resistance against sulfuric acid attack of the OPG for applications as protective coatings, e.g. as repair mortars in sewers. Therefore, also the bond behavior and the drying shrinkage, as well as in situ applications of fresh OPG mortars are considered.

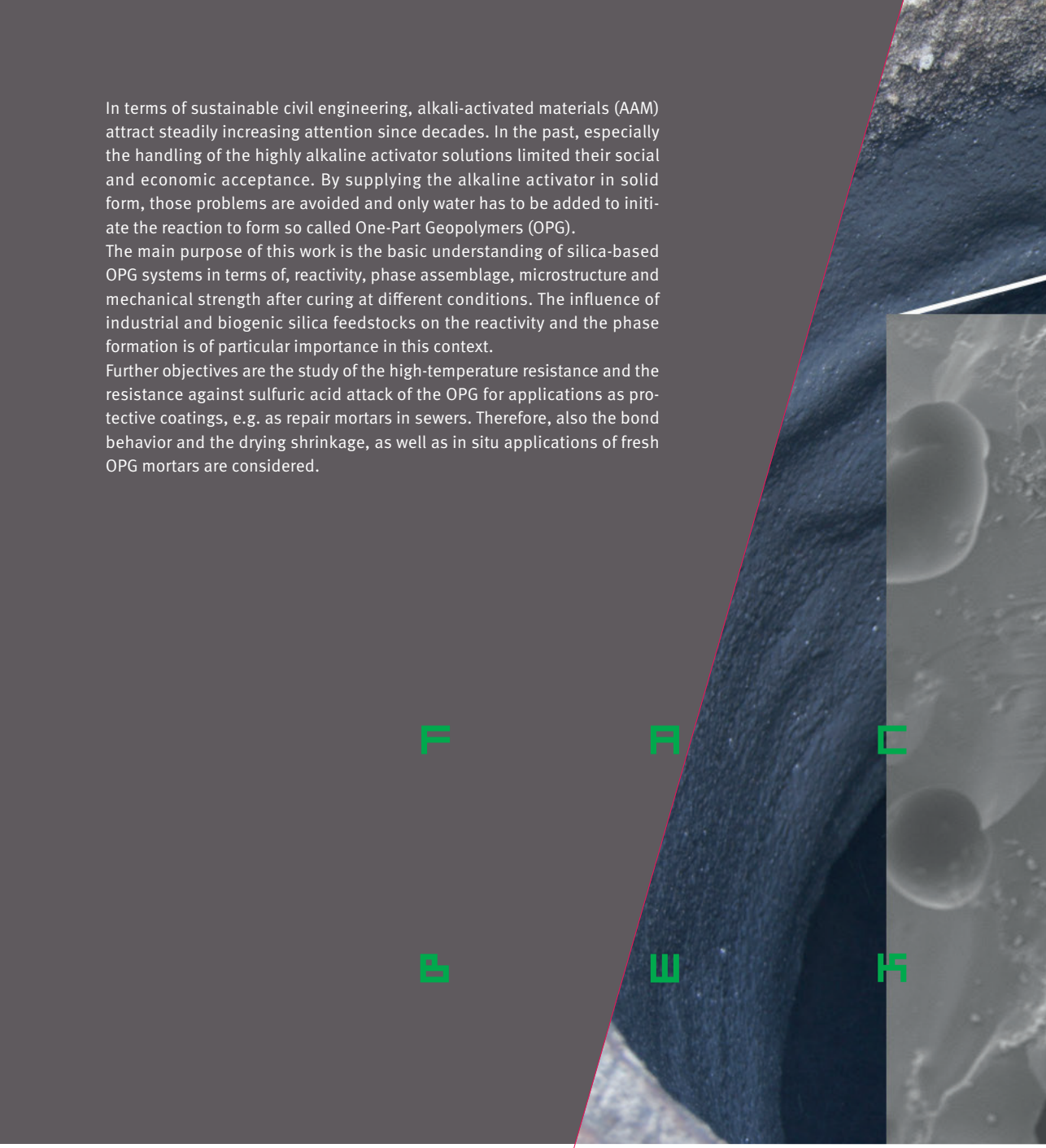

F A C

B W K

E H T

/ Department of the Built Environment

TU/e Technische Universiteit **Eindhoven** University of Technology